

Investigations into Asphaltene Deposition, Stability, and Structure

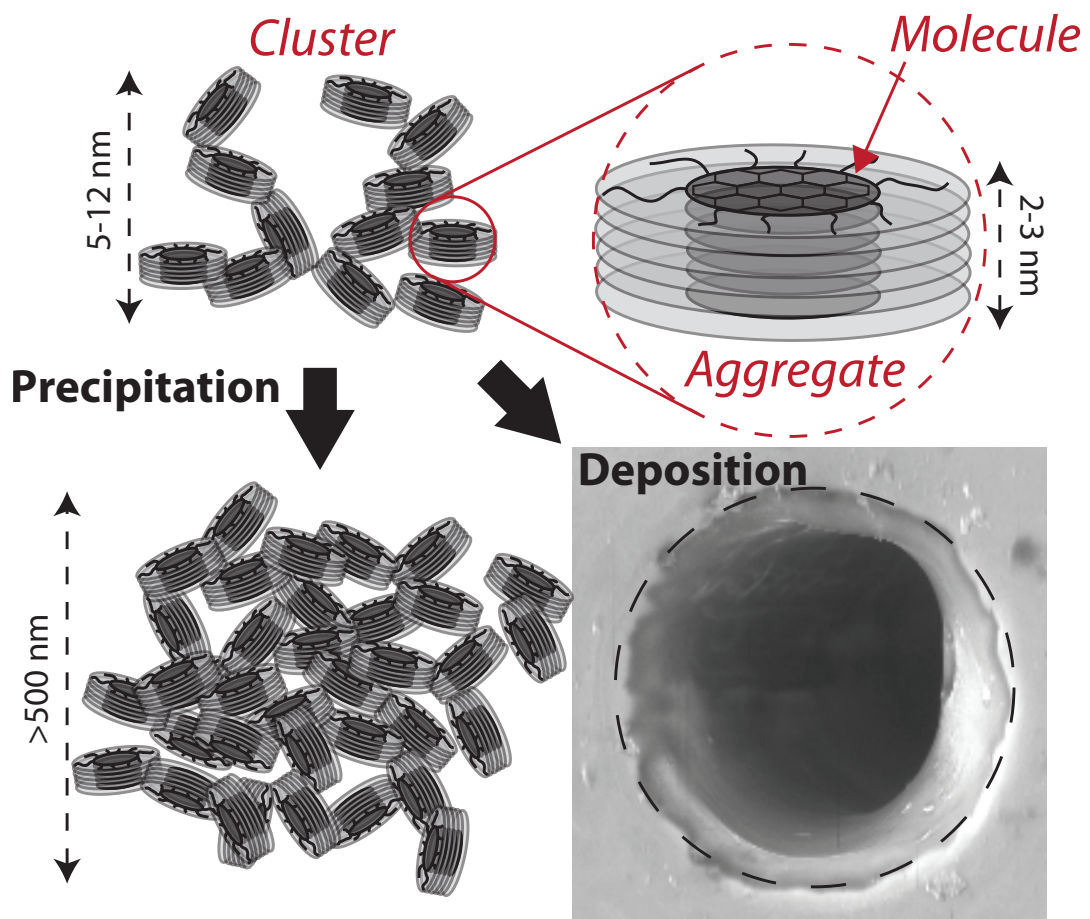
by

Michael Paul Hoepfner

A dissertation submitted in partial fulfillment
of the requirements for the degree of
Doctor of Philosophy
(Chemical Engineering)
in The University of Michigan
2013

Doctoral Committee:

Professor H. Scott Fogler, Chair
Professor Peter Green
Professor Ronald G. Larson
Professor Michael J. Solomon



© Michael Paul Hoepfner 2013
All Rights Reserved

To Susan and Greg,
the most supportive parents I could have ever asked for.

ACKNOWLEDGEMENTS

Many individuals are to thank for not only the successful completion of this dissertation, but also for the high quality of life I was fortunate to have throughout my doctoral studies. My experience in completing my doctoral studies has been both the most challenging and most enjoyable experience in my life to date. I am certain this is a non-unique perspective, and I believe most acknowledge that completing a dissertation is both immensely frustrating and rewarding. All graduate students look forward to a payoff after months (or years) of struggle on a difficult problem, and this dissertation contains a thorough discussion of these events that I have experienced. However, I believe that the *real* goal of doctoral studies is not to produce a dissertation that outlined successful projects, but rather the lessons learned while on the painstaking journey to do so. Personal development is linked to the *frustrating* times of independent research, and I could not have made it through the seemingly endless supply of these moments without the support of mentors, advisors, colleagues, friends and family.

I would first like to acknowledge and thank Prof. H. Scott Fogler, my research advisor and the chair of my doctoral committee. Prof. Fogler has had a long and immensely successful academic career, and I am thankful that he made the decision to prolong it in order to supervise my research and intellectual development. I am continually impressed by his commitment to education and mentorship. After having literally written the book on chemical reaction engineering, he still treats every lecture as a new and unique experience. I can only hope to maintain a similar level of focus

throughout my career, and Prof. Fogler will always be my gold standard for excellence in education. I would also like to thank Prof. Fogler for allowing me great flexibility in selecting research projects. While open-ended projects can initially be confusing and frustrating, I firmly believe that this approach allowed me to develop valuable confidence to conduct independent research. In addition, I am thankful for the unique opportunities that I have been offered as a member of Prof. Fogler's research group. I have been incredibly fortunate to be able to frequently present my research at national and international conferences. The opportunity to travel to the PetroPhase conference each year allowed me to stay at the cutting edge of asphaltene science. The chance to supervise visiting scholars taught me that I truly cherish mentorship and developing research abilities in students. This experience was a strong driving force encouraging me to pursue an academic career. I am forever grateful to have been a member of Prof. Fogler's research group.

The remaining members of my doctoral committee: Prof. Peter Green, Prof. Ronald Larson and Prof. Michael Solomon have provided valuable insight into my dissertation studies and I am grateful for their assistance throughout the years. In fact, the entire course of my research shifted focus after my Preliminary Exam at the suggestion of my committee. The push to pursue scattering techniques in order to better understand asphaltenes on the nanometer length scale originated with my committee members. I am grateful for this shift because I have found immense enjoyment in the application of scattering techniques and I plan on continuing a lifelong use of such tools. I am thankful for the time sacrifice and valuable insight from my doctoral committee members.

I have been fortunate to have been able to serve as a graduate student instructor (GSI) on four occasions with Prof. Michael Solomon, Prof. Henry Wang, Prof. H. Scott Fogler and Prof. Timothy Scott. My experience as a GSI has been truly valuable and a strong motivator of my desire to pursue an academic career. I learned

the difficulty associated with managing a classroom full of students and the delicate time balance that must occur between research and instruction. In addition, my opportunity serving as a GSI under Prof. Scott taught my invaluable lessons about the early stages of academic careers. I am very grateful for the numerous discussions and assistance that Prof. Scott provided to me while applying for academic job positions.

The Department of Chemical Engineering staff are also in need of a generous acknowledgement, and my long stay in the department would have certainly been even longer if it were not for their support and assistance. Laura Bracken has been a selfless helper in all activities of the Fogler Research Group and the group could not operate without her. I am thankful for the time that Michael Africa, Pamela Bogdanski, Harald Eberhart, Shelly Fellers, Pablo Lavalle, Susan Hamlin, Christine Mollering, Laurel Neff and Sandra Swisher have all spent helping me with all sorts of projects and odd jobs.

I also owe a tremendous debt of gratitude to my colleagues in the Fogler Research Group. The early mentorship that I was provided from Dr. Tabish Maqbool, Dr. Michael Senra and Dr. Zhenyu Huang were invaluable in developing my research project and abilities. In addition, the numerous travels and research discussions that I had with Tabish were always an enjoyable experience. The interactions I have had with the former and current members of the Fogler Research Group have greatly impacted my development and work in an incredibly positive manner. I would like to thank Nasim Haji Akbari Balou for her ability to translate her immense comprehension of scientific principles into direct and very difficult lines of questioning into my research projects. The quality of my work would not be as it is without her contributions to research discussions and group meetings. Cláudio Vilas Bôas Fávero is only recently starting his official doctoral studies, but his involvement in the Fogler Research Group began many years ago. Claudio is an invaluable contributor to not

only my research but also the entire research group. Chapter IV would not have been possible with Claudio's assistance, and I will always remember our amazement when we first arrived at the neutron scattering facility. I would also like to thank the remaining doctoral students in the Fogler Research Group, Yingda Lu and Nina Gasbarro, for their positive impact on the group overall.

In addition to current and previous doctoral students, there are numerous visiting researchers that deserve specific mention. I would like to thank Varun "Sam" Chuenmeechao, Vipawee "Yen" Limsakoune and Wattana "Zack" Chaisoontornytin for their dedicated work ethic and help in completing the asphaltene deposition research project. The visiting students from the Petroleum and Petrochemical College at Chulalongkorn University that frequent the Fogler Research Group have a long reputation of being immensely dedicated workers. I am very happy to say that Sam, Yen and Zack exceeded all expectations and contributed vastly into the capillary deposition studies. Chapter II would have not been possible without their assistance.

My research would not have been possible without the financial assistance, research suggestions and crude oil samples, all provided by the University of Michigan Industrial Affiliates Program. Throughout my studies, program members have included: BP, Chevron, ConocoPhillips, MSIKenny, NALCO Champion, Schlumberger, Shell, StatOil, and Total. The numerous scattering experiments that I performed were all possible though beamtime proposals from the High Flux Isotope Reaction (HFIR) and the Spallation Neutron Source (SNS) at Oak Ridge National Laboratory, the Institut Laue-Langevin (ILL), and the Advanced Photon Source (APS) at Argonne National Laboratory. In addition, my understanding of scattering techniques was greatly enhanced through my interactions with Dr. Paul Butler at the National Institute of Standards and Technology's (NIST) Center for Neutron Research. I would also like to acknowledge the support of NIST for allowing me to attend a two-week course on scattering techniques. Individually, I would like to thank Dr. Yuri Mel-

nichenko (HFIR), Dr. Lilin He (HFIR), Dr. William Heller (SNS), Dr. Lionel Porcar (ILL), and Dr. Byeongdu Lee (APS) for their invaluable assistance in helping me learn about and using the various scattering instruments that were utilized in this dissertation.

I want to thank my parents, Susan and Gregory, for being supportive of my long move across the country and for all of the help (and care packages) that have pulled me through my graduate studies. Throughout my entire life, I have always had consistent and strong encouragement from my parents. I have grown up knowing that no matter the situation, I have two loving and supportive parents that would do anything to make sure I always have a home. While in Michigan our family was stricken with major medical emergencies and I regret that I was not nearer during these hard times. I am forever grateful that we are all still here. I hope that some day I can return the favors and privileges that I received while growing up in an amazing household.

In a few years, my dissertation will be joined by the works of my brother Danial (Political Science) and my sister Amanda (Biology), who are both in the process of completing their doctoral studies. I have a deep respect for the time and efforts that both of them are devoting to their studies, and my efforts pale in comparison to theirs. I have been fortunate to avoid employment while in school, and I can only image the struggles that Danial has undergone in participating in both simultaneously. As for Amanda, it is clear that my comfortable desk and laboratory represent a significantly more habitable environment when compared to the jungles of Borneo where Amanda is currently studying Orangutans.

The friendly interactions of the students in the department was a pivotal deciding factor for me choosing the University of Michigan for my doctoral studies. I would like to specifically thank Adam Holewinski, Christine Andres and Elizabeth Stewart for being trusted friends throughout all of our studies. One positive aspect of a six-

year long doctoral degree is that I have had the fortune to acquire more friends that I can list. I hope to see all of these people in the future during my return trips to the Big House and the Michigan Summer Beer Festival.

I would also like to thank my Michigan family, starting with my best friend, Allison Dickie. I have grown so much as a person over the past five years with her and without her love and support, this dissertation would not have been possible. Through Allison I have had the great opportunity to be introduced to the wonderful Dickie and Bowman families. I want to thank Steve and Lori Dickie and Mona Bowman for inviting me to every family occasion so I always felt included. I have thoroughly enjoyed my adventures with Lindsay, Sean and Emily I hope to continue heading up to the cottage for many more summer vacations. In addition I'd like to thank Kristie, Neil, Pat and Stacy for taking me in as another family member. I would also like to thank the people at the Main St. house (now at the 7th St. house), Nikki, Frances, Amanda and Josh for being friendly to such a strange engineer.

TABLE OF CONTENTS

DEDICATION	ii
ACKNOWLEDGEMENTS	iii
LIST OF FIGURES	xii
LIST OF TABLES	xviii
LIST OF APPENDICES	xix
NOMENCLATURE	xx
ABSTRACT	xxii
CHAPTER	
I. Introduction	1
1.1 A Brief History of Asphaltenes	3
1.2 Contemporary Asphaltene Research	6
1.3 Asphaltene Molecular and Aggregate Structure	9
1.4 Asphaltene Precipitation Kinetics	10
1.5 Asphaltene Research Philosophy	11
1.6 Scope, Format and Outline of Dissertation	13
II. Capillary Deposition	20
2.1 Introduction	20
2.1.1 Previous Deposition Studies	23
2.2 Experimental Methods	27
2.2.1 Experimental Apparatus	27
2.2.2 Mixing Considerations	30
2.3 Results and Discussion	33
2.3.1 Electron Microscopy of Deposits	33
2.3.2 Oil Properties and Instantaneous Onset Point	34

2.3.3	Deposition as a Function of Precipitant Concentration	39
2.3.4	Application of Population Balance Model	43
2.3.5	Deposition of WY Oil	44
2.3.6	Deposition of Precipitated and Aged Asphaltenes	47
2.3.7	Oil A Normalized Plot	47
2.3.8	Deposit Profile and Previous Results Comparison	53
2.3.9	Laboratory vs. Field Asphaltene Deposition	56
2.4	Conclusions	57
III. Introduction to Small-Angle Scattering and Fractals		59
3.1	Introduction	59
3.2	Small-Angle Scattering Background	60
3.3	Introduction to Fractals	69
IV. Asphaltene Instability by Small-Angle Neutron Scattering		72
4.1	Introduction	72
4.2	Experimental Methods	77
4.2.1	Model Oil Preparation	78
4.2.2	Time-Resolved Asphaltene Destabilization Sample Preparation	78
4.2.3	SANS Experiments	79
4.2.4	Scaling of Results	83
4.2.5	Review of Key Concepts and Findings Presented Above	84
4.3	Results and Discussion	85
4.3.1	Fractal Structure of Asphaltenes	85
4.3.2	Fractal Dimension of Insoluble Asphaltenes	91
4.3.3	R_g and M_W Measurements	95
4.3.4	Scattering Intensity vs. Asphaltene Content	103
4.4	Conclusions	106
V. Multi-scale Scattering Investigations of Asphaltene Cluster Breakup, Nanoaggregate Dissociation, and Molecular Ordering		111
5.1	Introduction	111
5.2	Experimental Methods	114
5.2.1	Small-Angle Scattering Background	114
5.2.2	Two-State Aggregation Model	118
5.2.3	Asphaltene Extraction and Solution Preparation	119
5.2.4	Scattering Procedure	120
5.3	Results and Discussion	122
5.3.1	Synchrotron SAXS Results	122
5.3.2	Cluster Breakup: Shape-Independent Fits	124
5.3.3	Local Structural Moieties	129

5.4	Asphaltene Nanoaggregate Dissociation	129
5.4.1	Two-State Aggregation Model Results	133
5.4.2	Local Molecular Ordering	137
5.5	Conclusions	140
VI.	Conclusions and Future Work	142
6.1	General Conclusions	142
6.2	Further Asphaltene Deposition Studies	145
6.2.1	Asphaltene Flow-Loop Design and Operation	146
6.2.2	Asphaltene Deposition Modeling	147
6.3	Simulation and Measurement of Asphaltene Superstructures	148
6.3.1	Simulation Tools and Validation	149
6.4	Asphaltene Clustering Population Balance Model	153
	APPENDICES	158
	BIBLIOGRAPHY	194

LIST OF FIGURES

Figure

1.1	Asphalt advertisement reproduced from <i>Paving and Municipal Engineering</i> (vol. 7, p. 17, 1894) for the organization represented by Dolphus Torrey.	7
1.2	Asphalt advertisement reproduced from <i>Paving and Municipal Engineering</i> (vol. 7, p. 18, 1894) for the organization represented by Prof. Edward J. de Smedt.	8
1.3	(A) Schematic representations of the island and archipelago possible asphaltene molecular structures. (B) Best accepted asphaltene structural hierarchy.	10
1.4	Schematic of the wellbore asphaltene deposition process.	15
2.1	Diagram of the primary experimental deposition apparatus used in this study. 1: Micrometering valve (closed during experiment). 2: Mixing capillary, 5 cm long. 3: Deposition capillary, 5 or 30 cm long. 4: Microsplitter valve. 5: Back pressure regulator, 40 psi. 6: Differential pressure transducer. 7: Pressure relief valve (closed during normal operation). 8: Pressure gauge. 9: Constant temperature water bath. 10: 10 μm porous frits.	28
2.2	Diagram of the recirculating deposition experimental apparatus. 1: Premixed oil-precipitant reservoir. 2: Magnetic stirrer. 3: Deposition capillary. 4: Differential pressure transducer. 5: Back pressure regulator, 40 psi. 6: Pressure gauge. 7: Pressure relief valve (closed during normal operation).	31
2.3	SEM images of a clean, unused capillary (left) and control experiment where only Oil A was flowed through the system (right). Both capillaries have a 0.02" ID.	33

2.4	SEM images of the deposition capillary inlet (left) and outlet (right) for three runs (#1-3) of 30 vol. % heptane in Oil A with 0.02" ID and 5 cm length capillaries. The large material found at the bottom of the run #1 capillary outlet is a contaminant, see text for rationale. Dashed circles are drawn to aid identification of inner capillary wall edge.	35
2.5	Transient pressure drop profiles for 30% Oil A in with 0.02" ID and 5 cm length capillaries. Run numbers 1-3 correspond to SEM images in Figure 2.4. Decreases in the pressure drop are believed to be due to deposits partially clearing from capillary.	36
2.6	Micrographs of deposition apparatus effluent used for onset determination at various heptane volume percents (0% to 40%). The instantaneous onset point is measured to be 40 vol. % heptane.	37
2.7	Asphaltene solubility in units of g of asphaltenes per 100 g of crude oil at 60 °C for heptane in Oil A. The dashed line represents the total asphaltene content, 9.90 ± 0.07	38
2.8	Pressure drop vs. time for Oil A diluted with various heptane volume percents in 0.01" ID capillaries of 5 cm and 30 cm lengths. All runs performed at 60 °C and 5 mL/hr.	40
2.9	Measured deposition detection times, t_d , for the first deposit to be detected as a function of heptane concentration for Oil A. Line represents a linear regression of the results.	41
2.10	Comparison of $(\Delta P - \Delta P_o)$ vs. time plot for the short (5 cm) and long (30 cm) capillaries. Two experiments for each length are shown and all experiments were performed with 30 vol. % heptane. Differences represent experimental reproducibility and results clearly demonstrates non-uniformity and that the deposit is occurring preferentially near the capillary inlet.	43
2.11	Asphaltene particle size distribution at times of 1 second (\times), 16.7 seconds (capillary inlet, $+$) and 24.1 seconds (capillary outlet, \circ) for a 35% heptane in Oil A mixture at 60 °C.	45
2.12	SEM images of the deposition capillary inlet (left) and outlet (right) for the WY Oil deposits generated in a 0.01" ID capillary with a 5 cm length at 35 vol. % heptane at 60 °C (top) and 25 vol. % and 25°C (bottom). As with Oil A, the deposit is thicker at the inlet.	46

2.13	Pressure drop profile for the 40% heptane in Oil A premixed solution that was aged for 95 hours. No deposition was detected after 14 hours of run time. Inlay is optical micrograph of the recirculating fluid. . .	48
2.14	Normalized deposition pressure drop profiles for heptane in Oil A, scaled by viscosity and the concentration of insoluble asphaltenes in the capillary. Time is shifted by the deposition detection time, t_d . . .	50
2.15	A zoomed version to show detail of the normalized deposition pressure drop profiles shown in Figure 2.14.	51
3.1	A general schematic of small-angle scattering experiments.	61
4.1	SANS results for Oil A at various heptane concentrations with a one week destabilization time. Solid line represents a fractal dimension of 1.69 and dashed line represents a slope of -4, characteristic of surface scattering.	86
4.2	SANS results of the Model Oil diluted with deuterated heptane at various concentrations and times. Solid line represents a fractal dimension of 1.98 and dashed line represents a slope of -4, characteristic of surface scattering.	87
4.3	SANS results of Oil B diluted with heptane at various concentrations and times. Solid line represents a fractal dimension of 1.23 and dashed line represents a slope of -4, characteristic of surface scattering.	88
4.4	Fractal dimension measurements of soluble (1.69 ± 0.03 , blue \circ) and insoluble (2.12 ± 0.03 , red X) asphaltenes in a sample of 30% heptane in Oil A. The scattering of the combined sample (black \bullet) from where the insoluble scattering is inferred is also included.	93
4.5	Summary of the fractal dimension measurements of soluble and insoluble asphaltenes.	94
4.6	Measured Zimm radii of gyration for Oil A, Oil B, and the Model Oil (MO) as a function of the destabilization time and heptane volume percent. Lines are intended to guide the eyes and differentiate destabilization times.	96
4.7	Asphaltene cluster molecular weight for Oil A, Oil B and the Model Oil (MO) as a function of destabilization time and heptane volume percent. Aggregation number is the number of asphaltene nanoaggregate monomers in each fractal cluster. Lines are intended to guide the eyes and differentiate destabilization times.	97

4.8	Graphical representation of the influence of heptane on the size and stability threshold of asphaltenes. As heptane is added to crude oil, the size of asphaltene clusters increases while the stability threshold decreases.	100
4.9	Log-log plot of M_W vs. R_g for <i>soluble</i> Oil A asphaltenes to determine the fractal dimension. Line represents linear regression with a slope corresponding to $D_f = 1.8 \pm 0.1$. This fractal dimension measurement is within 7% of the value obtained using Equation (4.1).	102
4.10	Comparison of the asphaltene solubility measured by the scattering intensity and by centrifugation.	105
4.11	Schematic of the proposed asphaltene precipitation mechanism. R_g^0 and D_f^0 refer to the radius of gyration and fractal dimension, respectively, of the asphaltene fractal clusters in the undiluted crude oil. Fractal clusters are not drawn to scale or to the measured fractal dimension and are intended as only rough structural guides.	108
4.12	Schematic of a possible mechanism to explain to changes in asphaltene cluster fractal dimension.	109
5.1	Schematic representation of the multiple length scales investigated in this chapter and their respective q -ranges.	114
5.2	SAXS results of A1 asphaltenes in THF, normalized by scattering contrast and volume fraction.	123
5.3	Radii of gyrations for the SAXS samples as obtained by the Zimm Approximation.	125
5.4	Molecular weights of the asphaltenes in the SAXS samples using the Zimm Approximation to calculate the zero-angle intensity.	126
5.5	Plot of the molecular weight vs. radii of gyration to estimate the average fractal dimension. Solid line represents a fractal dimension of 1.7 ± 0.1	128
5.6	SANS (markers) and SAXS (solid lines) results of A1 asphaltenes in THF, normalized by scattering contrast. Scattering intensity decreases with with decreasing asphaltene concentration and only one third of the measured SANS scattering intensities are shown to avoid cluttering the figure.	130

5.7	The relative fraction of asphaltenes in the nanoaggregate state for A1 in THF (A), K1 in THF (B), and K1 in toluene (C) as a function of the volume fraction. Solid line represents the best fit from two-state aggregation model and dashed line represents fit with a large aggregation number of $n=50$	132
5.8	WAXS results for A1 asphaltenes in THF, K1 asphaltenes in toluene, THF, and 1-MN. All samples have an asphaltene concentration of 5 vol. %. Results are arbitrarily shifted for clarity. Dashed lines represent individual Gaussian fits and background level. Red line represents the combined fit of the three Gaussians and background.	138
5.9	Schematic representation of the the three characteristic separation distances in an asphaltene nanoaggregate based on WAXS results of asphaltenes in a liquid environment.	140
6.1	Proposed temperature-induced asphaltene deposition flow-loop apparatus.	147
6.2	Schematic representation of the asphaltene nanoaggregate coarse graining procedure. A) Representation of a core-shell asphaltene nanoaggregate as a collection of spherical entities. B) Three possible binary interaction parameters between the two coarse grained type particles: core and shell. C) Qualitative representation of the interaction potential for binary interactions.	151
6.3	Potential structural variables in coarse graining procedure.	152
C.1	Top view of the CFD simulations of the mixing system. NOTE: the connecting line extends for 5 cm but not all of the result was shown due to the large aspect ratio.	170
C.2	Side view (left) and outlet view (right) of the CFD simulations of the mixing system. NOTE: the connecting line extends for a full 5 cm but figure was shortened due to the large aspect ratio. By the time the mixture reaches the outlet, it is completely mixed.	170
E.1	The quantity of heptane-insoluble asphaltenes remaining in each sample after centrifugation in units of g asphaltenes per 100 g crude oil. Dashed lines represent the total asphaltene contents for Oil A, Oil B and the MO.	179
E.2	The volume fraction of asphaltenes in each scattering sample after centrifugation as a function of mixing time, precipitant concentration, and oil type.	181

E.3	SANS results of Oil A and Model Oil before and after incoherent background removal. Dashed line represents a slope of -4, characteristic of surface scattering. As expected, Oil A has significantly higher incoherent scattering due to the strong incoherent scattering of hydrogen.	182
E.4	SANS results of Oil A and Oil A +20% heptane before and after centrifugation. Dashed line represents a slope of -4, characteristic of surface scattering. The centrifugation procedure had no influence on the scattering of Oil A and resulting in a minor decrease in scattering intensity at low- q for Oil A +20% heptane.	183
E.5	Fractal dimension measurements of soluble (1.56 ± 0.06 , blue \circ) and insoluble (2.34 ± 0.04 , red X) asphaltenes in a sample of 40% heptane in Oil A. The scattering of the combined sample (black \bullet) from where the insoluble scattering is inferred is also included.	185
E.6	Fractal dimension measurements of soluble (1.92 ± 0.05 , blue \circ) and insoluble (2.53 ± 0.07 , red X) asphaltenes in a sample of 45% d-heptane in MO. The scattering of the combined sample (black \bullet) from where the insoluble scattering is inferred is also included.	186
E.7	Fractal dimension measurements of soluble (1.70 ± 0.07 , blue \circ) and insoluble (2.43 ± 0.13 , red X) asphaltenes in a sample of 55% d-heptane in MO. The scattering of the combined sample (black \bullet) from where the insoluble scattering is inferred is also included.	186
F.1	SAXS results for K1 asphaltenes in toluene (A); SAXS results for K1 asphaltenes in THF (B); SAXS results for A1 and K1 asphaltenes in 1-MN (C); SAXS and SANS runs for K1 asphaltenes in toluene (D). Only one third of the measured scattering intensities are presented to avoid cluttering the figures. (A-C) are normalized by scattering contrast and volume fraction, while (D) is normalized by the volume fraction.	193

LIST OF TABLES

Table

2.1	Select crude oil properties used in this investigation.	38
5.1	Two-state aggregation model results of the aggregation number and free energy of association, ΔG , which has been divided by $n - 1$ to highlight the average free energy change of each individual asphaltene-asphaltene interaction. Results were calculated based on $\chi_{Ref} = 0.997$.	134
5.2	Summary of WAXS separation distances for the γ , [002]', and [002] peaks.	138
A.1	Summary of key parameters for surface reaction rate constant calculation.	164
C.1	Input parameters for the CFD simulations.	169
E.1	Elemental analysis (wt. %) and scattering length density (SLD) of solvents and asphaltenes	178
F.1	Elemental analysis (wt. %) and scattering length density (SLD) of solvents and asphaltenes	189

LIST OF APPENDICES

Appendix

A.	Theoretical Analysis on the Dynamics of Deposit Buildup for Chapter II	159
B.	Capillary Deposition Apparatus Standard Operating Procedure for Chapter II	165
C.	CFD Simulations on Capillary Deposition Apparatus Mixing for Chapter II	168
D.	Derivation of Pressure Drop Comparisons for Deposit Locations for Chapter II	171
E.	Additional Scattering Calculations and Results from Chapter IV . . .	175
F.	Additional Scattering Calculations and Results from Chapter V	188

NOMENCLATURE

A_W	Atomic weight
b	Scattering length
C_A^o	Concentration of asphaltenes
d	Mass density
D_f	Fractal or Hausdorff dimension
E	Extent of reaction
F	Mass fraction
$I(q)$	Scattering intensity
I_0	Zero-angle scattering intensity
J_{Dep}	Flux to deposit
k	Rate constant
K_{Eq}	Equilibrium constant
L	Capillary length
m	Mass
M	Total system mass or maximum aggregation number
M_W	Molecular weight
n	Number, number concentration or aggregation number
N_A	Avogadro's number
$P(q)$	Form factor
q	Scattering vector
Q	Volumetric flow rate
r	Particle radius or constricted capillary radius
R	Ideal gas constant or initial capillary radius
R_g	Radius of gyration or Guinier radius
$S(q)$	Structure Factor
t	Time
t_d	Deposition detection time
T	Temperature
v	Volume of component
V	Total system volume
V_{Dep}	Volume of deposit
V_P	Particle volume
x	Mole fraction

Greek

ΔG	Free energy change
ΔP	Differential pressure
$\Delta\rho^2$	Scattering contrast
λ	Scattering radiation wavelength
ρ	Scattering Length Density (SLD)
μ	Viscosity
θ	Bragg scattering angle
ϕ	Volume fraction
Φ	Oil volume fraction (asphaltenes and maltenes)
$\frac{d\sigma}{d\Omega}$	Absolute scattering cross section
χ	Fraction of asphaltenes in aggregated state or capture efficiency
ξ	Fractal correlation length

Subscripts

X_{Asph}	Property of the asphaltenes
X_{Cent}	Property of the asphaltenes separated by centrifugation
X_{Dil}	Property of the diluent (e.g., precipitant)
X_i	Property of component i
X_{Ref}	Property of reference Ref
X_{Oil}	Property of the crude oil
$X_{Oil,Solv}$	Property of the crude oil solvent (i.e., maltenes/without asphaltenes)
X_{Solv}	Property of the solvent (i.e., crude oil and diluent combined)

Superscripts

X^0	Nominal value or value before centrifugation
X^{Oil}	On an oil basis
$X^{Oil,Solv}$	On a basis of the oil solvent (i.e., maltenes/without asphaltenes)
X^{Solv}	On a basis of the solvent (i.e., crude oil and diluent combined)

Abbreviations

1-MN	1-Methylnaphthalene
HTHP	High Temperature High Pressure
SAS	Small-angle Scattering
SANS	Small-angle Neutron Scattering
SAXS	Small-angle X-ray Scattering
SLD	Scattering Length Density
THF	Tetrahydrofuran
WAXS	Wide-angle X-ray Scattering

ABSTRACT

Investigations into Asphaltene Deposition, Stability, and Structure

by

Michael Paul Hoepfner

Chair: H. Scott Fogler

Asphaltenes are known to cause a number of petroleum production, transportation and processing concerns. The overarching goal of this body of work was to elucidate the fundamental structure and behavior of asphaltenes for ultimate application in a number of different fields. In this dissertation, asphaltenes were studied over length scales ranging from the macro to the micro scale.

The dissertation begins by reporting the results of a study on the destabilization and deposition of asphaltenes using a capillary flow apparatus. Asphaltenes were destabilized by adding a precipitant to crude oil, and deposition was detected by an increase in the differential pressure across a capillary. These experiments revealed that the asphaltene deposition rate decreases continuously with decreasing precipitant concentration and no critical onset concentrations were observed. In addition, it was observed that sub-micrometer sized asphaltenes dominate the deposition process and the deposition rate is proportional to the concentration of insoluble asphaltenes.

The destabilization of asphaltenes from crude oil after precipitant addition was also studied using small-angle neutron scattering (SANS) to detect precipitation at the incipient stages. No critical stability conditions were observed and at least a

small quantity of insoluble asphaltenes were detected with any amount precipitant added, which was in agreement with the capillary deposition results. In addition, these experiments revealed that the fractal dimension of asphaltene clusters changes from approximately 1.7 to 2.1 when transitioning from soluble (not precipitating) to insoluble (precipitating) asphaltenes.

In the last phase of this investigation, the structure of asphaltenes was further studied using both small-angle X-ray and neutron scattering (SAXS/SANS). For the first time, the relative fraction of asphaltenes in the aggregated vs. molecular state was estimated and fit to a thermodynamic aggregation model. The model results reveal moderate aggregation numbers (3-5) and free energies of association of approximately -31 kJ/mol. In addition, novel solvent background corrected wide-angle X-ray scattering results (WAXS) of asphaltenes in a liquid environment are presented which reveal the local molecular ordering in asphaltene nanoaggregates.

CHAPTER I

Introduction

Despite the tremendous amount of modern research, the process of defining asphaltenes is not a trivial matter. Rigid definitions, such as ASTM D 6560 – 00, where asphaltenes are the solid fraction of petroleum crude oil after dilution of 1 g oil with 30 mL n-heptane and subsequent separation and washing procedures, fail to capture the full story of this complex material (*ASTM D 6560 - 00*, 2005). This ASTM method is not universally accepted, and no uniform definition exists for what asphaltenes actually are. In the United States, asphaltenes are generally regarded as the n-heptane insoluble fraction of crude oil (1 part oil to 40 parts n-heptane), while many Canadian researchers classify asphaltenes as the n-pentane insoluble fraction. Qualitatively, petroleum asphaltenes are a massive collection of largest/heaviest molecules that are separated from petroleum by a number of techniques.

Due to the uncountable number of unique components in crude oil, every sample of oil from a particular oilfield will produce a unique collection of asphaltenes. Asphaltenes from oils of different sources will be not be the same, but even asphaltenes from the same reservoir but at different wells or sampled at different times will indeed be dissimilar. This complication clearly causes difficulty in the scientific investigation of asphaltenes as each sample of oil is unique and cannot be recreated. Even within the asphaltene fraction, high-resolution mass spectrometry has identified ap-

proximately 12,000 unique empirical formulas (*Klein et al.*, 2006b). This value is a gross underestimate of the of the total number of unique asphaltene molecules. This underestimate was clearly illustrated recently in 2012 by Howard Freund and coworkers with mass spectrometry work presented at the 13th International Conference on Petroleum Phase Behavior and Fouling (PetroPhase) (*Freund et al.*, 2012). In this presentation, FTICR-MS (Fourier Transform Ion Cyclotron Resonance Mass Spectrometry, high-resolution but poor ionization efficiency) was performed on asphaltenes, and the results were directly compared of to FDMS (Field-Desorption Mass Spectrometry, low resolution but high ionization efficiency). It was found that although the FDMS could not resolve each mass spectrometry peak, it identified a significantly broader distribution when compared to the FTICR-MS. Additionally, it is important to note that each empirical formula for asphaltenes can have a tremendous number of different isomers. For example, a relatively simple molecule of a fully saturated hydrocarbon with 44 carbons (tetracosane, Molecular Weight = 338.65 g/mol) has over 62 trillion isomers (*Creek*, 2005). Asphaltenes have molecular weights ranging from 500-1200 g/mol, revealing that asphaltenes are one of the most complex materials ever studied.

A general improved understanding of asphaltene structure and behavior is of great interest due to the large number of industrial problems asphaltenes cause during petroleum production and processing. Asphaltenes have been known to stabilize water-in-oil emulsions (*Kilpatrick*, 2012), destabilize in the refinery when blending crude oils (*Wiehe and Kennedy*, 2000) and deposit in the wellbore (*Haskett and Tartera*, 1965). In addition, it is desirable to understand the molecular structure of asphaltenes in order to predict the products of crude oil processing and forecast the economic value of heavy oils; however, there is continued debate on the molecular structure of asphaltenes (*Andrews et al.*, 2006; *Spiecker et al.*, 2003). Despite nearly a century of scientific investigation, (*Mack*, 1932; *Katz and Beu*, 1945) there are still sig-

nificant gaps in the understanding of asphaltenes, including the molecular structure, aggregation state, (de)stabilization mechanism (*Hoepfner et al.*, 2013b), and deposition mechanism (*Hoepfner et al.*, 2013a) than need to be filled before petroleum reserves can be efficiently extracted and processed.

Additionally, unconventional oil reserves (e.g., oil sands and bitumen) are viewed as the future of petroleum production until renewable sources can provide sufficient needs for electricity generation, transportation fuels, and commodity chemicals. It is estimated that 2.1 trillion barrels of recoverable unconventional oil reserves exist worldwide (*Jaffe et al.*, 2011). According to the US Energy Administration, the United States consumed approximately 7 billion barrels of oil in 2011, illustrating large scale of the total unconventional reserves. Unconventional oil reserves are characterized by their young geological age, high viscosity, high density (low API) and high fraction of asphaltenes (*Speight*, 2009). The Athabasca bitumen in Alberta, Canada is the only large scale oil sands production operation in the world, and the bitumen contains approximately 15 wt. % asphaltenes, which highlights the impact of asphaltenes on heavy oils (*Zhao et al.*, 2009). Crude oil is a complex mixture and the asphaltene fraction represents the least understood component.

1.1 A Brief History of Asphaltenes

The earliest known use of petroleum-like materials dates back to approximately 3000 B.C. when ancient Sumerians used asphalt to cement stones together in sculptures, walls, and buildings (*Abraham*, 1920). It is interesting to discover that while petroleum in today’s society is of such great political and commercial value, it had its humble origins in the application of mere adhesion. Without the technological capabilities of modern times, the composition and properties of different tar-like substances may have appeared to be similar. Therefore, terms such as “asphalt”, “bitumen”, “tar”, and “pitch” all commonly and interchangeably appear in early descriptions

of heavy oil and asphalts (*Abraham*, 1920). An early definition of “bitumen” from 1656 read, “A kind of clay or slime naturally clammy, like pitch, growing in certain countries of Asia” (*Abraham*, 1920). From the 17th century onward, scientific investigation and application of naturally occurring organic compounds increased until entire books were written on the subject.

The history of asphaltenes began with the study of bitumen and asphalt, a hard rock-like organic material. In 1837, the French chemist M. Boussingault first distilled bitumen and separated a volatile liquid, which he named “petrolene” (*Boussingault*, 1836, 1837). After separating the petrolene, all that remained of the bitumen was a solid black material. Because of the visual similarity to asphalt, Boussingault described the solid fraction of bitumen as “asphaltenes”. The earliest description of asphaltenes is not all that dissimilar from today’s definition, being insoluble in alcohol and soluble in the “oil of turpentine” (*Boussingault*, 1836, 1837). The asphaltenes were heavier than water and the Bechelbronn bitumen sample (from northeastern France) contained 14.6 wt. % asphaltenes. The asphaltenes were comprised of 75.3% carbon, 9.9% hydrogen, and 14.8% oxygen, which results in a H:C ratio of 1.58. This H:C ratio is higher than commonly accepted for petroleum asphaltenes that are currently studied, but considering the early date, it bears a remarkable similarity to results generated in modern literature.

Early asphaltene research focused on identifying the ideal properties of asphalt for the purpose of road paving. Prof. Edward J. de Smedt of Columbia University was a pioneer in the development of modern asphalt paving, and he laid the first asphalt road in the United States, which was in front of the Newark, NJ City Hall (*Abraham*, 1920). In 1893, while acting as a chemist for The New York and Bermudez Co., de Smedt published an article in *Paving and Municipal Engineering* where he compared two asphalts, Bermudez and Trinidad Lake, to identify which had more ideal paving characteristics (*De Smedt*, 1893). In this article he discusses the ideal asphalt having

less than 20% asphaltenes otherwise the paving asphalt will be too brittle. The work by de Smedt represents some of the earliest research in classifying and identifying ideal characteristics of bitumen and asphaltenes; however, his attempt was not without harsh criticism. The following anecdote is discussed because it serves as a mirror for similar research discussions that exist until this day.

Captain Dolphus Torrey, a representative of the Trinidad Asphalt, took strong objection to many of the points made by de Smedt in his 1893 article and published a scathing criticism of de Smedt's article (*Torrey*, 1894b). Likely motivated by financial interest, Capt. Torrey took strong objection to de Smedt's conclusion that Bermudez asphalt was superior to the Trinidad Lake asphalt. Throughout a series of exchanges published in *Paving and Municipal Engineering* between de Smedt and Torrey over the next year, arguments are made against the asphalt fractionation procedure, the uncertainty in knowing what molecules exist in each fraction, and the inability to synthetically create asphalt. Torrey ultimately references the original work by Boussingault by stating that (*Torrey*, 1894a):

“The name asphaltine [*sic*] was given to the remaining portion of asphalt obtained from Brechelbrunn, left after distilling off the oils for forty-eight hours at 250° C. The name applied to the substance so obtained should, according to the well established usage, be retained for it, and not applied to anything different, obtained in some other way, and not having the same composition.”

While Torrey's criticism is accurate that the *original* Bechelbrunn asphaltenes are not identical to asphaltenes obtained by some other means, perhaps it is too narrow of a definition to facilitate discussion of complex organic materials. Common contemporary arguments regarding asphaltene behavior mirror exactly those by de Smedt and Torrey, over a century after this exchange. The endless pursuit of

classifying petroleum and complex organic materials continues to this day, and unfortunately, no uniform classification system exists. Additionally for the sake of novelty, Figures 1.1 and 1.2 show two advertisements (that originally appeared on side by side pages nonetheless) for the respective organizations of Dolphus Torrey and Prof. Edward J. de Smedt taken from volume 7 of *Paving and Municipal Engineering* in 1894.

1.2 Contemporary Asphaltene Research

In the early 20th century, asphaltene research shifted to areas of petroleum. As early as the 1930s, asphaltenes were already considered to be colloidal particles in crude oil (*Mack, 1932*). The work of Charles Mack investigated the viscosity of petroleum with increasing amounts of asphaltenes, and it was concluded that asphaltenes are the leading source of high viscosity in crude oils (*Mack, 1932*). Nearly 80 years later, the influence of asphaltenes on viscosity remains a topic of continued research (*Luo and Gu, 2007; Barré et al., 2008*). Research on asphaltenes at the University of Michigan dates back to the 1940s where Donald Katz investigated the colloidal structure of asphaltenes with electron microscopy and concluded that the size of asphaltene colloids are below 65 Å (*Katz and Beu, 1945*).

The pace of asphaltene research accelerated rapidly from the 1960s onward. In 1961, T. F. Yen *et al.* published his account of the asphaltene structure based on X-ray diffraction measurements (*Yen et al., 1961*), which still remains a well-regarded model for the structure of asphaltene colloids/nanoparticles (modern nomenclature refers to these aggregates as ‘asphaltene nanoaggregates’) (*Mullins et al., 2012*). Small-angle scattering techniques were developed in the 1940s and 1950s and were first applied to crude oil in 1965 by C. W. Dwiggin (*Guinier and Fournet, 1955; Dwiggin, 1965*). The research from the 1960s reveals a few key findings that are still well-accepted today regarding the asphaltene structure. The X-ray diffraction results of Yen *et al.*

Fruin=Bambrick
Construction
 ▲▲▲▲▲ **Company** ▲▲▲▲▲

922 Olive Street, St. Louis, Mo.

DEALER IN

Trinidad Asphalt

FOR COMMERCIAL USES

Is prepared to bid for Contracts to Lay Asphalt
 Street Pavements in any City of the United
 States and Canada.

Geo. W. Scharf,
 Superintendent of Asphalt Work.

Dolphus Torrey,
 General Agent.

Figure 1.1: Asphalt advertisement reproduced from *Paving and Municipal Engineering* (vol. 7, p. 17, 1894) for the organization represented by Dolphus Torrey.

The
New York
Bermudez
Company



Having acquired by purchase the largest lake or deposit of Asphalt in the world, covering an area of over one thousand acres, situated in State of Bermudez, Venezuela, and having expended large sums of money in perfecting shipping facilities, are now prepared to sell and deliver a refined Asphalt of over ninety-five per cent. purity and of a quality far superior to any other for paving, roofing, etc. It will do fifty per cent. more work than any other Asphalt. We guarantee its excellence and purity, and Prof. E. J. De Smedt, our chemist, will give scientific and expert instructions to parties using it.

NEW YORK & BERMUDEZ CO.
25 BEAVER STREET, NEW YORK.

Figure 1.2: Asphalt advertisement reproduced from *Paving and Municipal Engineering* (vol. 7, p. 18, 1894) for the organization represented by Prof. Edward J. de Smedt.

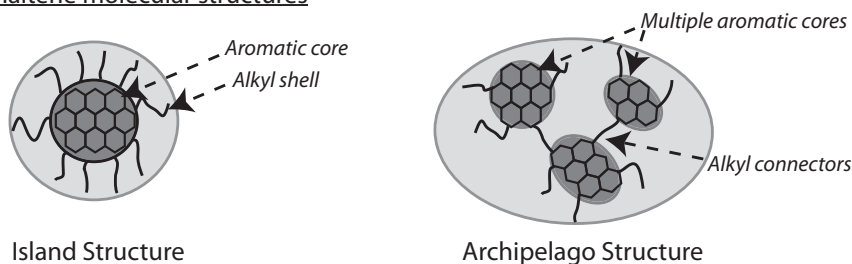
identified that the large aromatic cores of asphaltenes stack at a similar separation distance to graphite, approximately 3.6 Å (*Yen et al.*, 1961). The small-angle scattering results of Dwiggins revealed that the size of the asphaltene nanoparticles are on the order of 10 Å (*Dwiggins*, 1965). From this point onwards, the quantity of research publications investigating asphaltenes exploded due to their industrial importance and their curiosity-inspiring complexity. In 1965, the most prominent and one of the few publicly available accounts of an oilfield asphaltene deposition problem was reported by Haskett and Tartera (*Haskett and Tartera*, 1965). Their account, despite being almost half a century old, remains the most complete report of oilfield asphaltene deposition that is publicly available and is used for modern asphaltene deposition modeling validation (*Kurup et al.*, 2011).

1.3 Asphaltene Molecular and Aggregate Structure

The current and best accepted structure for asphaltenes is complex, hierarchical, and still an issue of debate. Two primary schools of thought exist for the molecular structure of asphaltenes, the “island” and the “archipelago” models (*Mullins et al.*, 2012). The island model of an asphaltene is the best accepted asphaltene molecular structure, and it consists of a polyaromatic condensed hydrocarbon core (approximately 7 joined rings) and a shell of alkyl side chains that are believed to provide stability to the molecule (*Mullins et al.*, 2012). The archipelago model is similar in nature to the island model, but instead of a single large aromatic core, there are several which are connected by alkyl chains (*Spiecker et al.*, 2003). These two competing molecular structures are represented schematically in Figure 1.3 (A). The exact specifics of the molecular structure of asphaltenes is not a critical component of the work presented in this dissertation and little emphasis will be placed on these two structures. However, the prevailing opinion is that there is no *single* asphaltene structure and that best describes such a complex class of molecules. Although, a majority

of researchers believe that the island model *best* describes the general asphaltene molecular structure. The aggregated structure, not the molecular structure, will be a major focus of the work in this dissertation and a schematic of the aggregation structural hierarchy is shown in Figure 1.3 (B).

A) Proposed asphaltene molecular structures



B) Traditional asphaltene structural hierarchy



Figure 1.3: (A) Schematic representations of the island and archipelago possible asphaltene molecular structures. (B) Best accepted asphaltene structural hierarchy.

1.4 Asphaltene Precipitation Kinetics

A large fraction of contemporary asphaltene research centers around the development of thermodynamic models to predict asphaltene phase behavior (*Ting et al.*, 2003; *Kraiwattanawong et al.*, 2007; *Gonzalez et al.*, 2007). The standard procedure to extract asphaltene thermodynamic parameters (e.g., solubility parameter) is to dilute crude oils or model asphaltene mixtures with a liquid precipitant in order to induce asphaltene precipitation. The most common liquid precipitants are normal alkanes, with n-heptane and n-pentane being by far the most prolific. The set of

thermodynamic variables where asphaltene precipitation occurs is commonly called the “onset” point (or concentration when the primary destabilizing factor is a liquid precipitant.) Any inaccuracy in the measurement of asphaltene onset points will directly translate into errors in predictive thermodynamic models. Recent work by Maqbool *et al.* has revealed that the detection of onset points is inhibited by slow asphaltene precipitation kinetics (Maqbool *et al.*, 2009, 2011b). Maqbool *et al.* modified the concept of an onset point or concentration to the *instantaneous onset point*, where the “instantaneous” onset point refers to the detection of asphaltene precipitation within approximately 15 minutes of a change in the thermodynamic state of an asphaltene solution.

The discovery of asphaltene precipitation kinetics is significant because it questions whether asphaltenes possess a well-defined phase envelope. Maqbool *et al.* showed that decreasing the heptane concentration in a crude oil mixture still destabilized asphaltenes; however, it takes an exponentially longer time to detect the instability (Maqbool *et al.*, 2009, 2011b). The delay in detecting asphaltene instability is due to asphaltene nanoaggregates growing in size from the nanometer length scale to a detectable size of 0.5 microns (Maqbool *et al.*, 2011a). Asphaltene precipitation kinetics are believed to be a universal property of asphaltenes, and Haji-Akbari *et al.* demonstrated similar behavior with several crude oil and model mixture asphaltene systems (Haji-Akbari *et al.*, 2013).

1.5 Asphaltene Research Philosophy

The criticism presented by Torrey in 1894, that asphaltenes of different origin should not be considered equivalent, is a concern echoed in contemporary asphaltene research. Additionally, an overarching uncertainty exists in the study of asphaltenes, even for those of the same origin. Due to the complexity of crude oil, it is not currently possible to completely account for all properties and parameters of asphaltenes

or crude oil. Evoking the Gibbs phase rule, where $F = C - P + 2$, it is clear that the study of crude oil is ill-defined because the number of degrees of freedom (F) is essentially infinite because the number of components (C) is essentially infinite (*Sandler, 2006*). In addition, it is not uncommon to encounter a system with four or more phases (P) if there is an oil in water dispersion, a hydrocarbon vapor phase, and dispersed solids. Because a petroleum system cannot be fully accounted for thermodynamically, petroleum-related research has primarily focused on the laboratory imitation of production scenarios and conditions. Significant deviation from reservoir conditions or oil fluid properties is often met with sharp criticism, especially for the study of asphaltenes (*Creek, 2005*).

From an industrial perspective, the fear of simplified laboratory systems is not wholly unwarranted. The compositional continuum and complexity of petroleum has the potential to cause deviations between simple well-controlled laboratory experiments and the true behavior of oil in a production scenario that are difficult to detect and consider (*Podgorski et al., 2012; Klein et al., 2006a,b*). A crude oil at the elevated temperatures and pressures that are experienced in the reservoir is called a “live” crude oil. Whereas a crude oil at room temperature and pressure (i.e., without the light and volatile components) is called a “dead” crude oil. The analogy between crude oil systems and living biological ones is not purely coincidental, because for both systems, the complexity and number of unique components still remain effectively unaccounted for.

Regardless of petroleum’s complexity, the significance of novel scientific discoveries with conservative research approaches are limited. It is my belief that while petroleum will undoubtedly behave differently at elevated temperature and pressure, the fundamental mechanisms for various processes will remain similar. The overarching goal of this dissertation is to investigate the fundamental deposition, destabilization, and aggregation mechanisms of petroleum asphaltenes. This approach has the potential

to improve our understanding of the fundamental behaviors of asphaltenes and yield new transformative technologies in the field of petroleum processing. While it is true that the absolute behavior of asphaltenes in the laboratory will deviate from the reservoir, the relative behavior and mechanisms will likely stay similar. The discovery of mechanisms for asphaltene deposition and precipitation processes will provide a road map of future hypotheses to test using experiments designed to more closely imitate a live crude oil.

1.6 Scope, Format and Outline of Dissertation

From the discussion on the preceding pages, it is evident that asphaltenes are a complex material and that significant gaps in understanding the behavior of this material exist. The primary emphasis of the research contained within this dissertation was to investigate the fundamental mechanisms of asphaltene behavior. Because there are numerous asphaltene-related industrial concerns, it was decided that a fundamental understanding would impact numerous fields. The general format of this dissertation is to assemble a collection of individual works which investigate asphaltene behaviors from a variety of different angles. Although this format introduces minor redundancy into the presentation of information, it allows for each project to be self contained for rapid access to the background and findings for each project. Below is discussion of the initial dissertation motivation followed by a brief introduction to each chapter.

A large motivator to understand asphaltene behavior (and the initial motivation for this dissertation) is to predict, prevent and remediate asphaltene wellbore deposition. As oil production moves to deeper water and well depth, the consequence of production complications become greatly magnified. Remediation of a wellbore asphaltene deposit can cost up to \$3,000,000 if access to the wellbore is required in a deepwater well (*Creek*, 2005). This cost estimate does not include the lost produc-

tion, which can be massive. For example, as of May 29th, 2013 the price of oil was \$95.05 per barrel, and for a well producing 40,000 barrels per day, the loss off one day of production amounts to approximately \$4,000,000.

The qualitative mechanism of asphaltene wellbore deposition is reasonably well understood (*Haskett and Tartera, 1965*). In the oil reservoir, asphaltenes are stable in the crude oil at elevated temperature and pressure. As the oil travels vertically up the wellbore, the loss of hydrostatic head in the oil causes the light (volatile) components of the crude oil (e.g., methane) to expand, which lowers the solubility parameter of the crude oil. The change in the thermodynamic properties of the system destabilizes the asphaltenes, which forces them out of the liquid phase and initiates asphaltene deposition. Once the pressure is reduced below the bubble point and a second vapor phase forms, the liquid solubility parameter increases and the asphaltenes become stable. Above the bubble point, asphaltene deposition ceases (*Haskett and Tartera, 1965*). This process is represented schematically in Figure 1.4.

Numerous model exist to predict the asphaltene wellbore deposition process (*Mansoori, 1997; Ramirez-Jaramillo et al., 2006; Vargas et al., 2009; Kurup et al., 2011, 2012*); however, no model can predict the rate of deposition *a priori*. Early models had little to no experimental validation of predicted deposits, and the conclusions of such models can not be relied upon for design purposes. More recently, capillary deposition experiments have been used as a benchmark/validation for asphaltene deposition models (*Vargas et al., 2009; Kurup et al., 2011, 2012*). However, the largest uncertainty that exists in asphaltene deposition models is how to structure the deposition boundary conditions and estimate the necessary parameters. From an early stage in the development of this dissertation, it was apparent that until the behavior of asphaltenes at a deposit interface is well-understood, there is little utility for deposition models. Therefore, the first project investigated in this dissertation was to understand the driving force and mechanism of the asphaltene deposition process.

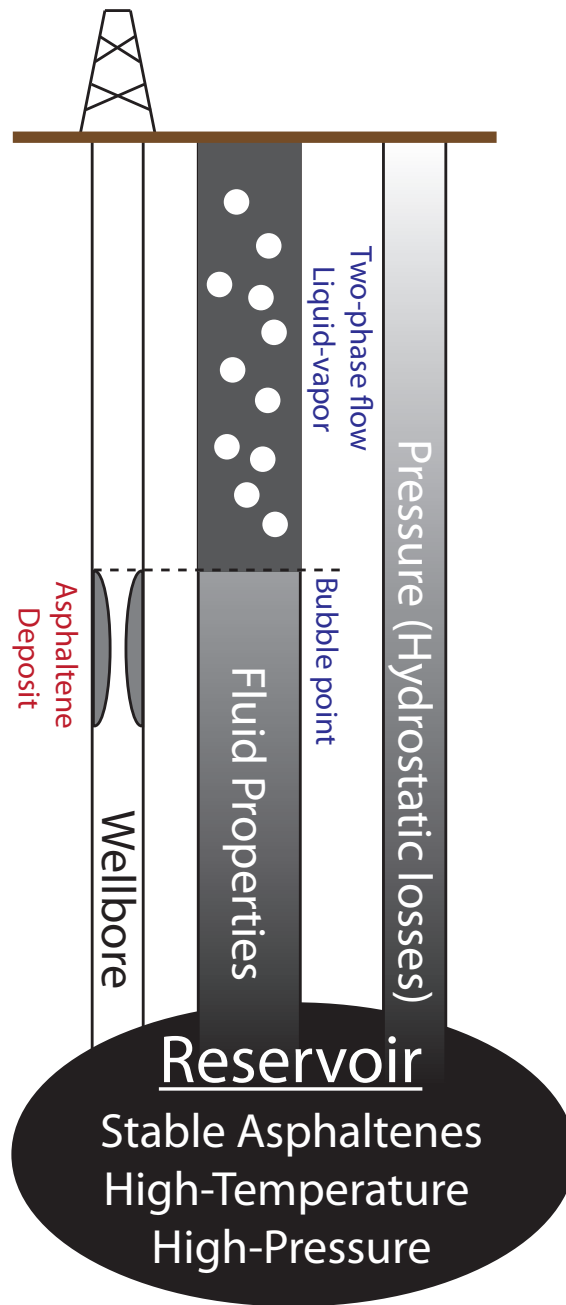


Figure 1.4: Schematic of the wellbore asphaltene deposition process.

In Chapter II, the macroscopic deposition behavior of asphaltenes was investigated using a capillary deposition apparatus. In this study, asphaltene deposits were generated in metal capillaries by heptane addition to crude oils, and it was found that deposition is caused by sub-micron asphaltene aggregates. Deposits were generated at heptane concentrations above and significantly below the instantaneous onset point. Analysis of the results reveals that the governing factor controlling the magnitude of asphaltene deposition is the concentration of insoluble asphaltenes present in a crude oil-precipitant mixture and the instantaneous onset point is irrelevant to the deposition process. Electron microscopy images of the deposits represent the first images and confirmation of arterial growth in laboratory generated asphaltene deposits. The axial deposit profile was found to be highly non-uniform. In addition, deposits formed shortly after when oil and heptane mix, revealing that the destabilization of asphaltenes occurs virtually immediately after a precipitant is added. The results were reproduced with a second crude oil, indicating that asphaltene deposition behavior is broadly applicable. The results presented in Chapter II revealed that asphaltenes are unstable under conditions not previously considered. This discovery was motivation to initiate further studies that investigated the overall stability of asphaltenes, which is discussed in Chapter IV.

In Chapter III, a general overview of the theory behind scattering techniques is discussed. The subsequent chapters in the dissertation rely heavily on small-angle scattering techniques to investigate various asphaltene behavioral and structural properties. Small-angle scattering is a common technique to study nanometer length scale colloidal structures, and it is a useful technique for investigating asphaltene behavior in solution. In addition, a brief introduction to fractals is also provided.

In Chapter IV, the precipitation of asphaltenes from crude oil and solvents was investigated using small-angle neutron scattering (SANS). This chapter discusses time-resolved small-angle neutron scattering results that were used to investigate asphal-

tene structure and stability with and without a precipitant added in both crude oil and model oil. A novel approach was used to isolate the scattering from asphaltenes that are insoluble and in the process of aggregating from those that are soluble. It was found that both soluble and insoluble asphaltenes form fractal clusters in crude oil and the fractal dimension of the insoluble asphaltene clusters (2.1) is higher than that of the soluble clusters (1.7). Adding heptane also increases the size of soluble asphaltene clusters without modifying the fractal dimension. Understanding the process of insoluble asphaltenes forming fractals with higher fractal dimensions will potentially reveal the microscopic asphaltene destabilization mechanism (i.e., how a precipitant modifies asphaltene-asphaltene interactions). It was concluded that because of the polydisperse nature of asphaltenes, no well-defined asphaltene phase stability envelope exists, and small amounts of asphaltenes precipitated even at dilute precipitant concentrations. Asphaltenes that are stable in a crude oil-precipitant mixture are dispersed on the nanometer length scale. An asphaltene precipitation mechanism is proposed that is consistent with the experimental findings. Additionally, it was found that the heptane-insoluble asphaltene fraction is the dominant source of small-angle scattering in crude oil and the previously unobtainable asphaltene solubility at low heptane concentrations was measured.

In Chapter V, the structure of asphaltenes was investigated with a combination of small-angle neutron and X-ray scattering (SANS and SAXS) along with wide-angle X-ray scattering (WAXS). Samples ranged in concentration from 5 vol. % to 0.00125 vol. %. As asphaltenes are diluted, the cluster size decreases and follows a fractal scaling law. This observation reveals that asphaltene associations are always fractal, with clusters persisting to dilute concentrations, and previous measurements on asphaltene nanoaggregates may be influenced by clustering. Dissociation of asphaltene aggregates into molecules was observed by a reduction in the concentration-normalized scattering intensity. The dissociation occurred the most significantly at similar con-

centrations to previous reports of the critical nanoaggregate concentration (CNAC); however, the dissociation was observed to occur gradually as a function of concentration. Complete dissociation was not detected and aggregates persisted down to asphaltenes concentrations as low as 15 mg/L (0.00125 vol. %). For the first time, the fraction of asphaltenes in the aggregated vs molecular state was estimated by the scattering intensity. A two-state model was applied to the measurements and the free energy change of association per interaction was calculated to be approximately -31 kJ/mol. Finally, novel solvent-corrected WAXS results of asphaltene in a liquid environment are presented and reveal three distinct separation distances, in contrast to the two separation distances observed in diffraction studies of solid phase asphaltenes. The WAXS and free energy results may prove invaluable for validation and benchmarking of future molecular dynamic simulations of asphaltenes.

Chapter VI discusses the major conclusions of this dissertation and presents several potential future projects.

In addition, the Appendices contain a tremendous amount of results and theoretical calculations that are necessary to fully understand the results and discussion of the primary chapters. Appendix A contains a simplified asphaltene deposition model that approximates the capillary used in Chapter II as a differential reactor with an internally homogeneous liquid composition. Transport limitations hinder accurate application of this model to the results in Chapter II; however, future redesigns of the capillary deposition apparatus, as discussed in the Chapter VI may provide utility to this model. Appendix B contains the standard operating procedure to perform a capillary deposition experiment, which is critical to obtain accurate and reproducible results. Appendix C presents computational fluid dynamic calculations on the mixing quality of the capillary deposition apparatus. Appendix D contains additional derivations necessary for complete comprehension of Chapter II. Appendix E contains many derivations, calculations and results that complete the presentation

of information in Chapter IV. Finally, Appendix F contains additional results and derivations, necessary for a full understanding of Chapter V.

CHAPTER II

Capillary Deposition

2.1 Introduction

Asphaltenes are a complex fraction of petroleum crude oil that are defined by their solubility in aromatics (typically toluene) and insolubility in normal alkanes (typically n-pentane or n-heptane) (*Speight, 2007*). Asphaltenes are of great industrial interest and significance because of their tendency to deposit in porous rock formations, well-bores, production lines and refineries (*Haskett and Tartera, 1965*). Injecting miscible or immiscible compounds into a reservoir can cause a compositional change in the crude oil and can lead to asphaltene precipitation in the porous rock formation (*Gonzalez et al., 2005; Kraiwattanawong et al., 2007; Vafaie-Sefti and Mousavi-Dehghani, 2006*).

The asphaltene molecular structure, aggregation state and destabilization mechanism remain as areas of intense debate despite decades of research. High-resolution mass spectrometry has identified the elemental composition of approximately 7,200 unique asphaltene molecules (*Klein et al., 2006b*). Several small-angle scattering studies suggest that asphaltenes exist either as stable aggregates or clusters of ag-

This chapter is reproduced in part with permission from Michael P. Hoepfner, Vipawee Lim-sakoune, Varun Chuenmeechao, Tabish Maqbool, and H. Scott Fogler. A Fundamental Study of Asphaltene Deposition. *Energy & Fuels*, 27(2):725-735, January 2013. Copyright 2013 American Chemical Society.

gregates with a radius of gyration of approximately 10 nm or less in both crude oil and toluene (*Roux et al.*, 2001; *Headen et al.*, 2009b; *Gawrys and Kilpatrick*, 2005; *Eyssautier et al.*, 2011). However, asphaltene scattering results have been successfully analyzed by assuming asphaltene molecules exist as solid nanoparticles and as liquid-liquid concentration fluctuations in an otherwise homogenous fluid (*Sirota*, 2005; *Sirota and Lin*, 2007). The ambiguity of whether asphaltenes behave as colloidal suspensions or as a liquid-liquid mixtures adds to the uncertainty of understanding the asphaltene destabilization mechanism.

To establish consistent and clear terminology, the usage of several terms which will be used in this work are defined now. First, the term “destabilization” will be used to describe the transition an asphaltene undergoes on the nanometer length scale from stable (not allowed to aggregate or grow in size) to unstable (able to aggregate or grow in size). Second, “aggregation” will be used to describe the generic growth process of increasing the size of an asphaltene from the nanometer to micron length scale. Finally, “precipitation” will refer to the entire process of asphaltenes transitioning from stable to micron-sized asphaltene aggregates or precipitates. For the purpose of this investigation, assigning a detailed description of the asphaltene precipitation process is not necessary and no predictive thermodynamic modeling efforts are attempted. However for simplicity, stable asphaltenes in oil will be referred to as nanoaggregates as most researchers agree that asphaltenes are highly associating molecules.

Asphaltene nanoaggregates can be destabilized by changes in pressure, temperature, and composition (*Gonzalez et al.*, 2005; *Kraiwattanawong et al.*, 2007; *Joshi et al.*, 2001; *Hammami et al.*, 2000; *Peramanu et al.*, 2001; *Buenrostro-Gonzalez et al.*, 2004; *Bayat et al.*, 2008). Pressure depletion is the primary cause of arterial deposition in a wellbore (*Haskett and Tartera*, 1965). To force asphaltenes out of solution in the laboratory and to simulate field conditions, a common approach is to add an

n-alkane precipitant to a sample of stock tank or dead oil (oil that has been cooled and depressurized to room temperature and pressure). The problematic asphaltenes will have already precipitated by pressure depletion during oil recovery, so adding an artificial precipitant is necessary to study asphaltene behavior unless a high temperature and pressure recombined oil is used. A recombined oil is a dead oil sample that has been recombined with the dissolved hydrocarbon gasses that were previously removed and then brought to the temperature and pressure of the reservoir. Adding a precipitant to dead oil is a widely used technique for validating thermodynamic models and measuring asphaltene properties and aggregation mechanisms (*Gonzalez et al.*, 2007; *Maqbool et al.*, 2009). Unfortunately, asphaltene destabilization and behavior in systems with low precipitant concentrations (i.e., below the instantaneous onset) has largely been ignored except for a few recent studies (*Maqbool et al.*, 2009, 2011a,b).

Slow kinetics of asphaltene precipitation have been observed by Wang and other researchers, adding experimental difficulty in determining asphaltene behavior (*Wang*, 2000; *Angle et al.*, 2006; *Rastegari et al.*, 2004; *Maqbool et al.*, 2009, 2011b,a). *Maqbool et al.* questioned whether an onset point for asphaltene precipitation exists and reported that detecting asphaltene precipitation by optical microscopy may take 6 months or longer at sufficiently low precipitant concentrations (*Maqbool et al.*, 2009). Recent work suggests that once a precipitant is added to an oil, nanometer-sized asphaltenes are destabilized and undergo a reaction-limited aggregation process to form larger aggregates (*Maqbool et al.*, 2011a). Application of a geometric population balance model allowed *Maqbool et al.* to estimate the asphaltene-asphaltene collision efficiency, the number of adhesions divided by the number of collisions, to be on the order of 1×10^{-6} adhesions per collision (*Maqbool et al.*, 2011a). The collision efficiency and asphaltene aggregation rate are strong functions of the precipitant concentration, which causes the time to detect asphaltene precipitation to vary from nearly instantaneous to several months (*Maqbool et al.*, 2009). This detection limitation is due to

the low collision efficiency between growing asphaltene aggregates and the need to increase in size from the nanometer scale to an observable size for optically microscopy, roughly $0.5 \mu\text{m}$.

The asphaltene deposition rate is also likely to be strongly controlled by precipitant concentration, as is the case with asphaltene precipitation and aggregation. The work of Maqbool *et al.* suggested that there may not be a critical precipitant concentration for asphaltene stability, and as such, it is necessary to investigate whether asphaltenes deposit at increasingly dilute precipitant concentrations. Additionally, asphaltene instability may be detected sooner by capillary deposition than a batch aggregation process because of a continuous source of destabilized nanoaggregates at the capillary entrance. The detection mechanism, pressure drop, does not depend on the size of asphaltene aggregates and sub-micron asphaltenes can deposit to contribute to the instability detection. A capillary with a small inner diameter will allow for sensitive detection due to the significant increase in the pressure drop caused by a thin deposit. The work presented here on asphaltene deposition in dilute precipitant systems represents a new investigative tool to better understand asphaltene behavior.

2.1.1 Previous Deposition Studies

The following literature review will focus on deposition as measured in a capillary (Broseta *et al.*, 2000; Wang *et al.*, 2004; Nabzar and Aguilera, 2008; Boek *et al.*, 2008; Lawal *et al.*, 2012). The capillary deposition technique on asphaltenes was first used to measure the solubility parameter where asphaltenes precipitate from solution (Broseta *et al.*, 2000). Later, Wang *et al.* quantified the thickness and mass of material depositing in a capillary and concluded that the deposit is approximately uniform over a roughly 100 foot long capillary; however, only two precipitant concentrations for each oil were considered, near and above the instantaneous onset conditions for asphaltene precipitation (Wang *et al.*, 2004). Wang and Buckley have

developed a technique, called the “Displacement Test”, to determine the deposit profile inside a capillary by forcing a viscous fluid out of the capillary and monitoring the mass that exits the capillary as a function of time (*Wang and Buckley, 2006*). This technique shows promise, however, it lacks an estimate of the axial resolution and thickness profile uncertainty, does not have any validation of predicting a known profile, and has not undergone peer review.

Nabzar *et al.* determined that there are critical shear conditions under which asphaltenes will not deposit, highlighting the importance of hydrodynamics (*Nabzar and Aguilera, 2008*). At low shear rates, Nabzar *et al.* states that deposition follows the colloidal deposition scaling of diffusion limited deposition. As the shear rate increases, asphaltenes pass through a shear limited deposition process and at high enough shear rates, there is no detectable deposition. Deposition under shear conditions has promise to aid in the understanding of the deposition mechanism, however no attempt was made by Nabzar *et al.* to measure or predict the particle size distribution in the capillary to validate whether the shear effects are reasonable. Modeling work by Eskin *et al.* estimates that asphaltene aggregates need to have a diameter greater than 1 μm before shear effects are significant (*Eskin et al., 2011b*). The most studied sample used by Nabzar *et al.* for shear effects was a 20% toluene and 80% heptane model oil system. With such a high heptane concentration, aggregation will occur quickly, however the residence time in the mixing system was not specified. Consequently, it could be that the shear effects observed by Nabzar *et al.* may be due to the deposition behavior of large aggregates, with a diameter of hundreds of nanometers or microns and thus susceptible to shear inhibition, if the estimate by Eskin *et al.* is accurate.

Optical microscopy images perpendicular to the axial direction of flow for asphaltene deposition in round glass capillaries revealed that there is some non-uniformity associated with the axial deposition profile, with the inlet deposit being thicker than

the outlet in a 12.7 cm long capillary (*Lawal et al.*, 2012). The non-uniformity of the deposit could only be inferred based on the light transmission in the micrographs, and thus the variation in sample thickness vs. axial position was not able to be quantitatively estimated.

The experimental work associated with the model by Eskin *et al.* was performed in a Taylor-Couette flow device and deposition was induced by pressure depletion of a recombined oil (*Eskin et al.*, 2011a). A few interesting experimental findings resulted from this investigation. First, it was determined that in a batch deposition configuration, the deposition of asphaltenes ceased after a particular period of time, suggesting that there is a size limitation above which asphaltenes do not deposit. Second, a crude oil was run in the apparatus one time, heated and pressured back to the initial conditions for a second run. The deposit mass collected between the first and second experiment was nearly identical, revealing that total amount of asphaltenes depositing in the first run was not sufficient to significantly alter the deposition driving force when the experiment was repeated.

Eskin *et al.* modeled the deposition of asphaltenes induced by pressure depletion by imposing a critical asphaltene aggregate size, above which no deposition could occur and at a size below previous estimates for shear inhibition (*Eskin et al.*, 2011a). However, a geometric population balance is successful at modeling batch asphaltene aggregation without imposing a critical particle size and maintaining a constant collision efficiency (*Maqbool et al.*, 2011a). Both aggregation and deposition after an initial layer has formed are due to asphaltene-asphaltene interactions, so there should not be a different mechanism for adhesion/sticking between the two processes. Once an initial asphaltene deposit has formed, additional deposition can be considered to be aggregation between a large and immobile particle and a small and mobile one. Thus, if aggregation can occur in the bulk, deposition should occur at the deposit interface unless shear forces, which are largest at the deposit interface, limit either

process. Additionally, experiments designed to measure the sticking probability of latex spheres depositing on glass beads revealed that particle size did not alter the likelihood of adhesion (*Elimelech and O'Melia, 1990*).

The discovery of the true kinetic nature of asphaltene aggregation at low precipitant concentrations has opened the door for new asphaltene deposition investigations (*Maqbool et al., 2009, 2011a,b*). The experimental work presented here will focus on asphaltene deposition measured in a capillary tube. The effect of precipitant concentration, confirmation of good mixing, and validation of the deposit location, all of which have been largely overlooked previously, will be explored in-depth in this investigation.

The goal of this investigation is to relate the extent of asphaltene deposition to a driving force, which has not been previously accomplished. Previous asphaltene deposition investigations have focused only on the transient pressure drop profile to compare variations in experimental conditions, such as the effect precipitant type (n-hexane, n-heptane, etc.) (*Wang et al., 2004; Lawal et al., 2012*) It is doubtful significant progress will be realized in understanding the asphaltene deposition process until a driving force can be related to the extent of deposition. Recent asphaltene modeling attempts have achieved qualitative (*Vargas et al., 2010*) and quantitative (*Eskin et al., 2011a*) agreement with experiments; however, modeling results still rely heavily on tunable parameters, and the bounds of these parameters do not yet have experimental backing. Until the mechanism or driving force for asphaltene deposition has been determined, the accuracy of predictive asphaltene deposition models is limited. However, once the driving force for asphaltene deposition is determined, accurate modeling of asphaltene fouling may be possible and can be improved if combined with an aggregation and precipitation model.

2.2 Experimental Methods

2.2.1 Experimental Apparatus

The primary experimental deposition apparatus consists of syringe pumps (Teledyne ISCO, 500D) filled with DI water that are used to displace canisters of oil and n-heptane, used as the precipitant, to pump the fluids through a capillary. Toluene (T290, >99.9%) for washing and n-heptane (H350, >99.5%) were HPLC grade and supplied from Fisher Scientific. The oil and heptane lines flow into a constant temperature water bath and meet in an ultra-low volume tee (Upchurch Scientific, U-428) and are forced through a 10 μm porous mixing frit (Upchurch Scientific, A-105-02) to disrupt any interface that may form where the oil and heptane meet and promote mixing. After the mixing frit, there is a 5 cm long stainless steel section of 0.03 inch inner diameter capillary (0.03" ID nominal value; Upchurch Scientific, U-115) that allows the oil and heptane to mix and is called the "mixing capillary". After mixing, the oil-heptane mixture flows through a second 10 μm porous frit that acts as a prefilter to prevent large flocs from entering the capillary test section that could potentially be formed in the mixing section due to pockets of high heptane concentration. The mixture then flows through another ultra-low volume tee to connect the positive side of the differential pressure transducer (either Sensotec, Z/741-08ZD, 100 psi range, ± 0.5 psi or Sensotec, A-5/882-15, 10 psi range, ± 0.05 psi). The fluid then flows through the stainless steel "deposition capillary" test section (Upchurch Scientific, U-101, U-111 or U-114) where the differential pressure is monitored, past an additional tee to connect the negative side of the pressure transducer, through a 40 psi back pressure regulator (BPR, Upchurch Scientific, U-469), and then into a collection container. A diagram of the primary experimental deposition apparatus used in this study is shown in Figure 2.1.

The primary experimental apparatus shown in Figure 2.1 was designed to pre-

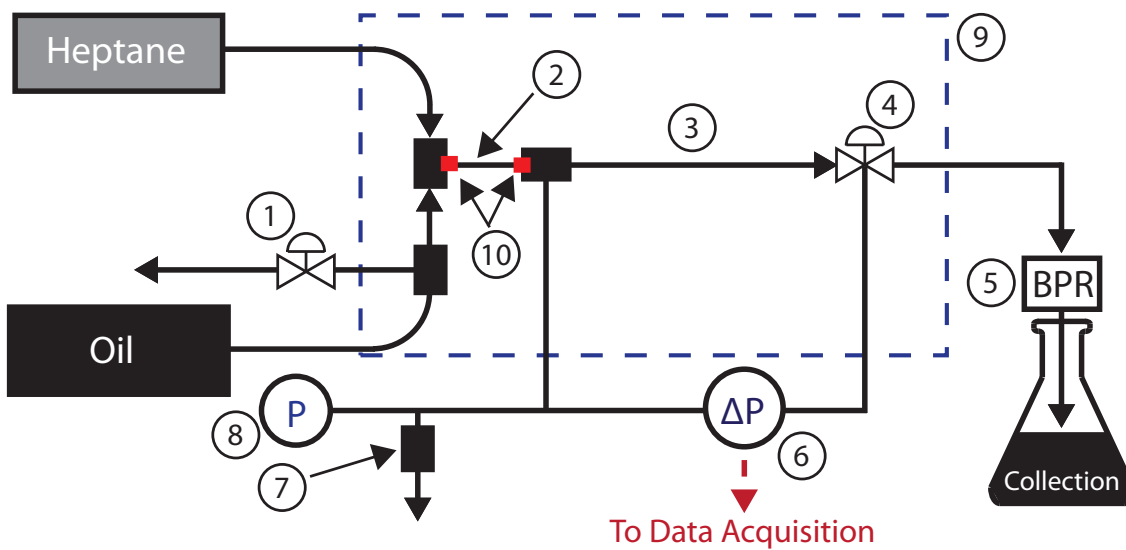


Figure 2.1: Diagram of the primary experimental deposition apparatus used in this study. 1: Micrometering valve (closed during experiment). 2: Mixing capillary, 5 cm long. 3: Deposition capillary, 5 or 30 cm long. 4: Micro-splitter valve. 5: Back pressure regulator, 40 psi. 6: Differential pressure transducer. 7: Pressure relief valve (closed during normal operation). 8: Pressure gauge. 9: Constant temperature water bath. 10: 10 μm porous frits.

vent removal of the deposit by shear effects during experimental shutdown when the elevated pressure in the system was bled to atmospheric conditions. When shutting down the experiment, the microsplitter valve (Upchurch Scientific, P-451) at the deposition capillary outlet was closed to prevent any fluid from traveling through the system and potentially removing the asphaltene deposit. The micrometering valve (Upchurch Scientific, P-446) near the mixing capillary inlet was then slowly opened to relieve the system pressure. The deposition capillary was drained by holding the outlet against a piece of paper towel and allowing the oil-precipitant mixture to drain. Prior to performing deposition experiments, the oil was centrifuged at 14,000 g for 3 hours to remove already precipitated asphaltenes, sand particles and water. The two oils used in this study, Oil A and WY Oil, were free of any production chemicals that are commonly used to prevent deposition or corrosion. All experiments were performed at a total volumetric flow rate (oil + heptane) of 5 mL/hr in order to keep the residence time in the mixing capillary constant. The length of the mixing capillary was not varied to ensure consistency between experiments. For Oil A, the temperature was kept at 60 °C for all experiments, while the temperature was varied for WY Oil.

When starting a deposition experiment, the system was first pre-filled with only oil and all lines were bled to eliminate air pockets. During the pre-filling step, a small pocket of air was trapped between the oil and heptane to prevent mixing of the two liquids prior to experimentation, and oil was allowed to flow into the heptane line. Once the system was filled with oil and back-pressure was established, the heptane flow was started. The heptane flow pushed the air pocket and oil into the deposition apparatus at the initial stages of the experiment. Strictly adhering to this startup procedure will allow for accurate measurement of when the heptane is introduced into the system, identifiable by a sharp decrease in the pressure drop due to the lower viscosity of the fluid inside the capillary with heptane added. The time, t , when

heptane enters the system is defined as $t = 0$. This procedure only allows heptane to enter the system once the proper flow rate and back-pressure have been established, minimizing error and enhancing reproducibility. All of the generated pressure drop profiles are shifted based on the initial steady state pressure drop, ΔP_o , which is the pressure drop of the oil-heptane mixture flowing through the apparatus before any deposition is detected. New precut capillaries and porous frits were used as supplied from Upchurch Scientific and replaced for each new run. All heptane in oil concentrations are reported as volume percent heptane because the concentration in the deposition apparatus was controlled by varying the volumetric flow rate of oil and heptane pumps. The standard operating procedure (SOP) for performing a capillary deposition experiment is included in Appendix B.

In order to study the effect of particle aging on the asphaltene deposition process, a second configuration of the deposition apparatus was used to recirculate premixed oil and heptane mixtures through a capillary. A single peristaltic pump (Masterflex #7523-20) replaced the syringe pumps and mixing system in Figure 2.1. The intake for the pump and outlet of the deposition apparatus was a continuously stirred flask containing a premixed oil and heptane solution. The flow rate for these experiments was 36 mL/hr and a 0.01" ID and 30 cm length deposition capillary was used. As with the primary apparatus shown in Figure 2.1, the pressure drop was monitored across the deposition capillary to determine the extent of fouling. The recirculating deposition apparatus that is used to study particle aging is shown in Figure 2.2.

2.2.2 Mixing Considerations

When the oil and heptane first come into contact in the primary deposition apparatus near the entrance of the mixing capillary, shown in Figure 2.1, heptane will migrate to the top of the mixing capillary because it is the less dense material. If the heptane is concentrated at the top of the mixing capillary, the local concentration

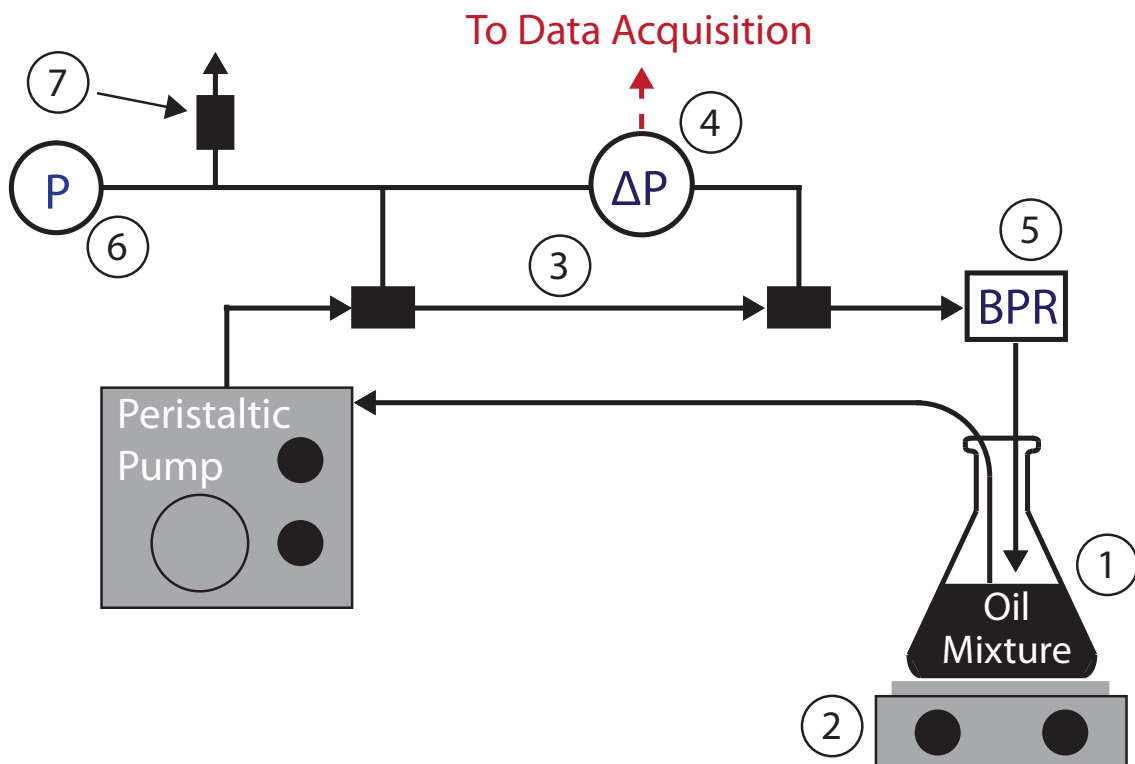


Figure 2.2: Diagram of the recirculating deposition experimental apparatus. 1: Pre-mixed oil-precipitant reservoir. 2: Magnetic stirrer. 3: Deposition capillary. 4: Differential pressure transducer. 5: Back pressure regulator, 40 psi. 6: Pressure gauge. 7: Pressure relief valve (closed during normal operation).

will be greater than intended, compared to a well-mixed system, and could potentially destabilize asphaltenes to a higher degree than desired. Computational Fluid Dynamic (CFD) calculations of the mixing process confirmed that gravitational flow is significant and predicted that mixing of oil and heptane will be complete by the entrance of the deposition capillary. Appendix C contains the details and results of the CFD simulations. Experimentally, the quality of the mixing in the deposition apparatus can be determined by visualization of the deposition capillary inlet with electron microscopy. If it is assumed that the thickest deposits occurs in the region of greatest heptane volume fraction and oil and heptane form a single phase, three mixing scenarios are possible:

1. A deposit observed only on the top of the deposition capillary would suggest that mixing is poor and asphaltene deposition is due to higher than intended heptane concentrations.
2. A deposit that is thicker on the top compared to the bottom of the deposition capillary would suggest there is poor mixing in the system, but asphaltenes are still depositing at a precipitant concentration lower than the mean or bucket value (near the bottom of the capillary).
3. A deposit that is uniform radially at the inlet confirms good mixing due to the homogenous concentration distribution of heptane.

To validate the mixing in the apparatus, these deposition locations will be considered when interpreting the scanning electron microscopy (SEM) images of the asphaltenes deposits. The SEM images were generated using a FEI Quanta 200 3D instrument operating in the low vacuum mode (0.5 Torr). Proper mixing is not a concern for the recirculating deposition apparatus in Figure 2.2 because the reservoir is premixed and continuously stirred.

2.3 Results and Discussion

2.3.1 Electron Microscopy of Deposits

Before visualization of asphaltene deposits was performed, a blank capillary and a control experiment with only Oil A flowing through the system for approximately 4 hours were viewed by SEM. Figure 2.3 shows two 0.02” ID capillaries with the left image being a new and clean capillary and the right image shows the control experiment of only Oil A. In both of the images, it can be seen that there is visible surface roughness on the inner surface of the capillary, which can be used to aid in the identification asphaltene deposits. The control experiment with only Oil A did not produce any visible deposit.

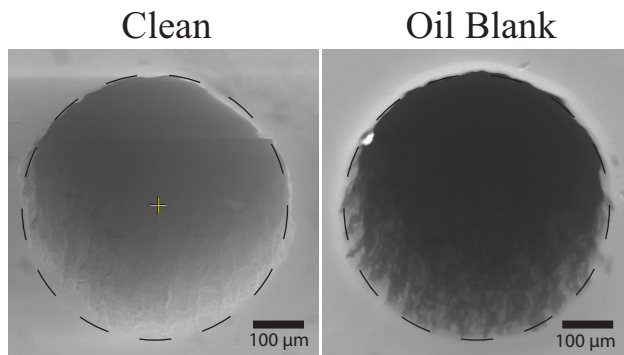


Figure 2.3: SEM images of a clean, unused capillary (left) and control experiment where only Oil A was flowed through the system (right). Both capillaries have a 0.02” ID.

The deposits shown in Figure 2.4 were generated by flowing mixtures of 30 vol. % heptane in Oil A through 0.02” ID and 5 cm length capillaries at 60 °C. The SEM images have been rotated to match their orientation during the deposition experiment and dashed circles have been drawn on the SEM images to aid in the identification of the inner capillary wall edge. The SEM images of the deposit at the deposition capillary inlet (left) and at the outlet (right) are shown for three different experiments (runs #1-3) terminated at different times. Runs 1 and 2 were terminated after 4

hours to visualize the deposit and run 3 was stopped after 2.25 hours. While the run 2 deposition experiment was being performed there was a decrease in the measured pressure drop at approximately 3 hours, dropping from roughly 1 to 0.25 psi. This decrease in pressure drop is believed to be caused by a deposit partially clearing from the capillary. Runs 1 and 3 had no deposits clearing. Since it is unknown what portion of the deposit has been removed in run 2, it is ultimately less conclusive than the others. The deposits shown in Figure 2.4 are roughly uniform radially, indicating proper mixing is obtained in the deposition system. The transient pressure drop profiles for the SEM runs in Figure 2.4 are shown in Figure 2.5

The SEM images of the asphaltene deposits represent the first confirmation of arterially forming deposits generated in a laboratory. For all runs, the deposit is thicker at the inlet than at the outlet. The asphaltene deposit can clearly be identified by the smooth surface of the deposit compared to the visible roughness in a clean capillary or the oil control experiment found in Figure 2.3. The deposition capillary outlet for run 1 in Figure 2.4 shows a large particle at the bottom of the capillary. An energy dispersive X-ray spectroscopy (EDX) unit on the SEM instrument did not detect the presence of carbon on the large particle and it is consequently a contaminant that likely adhered while draining the capillary or transportation to the electron microscopy laboratory.

2.3.2 Oil Properties and Instantaneous Onset Point

After proper mixing was confirmed in the apparatus, the concentration of precipitant needed to cause instantaneous precipitation (i.e. less than 15 minutes) was determined. This condition, often called the instantaneous onset point of the oil, was determined by controlling the composition of the oil-heptane mixture by varying the flow rates in the deposition apparatus and collecting samples after mixing with a short collection line. The total flow rate for the system was 5 mL/hr and approx-

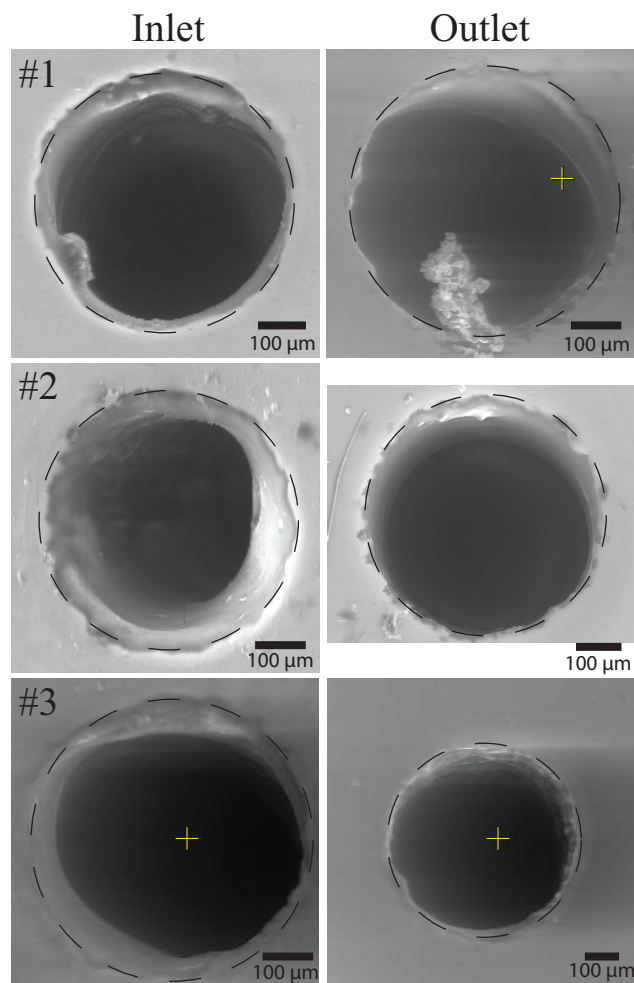


Figure 2.4: SEM images of the deposition capillary inlet (left) and outlet (right) for three runs (#1-3) of 30 vol. % heptane in Oil A with 0.02" ID and 5 cm length capillaries. The large material found at the bottom of the run #1 capillary outlet is a contaminant, see text for rationale. Dashed circles are drawn to aid identification of inner capillary wall edge.

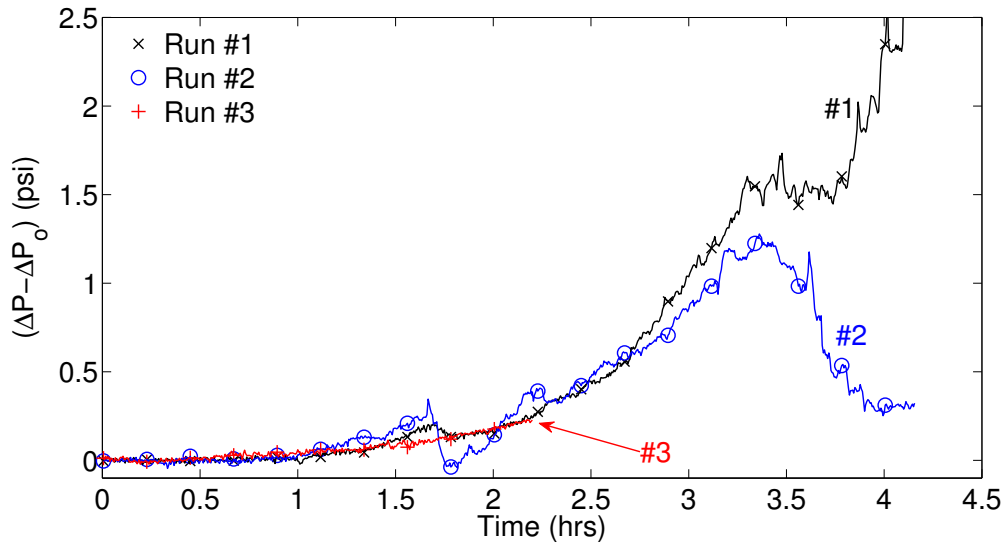


Figure 2.5: Transient pressure drop profiles for 30% Oil A in with 0.02" ID and 5 cm length capillaries. Run numbers 1-3 correspond to SEM images in Figure 2.4. Decreases in the pressure drop are believed to be due to deposits partially clearing from capillary.

imately 1 mL of effluent was collected for each concentration for viewing under an optical microscope. The total time between mixing oil and heptane and microscopy observation was approximately 15 minutes for each sample. The determination of the onset by optical microscopy for Oil A can be seen in Figure 2.6.

As can be seen in Figure 2.6, the instantaneous onset point is between 30 and 40% heptane. Additional experiments (not pictured) further narrowed the onset to between 37.5 and 40 vol. %. It is unnecessary to obtain a more precise estimate of the instantaneous onset point because it would be a function of how much time passed between mixing and microscopy observation, 15 minutes for this measurement (*Maqbool et al.*, 2009). The SEM images in Figure 2.4 confirm that deposition is occurring at 30% heptane, significantly below the instantaneous onset point. Additionally, the lack of visible asphaltenes at the system effluent reveals that all of the asphaltene deposition is caused by sub-micron aggregates.

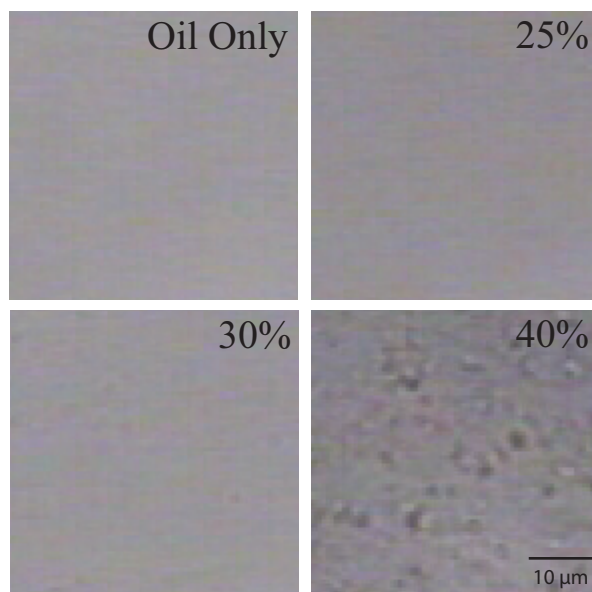


Figure 2.6: Micrographs of deposition apparatus effluent used for onset determination at various heptane volume percents (0% to 40%). The instantaneous onset point is measured to be 40 vol. % heptane.

Oil densities were measured using a pycnometer and the asphaltene content for Oil A was measured with a 40:1 heptane dilution and a centrifugation procedure described previously (*Maqbool et al.*, 2009). The total asphaltene content for WY Oil was measured with 90% vol. heptane dilution due to the low asphaltene content. Oil viscosities were measured by the pressure drop through a long capillary and compared to a liquid with known viscosity. The viscosity for mixtures of oil and heptane was estimated by volumetric logarithm mixing. The properties of each of the oils can be found in Table 2.1.

The solubility of asphaltenes in Oil A (g of soluble asphaltenes per 100g of crude oil) at 60 °C and various heptane volume percents was measured by the same technique as the total asphaltene content and is shown in Figure 2.7. As expected, the solubility of asphaltenes in Oil A decreases at increasing heptane concentrations. The dashed line at the top of the Figure 2.7 represents the total heptane asphaltene content. The solubility below 30 vol. % heptane is significantly limited by precipitation

Table 2.1: Select crude oil properties used in this investigation.

	Oil A	WY Oil
Heptane Asphaltene Content (wt. %)	9.90±0.07	0.69±0.04
Room Temperature Density (kg/m ³)	869.2±0.2	854.8±0.1
Viscosity @ 60 °C (mPa*s) @ 20 °C	6.78±0.07	2.83±0.01
Instantaneous Onset @ 60 °C (vol. % heptane @ 20 °C	40%	35%
	-	25%

kinetics and was not measured, in agreement with previous observations (*Maqbool et al.*, 2009).

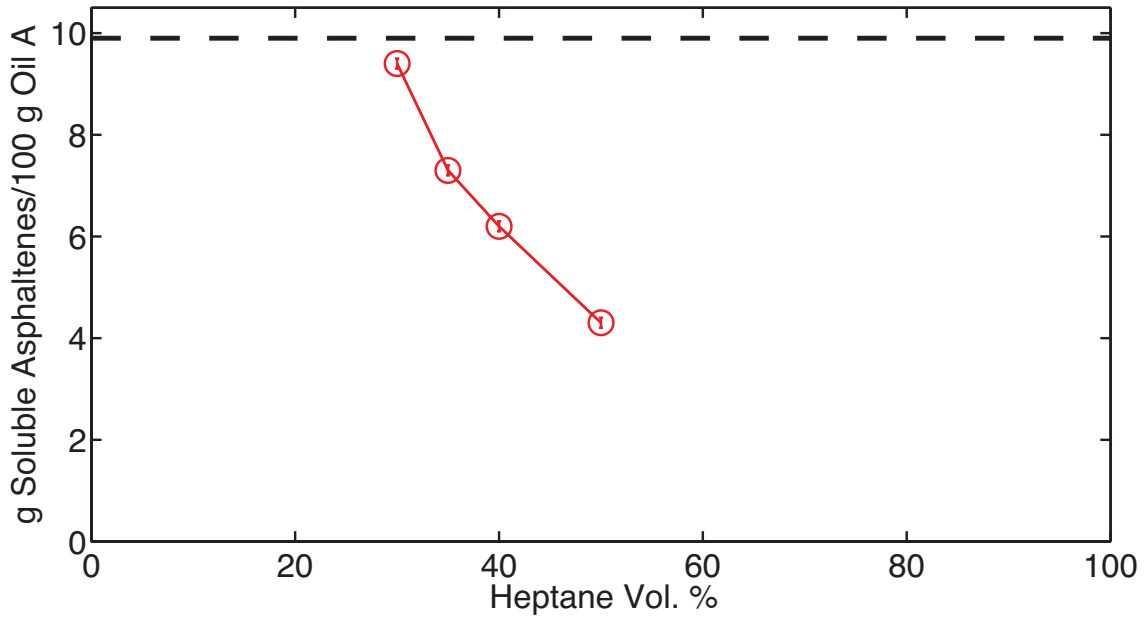


Figure 2.7: Asphaltene solubility in units of g of asphaltenes per 100g of crude oil at 60 °C for heptane in Oil A. The dashed line represents the total asphaltene content, 9.90 ± 0.07 .

2.3.3 Deposition as a Function of Precipitant Concentration

Mixtures of different volume fractions of heptane in oil were flowed through 0.01” ID stainless steel capillaries of either 5 cm or 30 cm length and the differential pressure, ΔP , was measured as a function of time. The initial pressure drop without deposition, ΔP_o , was subtracted from transient differential pressure measurement, as described in the Experimental Methods section. There was no difference between the measured pressure drop in a 5 cm vs. 30 cm deposition capillary, which will be discussed later on in the Results and Discussion section. The results shown in Figure 2.8 show $(\Delta P - \Delta P_o)$ vs. time for Oil A at a total flow rate of 5 mL/hr and 60 °C for various heptane concentrations. One observes that the deposits are detected sooner at high heptane concentrations than at lower heptane concentrations and also have a greater rate of deposition, as indicated by the slope of the $(\Delta P - \Delta P_o)$ vs. time plot in Figure 2.8. The time required to detect the deposit by pressure drop will be referred to as the “deposition detection time”.

For quantitative determination of the deposition detection time, t_d , it is defined as the time where an upward trend the pressure drop is first observed. Due to the noise in the pressure drop measurements at the first measurable deposit, some degree of error is to be expected in the deposition detection time measurement. An estimate of this error is included in the deposition detection time measurements, shown in Figure 2.9. The solid line represents a linear regression of the detection time results. The results reveal that there is an exponential dependence on the deposition detection time with respect to the heptane concentration with the detection time being longer at lower heptane concentrations, varying from 7.6 ± 0.6 hours at 20 vol. % heptane to 0.08 ± 0.01 hours at 50 vol. % heptane. It is unclear from the experimental results in Figure 2.9 whether the deposition detection time is a result of experimental detection limitations in measuring small differential pressures or slow kinetics of asphaltene adsorption on the metal capillary surface.

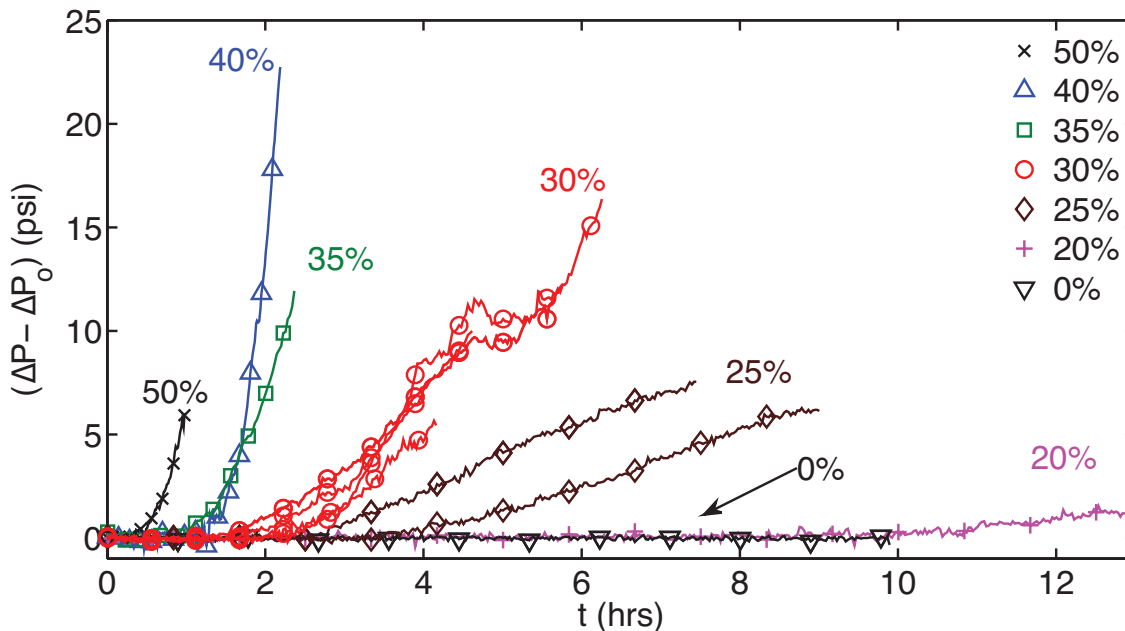


Figure 2.8: Pressure drop vs. time for Oil A diluted with various heptane volume percents in 0.01" ID capillaries of 5 cm and 30 cm lengths. All runs performed at 60 °C and 5 mL/hr.

The asphaltene precipitation kinetics research performed in our lab by Maqbool *et al.* revealed that when an oil-heptane solution is observed over time, asphaltenes will eventually precipitate for concentrations lower than the instantaneous onset point, but it may take several months or longer to detect the precipitation (Maqbool *et al.*, 2009). Slow aggregation could potentially occur inside the capillary due to a distribution of residence times for the fluid flowing through the capillary, possibly allowing for micron-sized aggregates to form inside the capillary. In order to illustrate that deposits were being formed by sub-micron aggregates, microscopy experiments at 25 vol. % heptane and 60°C were performed and the onset time (i.e., the time for asphaltenes to grow to 0.5 μm and be detected by optical microscopy) was measured and found to be approximately one month. Deposition in the capillary is detected after only three hours, highlighting the sensitivity of the deposition apparatus and revealing that all asphaltene aggregates in the capillary are below 0.5 μm . This observation and the

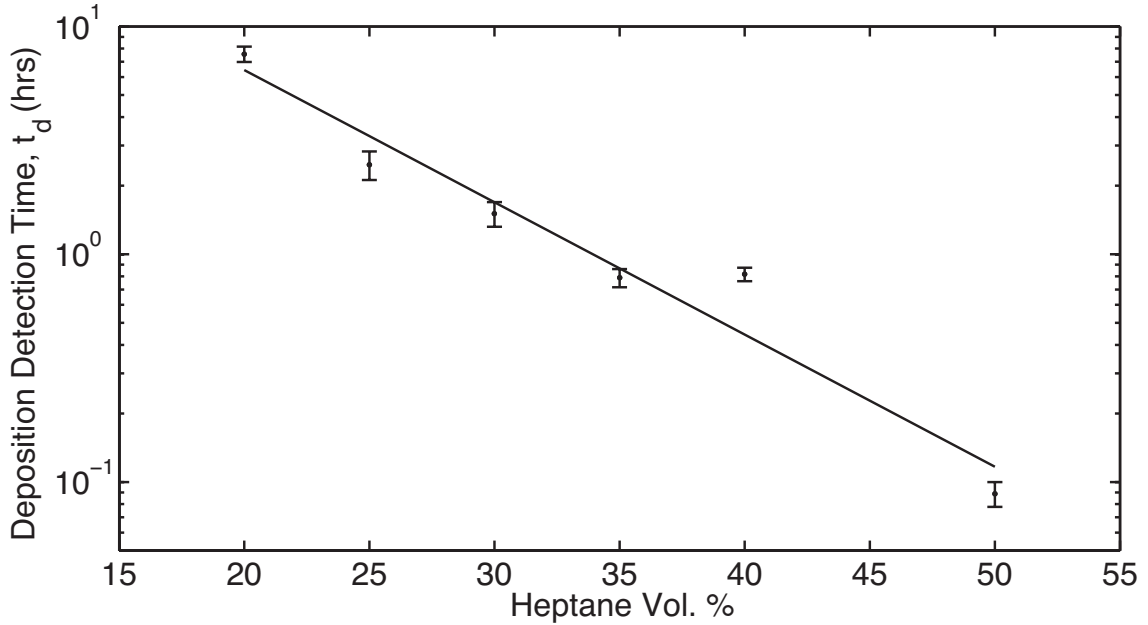


Figure 2.9: Measured deposition detection times, t_d , for the first deposit to be detected as a function of heptane concentration for Oil A. Line represents a linear regression of the results.

lack of detectable particles in the effluent below 40 vol. % heptane in Figure 2.6 confirms that asphaltene deposition is dominated by sub-micron asphaltenes at low heptane concentrations.

The deposition results at heptane concentrations as low as 20 vol. % further show that the asphaltenes are destabilized and have the ability to deposit before the instability can be identified by microscopy. Although it takes roughly 8 hours to detect the deposits formed at 20 vol. % heptane, the deposition apparatus is a continuous flow process and the asphaltenes that are responsible for the deposit have only been in contact with heptane for approximately 16 seconds, the mean residence time of the mixing section. This finding reveals that asphaltenes are destabilized and able to deposit virtually immediately after a precipitant is added, and the kinetic effects detected by Maqbool *et al.* (Maqbool *et al.*, 2009) are due to a slow aggregation process and not a delay in when the destabilization first occurs. Additionally, the gradual

decrease in deposition as the heptane concentration is reduced clearly demonstrates that *the definition of an instantaneous onset point is irrelevant with regards to asphaltene deposition*. Just as there is no well-defined onset condition for asphaltene precipitation, asphaltene deposition also occurs below the instantaneous precipitation onset point and at lower precipitant concentrations that previously believed.

The axial uniformity of the deposits generated in the 0.01” ID capillaries can be assessed by comparing the pressure drop vs. time profiles for experiments performed in deposition capillaries of different lengths. If the deposit is non-uniform and exists primarily in the short capillary, the pressure drop profiles of the long and short capillaries will superimpose after shifting by the initial pressure drop, ΔP_o . The section of the capillary at a farther axial position from the inlet that does not have a deposit will have a constant pressure drop vs. time, and its contribution to the pressure drop will be eliminated by subtraction of ΔP_o . Only the section with deposition will cause an increase in pressure over time, and if the deposition section is entirely contained within the short capillary, the pressure drop vs. time profiles will superimpose between a long and short capillary once ΔP_o for each experiment is subtracted. The mathematical validation of this comparison and other axial deposit profiles is found Appendix D.

In order to investigate the axial deposit profile by comparing the pressure drop between capillaries of different length, 30 vol. % heptane in Oil A deposition experiments were performed in 5 cm and in 30 cm length deposition capillaries. Two experiments were performed for each of the two capillary lengths and all four deposition experiments are shown in Figure 2.10. The pressure drop vs. time profiles of the long and short capillaries superimpose, within experimental reproducibility, after shifting by the initial pressure drop, ΔP_o , revealing that the deposit is axially non-uniform and formed primarily in the first 5 cm of the capillary, in agreement with the SEM images. The result does not eliminate the possibility of deposits forming at po-

sitions farther down the capillary, but it clearly illustrates that the rate of deposition is significantly higher near the capillary inlet and that the pressure drop measurement is dominated by the deposit near the capillary inlet. If the deposits were uniform in the long and short capillaries, the pressure drop profiles would superimpose if normalized by the capillary length, see Appendix D for the mathematical validation. This is clearly not the case, because the pressure drop in the long capillary is not six times the magnitude as the short capillary.

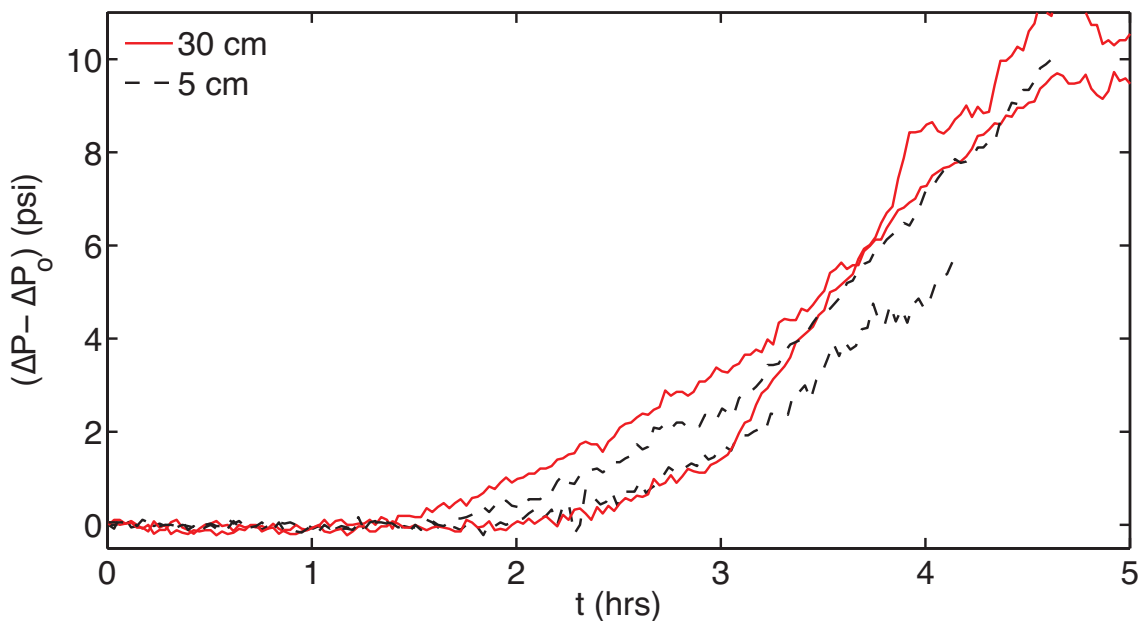


Figure 2.10: Comparison of $(\Delta P - \Delta P_0)$ vs. time plot for the short (5 cm) and long (30 cm) capillaries. Two experiments for each length are shown and all experiments were performed with 30 vol. % heptane. Differences represent experimental reproducibility and results clearly demonstrates non-uniformity and that the deposit is occurring preferentially near the capillary inlet.

2.3.4 Application of Population Balance Model

In order to determine the particle size distribution (PSD) of asphaltenes aggregates in the deposition apparatus, a previously published geometric population bal-

ance model was utilized (*Maqbool et al.*, 2011a). The population balance model provides the concentration of asphaltene aggregates of a given size as a function of time by solving a discretized and geometrically scaled formulation of the Smoluchowski equation. The diffusion limited collision kernel is scaled by the particle-particle collision efficiency, β_{P-P} , to approximate the fact that only a fraction of actual particle-particle interactions result in a successful collision/aggregation process. The collision efficiency between aggregates (sticking probability) was determined from the model results to predict the mass precipitated vs. time for a sample of 35% heptane in Oil A at 60 °C.

The collision efficiency that best fit the experimental results was 1.79×10^{-5} for an initial particle diameter of 2.5 nm, which was the value used previously (*Maqbool et al.*, 2011a). The PSD was calculated at 1 second, 16.7 seconds and 24.1 seconds. The mixing section in the experimental apparatus has a mean residence time of 16.7 seconds and the PSD at this time represents the distribution at the capillary inlet. The PSD at 24.1 seconds represents the conditions at the capillary outlet of a 2” long capillary with a 0.02” ID. The PSD at each of the three times are shown in Figure 2.11.

There is little difference in the particle size distribution between the capillary inlet (16.7 seconds) and outlet (24.1 seconds) shown in Figure 2.11. However, it can be seen by the 1 second PSD that the size does rapidly grow from the initial diameter of 2.5 nm once a precipitant is added. The PSD obtained from the population balance model further confirms that asphaltene deposition is occurring from sub-micron aggregates, and for the 35% heptane sample, aggregates are smaller than 100 nm.

2.3.5 Deposition of WY Oil

Deposition experiments were also performed on a second crude oil, WY crude oil, at both 60 °C and at 25 °C in 0.01” ID and 5 cm length capillaries. The pressure

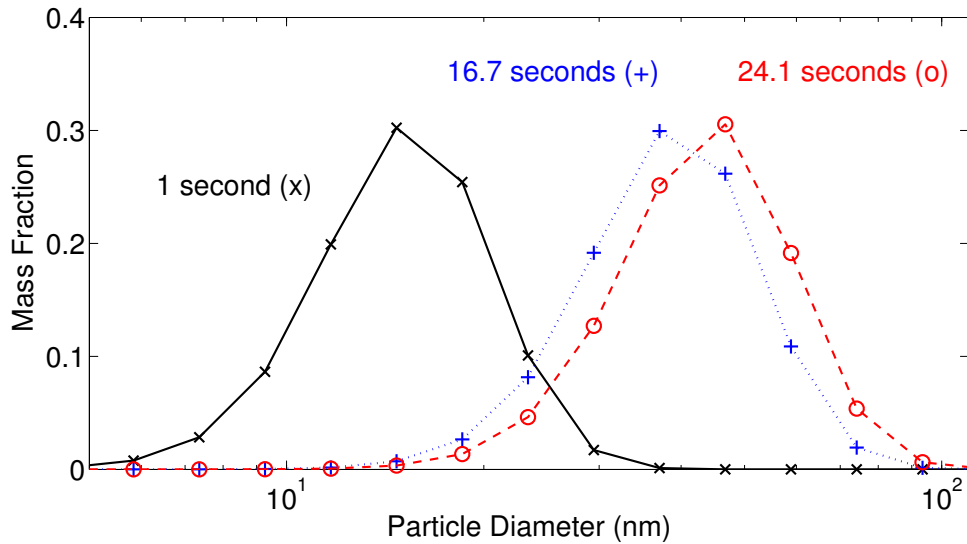


Figure 2.11: Asphaltene particle size distribution at times of 1 second (×), 16.7 seconds (capillary inlet, +) and 24.1 seconds (capillary outlet, o) for a 35% heptane in Oil A mixture at 60 °C.

drop for WY Oil was an order of magnitude smaller than that of Oil A, and was on the order of the error of measurement for the transducers used, owing to the low asphaltene content and viscosity. Consequently, it is expected for the deposit to be less severe and more difficult to detect. Nevertheless, electron microscopy measurements were performed on the WY Oil capillaries, despite the minimal pressure drop. The 0.01” capillaries had a less circular inlet and showed some irregularities compared to the 0.02” capillaries, likely due to difficulties in manufacturing small ID capillaries. Figure 2.12 shows SEM images of the deposition capillary inlet and outlet for 35 vol. % heptane at 60 °C and 25 vol. % heptane at 25 °C. The images reveal axially non-uniform deposition, thicker at the inlet compared to outlet, as observed with Oil A. The low pressure drop measured for WY Oil reveals that the capillary deposition technique is most accurate when the oil has a relatively high asphaltene content.

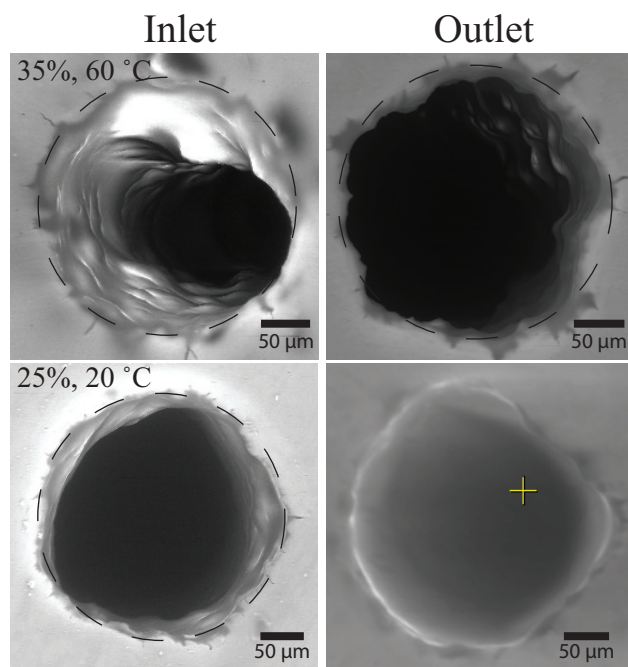


Figure 2.12: SEM images of the deposition capillary inlet (left) and outlet (right) for the WY Oil deposits generated in a 0.01" ID capillary with a 5 cm length at 35 vol. % heptane at 60 °C (top) and 25 vol. % and 25°C (bottom). As with Oil A, the deposit is thicker at the inlet.

2.3.6 Deposition of Precipitated and Aged Asphaltenes

Additional deposition experiments were performed with a peristaltic pump to study whether crude oil containing asphaltene particles previously precipitated with heptane would deposit in a capillary. Oil A was diluted to 40 vol. % heptane and a total volume of 50 mL, and continuously stirred for 95 hours prior to the start of the experiment to ensure complete precipitation. At 40 vol. % heptane, the insoluble asphaltene fraction on a crude oil basis is 4.7 ± 0.2 wt. %, roughly half of the asphaltenes in the oil. After 14 hours of flowing the premixed mixture through a 0.01" ID capillary, no deposition was detectable from either pressure drop measurements or SEM images of the capillary inlet. A snapshot of the pressure drop vs. time for the deposition experiment with already precipitated asphaltenes is shown in Figure 2.13 that shows no deposition is detectable from pressure drop measurements. The inlay image in Figure 2.13 is an optical micrograph of the 40% heptane in Oil A mixture, clearly showing particles. It can be seen that in contrast to the previous section, where heptane was added continuously during the flow deposition experiments, there is no measurable deposit formed with the precipitated and aged oil-precipitant system. This finding demonstrates that asphaltenes only deposit when they are in the process of aggregating and that *aged asphaltene aggregates do not deposit*. Wang *et al.* also concluded that precipitated asphaltenes do not deposit, however, the amount of precipitated asphaltenes was not quantified in their experiment and the lack of observed deposition could have be due to a small precipitated fraction, which is not the case here (Wang *et al.*, 2004).

2.3.7 Oil A Normalized Plot

It is common practice to convert pressure drop measurements to an estimate of the deposit thickness, assuming an axially uniform deposit thickness (Wang *et al.*, 2004; Lawal *et al.*, 2012). While this is a useful procedure for visualizing the deposit

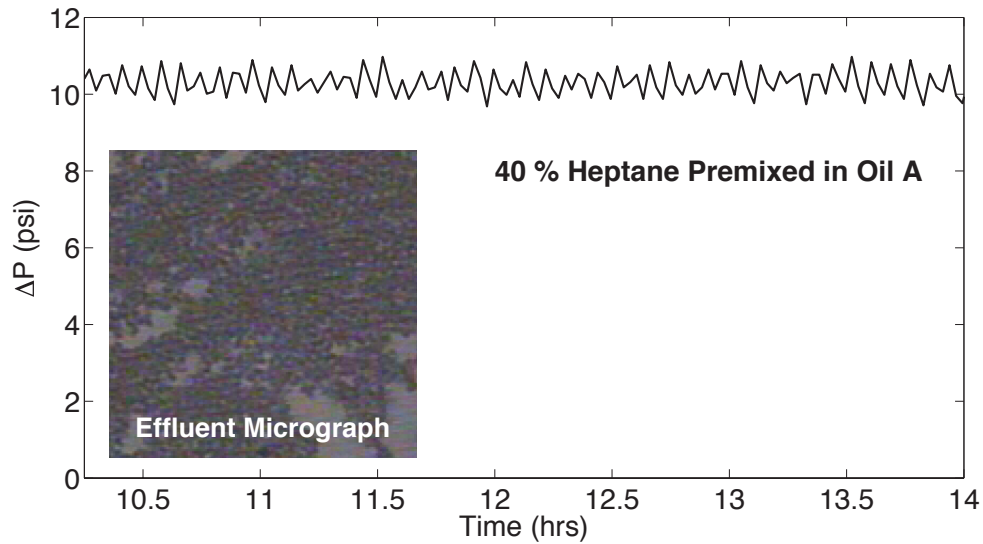


Figure 2.13: Pressure drop profile for the 40% heptane in Oil A premixed solution that was aged for 95 hours. No deposition was detected after 14 hours of run time. Inlay is optical micrograph of the recirculating fluid.

in the capillary and factoring out the influence of viscosity or flow rate, it does not aid in the understanding of the mechanism or driving force for deposition. In contrast to previous approaches, the deposition profiles shown in Figure 2.8 will be normalized by the insoluble asphaltene concentration, C_A^o (kg/m^3), at the experimental heptane volume percent. Additionally, the experimental results will be normalized by the mixture viscosity, μ , because the pressure drop for capillary flow is proportional to viscosity. This normalization scheme will allow of for a qualitative assessment of the effect of heptane concentration on the deposition process. Unfortunately, due to the non-uniform deposition profile, the pressure drop cannot be simply related to a deposit thickness. Normalization by the concentration of insoluble asphaltenes in each oil-heptane mixture will account for the total number of asphaltenes that can potentially deposit. The concentration of insoluble asphaltenes as a function of volume percent heptane can be calculated by examination of the solubility of asphaltenes shown in Figure 2.7. The difference between the solubility measurements and total asphaltenes

content divided by 100, provides the mass fraction of asphaltenes precipitating from the crude oil, F . The concentration of insoluble asphaltenes, C_A^o , is lowered due to the dilution of heptane and can be calculated by the following expression:

$$C_A^o = d_{Oil}\phi_{Oil}F \quad (2.1)$$

where d_{Oil} is the mass density of the crude oil (inclusive of asphaltenes), ϕ_{Oil} is the volume fraction of crude oil in the deposition experiment, and F is the mass fraction of insoluble asphaltenes precipitating from the crude oil (g insoluble asphaltene per g crude oil). The density of Oil A and total volumetric flow rate do not change between experiments and are not used in normalization. The volume fraction of oil in the system is necessary to account for the dilution effect of heptane on the concentration of asphaltenes. The pressure drop profiles will be divided by both the mass fraction of insoluble asphaltenes on an oil basis (calculated from Figure 2.7) and the oil volume fraction to correct for the differences in asphaltene solubility at various heptane concentrations.

Deposition experiments for heptane concentrations between 30 and 50 vol. % heptane can be normalized because a measurement of the asphaltene solubility is available, thus each pressure drop was divided by $\mu\phi_{Oil}F$. In addition, the time for each experiment was shifted by an individually measured detection time, t_d , and the difference, $t - t_d$, was used for the x -axis. Each of the multiple experiments at 30 vol. % heptane was shifted by an individually measured deposition detection time to account for deviations in the capillary inner diameter which will shift the deposition detection time. A slight variation in the capillary inner diameter will change the minimum deposit thickness required to cause a pressure drop increase greater than the experimental measurement noise. Thus, for a constant flux of asphaltenes to the deposit at a given heptane concentration, a capillary with a larger inner diameter will have a longer deposition detection time. The scaled deposition profiles that are

shifted by deposition detection time are shown in Figure 2.14. In addition, Figure 2.15 shows a zoomed in view from 0 to 1.5 hours to show detail. The normalization results reveal that the large variations in the pressure drop profiles between experiments with different heptane concentrations (Figure 2.8) roughly collapse to a single curve (Figure 2.14) when viscosity and, more importantly, the asphaltene solubility are used to scale the results.

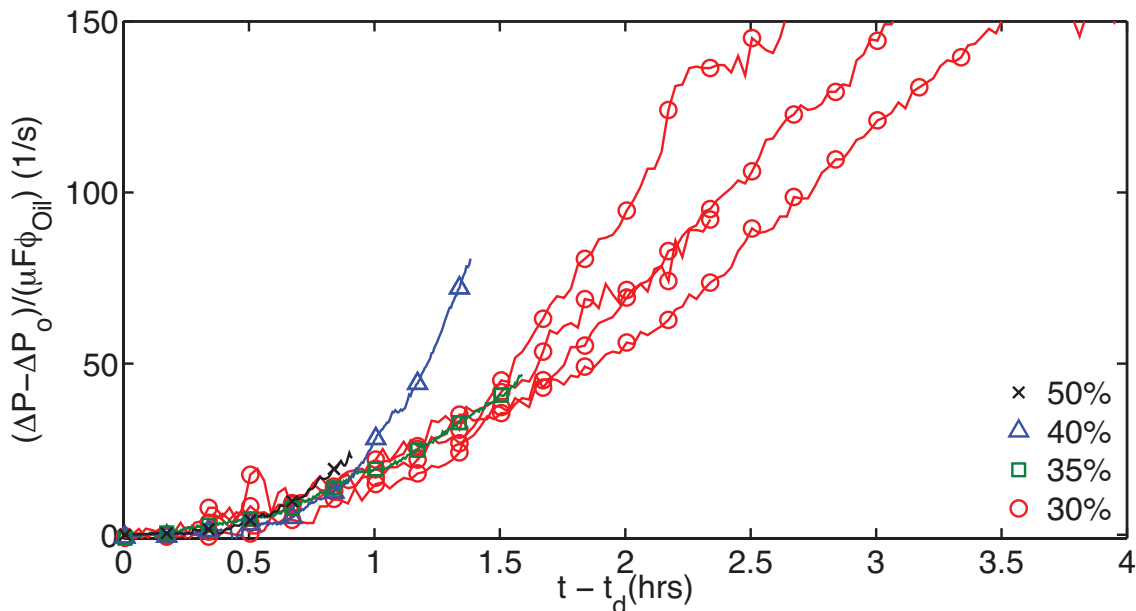


Figure 2.14: Normalized deposition pressure drop profiles for heptane in Oil A, scaled by viscosity and the concentration of insoluble asphaltenes in the capillary. Time is shifted by the deposition detection time, t_d .

The normalization procedure reveals that the deposition behavior of asphaltenes is nearly identical at different heptane concentrations when the solubility of asphaltenes is taken into account. Qualitatively, the normalized pressure profiles reveal the relative propensity for an individual asphaltene aggregate to deposit. Thus, the deposit that forms with 50 vol. % heptane grows more rapidly because there are more insoluble asphaltenes in the oil-precipitant mixture, as observed in Figure 2.8. Additionally, the normalized pressure drop profile reveals that each asphaltene aggregate

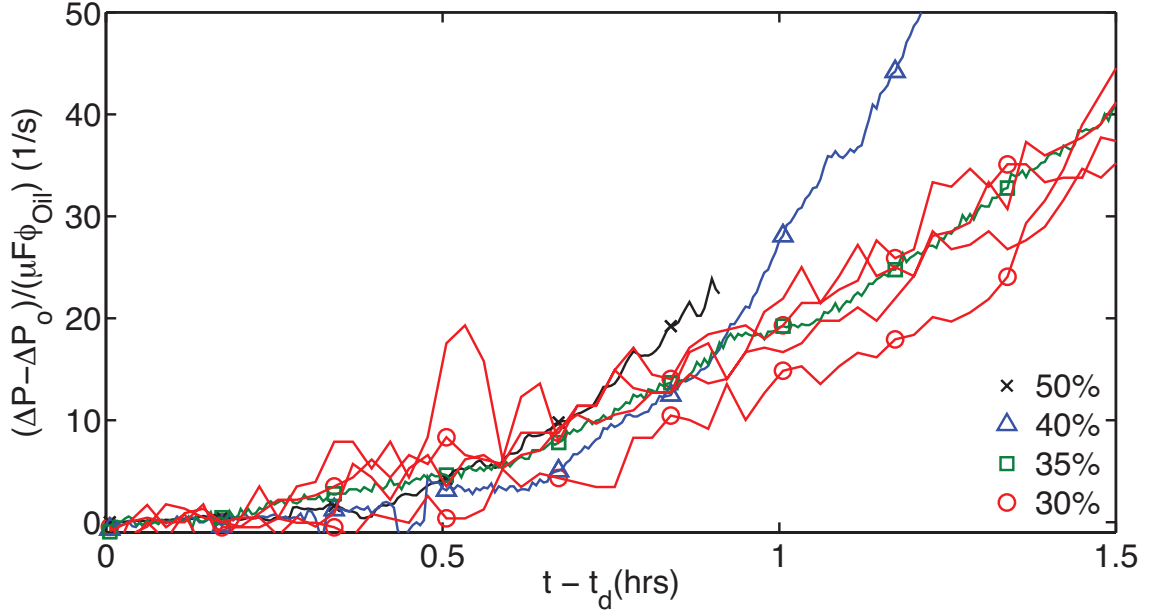


Figure 2.15: A zoomed version to show detail of the normalized deposition pressure drop profiles shown in Figure 2.14.

has a similar probability or propensity to deposit. However, the 40 and 50 vol. % heptane experiments begin to deviate from the normalized behavior once the pressure drop increases significantly, and hence, the deposit becomes sufficiently thick. The deviation occurs at a shorter time for at 50% heptane compared to the 40% experiment, possibly indicating that at higher heptane concentrations, asphaltenes may have a higher propensity to deposit, as observed in previous asphaltene aggregation modeling results (*Maqbool et al.*, 2011a).

Normalization of the deposition results by the concentration of insoluble asphaltenes can be justified by examining the dimensionless diffusion-advection equation with cylindrical coordinates, also known as the Graetz problem (*Papoutsakis et al.*, 1980). In the Graetz problem, the dimensionless concentration as a function of position is only a function of the Reynolds and the Schmidt numbers and the dimensions of the capillary. The dimensionless concentration is obtained after normalizing the concentration of insoluble asphaltenes by the inlet concentration, C_A^o . Increasing the quan-

tity of destabilized asphaltenes in the capillary, C_A^o , will not change the dimensionless solution; however, the absolute concentration everywhere will increase proportionally. Therefore if the deposition process can be modeled as a first order surface reaction, doubling the concentration of insoluble asphaltenes will double the concentration of insoluble asphaltenes at the deposit interface, which will subsequently double the deposition rate. For the case of Brownian particle deposition, a first order surface reaction is the most appropriate approach to modeling the deposition process (*Spielman and Friedlander, 1974; Eskin et al., 2011a,b*). Consequently, the asphaltene deposition process should be modeled as Brownian particle deposition because of the success of the normalization procedure shown in Figures 2.14 and 2.15.

Normalization of the two most dilute experiments, 20 and 25 vol. % heptane, was not possible *a priori* because the solubility is unknown for these heptane concentrations due to the long times required for the equilibrium amount of precipitating asphaltenes to be measured. For example, the solubility measurement performed on a 30 vol. % heptane in Oil A mixture at 60°C took approximately three weeks to reach the equilibrium value due to slow asphaltene precipitation/aggregation kinetics. Determining the equilibrium solubility for concentrations below 30 vol. % heptane would take a significantly longer time with conventional means, such as batch filtration or centrifugation (*Maqbool et al., 2009*). The fraction of asphaltenes precipitating from Oil A at the two most dilute heptane concentrations was used as the sole tunable parameter to force the pressure profiles to superimpose with the normalized pressure drop profile. The estimated weight percent of asphaltenes precipitating from the crude oil for the 20 and 25 vol. % heptane experiments to fit the normalized deposition curve in Figure 2.14 was 0.035 and 0.19 ± 0.06 wt. %, respectively. These values can be subtracted from the total asphaltene content line shown in Figure 2.7 to extend asphaltene solubility measurements to previously unobtainable conditions of low heptane concentration for use in thermodynamic model validation. Previous estimates of

the critical stability point of asphaltenes are inaccurate and the development of more sensitive solubility detection techniques, such as the capillary deposition apparatus shown here, should hopefully yield more accurate thermodynamic solubility models. In addition, the slow rate of deposition at 20 and 25 vol. % heptane is caused by the most unstable asphaltenes in Oil A, and the deposition apparatus could potentially be used to capture these problematic asphaltenes for characterization.

The concentration of insoluble asphaltenes is the dominant factor controlling the magnitude of asphaltene deposition, as shown by the virtually identical pressure drop profiles once normalized. Generation of the normalized plot now allows one to estimate the solubility of asphaltenes in dilute precipitant mixtures where slow precipitation kinetics previously rendered similar measurements impossible using conventional techniques. This new procedure is able to estimate the mass percent of asphaltenes precipitating from Oil A over a range spanning two orders of magnitude, from 0.035% precipitating at 20 vol. % heptane to 5.6% at 50 vol. % heptane. These results represent the first experimental evidence that the *dominant influence on asphaltene deposition is simply the solubility of asphaltenes*. The exact mechanism of asphaltene deposition that occurs at the oil-deposit interface is still not well understood; however, the extent of deposition can be estimated via the solubility without knowledge of the deposition surface phenomena.

2.3.8 Deposit Profile and Previous Results Comparison

For both of the crude oils investigated, the deposit was thicker near the inlet of the deposition capillary, compared to the outlet. This finding is in contrast to the work of Wang *et al.*, who reported a uniform axial deposit profile in 100 ft long capillaries (Wang *et al.*, 2004). The experimental evidence for a uniform deposit came only from the mass of the asphaltene deposit and no comparison between capillaries of different length or visualization of the deposits was performed, as was done in the inves-

tigation reported here. Additionally, Wang *et al.* also reported a highly non-uniform deposit using a model system of asphaltenes dispersed in 1-methylnaphthalene. (Wang *et al.*, 2004)

The most probable cause for the observed non-uniform axial deposition profile reported here is local mass transport limitations. The mass transfer entrance region is where the Sherwood number, Sh , and consequently the mass transfer coefficient, k_m (m/s), are functions of the axial position near the capillary entrance (Deen, 1998). Recall that the Sherwood number for internal flow through a capillary of inner diameter, a , is defined as $Sh = \frac{k_m a}{D_A}$, where D_A is the diffusivity of asphaltene nanoaggregates, assumed to be governed by the Stokes-Einstein equation with a diameter of 2.5 nm. The Sherwood number is at a maximum at the entrance of the capillary and decreases with increasing axial position until the fully developed region is reached where it is independent of axial position. The mass transfer entrance length for asphaltenes in the experimental apparatus is calculated to be between 4 and 11 feet, depending on the mixture viscosity, revealing that the deposition in the apparatus is occurring in the entrance region (Deen, 1998). Larger aggregate sizes will result in a longer entrance region due to lower Stokes-Einstein diffusivity values.

In the mass transfer entrance region, the concentration of asphaltenes and the concentration gradient at the capillary wall both decrease rapidly as the mixture travels axially down the capillary. The normalization scheme revealed that the concentration of insoluble asphaltenes is the governing factor controlling deposition, and consequently, the depletion of destabilized asphaltenes near the wall will reduce the deposition flux. Thus, the axial deposition profile that will form in the entrance region will be highly non-uniform, while the profile that forms in the fully developed region will be more uniform. Asphaltene deposition in the entrance region vs. the fully developed region is likely the explanation for the observed uniform deposition profile reported previously by Wang *et al.* in 100 ft long capillaries (Wang *et al.*,

2004). The length of the capillary in the mixing section for the apparatus used by Wang *et al.* is unspecified and the mass transfer entrance region may be entirely contained within that section. Additionally, the deposition rate will be the highest at the entrance of the capillary, highlighting the importance of limiting the length of the mixing section in a deposition apparatus.

Other possible explanations for the observed non-uniform axial deposit profile include asphaltene aggregate size effects (i.e., asphaltenes of different sizes deposit at different rates) and depletion of asphaltenes due to deposition. Size effects are unlikely, because the aggregates are well below the size where shear is expected to influence deposition. Additionally, because of the short residence time (1.8 seconds for a 0.01" ID and 5 cm long capillary) there is likely little difference between the inlet and outlet particle size distributions. Depletion effects can be investigated by calculating the capture efficiency, defined as the mass of insoluble asphaltenes that deposit compared to the mass of insoluble asphaltenes that have entered the capillary. For a 0.01" ID and 5 cm length capillary, the total internal volume is 2.6 μL . For a deposition experiment with 30 vol. % heptane in Oil A, after 4 hours a total of 50.7 μL of insoluble asphaltenes have flowed through the capillary. Thus, the total capture efficiency must be less than 5% (otherwise the entire capillary will be blocked) and the deposition profile is not caused by depletion.

The detection of asphaltene deposits at dilute precipitant concentrations has likely been overlooked previously for a number of reasons: short experiment times, large inner diameter capillaries, and fully developed mass transfer. First, Broseta *et al.* also used 0.01" ID capillaries; however, the precipitant concentration was increased approximately every hour to search for the onset concentration (Broseta *et al.*, 2000). As seen in Figure 2.9, deposits took up to 7.6 hours to detect at low precipitant concentrations, significantly longer than Broseta *et al.* waited. Wang *et al.* utilized 0.02" ID capillaries, which will have a less sensitive pressure drop response to deposit

formation than the 0.01" ID capillaries used here. (*Wang et al.*, 2004) Additionally as mentioned above, the apparatus used by *Wang et al.* may have deposition occurring in the fully developed mass transfer region and the deposition rate in the entrance region will be greater than that further into the capillary. Ultimately, there are number of factors that allowed for the detection of asphaltene deposition at dilute precipitant concentrations that are reported here. The high asphaltene content of Oil A was also advantageous because even a small relative fraction of asphaltene precipitating still represented a large total amount of asphaltenes that can potentially deposit. Finally, not detecting asphaltene deposition after a certain time period of flow does not eliminate the possibility of a deposit slowly forming.

2.3.9 Laboratory vs. Field Asphaltene Deposition

The axially non-uniform deposit profile reported here is not directly comparable to a deposition profile measured in a production wellbore such as the profile reported by *Haskett et al.* (*Haskett and Tartera*, 1965). Thermodynamics dictate that at a particular oil-precipitant composition, a fixed quantity of asphaltenes will precipitate. The quantity of asphaltenes that precipitate resulting from heptane addition to a dead oil will not vary as the mixture travels axially down the capillary because the thermodynamic variables of temperature and composition do not change and the pressure only changes slightly. Additionally, the dead oil-precipitant mixture used in this investigation contains no dissolved light ends and the mixture properties are insensitive to changes in pressure. In a production wellbore, the thermodynamic conditions do vary significantly as a function of axial position, and the hydrostatic pressure decreases when the oil flows vertically toward the surface, which can cause additional asphaltenes to precipitate. Deposition, precipitation, and aggregation all occur simultaneously in the field. Laboratory deposition experiments with a precipitant added can be viewed as a simplified setup that is useful for determining kinetic

asphaltene behavior, both aggregation and deposition, in an apparatus with defined thermodynamics.

2.4 Conclusions

In this work, a capillary deposition apparatus was used to demonstrate that asphaltene deposition occurs before the asphaltene precipitation can be detected by standard techniques, such as optical microscopy. Micrographs of the capillary effluent reveal that asphaltene aggregates that grow to $0.5\ \mu\text{m}$ or greater are not necessary for deposition to occur. This observation reveals that the damage from asphaltene fouling is likely dominated by sub-micron asphaltene aggregates and that large and mature aggregates do not deposit. For the first time, arterial asphaltene deposits generated in the laboratory have been directly observed. The SEM images show that the deposit is significantly thicker at the capillary inlet when compared to the outlet and the deposition profile is most likely caused by transport limitations of asphaltene aggregates diffusing to the deposit interface. Good mixing in the apparatus was confirmed by SEM and supported by CFD simulations.

Contrary to previous results, there is no difference in asphaltene deposition when comparing experiments above and below the instantaneous onset conditions other than the solubility of asphaltenes. No critical precipitant concentration was observed and the extent of asphaltene deposition was a smooth and continuous function of heptane concentration. Attempting to assign an absolute set of conditions, such as an onset point, that will dictate whether or not asphaltenes will deposit fails to describe the complex process of asphaltene stability and fouling. Although it takes some period of time to detect the deposition, the asphaltenes that are responsible for the observed deposits have only been in contact with heptane for a short period of time, approximately 16 seconds. This finding clearly illustrates that asphaltene precipitation kinetics are only a detection limitation in observing asphaltene instability

and not a delay in when asphaltenes begin to precipitate or aggregate. These experimental results stress the importance of understanding asphaltene precipitation and aggregation in the kinetic regime (*Maqbool et al.*, 2009, 2011b,a), where asphaltene aggregates are in the process of growing, and are too small to be detected by conventional means (i.e. optical microscopy, refractive index, etc). The kinetic regime for asphaltenes may be the most critical in the deposition process and has unfortunately, largely been overlooked.

Normalization of the deposition results revealed that the severity of asphaltene deposition is controlled by the concentration of insoluble asphaltenes present in an oil-heptane mixture. Considering the effect of the insoluble asphaltene concentration allowed for all deposition experiments with a single oil to superimpose onto one normalized pressure drop vs. time profile. The previously unobtainable solubility of asphaltenes at extremely low heptane concentrations can now be estimated by the normalized deposition curve and provides additional solubility measurements for thermodynamic precipitation model validation.

CHAPTER III

Introduction to Small-Angle Scattering and Fractals

3.1 Introduction

Removing asphaltenes from solution or modifying their surroundings will change the structure and interactions of asphaltene aggregates such that they must be studied *in situ*; therefore, non-invasive scattering techniques are the most appropriate tool for investigating the structure asphaltenes in a liquid environment. The remainder of this dissertation will rely heavily on scattering techniques to explore the structure and behavior of asphaltenes. Chapters IV and V are written assuming that the reader has a basic understanding of small-angle scattering (SAS) principles. Consequently, it is prudent to provide a brief and general overview of scattering techniques before proceeding. This introduction to scattering will have an emphasis on previous applications to techniques performed on asphaltenes to provide relevant examples. In addition, the structure of asphaltenes is best described as fractal in nature, and a portion of this chapter will be devoted to describing fractals and their structure. This chapter should not be used as the sole source of scattering background, and it is suggested that early investigators to scattering techniques read *Elementary Scattering Theory for X-ray and Neutron Users* by D. S. Siva, which is an excellent introductory

text (*Sivia*, 2011). Readers more familiar with the basics of scattering techniques are directed to *Neutrons, X-rays and Light: Scattering Methods Applied to Soft Condensed Matter* edited by Peter Lindner and Thomas Zemb, which has proven to be a comprehensive guide for scattering theory and experimentations (*Lindner and Zemb*, 2002).

3.2 Small-Angle Scattering Background

Small-angle scattering is an inelastic scattering technique where monochromatic radiation, with a wavelength described by λ , interacts with a sample and scatters without energy transfer (*Sivia*, 2011). The angle (θ) that the radiation is scattered at can be converted to a scattering vector (q) to eliminate the effects of comparing results from different sources (e.g., X-rays or neutrons) and at different wavelengths.

$$q = \frac{4\pi \sin(\theta)}{\lambda} \quad (3.1)$$

The length scale investigated in real space for a scattering experiment can be determined by $2\pi/q$, and the length scale of asphaltene clusters/aggregates is between 1 and 10 nm. Thus, for the the length scale of asphaltenes and physical geometry for instrumentation, X-rays and cold neutrons are the most useful radiation sources. For SAS experiments, a 2D position sensitive detector is used to measure the number of X-rays or neutrons hitting each position over the course of an experiment. The intensity as a function of the scattering vector, q , is the result used for determining the size and shape of the scattering material in the sample. Figure 3.1 show a basic experimental schematic of a small-angle scattering experiment.

Before analysis can be performed on any SAS sample, the arbitrary scattering intensity, $I(q)$, must first be corrected by the sample transmission and background. Scattering processes are, in general, additive and the scattering from the sample

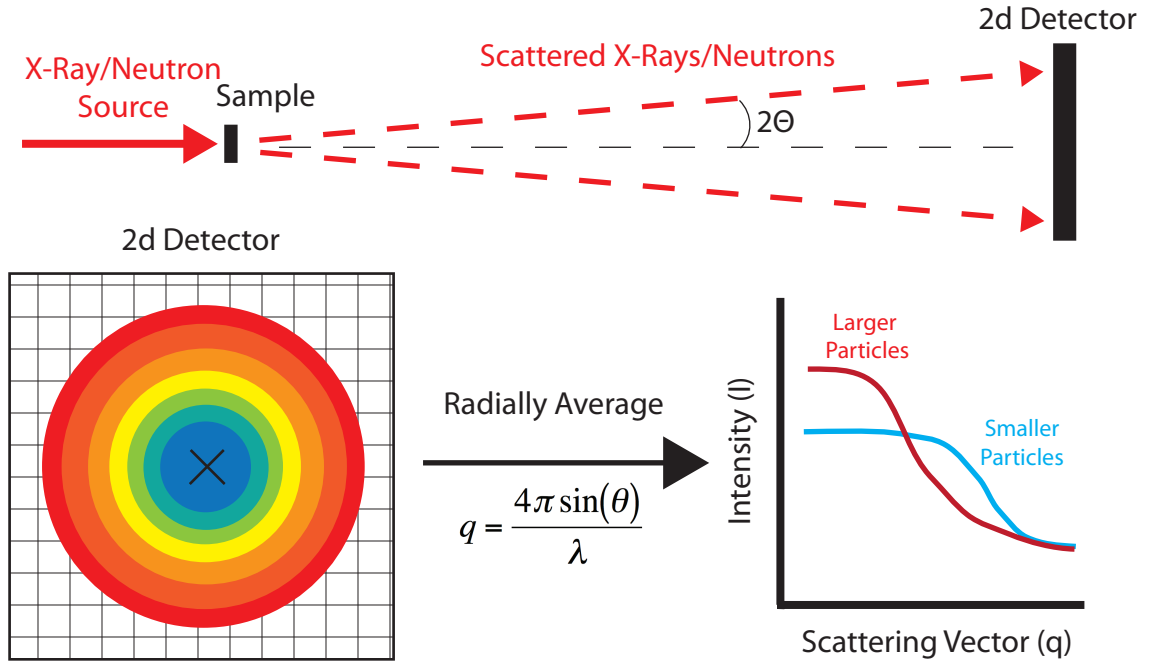


Figure 3.1: A general schematic of small-angle scattering experiments.

holder can be directly subtracted from the results of the sample. The Institut Laue-Langevin produces an excellent (and free) document outlining the procedure to background and transmission correct SAS results (*Gosh et al.*, 2006). Once corrected by transmission and background, quick and general analysis can be obtained directly from the arbitrary scattering intensity (i.e., without units and typically labeled a.u. or arb. u.) However, it is generally worth the time and effort to ensure SAS results are on an absolute scattering cross section, which is commonly written as $\frac{d\sigma}{d\Omega}$ with units of cm^{-1} . The units of reciprocal length arise from the normalization of the absolute scattering cross section (units of length squared) being normalized by the sample volume (length cubed). Mathematically, the scattering cross section has units of length squared and can be viewed as the effective “area” of scattering material in the system. The “area” of scattering material is related to the probability of scattering radiation and not the physical (geometric) projected area.

Once normalized by a standard or the absolute beam intensity, the arbitrary

scattering intensity, $I(q)$, is then converted to an absolute scattering cross section, $\frac{d\sigma}{d\Omega}$. While the most accurate method to write the absolute scattering intensity is $\frac{d\sigma}{d\Omega}$, all small-angle scattering results in this dissertation are converted to an absolute scale but are written as $I(q)$ for simplicity. The three dimensional absolute scattering cross section per solid angle ($\frac{d\sigma}{d\Omega}(\mathbf{q})$) is related to the physical structure, geometry and configuration of a sample via the modulus squared of the Fourier transform of the scattering length density function, $\rho(\mathbf{r})$:

$$\frac{d\sigma}{d\Omega}(\mathbf{q}) = \frac{1}{V} \left| \int \rho(\mathbf{r}) e^{-i\mathbf{q}\cdot\mathbf{r}} d^3\mathbf{r} \right|^2 \quad (3.2)$$

where V is the total volume of the sample, \mathbf{r} is the position vector in real space, and \mathbf{q} is the scattering vector in reciprocal space. Vectors are written in bold face typeset. The Fourier transform of the scattering length density function will provide the amplitude of the scattered radiation; however this cannot be measured by the detector. Therefore, taking the modulus squared of the Fourier transform will provide the intensity of the scattered radiation, which is actually measured by the scattering detector. This procedure results in a loss of the phase information (i.e., positive or negative amplitude) of the scattered radiation and prevents direct calculation of the scattering length density function via inverse Fourier transform of the scattering intensity. It is for this reason that scattering analysis is non-unique and that many theoretical structures can generate the same scattering profile, because there is no way to directly calculate the structure based on the scattering results.

Qualitatively, the 3D scattering length density function represents the probability that each point in space will scatter incoming radiation and is different for each technique (e.g., light, X-ray or neutron). In actuality, neutron scattering predominantly caused by the nuclei of atoms and X-ray scattering is predominantly caused by electrons. However, SAS theory is developed based on the approximation that these discrete scatters can be approximated as a continuous medium, called the scattering

length density (SLD). The SLD of a material can be calculated by:

$$\rho = dN_A \sum_{i=1}^N \frac{F_i}{A_{W,i}} b_i \quad (3.3)$$

where F_i , $A_{W,i}$, and b_i are the mass fraction, atomic weight and scattering length of element i , respectively. The scattering length of an element or isotope is measured experimentally for neutron scattering and can be calculated for X-rays by atomic number (*Feigin and Svergun, 1987*). The above expression is useful for calculating the SLD of a material with unknown molecular weight/volume (e.g., asphaltenes) but it is cumbersome for known materials. For materials with known molecular weight or volume, the SLD is simply the summation of the scattering lengths for each atom in the molecule divided by the molar volume of a single molecule. The SLD is typically written in of \AA^{-2} (i.e., length/volume units) and is on the order of 10^{-6}\AA^{-2} .

For the case of a collection of particles with uncorrelated positions (e.g., dispersed colloidal particles), the absolute scattering cross section can be written as the summation of the scattering of each individual particle as if it were centered at the origin (*Sivia, 2011*):

$$\frac{d\sigma}{d\Omega}(\mathbf{q}) = \frac{1}{V} \sum_{j=1}^N \left| \int_{V_{P,j}} \hat{\rho}_j(\mathbf{r}, \theta_j) e^{-i\mathbf{q}\cdot\mathbf{r}} d^3\mathbf{r} \right|^2 \quad (3.4)$$

where $V_{P,j}$ is the volume of each particle, θ_j is the particle orientation and $\hat{\rho}_j(\mathbf{r}, \theta_j)$ is the difference between the scattering length density function of particle j and the solvent scattering length density, ρ_o :

$$\hat{\rho}_j(\mathbf{r}, \theta_j) = \begin{cases} \rho_j(\mathbf{r}, \theta_j) - \rho_o, & \text{if inside particle} \\ 0, & \text{if inside solvent} \end{cases}$$

From Equation (3.4) it can clearly be seen that for an arbitrary distribution of

scattering material, as long as the positions are uncorrelated (i.e., dilute or ideal gas), the scattering intensity is simply the additive effects of the scattering for each particle. For a binary mixture of A and B, the measured scattering is the scattering of A alone added to the scattering of B alone. Thus if the scattering of one distribution is known, the other can be inferred from the scattering of a combined sample. Therefore, for a series of particle types, represented by subscript i , the total scattering intensity is:

$$I(q) = \sum I_i(q) \quad (3.5)$$

where $I_i(q)$ is the scattering for particle of type i . For the case where the particles are compositionally homogenous, the scattering length density function is constant inside a particle and can be expressed as:

$$\frac{\widehat{\rho}_j(\mathbf{r}, \theta_j)}{\Delta\rho} = \begin{cases} 1, & \text{if inside particle} \\ 0, & \text{if inside solvent} \end{cases}$$

The scattering contrast is the difference between the SLD of the solvent and the particles squared, and is written as $(\Delta\rho)^2$. If there is no difference in SLDs, there will be zero scattering contrast and no coherent scattering small-angle scattering, which clearly prevents structural analysis. The mean (volume averaged) scattering contrast, $(\Delta\rho)^2$, can be removed from inside the integral and summation:

$$\frac{d\sigma}{d\Omega}(\mathbf{q}) = \frac{(\Delta\rho)^2}{V} \sum_{j=1}^N \left| \int_{V_{P,j}} \frac{\widehat{\rho}_j(\mathbf{r}, \theta_j)}{\Delta\rho} e^{-i\mathbf{q}\cdot\mathbf{r}} d^3\mathbf{r} \right|^2 \quad (3.6)$$

The above expression is very useful because it states that once the mean scattering contrast is known, the small-angle scattering results from both X-rays and neutrons can be compared. If the absolute scattering cross section is normalized by the mean scattering contrast, the exact same sample scattered using either X-rays and neutrons

will produce identical scattering profiles. However, if there is a difference between X-ray and neutron scattering results, there must be compositional variations inside each particle and the scattering length density function normalized by the difference in contrast will not be same for X-ray and neutron scattering (i.e., $\hat{\rho}_j(\mathbf{r}, \theta_j)/\Delta\rho$ will not simply be either 1 or 0).

Returning to a more general scenario where we have not assumed that the scattering particles are internally homogenous, at very small-angles (low-q), the absolute scattering cross section express can be simplified:

$$\frac{d\sigma}{d\Omega}(0) = \frac{(\Delta\rho)^2}{V} \sum_{j=1}^N \left| \int_{V_{P,j}} d^3\mathbf{r} \right|^2 = \frac{(\Delta\rho)^2}{V} \sum_{j=1}^N V_{P,j}^2 \quad (3.7)$$

In the above equation, no assumptions have been made regarding the size, shape, or polydispersity of the scattering material. For a sample of realistic size, there are many scattering particles and an arbitrary size distribution can be defined, such that $n(V_{P,k})$ denotes the number of particles with volume $V_{P,k}$. The total volume of scattering particles, V_P^{Tot} is given by:

$$V_P^{Tot} = \sum_k n(V_{P,k})V_{P,k} \quad (3.8)$$

The total volume fraction of scattering material is:

$$\phi = \frac{V_P^{Tot}}{V} \quad (3.9)$$

The summation of the volume of each particle squared can be rewritten according to the arbitrary size distribution:

$$\sum_{j=1}^N V_{P,j}^2 = \sum_k n(V_{P,k})V_{P,k}^2 \quad (3.10)$$

If the zero-angle scattering intensity is multiplied by V_P^{Tot}/V_P^{Tot} , it can be rewritten

in terms of the volume/mass averaged mean volume:

$$\frac{d\sigma}{d\Omega}(0) = \frac{(\Delta\rho)^2 V_P^{Tot}}{V} \frac{V_P^{Tot}}{V_P^{Tot}} \sum_{j=1}^N V_{P,j}^2 = (\Delta\rho)^2 \phi \frac{\sum_k n(V_{P,k}) V_{P,k}^2}{\sum_k n(V_{P,k}) V_{P,k}} = (\Delta\rho)^2 \phi \bar{V}_P \quad (3.11)$$

The weight averaged molecular weight of the scattering material, \bar{M}_W can be determined by rearranging the above expression:

$$\frac{d\sigma}{d\Omega}(0) = \frac{\phi \bar{M}_W (\Delta\rho)^2}{d N_A} \quad (3.12)$$

where d is the mass density of scattering material and N_A is Avogadro's number. This expression to determine the mass/volume averaged molecular weight holds true even for particles that are not internally homogeneous, like asphaltenes, as long as the volume averaged scattering length density of each particle in the system is the same. For samples with polydispersity in size, the effective molecular weight will be more heavily weighted by the largest material in the system.

For the case of asphaltenes and most dispersed systems, the absolute scattering cross section is orientationally averaged to obtain a one-dimensional function because there is no long range order in the system. All results in this dissertation have been converted to an absolute scattering cross-section and no distinction between $I(q)$, the arbitrary scattering intensity, and $\frac{d\sigma}{d\Omega}(q)$, the absolute scattering cross-section will be made from this point onward.

Due to the loss of phase information of the scattered radiation, the absolute scattering cross section cannot be directly converted back into the scattering length density function via inverse Fourier transform. Because of this limitation, the standard method for scattering analysis is to propose a structure or form of the scattering length density function, $\rho(\mathbf{r})$, and then calculate the scattering, thus the interpretation results is strongly influenced by the model selected for fitting. The only way to

assess the accuracy of any structural assumptions is to check the feasibility of the fitted parameters and the fit quality compared to the measured scattering results. For hard particles or colloids, like metallic nanoparticles, other techniques can be used to narrow the fitting parameters by measuring the size or shape with TEM or other appropriate methods. However, structural conclusions on materials that must be studied in a solvated state (e.g., asphaltenes and polymers) rely heavily on fitted parameters and are model (i.e., form/structure factor) dependent. This uncertainty in the correctness of an assumed structure is responsible for much speculation about the proposed structures of asphaltenes. Unfortunately, scattering results cannot be used to absolutely prove a particular structure is correct, but it can definitively disprove incorrect ones because the scattering can be directly calculated from a defined structure.

Equation (3.2) is the basis for all small-angle scattering theory; however, it is not generally used in the analysis of experimental scattering results of colloidal systems. For a samples of realistic size, the exact position of each particle in the system is clearly not known and Equation (3.2) cannot be used. Instead, the orientationally averaged scattering of a single particle is calculated analytically and represented by the form factor, or $P(q)$. Approximating the particles in the sample as a dilute mixture (i.e., ideal gas), such that each particle can occupy all space with equal probability, the total scattering simply the scattering of an individual particle multiplied by the mean (volume averaged) scattering contrast, $(\Delta\rho)^2$ and the number density of particles. If particles interact through long-range potentials or elevated concentration, then the positions of the particles are correlated and thus will influence the true scattering length density function. In this scenario an additional term, the structure factor or $S(q)$, can be included to correct for the correlated positions of the particles in the sample. Under these conditions, the scattering can simply be calculated by (*Pedersen*, 1997):

$$I(q) = \phi(\Delta\rho)^2 V_p P(q) S(q) \quad (3.13)$$

where the number density of particle has instead been represented by ϕ , the volume fraction of particles, which is necessary for asphaltenes because of their unknown molecular weight. Particle anisotropy and polydispersity prevent decoupling of the form and structure factor as expressed in Equation (3.13). In fact, Equation (3.13) is only intended for use with mono disperse and spherically symmetric particles interacting with isotropic potentials. Equation (3.13) can be applied to anisotropic and to polydisperse samples by introducing an average form factor and utilizing decoupling approximations.

There are also general methods of analysis that do not rely heavily on fitting parameters. For example, a shape-independent measurement of the radius of gyration can be obtained by the Guinier approximation (*Guinier and Fournet, 1955*):

$$I(q) = I_0 \exp\left(-\frac{(qR_g)^2}{3}\right) \quad (3.14)$$

where I is the scattering intensity (y-axis), I_0 is the zero-angle intensity, q is the scattering vector (x-axis) and R_g is called either the radius of gyration or Guinier radius. The Guinier radius is a convenient way to obtain a rough estimate of the size of the scattering material in the system and in this paper it will be synonymous with the radius of gyration, R_g . Qualitatively, the Guinier radius is a measure of the size of the largest compositional variations in the sample, either solid or ephemeral associations of asphaltenes. In polydisperse systems, the Guinier radius is heavily influenced by the presence of the largest material in the system. For the case of special case of polydisperse spheres following a Schultz distribution an analytical expression can be generated for the Guinier radius (*Sivia, 2011*):

$$R_g^2 = \frac{3 \langle r^8 \rangle}{5 \langle r^6 \rangle} \quad (3.15)$$

where $\langle r^k \rangle$ represents the k^{th} moment of the number distribution $n(r)$, or $\langle r^k \rangle = \int r^k n(r) dr$. As an alternative to the Guinier approximation, the Zimm approximation was originally derived to model the scattering of polymer chains with an apparent fractal dimension of 2. This fractal dimension is similar to previous estimates of the asphaltene fractal dimension; therefore, it is commonly used to assess the qualitative size of asphaltenes (*Zimm*, 1948a; *Roux et al.*, 2001):

$$I(q) = I_0(q) \left[1 + \frac{(qR_g)^2}{3} \right]^{-1} \quad (3.16)$$

The radius of gyration as measured by the Zimm approximation will be used for all size measurements in this dissertation because it has been shown to provide the best fit for asphaltenes previously (*Roux et al.*, 2001). Random walk polymers, or Gaussian coils, exhibit a mass scaling which is equivalent to a material with fractal dimension of 2 (see *Lindner and Zemb*, 2002, pg. 266). Self-avoiding walk polymers exhibit mass scaling equivalent with a $D_f = 5/3$. Real polymers may exhibit more complex interactions and can potentially display a number of mass scalings. Often, the zero-angle intensity is inaccessible within the q -range available for experimentation for large particles; however, the Guinier or Zimm approximation can be used for extrapolation, assuming there is not surface scattering from very large material in the sample.

3.3 Introduction to Fractals

A fractal is “self similar” and possesses a mass distribution which is independent of length scale and obeys the following form (*Schaefer et al.*, 1984):

$$M \propto R_g^{D_f} \quad (3.17)$$

where M is the mass/molecular weight/number of particles, R_g is the radius of gyration, and D_f is the Hausdorff dimension, or more commonly, simply the fractal dimension. For a continuous object (or an object with uniformly distributed porosity), the fractal dimension will equal the spatial dimension (e.g., D_f for a line is 1, sheet is 2, and cube is 3). The ideal/mathematical fractal is infinite in size and exhibits self similarity on increasingly smaller length scales for infinite iterations. In working with real objects, this criteria can obviously never be satisfied as fractals must be limited by the length scale of the monomeric unit, r_o , and the total size of the cluster. Traditionally, in order to classify a material of finite size as a fractal, it must exhibit self-similarity and mass scaling as defined in Equation (3.17) for over an order in magnitude in the spatial dimension.

Small-angle scattering is a convenient way to measure the fractal dimension, D_f , of associating or aggregating systems, with r_o being the size/radius of a monomer and R_g representing the total size of the fractal (*Martin and Ackerson, 1985*). Based on the mass distribution inside a fractal cluster, the scattering length density function can be calculated and directly converted to a scattering profile for mass fractals via Fourier transform. For fractals with little polydispersity, the fractal dimension is related to the scattering intensity by the following relation:

$$I(q) \propto q^{-D_f} \quad (3.18)$$

where $r_o \ll q \ll R_g$. Any polydispersity in the size of the fractal clusters requires special consideration to eliminate the influence of smearing effects which will artificially lower the apparent fractal dimension from scattering (*Teixeira, 1988*). Much of the early foundation in fractal dimension measurements were to validate predictions of percolation clusters, which generally have the following number distribution of cluster sizes:

$$n(M_W) \propto M_W^{-\tau} f(M_W/M_W^*) \quad (3.19)$$

where $n(M_W)$ is the number distribution, M_W is the mass or molecular weight of the fractal cluster, the exponent τ is related to the polydispersity of the distribution, and $f(M_W/M_W^*)$ is a function which is rapidly decaying above a cutoff size, M_W^* , to limit the maximum cluster size. For $\tau < 2$ the slope of the scattering curve in Equation (3.18) is an accurate measurement of the fractal dimension of the clusters in the system (*Martin and Hurd, 1987*). For $\tau > 2$, the apparent fractal dimension D_f^* is related to the true fractal dimension through the following relation, $D_f^* = D_f(3 - \tau)$.

Fenistein *et al.* employed ultracentrifugation to measure the size distribution of asphaltene clusters to assess the accuracy of fractal dimension measurements (*Fenistein and Barré, 2001*). The results revealed that there was only a small difference in the density between separated fractions, indicating that the fractionation was based on cluster size. The measured size distribution fit the distribution outlined in Equation (3.19) with $\tau = 1.66$, indicating that there is little influence from polydispersity smearing and represents an accurate fractal dimension measurement of the asphaltene clusters. Additionally, the fractal dimension was measured by comparing the size and mass of the separated fractions using Equation (3.17), and the two measurements were found to be equivalent, which provided strong evidence of the accuracy of the measurement.

CHAPTER IV

Asphaltene Instability by Small-Angle Neutron Scattering

4.1 Introduction

Petroleum asphaltenes are a solubility class of crude oil that are defined as the compounds that are soluble in aromatics, such as toluene, and insoluble in normal alkanes (*Speight, 2007*). It is well known that changes in temperature, pressure, or composition can destabilize asphaltenes and cause aggregation and deposition in porous formations, production lines, and processing facilities. Remediation and prevention of asphaltenic deposits is costly and it is of great interest to know the thermodynamic conditions where asphaltene destabilization occurs. It has been recently shown that the detection of asphaltene instability by standard techniques (e.g., optical microscopy) is limited by a slow aggregation process that asphaltenes undergo while growing from the nanometer to the micron length scale (*Maqbool et al., 2009, 2011b,a*). The slow asphaltene aggregation process has been observed over time periods of two months or longer, and improper consideration of this effect can lead to inaccurate measurement of the asphaltene phase stability envelope, which will intro-

This chapter is reproduced in part with permission from Michael P. Hoepfner, Cláudio Vilas Bóas Fávero, Nasim Haji-Akbari, and H. Scott Fogler. The Fractal Aggregation of Asphaltenes. *Langmuir*, 29(28):8799-8808, May 2013. Copyright 2013 American Chemical Society.

duce systematic errors in thermodynamic models (*Ting et al.*, 2003; *Kraiwanawong et al.*, 2007; *Gonzalez et al.*, 2007). Thus, it is of critical importance to accurately measure the true stability envelope for asphaltene precipitation (i.e., the thermodynamic conditions where asphaltenes are destabilized and can deposit or precipitate).

In this investigation, small-angle neutron scattering (SANS) was used to increase the detection sensitivity of asphaltene instability compared to standard techniques. It is common practice to add a precipitant (or antisolvent) to crude oils to destabilize asphaltenes in order to characterize asphaltenes and to obtain thermodynamic modeling parameters (*Ting et al.*, 2003; *Kraiwanawong et al.*, 2007). The instantaneous onset point or concentration is one commonly measured parameter, and it is defined as the precipitant concentration where asphaltene destabilization and aggregation is fast and easily detectable within approximately 15 minutes after adding the precipitant (*Maqbool et al.*, 2009, 2011b). Additionally, the mechanism of asphaltene destabilization is poorly understood (*Creek*, 2005), and increased knowledge on how asphaltenes precipitate will improve techniques for modeling, prevention, and remediation of asphaltene-related problems.

Asphaltenes are believed to exist in solution as semi-crystalline aggregates, commonly called ‘nanoaggregates’, that exhibit stacking of large aromatic cores, surrounded by peripheral alkyl chains (*Mullins et al.*, 2012). X-ray diffraction measurements first identified the semi-crystalline structure of asphaltenes by the presence of a broad diffraction peak corresponding to a separation distance of roughly 3.6 Å (*Yen et al.*, 1961). This broad peak is interpreted as the stacking of the large aromatic asphaltene molecular cores and is the foundation for the ‘coin stack’ structure of asphaltene nanoaggregates (*Andersen et al.*, 2005). Small-angle X-ray scattering (SAXS) measurements of solid asphaltenes reveal an additional broad correlation peak that corresponds to the separation distance between colloidal asphaltenes of approximately 3-5 nm, which is a rough estimate for the size of an asphaltene nanoaggregate (*Sirota*,

1998). However, shape-independent fits (e.g., Guinier) of small-angle scattering investigations of asphaltenes dispersed in solvents reveal a larger asphaltene size, with a radius 2-3 times larger and on the order of 10 nm, indicating that there is some degree of asphaltene nanoaggregate clustering (*Roux et al.*, 2001; *Fenistein and Barré*, 2001). The numerous SAXS/SANS (*Ravey et al.*, 1988; *Espinat et al.*, 1993; *Storm and Sheu*, 1995; *Liu et al.*, 1995; *Bardon et al.*, 1996; *Fenistein et al.*, 1998; *Roux et al.*, 2001; *Tanaka et al.*, 2003; *Gawrys et al.*, 2003; *Gawrys and Kilpatrick*, 2005; *Sheu*, 2006; *Barré et al.*, 2008; *Eyssautier et al.*, 2011, 2012b) studies and nanofiltration (*Zhao and Shaw*, 2007) of asphaltenes provides strong evidence that at least a fraction of asphaltenes form stable aggregates on the nanometer length scale when dispersed in oil or other solvents. However, the fine structural details of asphaltene aggregates and molecules remains a subject of intense debate (*Andrews et al.*, 2006; *Spiecker et al.*, 2003).

The vast majority of SANS investigations have attempted to determine the size and shape of asphaltene aggregates dispersed in various deuterated solvents (*Ravey et al.*, 1988; *Espinat et al.*, 1993; *Storm and Sheu*, 1995; *Liu et al.*, 1995; *Bardon et al.*, 1996; *Fenistein et al.*, 1998; *Roux et al.*, 2001; *Tanaka et al.*, 2003; *Gawrys et al.*, 2003; *Gawrys and Kilpatrick*, 2005; *Sheu*, 2006; *Barré et al.*, 2008; *Eyssautier et al.*, 2011, 2012b). Analysis of SANS data using different fitting techniques have produced several potential asphaltene structures: prolate ellipsoid (*Tanaka et al.*, 2003), oblate cylinders (*Gawrys and Kilpatrick*, 2005), spherical micelles (*Storm and Sheu*, 1995), and thin discs (*Ravey et al.*, 1988; *Espinat et al.*, 1993; *Bardon et al.*, 1996). The diverse set of possible asphaltene structures is a likely a result of both the large number of tunable fitting parameters required to obtain quality curve fits and the potential structural differences between asphaltenes of different origin. In addition, the scattering of asphaltenes has also been studied as statistical fluctuations in a liquid-liquid system (*Sirota*, 2005; *Sirota and Lin*, 2007).

An alternative to curve fitting is to consider asphaltenes as fractal clusters that consist of smaller building blocks (i.e., asphaltene nanoaggregates). Previous scattering and viscosimetric investigations have determined that asphaltenes exhibit mass distributions that have a fractal dimension, D_f , of approximately two (*Roux et al.*, 2001; *Fenistein and Barré*, 2001; *Gawryś et al.*, 2003; *Barré et al.*, 2008; *Eyssautier et al.*, 2012b; *Barré et al.*, 2009; *Headen et al.*, 2009b). The scattering by a fractal with $D_f = 2$ is similar to that of a thin disc structure; however, the work of *Barre et al.* revealed that the disc structure is inconsistent with intrinsic viscosity measurements of asphaltenes (*Barré et al.*, 2008). *Gawryś et al.* reported that the fractal dimension of asphaltenes was modified from approximately 2 to 2.7 upon the addition of resins to an asphaltene-solvent mixture (*Gawryś et al.*, 2003). The fractal structure of asphaltenes has widespread support (*Roux et al.*, 2001; *Fenistein and Barré*, 2001; *Gawryś et al.*, 2003; *Barré et al.*, 2008; *Eyssautier et al.*, 2012b; *Barré et al.*, 2009; *Headen et al.*, 2009b) and will be the basis for scattering analysis and discussion. The ideal fractal has a self-similar structure and possesses a mass distribution which is independent of size and obeys the following form (*Schaefer et al.*, 1984):

$$M_W \propto R_g^{D_f} \quad (4.1)$$

where M_W is the molecular weight of the fractal and R_g is the radius of gyration. *Fenistein et al.* investigated the effect of heptane on the scattering of asphaltenes in toluene below the instantaneous onset concentration and found that adding heptane increases the radius of gyration (R_g) of the fractal cluster (*Fenistein et al.*, 1998). These measurements were not monitored over time and slow aggregation kinetics could have influenced the scattering measurements if a second distribution of insoluble and precipitating asphaltenes was formed. In a later investigation, *Fenistein et al.* utilized ultracentrifugation to measure the asphaltene fractal cluster size distribution and determined that the polydispersity is sufficiently low so as to not influence

the direct measurement of the fractal dimension by SAXS or SANS (*Fenistein and Barré, 2001*). Additionally, the largest asphaltene fractals that were separated by ultracentrifugation were found to exhibit mass fractal scaling for over an order of magnitude in q -space, providing strong evidence of the appropriateness of the fractal structure for asphaltenes (*Fenistein and Barré, 2001*). More recently, a fractal aggregate structure factor was used on contrast-variation SANS and SAXS results, and it was found that a core-shell cylinder shape fits the scattering profile of asphaltenes well; however, many fitting parameters were required to obtain the best fit of the scattering results (*Eyssautier et al., 2011*).

There have been a limited number of SANS studies that have utilized asphaltenes dispersed in their natural state in crude oil (*Mason and Lin, 2003a,b; Headen et al., 2009b*). *Mason et al.* performed time-resolved SANS experiments on destabilized asphaltenes and used mixtures of incompatible crude oils that were monitored for periods of approximately two weeks (*Mason and Lin, 2003b*). The scattering samples used by *Mason et al.* had significant surface scattering caused by insoluble asphaltenes that prevented detailed analysis of the nano-scale asphaltene structure. With the discovery of slow asphaltene precipitation kinetics (*Maqbool et al., 2009, 2011b,a*) and a desire to investigate the nano-scale structure of asphaltenes in crude oil-precipitant mixtures, several modifications of the procedure used by *Mason et al.* (*Mason and Lin, 2003b*) are prudent. First, scattering samples were monitored for periods of up to six months to fully explore the time-resolved aspects of slow asphaltene aggregation. Second, the precipitant concentration was varied both well below and well above the instantaneous onset in order to fully study the effect of precipitant on asphaltene stability and structure in crude oils and model mixtures. Third, the large insoluble asphaltenes that were precipitated by heptane were removed by centrifugation prior to scattering experiments to provide detailed information on the nanostructure of asphaltenes without the influence of surface scattering. Previous investigations have

attempted minimal manipulation of scattering results of asphaltenes in crude oil; however, the analysis procedure here will be uniform, regardless if the asphaltenes are dispersed in crude oil or in solvent. Because SANS has the potential to provide a wealth of information, this paper will present a diverse set of results in order to investigate a number of important items:

1. The fractal structure of asphaltenes in crude oil-precipitant systems.
2. The structural differences between soluble and insoluble asphaltenes.
3. The initiation of asphaltene destabilization at dilute precipitant concentrations.
4. The crude oil fraction(s) that causes small-angle scattering.

4.2 Experimental Methods

Two crude oils, Oil A and Oil B, and a Model Oil (MO) were diluted with a precipitant/antisolvent (n-heptane) to destabilize asphaltenes. Both crude oil samples were free of any production additives that are commonly used to prevent asphaltene deposition or pipe corrosion. The Model Oil was created by dispersing a third type of asphaltene in deuterated toluene (>99.5 % deuterated) and the asphaltenes were destabilized with the addition of deuterated heptane (>98 % deuterated). Deuterated isotopes were supplied from Cambridge Isotopes Laboratories, Inc. Heptane was HPLC grade (>99.5% heptane) and supplied by Fisher Scientific. The total mass fraction of asphaltenes was determined by centrifugation of a 40:1 heptane dilution of crude oil that was aged for over 24 hours (*Maqbool et al.*, 2009). The measured asphaltene contents of Oil A and Oil B were 9.90 ± 0.07 and 2.7 ± 0.3 wt. %, respectively. Crude oil densities were measured using a pycnometer and the densities for Oil A and Oil B were 869.2 ± 0.2 and 865.3 ± 0.2 kg/m^3 , respectively. The instantaneous onset of a crude oil is the concentration of heptane that results in insoluble asphaltenes

being observed by optical microscopy after less than 15 minutes of mixing with the precipitant. No insoluble asphaltenes will be detectable by standard techniques in oil-precipitant mixtures at heptane concentrations below the instantaneous onset unless several hours, days or months after destabilization has elapsed (*Maqbool et al.*, 2009). Lower precipitant concentrations will require longer destabilization times to detect the asphaltene instability. The instantaneous onset heptane concentration for Oil A and Oil B was measured to be 40 and 50 vol. % heptane, respectively.

4.2.1 Model Oil Preparation

Asphaltenes for the Model Oil were extracted from a third crude oil with a 40:1 heptane dilution. The mixture was stirred for 20 hours before separation of the solid fraction by centrifugation. The solid asphaltenes were washed by soxhlet with heptane for 23 hours to remove any trapped maltenes (non-asphaltene fraction) and dried at 70 °C to remove any residual heptane. The Model Oil was created by adding the asphaltenes to deuterated toluene (d-toluene) to a concentration of 2.87 ± 0.01 wt. % (2.26 vol. %). The Model Oil was continuously stirred for 8 days before addition of deuterated heptane (d-heptane) to allow the dissolved asphaltenes to reach their equilibrium state. Only deuterated toluene and heptane were used with the Model Oil to ensure strong scattering contrast. After preparation of the Model Oil, the instantaneous onset concentration was measured to be 50 vol. % heptane.

4.2.2 Time-Resolved Asphaltene Destabilization Sample Preparation

Heptane was slowly added to each oil at various concentrations and time intervals following the procedure of *Maqbool et al.* (*Maqbool et al.*, 2009). The destabilization time is the time that has elapsed between mixing an oil with precipitant and performing the scattering experiments. The destabilization times were different for each oil and the longest elapsed time between mixing and neutron scattering was six months.

A total of 31 heptane-diluted samples were prepared at different times and heptane concentrations. Samples prepared at the scattering facility are referred to as ‘one-day’ samples and were prepared immediately before scattering was performed. The maximum time between preparation of the one-day samples and neutron irradiation was less than 7 hours. The destabilization times for Oil A diluted with heptane were: 6 months, 1 week and the day of scattering. The destabilization times for Oil B were: 2 months and the day of scattering. The destabilization times for the Model Oil were: 1 week and the day of scattering. All samples were continuously stirred until the scattering experiments were performed, except for a period of less than 24 hours during transportation to the scattering facility where they were again continuously stirred.

All samples were centrifuged at 16,000 g for 10 minutes (Eppendorf 541R) to remove any precipitated asphaltenes prior to loading into the scattering sample cells. Without centrifugation, large flocculated particles would remain in solution and cause significant surface scattering, thereby making any analysis of the nanometer-sized asphaltenes nearly impossible. The centrifugation time and intensity was not strong enough to remove asphaltenes smaller than approximately 50 nm. Additionally, centrifugation allowed for measurement of the asphaltene solubility following the procedure of Maqbool *et al.* (Maqbool *et al.*, 2009), which was used to calculate the asphaltene volume fraction remaining in each sample. The mass separated by centrifugation (Figure E.1) and volume fraction of asphaltenes (Figure E.2) in each sample is provided in Appendix E.

4.2.3 SANS Experiments

The scattering intensity, $I(q)$, as a function of the scattering vector, q , is used to estimate the size and shape of the scattering material in the sample (Sivia, 2011). All results were normalized to an absolute scattering cross section (units of cm^{-1}). The

general expression for the scattering of a two-level system (e.g., particles in a liquid environment) is (Lindner and Zemb, 2002):

$$I(q) = \phi(1 - \phi)\Delta\rho^2V_pP(q)S(q) \quad (4.2)$$

where ϕ is the volume fraction of scattering particles (i.e., asphaltenes), $\Delta\rho^2$ is the scattering contrast, V_p is the particle volume, $P(q)$ is the form factor (describes particle shape), and $S(q)$ is the structure factor (describes positional correlation). The scattering contrast ($\Delta\rho^2$) is the square difference between the scattering length densities, ρ , of the particle and that of the solvent (see Chapter III for additional details.) Equation (4.2) can be applied to anisotropic and to polydisperse samples by introducing an average form factor and utilizing decoupling approximations; however, the scattering intensity remains proportional to $\phi(1 - \phi)(\Delta\rho)^2$ (Kotlarchyk and Chen, 1983).

Position correlation between fractal clusters is assumed to be negligible (i.e., $S(q) = 1$) and the asphaltene fractal structure is contained within the form factor, $P(q)$. Position correlation becomes significant once sample concentrations are outside of the dilute particle concentration regime (approximately 2-5 vol. % in toluene (Roux *et al.*, 2001; Barré *et al.*, 2008)); however, the effect of asphaltene concentration on their scattering profiles is uncertain. Conflicting reports exist for how the asphaltene scattering profiles change when transitioning from the dilute to concentrated regimes between asphaltenes in toluene compared to in vacuum residue (Barré *et al.*, 2008; Eyssautier *et al.*, 2012c). In toluene, the existence of cluster-cluster positional correlation at high asphaltene concentrations was observed by a decrease in scattering intensity at low- q (Roux *et al.*, 2001; Barré *et al.*, 2008), signifying a reduction in the apparent measured radius of gyration and molecular weight of asphaltene clusters. However, no difference in scattering profile was observed for asphaltenes in the dilute vs. concentrated regime in vacuum residue (Eyssautier *et al.*, 2012c). Regardless, the

scattering from the fractal structure of asphaltenes was measured with and without the existence of cluster-cluster correlation using both toluene and vacuum residue as solvents (*Barré et al.*, 2008; *Eyssautier et al.*, 2012c). Recently, a core-shell thin disc model was proposed by further decoupling the fractal structure of an asphaltene cluster into a form factor for a thin disc and a structure factor for the fractal organization (*Eyssautier et al.*, 2011). Because only the collective asphaltene fractal structure is of interest, no attempt will be made to isolate the scattering from individual asphaltene nanoaggregates. However, the scattering at high- q is from small scale structures and is used to qualitatively describe the asphaltene nanoaggregate structure, while the scattering at low- q is from larger length scales and qualitatively describes the collective fractal structure of asphaltenes.

The size of asphaltene fractal clusters was determined using the Zimm approximation (*Zimm*, 1948b), which has been previously used to assess the radius of gyration of asphaltene fractal clusters (*Roux et al.*, 2001; *Barré et al.*, 2008; *Eyssautier et al.*, 2012b):

$$I(q) = I_0 \left[1 + \frac{(qR_g)^2}{3} \right]^{-1} \quad (4.3)$$

where I_0 is the zero-angle scattering intensity and R_g , as discussed earlier, is the radius of gyration. For polydisperse samples of the same structure but different sizes, R_g^2 is the z -average square radius of gyration (*Guinier and Fournet*, 1955). At very small-angles (low- q), the zero-angle scattering intensity on an absolute scale, I_0 , can be used to determine the weight-averaged molecular weight, M_W , of the scattering material (*Lindner and Zemb*, 2002; *Eyssautier et al.*, 2012b):

$$I_0 = \frac{\phi(1 - \phi)M_W(\Delta\rho)^2}{dN_A} \quad (4.4)$$

where d is the mass density and N_A is Avogadro's number. Often the zero-angle

intensity, I_0 , is inaccessible within the q -range available for experiments with large particles or clusters; however, the Zimm approximation will be used for extrapolation. The fractal dimension, D_f , can be extracted from small-angle scattering results by the following relation (*Martin and Ackerson, 1985*):

$$I(q) \propto q^{-D_f} \quad (4.5)$$

If a sample has significant size polydispersity, the fractal dimension estimated by Equation (4.5) will be lower than the true fractal dimension (*Teixeira, 1988*). However, previous measurements have shown that the polydispersity in the asphaltene fractal cluster size is small enough so as to not influence the fractal dimension measurement using Equation (4.5) (*Fenistein and Barré, 2001*). In a system without particle-particle position correlation (i.e., $S(q) = 1$), the total scattering intensity, $I(q)$, is the summation of the scattering of each individual particle. If the sample is a mixture containing various types of particles with different sizes and shapes (e.g., soluble and insoluble asphaltenes), the total scattering intensity, $I(q)$, is the summation of the scattering intensity from each individual particle type, $I_i(q)$ (*Sivia, 2011*):

$$I(q) = \sum_i I_i(q) \quad (4.6)$$

SANS experiments were performed on the General-Purpose SANS Diffractometer (CG-2) at the High-Flux Isotope Reactor (HFIR) located at Oak Ridge National Laboratory. Samples were loaded in to quartz ‘banjo’ cells with a 2 ± 0.01 mm path length (Hellma Analytics, Part number: 120-000-2-40). Neutrons with a 6 Å wavelength and two sample-to-detector distances were used, 14 and 1 m, to span a q -range of $4 \times 10^{-3} < q < 0.55 \text{ \AA}^{-1}$. Data collection times were of the shortest possible duration in order to obtain good statistics and varied between 10 and 60 minutes for the far detector position and between 10 and 20 minutes for the near position. Asphaltene

aggregation is not expected to be significant during the neutron data collection time because the heptane concentrations used will result in the aggregation rate being in the slow kinetic regime, lasting as long as several months. The scattering results were converted to an absolute scattering cross section using the open beam intensity, and following a standard procedure in the reduction software provided by the scattering facility. All results are presented as the absolute scattering cross-section. Incoherent scattering was easily identified by the flat portion of the scattering profile at high- q and was subtracted from each sample individually. Examples of unmodified scattering profiles (before removal of incoherent scattering) are shown in Figure E.3 of Appendix E.

4.2.4 Scaling of Results

Many of the scattering intensity results are normalized by the mean scattering contrast, oil volume fraction, asphaltene volume fraction, or a combination of these factors. All normalization terms are calculated independently from the scattering results and are used to eliminate the influence of dilution and scattering contrast. The procedure to calculate the scattering length densities (SLD, ρ), contrast ($\Delta\rho^2$) and volume fraction (ϕ) for each sample is provided in Appendix E. Asphaltenes dispersed in a crude oil contribute to measurements of the density and elemental composition of the total crude oil. The scattering contrast for asphaltenes in crude oil arises from the difference between the asphaltenes and their surrounding media, the asphaltene-free oil or *oil solvent*. The scattering length density and mass density of the oil solvent were determined by eliminating the contribution of asphaltenes on the density and composition of the crude oil using the mass fraction of asphaltenes in the oil. The influence of the density of asphaltenes was eliminated from the oil by assuming an ideal mixture and a density of 1.2 g/mL for asphaltenes (*Roux et al.*, 2001; *Eyssautier et al.*, 2011; *Fenistein and Barré*, 2001). The SLDs for both Oil A

and MO asphaltenes were calculated to be $1.80 \times 10^{-6} \text{ \AA}^{-2}$ and the Oil A solvent SLD was $0.14 \times 10^{-6} \text{ \AA}^{-2}$. The SLDs of Oil B asphaltenes and oil solvent were assumed to be identical to the values for Oil A asphaltenes and oil solvent. Appendix E provides additional details on the elimination of the influence of asphaltenes on the composition and density of the oil solvent.

4.2.5 Review of Key Concepts and Findings Presented Above

Due to the complexity of crude oil and asphaltenes, a succinct review of the key concepts and assumptions is necessary for clarity. (1) All scattering samples will be treated as a four component mixture: soluble asphaltenes, insoluble asphaltenes, oil solvent and precipitant (i.e., antisolvent). The oil solvent represents the non-asphaltene fractions of crude oil and the procedure for determining the properties of this component is discussed above and in Appendix E. (2) Asphaltenes do not fully molecularly disperse in crude oil or solvents and describing asphaltenes as either ‘*soluble*’ or ‘*insoluble*’ may be initially confusing. *Soluble* or stable asphaltenes are the ones that remain dispersed on the nanometer length scale for all time. *Insoluble* asphaltenes are the ones that will grow to the micrometer or larger length scale after a precipitant is added, if given sufficient time to aggregate. Additionally, a mixture of soluble asphaltenes, oil, and solvent will be considered to be a single phase. The phase boundary or envelope represents a set of thermodynamic conditions (i.e., temperature, pressure, or composition) where an insoluble asphaltene fraction forms. (3) Previous evidence supports that soluble asphaltenes are fractal clusters that are assembled from the association of asphaltene nanoaggregates as the monomeric units, which will be the basis for SANS analysis (*Roux et al.*, 2001; *Fenistein and Barré*, 2001; *Gawrys et al.*, 2003; *Barré et al.*, 2008; *Eyssautier et al.*, 2012b; *Barré et al.*, 2009; *Headen et al.*, 2009b). (4) To simplify analysis, the cluster-cluster position correlation will be neglected, and in the worst case scenario, this approximation is only expected to

lower the measured molecular weight and radii of gyration for the more concentrated samples (*Barré et al.*, 2008). The major conclusions of this work will not be affected by neglecting cluster-cluster correlation. (5) Finally, the slow aggregation of insoluble asphaltenes reveals that depending on the size of insoluble clusters/aggregates, they may or may not be separated from the mixture by centrifugation at particular time after mixing with a precipitant.

4.3 Results and Discussion

4.3.1 Fractal Structure of Asphaltenes

The scattering results for Oil A, Model Oil (MO) and Oil B diluted with heptane were normalized by $\Delta\rho^2\phi(1 - \phi)$ to isolate the scattering from the fractal clusters. It will be shown later that the scattering from Oil A is dominated by the heptane-insoluble asphaltenes, and the volume fraction of scattering material, ϕ , for Oil A and Oil B was taken to be the volume fraction of the heptane-insoluble asphaltenes remaining in the sample. Figure 4.1 shows the scattering results for Oil A samples that were diluted with heptane at concentrations ranging from 0 to 70 vol. % heptane and then continuously stirred for one week (called the destabilization time.) Figure 4.2 shows the scattering results of the Model Oil diluted with d-heptane at concentrations ranging from 0 to 55 vol. % d-heptane and with a one week destabilization time. Figure 4.3 shows the scattering results of Oil B diluted with 0 to 45 vol. % heptane and with a two month destabilization time. Figure E.4 in Appendix E compares centrifuged and uncentrifuged samples and reveals that the centrifugation step does not significantly affect the nanometer sized asphaltene clusters.

As seen in Figures 4.1, 4.2, and 4.3, all oils studied exhibit similar scattering behavior when diluted with heptane. The three q -regions that need to be examined for each sample are the low, moderate and high q regions. Discussion of these three

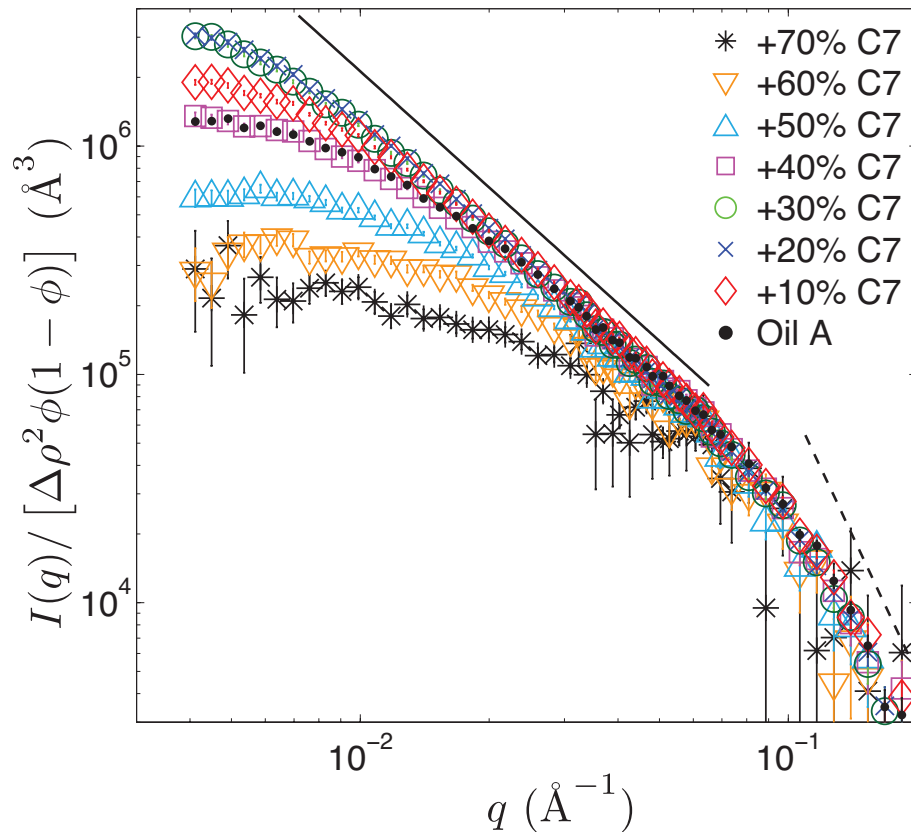


Figure 4.1: SANS results for Oil A at various heptane concentrations with a one week destabilization time. Solid line represents a fractal dimension of 1.69 and dashed line represents a slope of -4, characteristic of surface scattering.

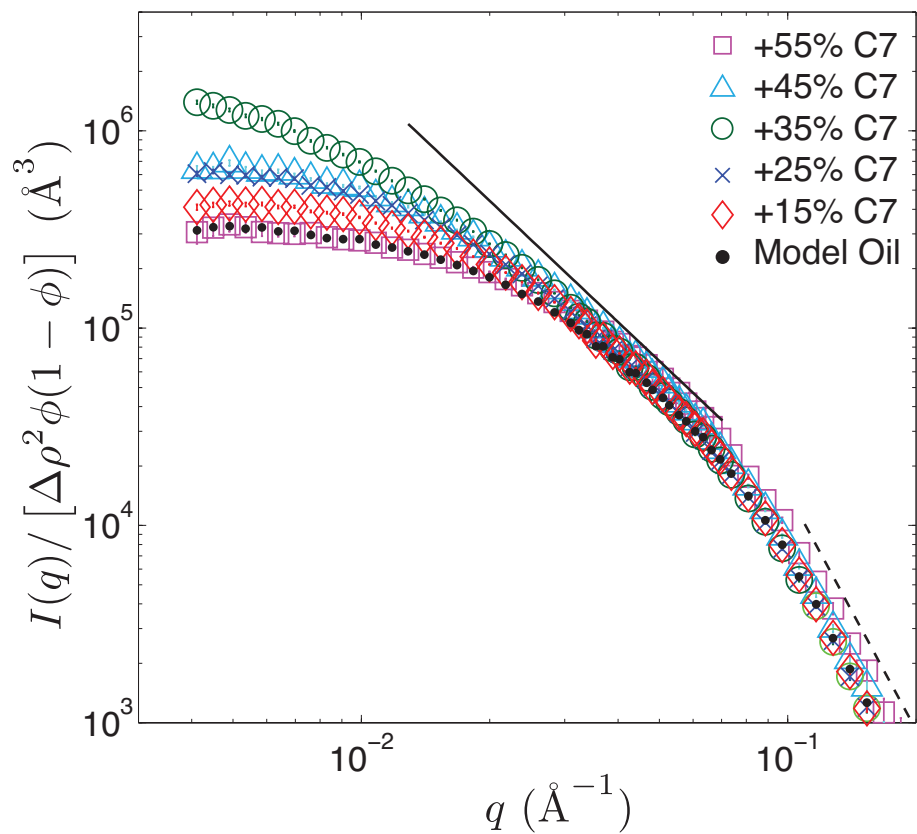


Figure 4.2: SANS results of the Model Oil diluted with deuterated heptane at various concentrations and times. Solid line represents a fractal dimension of 1.98 and dashed line represents a slope of -4, characteristic of surface scattering.

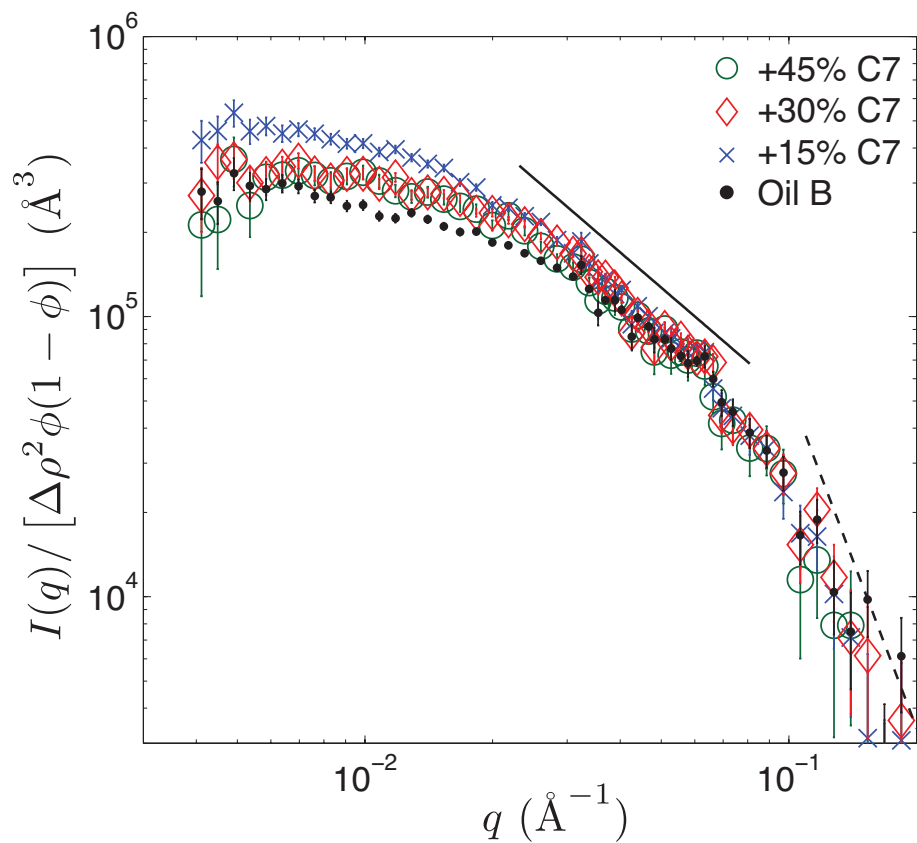


Figure 4.3: SANS results of Oil B diluted with heptane at various concentrations and times. Solid line represents a fractal dimension of 1.23 and dashed line represents a slope of -4, characteristic of surface scattering.

regions will focus on Oil A; however, similar conclusions were obtained for all three oils.

Low- q (approximately $4 \times 10^{-3} < q < 1 \times 10^{-2}$). The scattering intensity at low- q is commonly called the Guinier region and represents the range where the size (i.e., radius of gyration) of the largest particles in the system can be estimated. For example, the increase in the low- q scattering in Figure 4.1 when heptane is added to Oil A reveals that the asphaltene fractal cluster size grows, increasing from 15.2 ± 0.2 nm without heptane (black dots) to 28.9 ± 0.5 nm with 30 vol. % heptane (green circles). The Zimm approximation, Equation (4.3), was used to obtain quantitative measurements of the radius of gyration and molecular weight, which will be discussed in detail later. As the heptane concentration is increased from 30% to 70%, the size of the asphaltenes remaining dispersed in the oil-precipitant mixture decreases. This size decrease will also be discussed in detail later. Additionally, the flat scattering profile at low- q for samples with a high heptane concentration reveals that there are no large asphaltene particles present and also that the soluble asphaltenes are completely dispersed on the nanometer length scale.

Moderate- q (approximately $1 \times 10^{-2} < q < 7 \times 10^{-2}$). In this region, the scattering intensity is a linear function of q on a log-log scale, and therefore Equation (4.5) can be used to estimate the fractal dimension of asphaltene clusters. For example, the slope of the solid line in Figure 4.1 is -1.69 ± 0.03 , revealing that Oil A asphaltenes have a fractal dimension of 1.69 ± 0.03 . Analogously, in Figures 4.2 and 4.3 the fractal dimension for the Model Oil and Oil B were measured to be 1.98 ± 0.03 and 1.23 ± 0.07 , respectively. Qualitatively, a higher fractal dimension corresponds to a more compact structure. Adding heptane to crude oil increases the size of soluble fractal clusters, but does not appear to significantly change their fractal dimension. As such, the fractal dimension for the soluble asphaltene clusters in each oil was measured using the sample with the longest region of fractal scaling in q -space, which corresponded

to the sample with the largest fractal cluster size. For a concentration of 30 vol. % heptane in Oil A, the fractal scaling region spans nearly an order of magnitude in q , from $1 \times 10^{-2} < q < 7 \times 10^{-2}$. The fractal dimension for asphaltenes in the Model Oil was measured with the 35% d-heptane sample for $2 \times 10^{-2} < q < 5 \times 10^{-2}$, and the Oil B asphaltene fractal dimension was measured with the 30% heptane sample for $2 \times 10^{-2} < q < 7 \times 10^{-2}$. The linear region for determining the fractal dimension was obtained by trial and error to include all data points that followed a linear regression. It will be shown in the next section that the insoluble asphaltenes in a 30 vol. % heptane in Oil A sample had a fractal scaling region that spanned over an order of magnitude in length scale. At higher heptane concentrations (approx. $> 50\%$ heptane), the fractal dimension cannot be accurately estimated using Equation (4.5) because the relatively small size of the asphaltene clusters makes the fractal scaling region short and difficult to identify.

High- q (approximately $7 \times 10^{-2} < q < 0.2$). In this region, the length scale investigated by scattering is similar to the dimensions of individual asphaltene nanoaggregates. All asphaltenes for a particular oil exhibit nearly identical scattering regardless of heptane concentration at high- q , indicating that the structure of the asphaltene nanoaggregates is similar and independent of the heptane concentration. The dashed lines in Figures 4.1 and 4.2 show that at sufficiently high q (i.e., small length scale) the scattering intensity is proportional to q^{-4} , which is characteristic of a sharp interface or surface. The scattering at high- q is consistent with the surface scattering from compact (i.e., a well-defined boundary) asphaltene nanoaggregate monomers. This observation is in agreement with the fractal analogy, because the structure of individual monomers still influences the scattering at high- q in fractal systems (*Schaefer et al.*, 1984).

To summarize the section *Fractal Structure of Asphaltenes*, it was shown that the scattering of asphaltenes in crude oil can be described by fractal clusters that are

composed of individual asphaltene nanoaggregates. Adding heptane to oil increases the size of the soluble fractal clusters, but does not modify their fractal dimension for low to moderate heptane concentrations (approx. < 50% heptane in Oil A.) It will be shown in the next section that the insoluble fractal clusters that form after heptane addition have a markedly different fractal dimension.

4.3.2 Fractal Dimension of Insoluble Asphaltenes

It is of great interest to investigate the structure of insoluble asphaltenes as they are in the process of aggregating to search for differences between the soluble and insoluble fractions. Many of the scattering samples that were measured the day of mixing with heptane had insoluble asphaltenes present in addition to the soluble asphaltenes. The insoluble asphaltenes in these samples were too small to be separated out by the centrifugation procedure due to insufficient time to grow in size. Scattering profiles that were measured immediately after destabilization and contained contributions from both the soluble and insoluble distributions are designated $[I(q)]_{Combined}$. After a sufficiently long destabilization time had elapsed, all the insoluble asphaltenes grew to a size large enough to be fully separated from the oil-heptane mixture by centrifugation. The scattering of only the soluble asphaltenes, $[I(q)]_{Soluble}$, could be directly measured once the insoluble asphaltenes were fully separated from a sample. If asphaltenes are considered to be either soluble or insoluble, Equation (4.6) can be applied to isolate the scattering intensity of the insoluble asphaltenes, $[I(q)]_{Insoluble}$:

$$[I(q)]_{Insoluble} = [I(q)]_{Combined} - [I(q)]_{Soluble} \quad (4.7)$$

The scattering intensities used in Equation (4.6) are not normalized by any factors to determine the scattering of the insoluble asphaltenes. Appendix E contains additional details on the measurement of the insoluble asphaltene scattering.

The results of 30% heptane in Oil A proved to be an excellent system to measure

the scattering profile of insoluble asphaltenes. The combined asphaltene scattering profile, $[I(q)]_{Combined}$, was measured shortly after destabilization with heptane and was the sample prepared the day of the scattering experiments. The soluble scattering profile, $[I(q)]_{Soluble}$, was the one obtained six months after destabilization. The insoluble asphaltene scattering, $[I(q)]_{Insoluble}$, profile was obtained using Equation (4.7) and is shown along with $[I(q)]_{Combined}$ and $[I(q)]_{Soluble}$ in Figure 4.4. It was found that the fractal dimension for the soluble asphaltenes was 1.69 ± 0.03 while the insoluble asphaltenes had significantly higher fractal dimension of 2.12 ± 0.02 . The difference in the fractal dimension between soluble and insoluble asphaltenes reveals that the asphaltene destabilization mechanism is linked with the fractal dimension of the asphaltene clusters. Learning the mechanism for the formation of a more compact fractal structure will further aid in the understanding of asphaltene precipitation. The same procedure was repeated for all samples where combined and soluble asphaltene scattering profiles were available. The scattering profiles of the soluble and insoluble asphaltenes for 40% heptane in Oil A, 45% d-heptane in the MO, and 55% d-heptane in the MO are shown in Figures E.5 to E.7 in Appendix E. The fractal dimension measurements of the soluble and insoluble asphaltenes as a function of heptane concentration and oil are summarized in Figure 4.5.

The 30% heptane in Oil A results presented in Figure 4.4 show that the fractal scaling region of the insoluble asphaltene clusters stretches for over an order of magnitude in length scale, which strongly supports the premise that the insoluble asphaltenes are fractals. It was not possible to isolate the scattering from Oil B insoluble asphaltenes owing to the poor statistics caused by the low asphaltene content of Oil B. As can be seen in Figure 4.5, the insoluble asphaltene clusters have a higher fractal dimension than the soluble clusters for all oils. No clear trend was observed for the fractal dimensions of the soluble and insoluble asphaltenes as a function of heptane concentration in Figure 4.5; however, future investigations may discover subtle

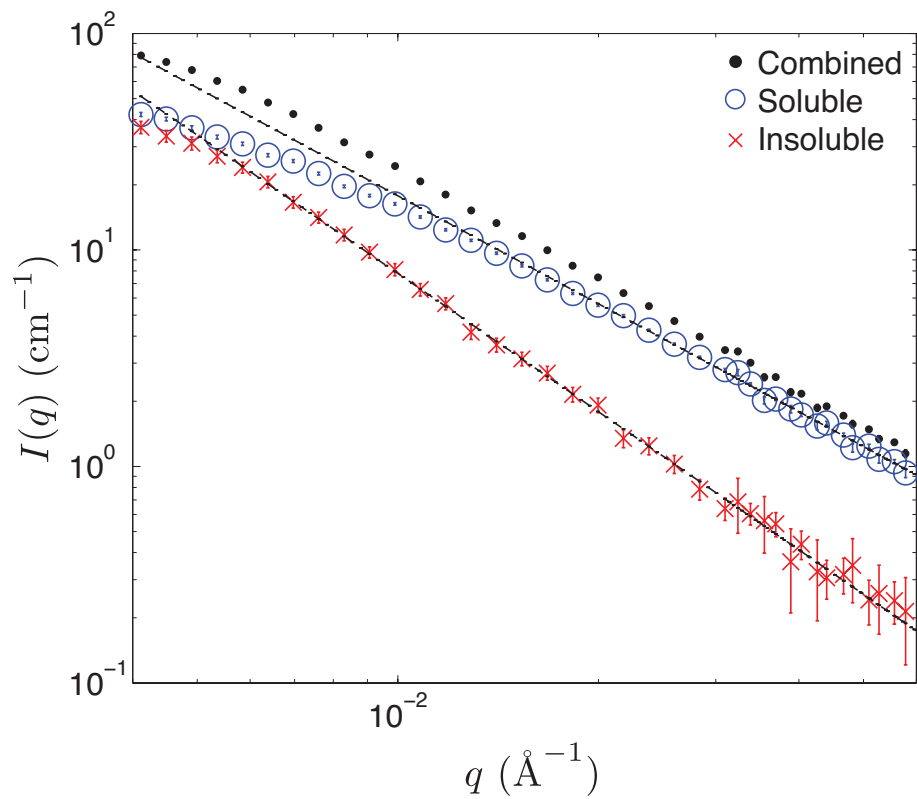


Figure 4.4: Fractal dimension measurements of soluble (1.69 ± 0.03 , blue \circ) and insoluble (2.12 ± 0.03 , red X) asphaltenes in a sample of 30% heptane in Oil A. The scattering of the combined sample (black \bullet) from where the insoluble scattering is inferred is also included.

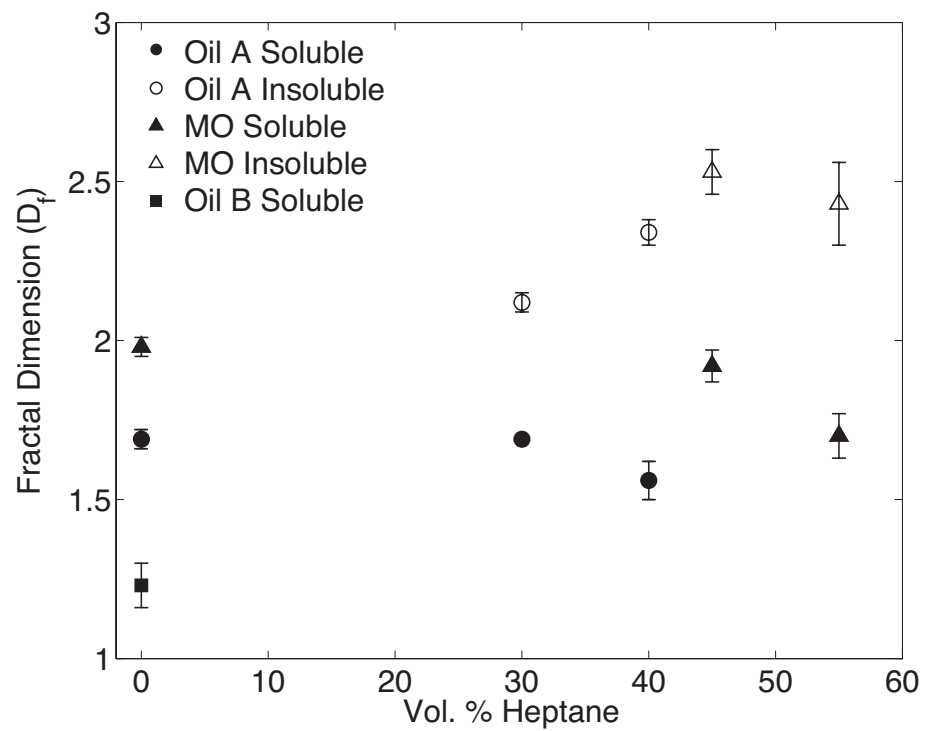


Figure 4.5: Summary of the fractal dimension measurements of soluble and insoluble asphaltenes.

differences in the fractal dimensions at different heptane concentrations.

To summarize the section *Fractal Dimension of Insoluble Asphaltenes*, it was shown that insoluble asphaltene clusters are also fractal and have a higher fractal dimension compared to the soluble asphaltene clusters. Determining the asphaltene-asphaltene interactions that cause the insoluble asphaltenes to have a more compact fractal cluster structure will greatly improve the understanding of the asphaltene destabilization mechanism.

4.3.3 R_g and M_W Measurements

The radius of gyration (R_g) for all samples was calculated using the Zimm approximation, Equation (4.3), by regression of linearized scattering data (i.e., plot $1/I(q)$ vs. q^2). The weight-average molecular weight (M_W) of the asphaltene clusters was calculated using the zero-angle scattering intensity, $I(0)$, and Equation (4.4). All samples were centrifuged before performing the scattering experiments, and the R_g and M_W results are for the asphaltenes that remain dispersed in the oil-heptane mixture after centrifugation. Recall, that some samples contain insoluble asphaltene clusters that were too small to be separated by centrifugation, which will scatter at low- q and artificially raise the R_g and M_W measurements. Figures 4.6 and 4.7 show the radius of gyration, R_g , and molecular weight, M_W , of the asphaltene fractal clusters as a function of both the destabilization time and the heptane volume percent. Figure 4.7 also shows the aggregation number, the number of asphaltene nanoaggregates per fractal cluster. For calculating the aggregation number, it was assumed that each nanoaggregate has 8 molecules and each molecule has a M_W of 1000 *g/mol*, both of these assumed values are within range of reported previous estimates (*Mullins et al.*, 2012). For a fixed destabilization time, both R_g and M_W follow the same trend and increase with increasing in heptane concentration until a maxima is reached, after which they decrease monotonically.

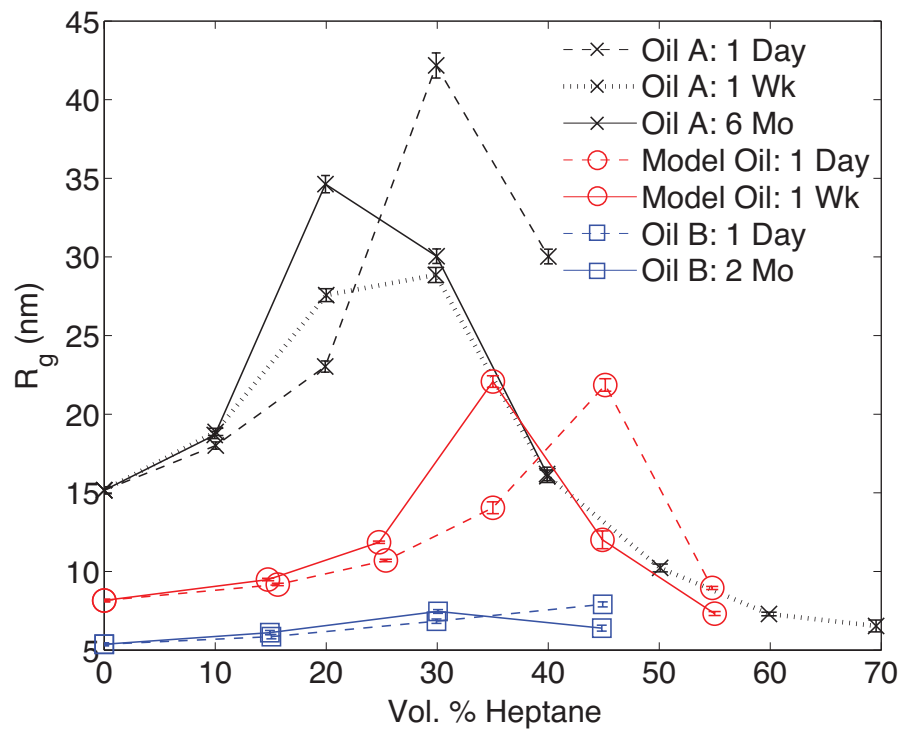


Figure 4.6: Measured Zimm radii of gyration for Oil A, Oil B, and the Model Oil (MO) as a function of the destabilization time and heptane volume percent. Lines are intended to guide the eyes and differentiate destabilization times.

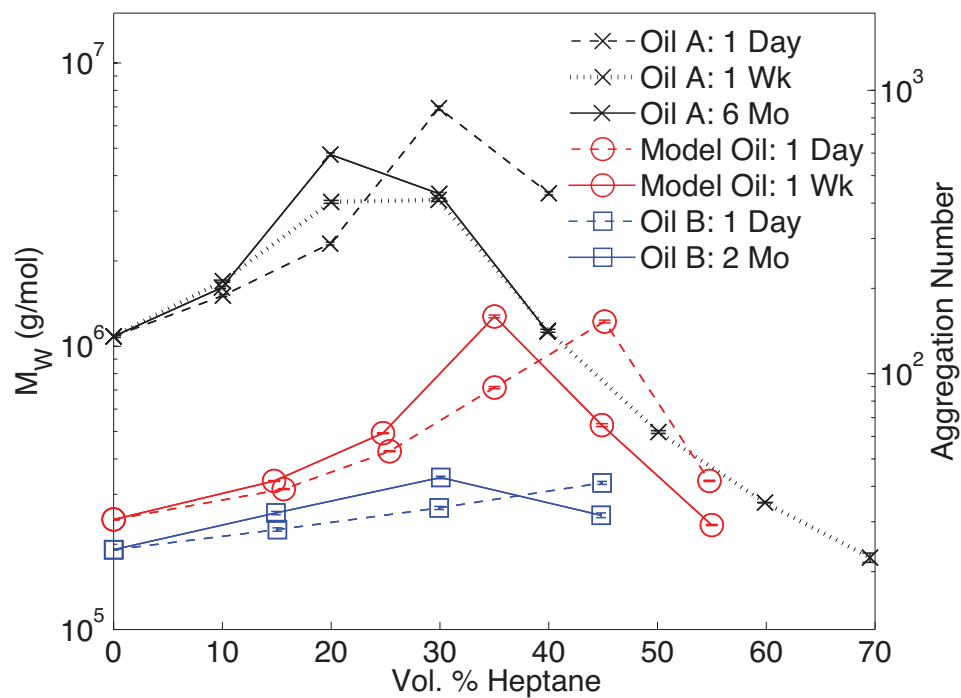


Figure 4.7: Asphaltene cluster molecular weight for Oil A, Oil B and the Model Oil (MO) as a function of destabilization time and heptane volume percent. Aggregation number is the number of asphaltene nanoaggregate monomers in each fractal cluster. Lines are intended to guide the eyes and differentiate destabilization times.

The scattering profiles of all the oils studied exhibited similar behavior for the R_g and M_W measurements. While the discussion of the results will focus on Oil A, similar conclusions can be obtained with the MO and with Oil B. It was observed that the R_g and M_W of asphaltenes increases with longer destabilization time for samples with slow aggregation kinetics at dilute heptane concentrations (10 and 20 vol. % heptane in Oil A). This size increase is believed to be the formation of insoluble asphaltene clusters that are slowly aggregating but are too small to be separated by centrifugation at the time of the scattering experiments. This finding demonstrates that *a well-defined critical precipitant concentration for asphaltene stability does not exist* and that small quantities of insoluble asphaltenes may be detected with more sensitive techniques at vanishingly low heptane concentrations. No insoluble asphaltenes were observable by optical microscopy in the 10 and 20% heptane samples six months after destabilization and the instability was only detectable because SANS is sensitive to changes in the asphaltene cluster size on the nanometer length scale. Ultimately as a consequence of slow aggregation kinetics, the definition of an asphaltene critical stability point is based on the sensitivity of the detection technique used and future investigations should assess the consequences of this effect on thermodynamic asphaltene stability models.

Several samples “*appeared at first*” to violate the trend of increasing size with increasing destabilization time (30% and 40% heptane in Oil A, 45% and 55% d-heptane in the MO, and 45% heptane in Oil B); however, the large values of R_g and M_W for the one day destabilization time for these samples was caused by the presence of large and insoluble asphaltenes that were not separated after one day of destabilization. The insoluble asphaltenes cause significant scattering at low- q and raise the measured values of R_g and M_W . After sufficient destabilization time has elapsed, the insoluble asphaltene clusters grew to a size where they are completely removed by centrifugation, after which the measured values of R_g and M_W decrease

to the value of the soluble asphaltene clusters that remain in the oil-heptane mixture. The samples with a maximum values of R_g and M_W for the one day destabilization time were the ones used to extract the scattering of the insoluble asphaltenes.

If asphaltenes could be accurately approximated as a single component, one would expect the R_g and M_W to only monotonically increase with heptane concentration. However for all oils studied, the asphaltene cluster R_g and M_W increased with increasing precipitant concentration up to a maximum size then decreased. This observation reveals that *there is polydispersity in the stability of asphaltenes that is directly related to the cluster size polydispersity*. Therefore, adding heptane to oil will destabilize different fractions of asphaltenes based on their solubility in the oil-heptane mixture. This conclusion will now be supported by a short discussion of the results in Figures 4.6 and 4.7. Adding heptane to crude oil causes two effects: (1) increases the size of all asphaltene clusters due to increased association, and (2) depletes the polydisperse system of the largest asphaltenes by precipitating them. The largest asphaltenes in the system are the closest to their instability point and will precipitate with a small addition of a precipitant. When the large asphaltene clusters in the size polydispersity distribution are destabilized, precipitate, and are separated by centrifugation, the weight-averaged M_W of the remaining asphaltene clusters is shifted to smaller values. At low heptane concentrations, the quantity of asphaltenes that precipitate and are separated is not sufficient to reduce the weight-averaged M_W measurement compared to the size increase effect caused by the heptane addition. However at high precipitant concentrations, large quantities of asphaltenes precipitate, which causes the measured weight-averaged M_W of the soluble material to shift to smaller values. This process is represented schematically in Figure 4.8. Similar size behavior as a function of precipitant concentration (increase to a maximum then decrease) was previously observed for asphaltenes in model systems (*Gawrys et al.*, 2003; *Sirota and Lin*, 2007).

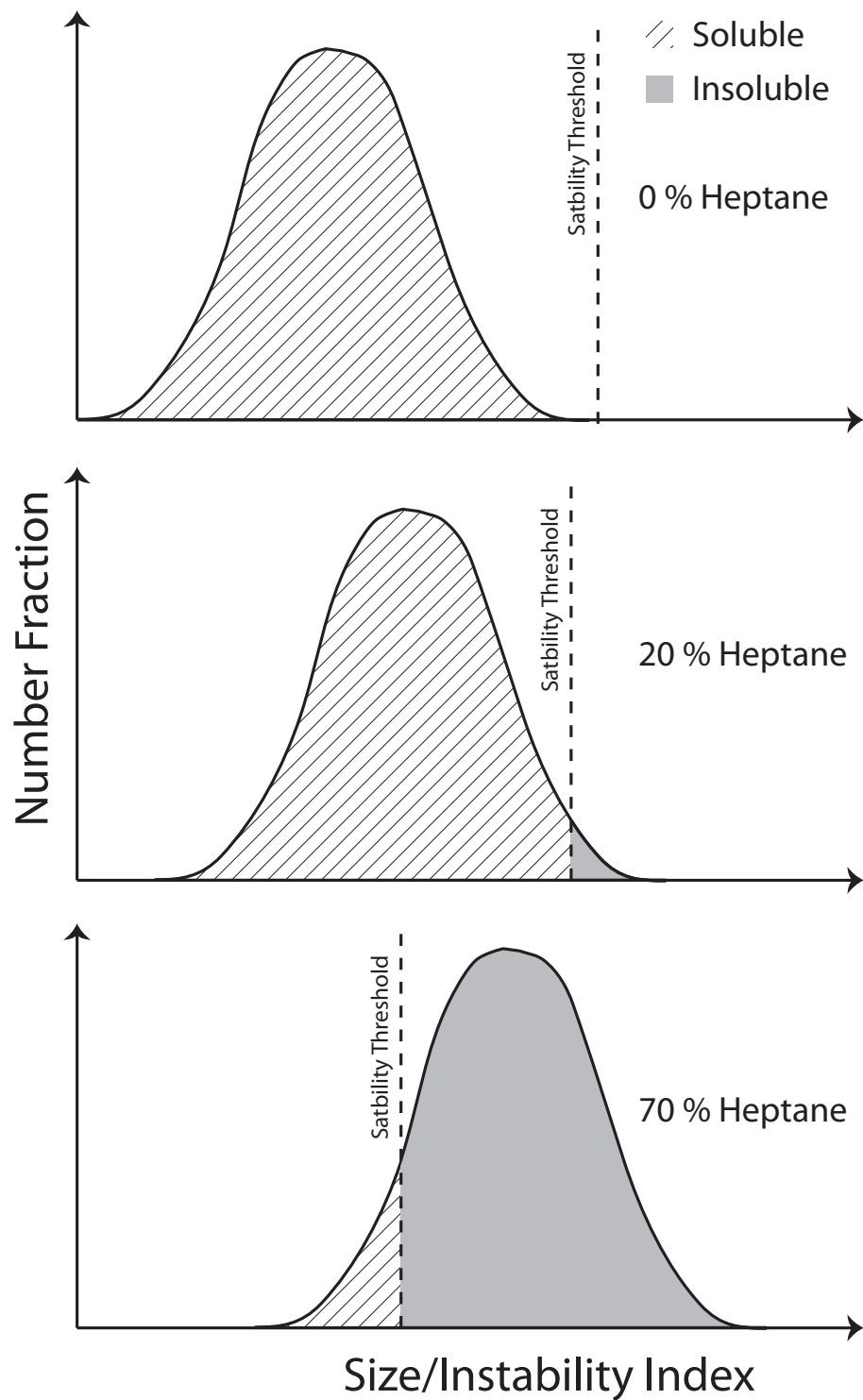


Figure 4.8: Graphical representation of the influence of heptane on the size and stability threshold of asphaltenes. As heptane is added to crude oil, the size of asphaltene clusters increases while the stability threshold decreases.

It is not known what properties of asphaltenes dictate their stability in oil-heptane mixtures, and the process of destabilizing asphaltenes by adding a precipitant and separating them with centrifugation will be generally referred to as an asphaltene solubility-based fractionation. Each solubility fraction of asphaltenes has a stability point, and adding heptane will only precipitate the asphaltene solubility fractions where the stability threshold has been exceeded. Therefore, the lack of an easily measurable asphaltene phase stability envelope is due to the broad distribution of asphaltene solubility fractions. Thermodynamic stability models that consider the vast solubility differences of asphaltenes will more accurately represent the complex process of asphaltene destabilization. The factors that govern why certain asphaltene solubility fractions precipitate at a given heptane concentration is not immediately clear; however, it is likely due to increased inter-aggregate attractions or the removal of a steric stabilization barrier (*Haji-Akbari et al.*, 2013). The solubility fractions of asphaltenes that are stable and left dispersed in the crude oil at high heptane concentrations form smaller clusters compared to the asphaltenes that precipitate at low heptane concentrations. The asphaltene solubility classes that will precipitate at low heptane concentrations are the most unstable asphaltenes in the oil and form the largest fractal clusters. Asphaltene cluster size is a new tool that can be used to assess asphaltene stability and determining the factors that control cluster size will likely result in an increased understanding of the asphaltene destabilization process.

The fractal dimension of the soluble asphaltene fractal clusters can also be determined from the relationship between M_W and R_g shown in Equation (4.1) and cross plotting the results in Figures 5 and 6 at each heptane concentration. A plot of the molecular weight of the clusters vs. their Zimm radius for Oil A and for Oil A diluted with heptane and held for one week after destabilization is shown in Figure 4.9. The linear fit reveals that the fractal dimension is 1.8 ± 0.1 , which is within 7% of the value measured from the slope of the scattering profiles. The 10 % and 20 vol. %

heptane dilutions were not used because the scattering measurements have a contribution from insoluble asphaltene clusters and the R_g and M_W measurements are not representative for the soluble asphaltene fraction. The 70 vol. % sample was not used due to the poor scattering statistics caused by the low volume fraction of remaining asphaltenes. A similar analysis could not be applied to the MO or to Oil B because the measured R_g and M_W for many samples contained low- q scattering contributions from an insoluble asphaltene fraction and as a result, a plot of M_W vs. R_g would not yield an accurate estimate of the fractal dimension of the soluble asphaltenes.

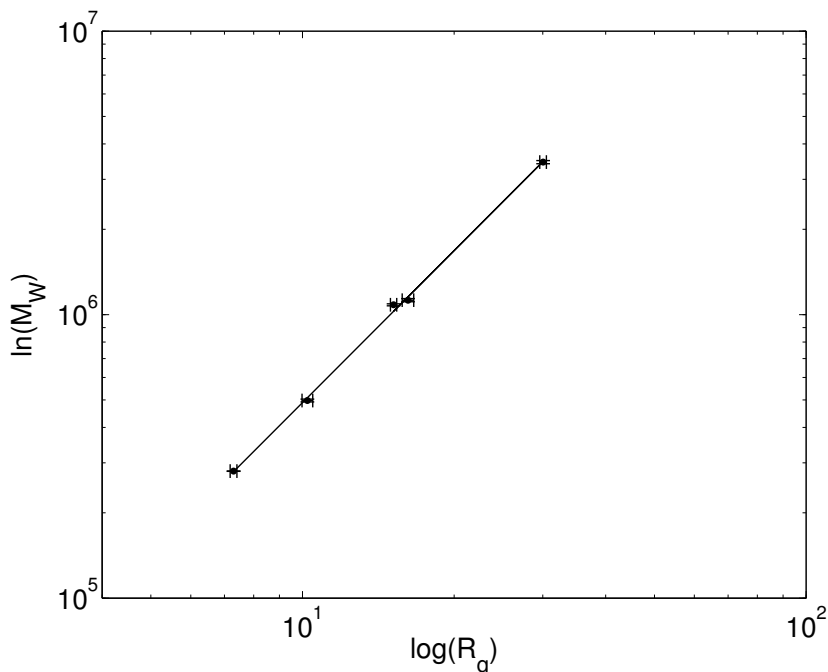


Figure 4.9: Log-log plot of M_W vs. R_g for *soluble* Oil A asphaltenes to determine the fractal dimension. Line represents linear regression with a slope corresponding to $D_f = 1.8 \pm 0.1$. This fractal dimension measurement is within 7% of the value obtained using Equation (4.1).

To summarize this section on R_g and M_W Measurements, it was shown that the lack of a well-defined phase stability envelope for asphaltenes is caused by the polydisperse nature of asphaltenes. Adding heptane to crude oil will only precipitate certain solubility fractions of asphaltenes and the asphaltenes that do not precipitate remain

dispersed on the nanometer length scale. Small amounts of destabilized asphaltenes were detected at low heptane concentrations, revealing that the definition of an asphaltene stability point is governed by the technique used to detect the asphaltene instability. In addition, the most unstable asphaltenes were found to form the largest fractal clusters.

4.3.4 Scattering Intensity vs. Asphaltene Content

An additional complication with small-angle scattering investigations of crude oil and asphaltenes is that it is not known what fraction of the oil or asphaltenes will form nanometer length scale aggregates or associations, which cause scattering. In this research investigation, asphaltenes are defined as the heptane-insoluble fraction of the crude oil; however, asphaltenes are sometimes defined as the pentane-insoluble material. Small-angle scattering of both heptane and pentane insoluble asphaltenes dispersed in solvents has been observed; however, little information exists as to how these distributions scatter in an unmodified crude oil (*Barré et al.*, 2009; *Sheu*, 2006). In addition, there may be certain fractions inside the heptane or pentane asphaltene distributions that do not form aggregated structures and are molecularly dispersed in the oil or solvent. This material will phase separate with excess precipitant, a criteria that must be met in order to be classified as an asphaltene, but does not necessarily contribute to the small-angle scattering intensity. From Equation (4.2), one observes that the scattering intensity is directly proportional to $\phi(1 - \phi)(\Delta\rho)^2$, which can be used to determine what oil or asphaltene fractions are causing scattering. Assuming no change in the structure of the scattering material, the following expression can be utilized to determine the relative volume fraction of scattering material between two scattering samples:

$$\frac{I_1(q)/\Delta\rho_1^2}{I_2(q)/\Delta\rho_2^2} = \frac{\phi_1(1 - \phi_1)}{\phi_2(1 - \phi_2)} \quad (4.8)$$

The scattering profiles of crude oil diluted with heptane revealed that the scattering profile from asphaltene nanoaggregates is observed at high- q and is independent of the heptane concentration. The high- q scattering intensity can be used to estimate the relative volume fraction of asphaltenes in each sample compared to the original crude oil that has not been diluted with precipitant. If only the heptane-insoluble asphaltene fraction is responsible for the measured scattering intensity, there should be a strong correlation between the reduction in the scattering intensity and the solubility of the heptane-insoluble asphaltene fraction, which will be now be examined.

Equation (4.8) was applied to determine the relative volume fraction of asphaltenes in each sample from the reduction in scattering intensity, assuming no change in the asphaltene nanoaggregate structure (see Appendix E for additional details on this calculation.) For better statistics, the reduction in scattering intensity was calculated and then averaged over the high q -range of 0.052 - 0.12 \AA^{-1} . In this range, the scattering from asphaltene nanoaggregates dominate and there is little influence on the scattering intensity from the asphaltene fractal structure. The solubility of asphaltenes was measured independently from the scattering samples by a centrifugation technique previously reported (*Maqbool et al.*, 2009). Slow aggregation kinetics prevent measurement of the asphaltene solubility at low heptane concentrations by physical separation techniques (e.g., centrifugation) (*Maqbool et al.*, 2009, 2011b,a; *Hoepfner et al.*, 2013a). The solubility samples were monitored over time to ensure complete precipitation to account for slow aggregation effects. Figure 4.10 shows the asphaltene solubility in oil (g soluble asphaltenes per 100 g oil) as measured by centrifugation and the reduction in scattering intensity as a function of the heptane concentration.

It can be seen in Figure 4.10 that both the centrifugation and scattering intensity solubility measurements follow the same functionality with heptane concentration and nearly fall on top of one another. On average, the two solubility measurements have

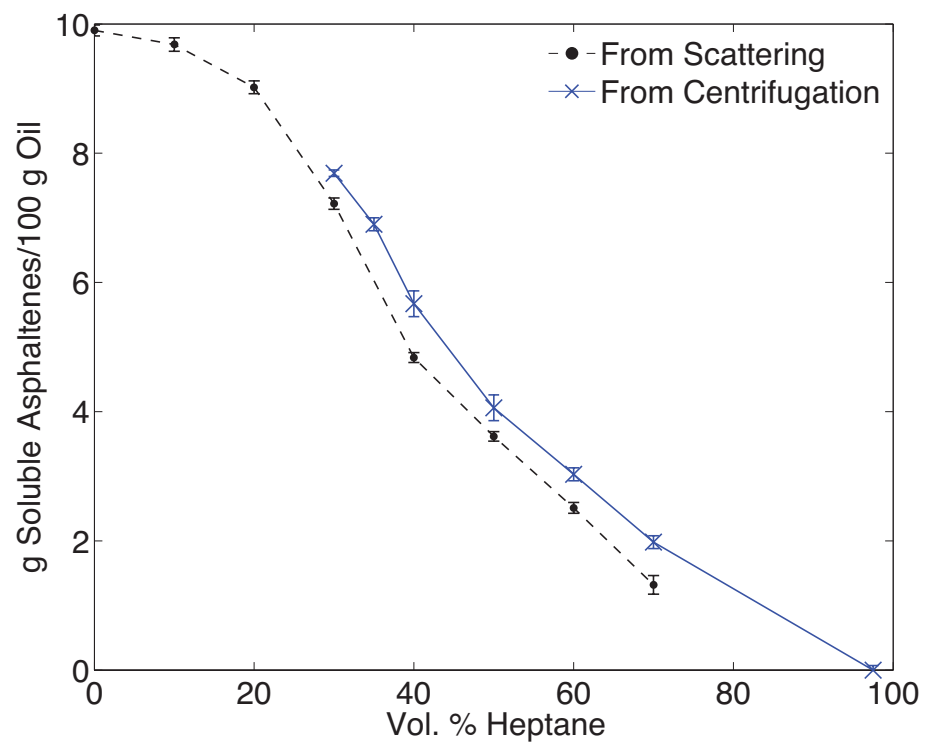


Figure 4.10: Comparison of the asphaltene solubility measured by the scattering intensity and by centrifugation.

an offset of only 0.5 g soluble asphaltenes per 100 g oil. This result reveals that the heptane-insoluble asphaltene fraction is the dominant source of the measured small-angle scattering intensity. Any reduction in the solubility of the heptane-insoluble asphaltene fraction causes a nearly identical reduction in the scattering intensity. Consequently, the asphaltene solubility at 10% and 20% heptane can be estimated from Figure 4.10, which is otherwise unobtainable using standard asphaltene analysis techniques, like centrifugation or filtration. The solubility results presented in Figure 4.10 are an important finding in that they represent the most complete solubility measurement of asphaltenes ever obtained and expands the range of instability detection to extremely low heptane concentrations. The capillary deposition experiments performed on Oil A in Chapter II also confirm that asphaltenes are destabilized at 20% heptane (*Hoepfner et al.*, 2013a).

To summarize the section *Scattering Intensity vs. Asphaltene Content*, it was shown that the heptane-insoluble asphaltenes are the dominant source of the small-angle scattering intensity. This finding allowed for the estimation of the solubility of asphaltenes at extremely low heptane concentrations, which was previously unobtainable.

4.4 Conclusions

Soluble asphaltenes in crude oil and model systems were found to associate into fractal clusters that have a characteristic fractal dimension that is independent of the heptane concentration. However after destabilization, insoluble asphaltene clusters have a significantly higher fractal dimension compared to the soluble ones. The fractal dimension changes when asphaltenes are destabilized and transition from soluble to insoluble, revealing that the structure of the fractal clusters is modified. This modification is the result of a change in the packing organization of individual asphaltene nanoaggregates. Determining the differences between the inter-aggregate interactions

between soluble vs. insoluble asphaltene nanoaggregates may potentially provide the microscopic destabilization mechanism of asphaltenes. An improved understanding of the microscopic asphaltene destabilization mechanism may be obtained through the treatment of asphaltenes as self-assembling anisotropic particles that associate into fractal clusters (*Glotzer and Solomon, 2007*). Asphaltene size, shape, polydispersity, and steric stabilization are variables that can be modified on individual asphaltene nanoaggregate monomers to achieve the measured self-assembling structure reported here for soluble and insoluble asphaltene fractal clusters.

The asphaltenes that precipitate with the smallest amount of precipitant addition form the largest fractal clusters. The large asphaltenes in the size polydispersity distribution are the most unstable asphaltenes and experience the strongest inter-aggregate attractions (or weakest repulsion). These asphaltenes will likely associate preferentially with one another due to the strong inter-aggregate attractions (e.g., London dispersion force). Because of the statistical fluctuations from thermal motion, the soluble asphaltene clusters are in a state of complex dynamic equilibrium where different asphaltene nanoaggregates and molecules continuously exchange and rearrange. This behavior is to be expected if asphaltenes dispersed in a solvent are to represent a system at thermodynamic equilibrium. At high precipitant concentrations, the highly unstable asphaltenes have precipitated and the asphaltenes that remain dispersed at the nanometer length scale are the most stable ones, which form the smallest fractal clusters, as evidenced in this investigation. The experimental findings of the asphaltene precipitation process are schematically represented in Figure 4.11.

The results further reinforce the notion that there is not a well-defined phase envelope for asphaltene stability and the polydisperse nature of asphaltenes allows for destabilization of small fractions of asphaltenes at low precipitant concentrations. As such, the initiation point of asphaltene phase separation as a function tempera-

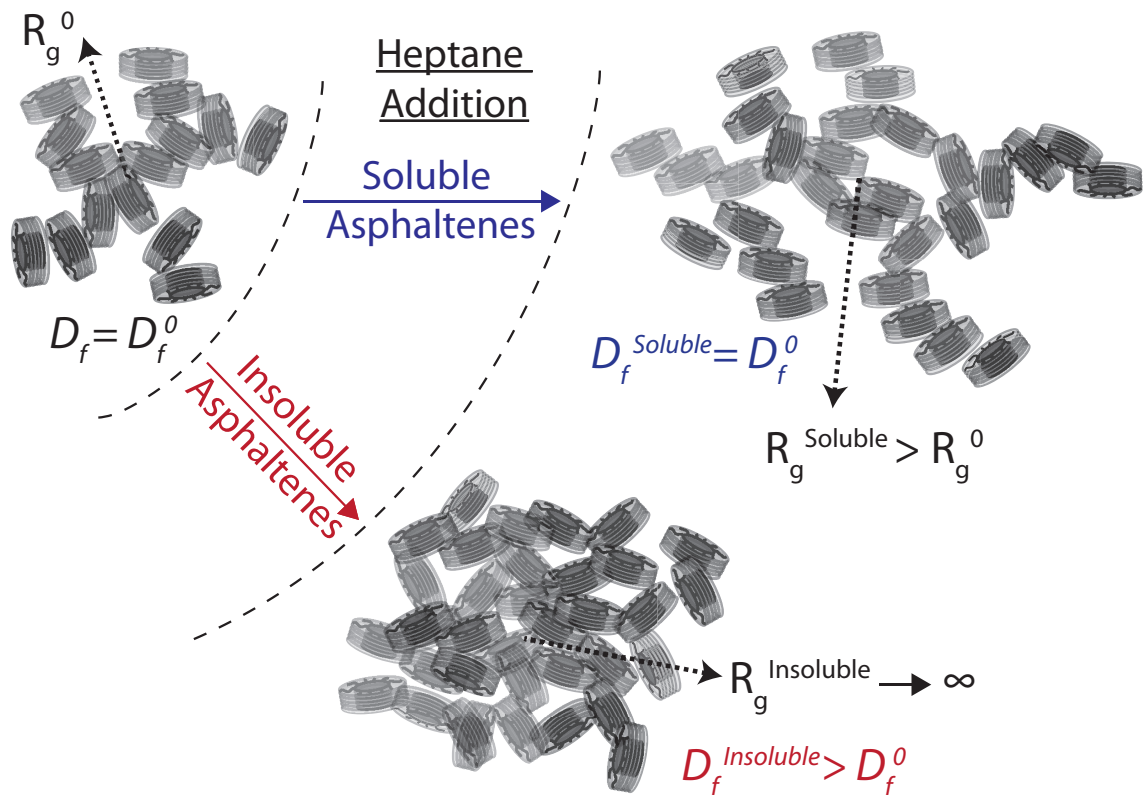


Figure 4.11: Schematic of the proposed asphaltene precipitation mechanism. R_g^0 and D_f^0 refer to the radius of gyration and fractal dimension, respectively, of the asphaltene fractal clusters in the undiluted crude oil. Fractal clusters are not drawn to scale or to the measured fractal dimension and are intended as only rough structural guides.

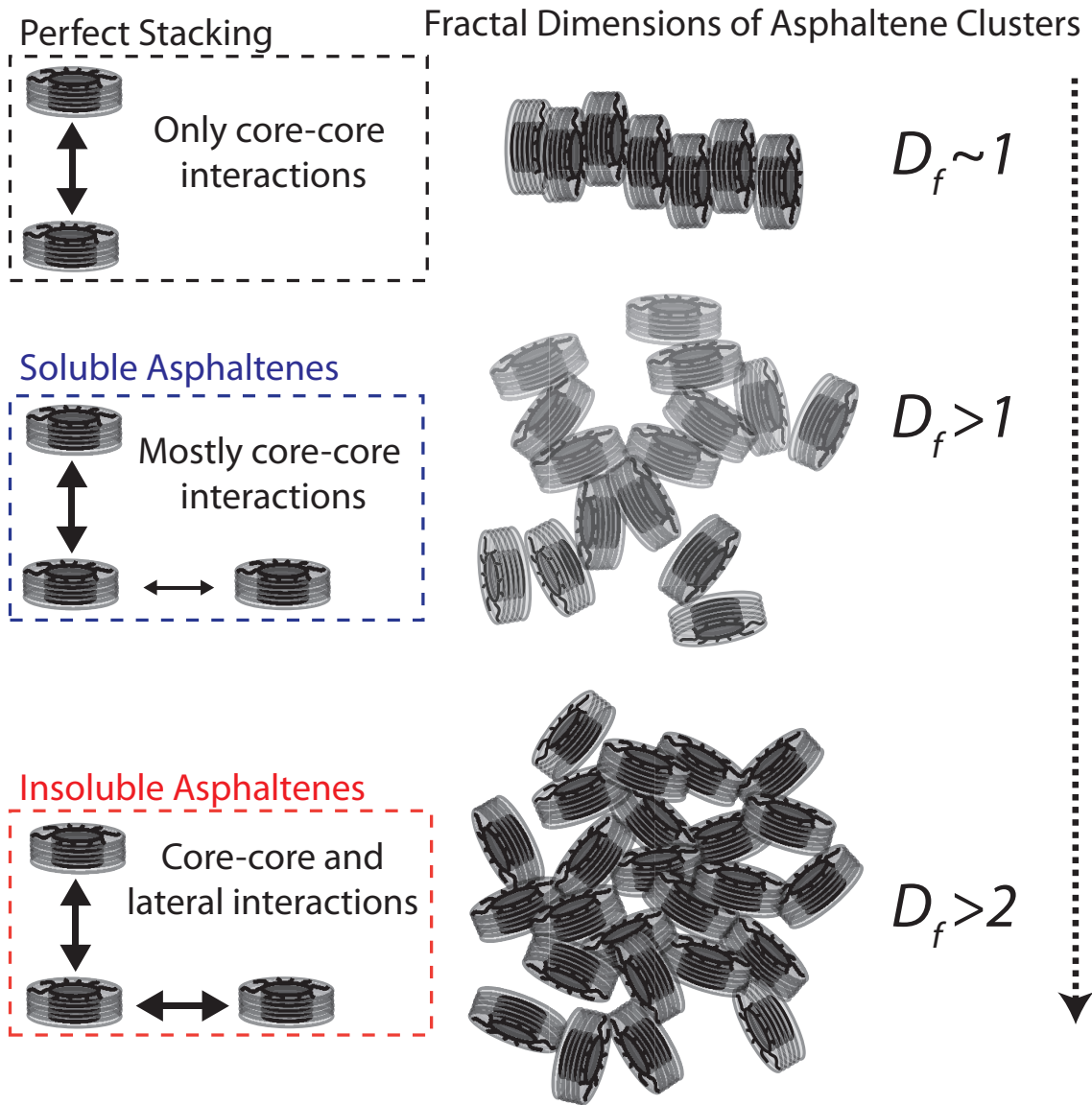


Figure 4.12: Schematic of a possible mechanism to explain to changes in asphaltene cluster fractal dimension.

ture, pressure or composition is not an easily determinable parameter. This result questions the experimental validation and basis of many thermodynamic asphaltene stability models that rely on onset points or concentrations. Results also suggest that the heptane-insoluble asphaltenes are the dominant source of small-angle scattering intensity in crude oil. Finally, the solubility of asphaltenes at extremely low heptane concentrations was uncovered from the scattering intensity.

CHAPTER V

Multi-scale Scattering Investigations of Asphaltene Cluster Breakup, Nanoaggregate Dissociation, and Molecular Ordering

5.1 Introduction

Asphaltenes are a polydisperse class of petroleum crude oil defined by their solubility in aromatic solvents (typically toluene) and insoluble in normal alkanes (typically pentane or heptane) (*Speight, 2007*). Nano-filtration (*Zhao and Shaw, 2007*), ultracentrifugation (*Fenistein and Barré, 2001*), along with numerous small-angle scattering investigations (*Fenistein et al., 1998; Fenistein and Barré, 2001; Barré et al., 2008; Hoepfner et al., 2013b*) have supported the notion that at least a fraction of asphaltenes exist in an aggregated state when dispersed in crude oil (*Mullins et al., 2007*) and solvents. The best accepted structural hierarchy for asphaltenes is that the aromatic core of asphaltene molecules associate into disk-like aggregates called “nanoaggregates” which then further associate into fractal clusters with fractal dimension typically ranging from 1.6 to 2.0 (*Yen et al., 1961; Mullins et al., 2012; Fenistein and Barré, 2001; Barré et al., 2008; Eyssautier et al., 2011; Hoepfner et al., 2013b*). It is unknown what relative fractions of asphaltenes exist in each “state”: molecule, nanoaggregate or fractal cluster. An improved understanding of the tran-

sition between molecule, nanoaggregate and fractal cluster will aid in uncovering the fundamental behaviors of asphaltene systems.

Recent measurements using high-Q ultrasonics (*Andreatta et al.*, 2005), static light scattering (*Evdokimov et al.*, 2006), DC conductivity (*Zeng et al.*, 2009), NMR (*Lisitza et al.*, 2009), and TOF-MS (*McKenna et al.*, 2013) have demonstrated that asphaltene molecules begin to form aggregated structures at concentrations below 100 mg/L in organic solvents. The concentration of asphaltenes when aggregation begins has been called the critical nanoaggregate concentration (CNAC) (*Mullins et al.*, 2012). At higher asphaltene concentrations (2-10 g/L) behavioral differences have been noted for asphaltenes, either called the critical micelle concentration (CMC) (*Sheu et al.*, 1992; *Rogel et al.*, 2000; *Oh et al.*, 2004) or the critical cluster concentration (CCC), depending on the source (*Goual et al.*, 2011; *Mullins et al.*, 2012). Evidence for the CMC has primarily been supported by surface tension measurements (*Sheu et al.*, 1992; *Rogel et al.*, 2000; *Oh et al.*, 2004) while the evidence for the CCC is limited to DC conductivity (*Goual et al.*, 2011) and oil reservoir vertical asphaltene concentration gradients (*Mullins et al.*, 2012). The potential initiation of primary aggregation at the CNAC and secondary clustering at the CMC or CCC warrants further structural investigation in order to elucidate fundamental asphaltene behaviors.

Small-angle X-ray and neutron scattering (SAXS and SANS) are valuable probes of the size and structure of material on the length scale of asphaltenes and can be used to verify the formation or dissociation of asphaltene nanoaggregates and clusters. Previous SAXS and SANS investigations have not observed asphaltene cluster breakup or nanoaggregate dissociation. However this lack of detection may be a result of the fact that the lowest asphaltene volume fraction previously studied with SANS was 2.97×10^{-3} (*Roux et al.*, 2001), which is 35 times more concentrated than reported values for the CNAC of approximately 100 mg/L (or vol. fraction of 8.33×10^{-5}). *Cosultchi et al.* used SAXS to investigate even lower concentrations, down to

volume fractions of 1.15×10^{-4} . Unfortunately, they did not vary the asphaltene concentration to identify changes in the scattering profile as a function of the asphaltene concentration (*Cosultchi et al.*, 2003). Recently, the distance distribution function was calculated from SAXS results of asphaltenes in toluene at concentrations ranging from 10 to 500 mg/L (*Morimoto et al.*, 2013). It was found that there was a general decrease in the size of asphaltenes as the concentration was reduced; however, solvent background correction was not performed and limited additional quantitative conclusions were obtained.

This study is designed to investigate the structure of asphaltenes in solvents from a number of perspectives. First, the size of the largest asphaltene associations, the fractal clusters, is studied with shape-independent fits of low- q SAXS results to identify any cluster breakup as a function of concentration. The asphaltene concentration range investigated spans the previously reported values for the CMC, CCC and CNAC. Second, the nanoaggregate structure is investigated by comparing the results of SAXS and SANS to identify any structural changes that may occur as a function of asphaltene concentration. Third, asphaltene nanoaggregate dissociation is investigated utilizing the mid to high- q region of SAXS results. In this q -region, the scattering from fractal cluster associations is minimal and the primary scattering contribution is from the structure of individual nanoaggregates (*Eyssautier et al.*, 2011; *Hoepfner et al.*, 2013b). The asphaltene concentration range utilized in this investigation spans from 5 to 0.00125 vol. % (15 mg/L). Finally, the smallest structures investigated (at the widest angles) utilize wide-angle X-ray scattering (WAXS) measurements. Novel WAXS results are presented and discussed that provide insight into the local molecular organization of asphaltenes in a liquid environment. The general outline of this chapter will be to progressively investigate smaller length scales, starting from the size of asphaltene fractal clusters (approximately 5-12 nm) and progressing to asphaltene molecular spacings (approximately 3.5 Å). These length scales

are represented schematically in Figure 5.1.



Figure 5.1: Schematic representation of the multiple length scales investigated in this chapter and their respective q -ranges.

5.2 Experimental Methods

5.2.1 Small-Angle Scattering Background

Both SAXS and SANS can be used to study the size and structure of asphaltenes in a liquid environment (i.e., dispersed in a solvent). For a dilute two-level system (e.g., particles in solvent) the small-angle scattering intensity can be described by the following relation (*Lindner and Zemb, 2002*):

$$I(q) = \Delta\rho^2 \phi V_p P(q) S(q) \quad (5.1)$$

where $I(q)$ is the scattering intensity as a function of the scattering vector, q , $\Delta\rho^2$ is the scattering contrast, and ϕ is the volume fraction of particles (asphaltenes). Following the same general procedure of Eyssautier *et al.*, V_p is the volume of an asphaltene nanoaggregate, $P(q)$ is the form factor or intra-particle structure factor for the scattering of a single asphaltene nanoaggregate, and $S(q)$ is the inter-particle structure factor, commonly called just the structure factor, for the fractal organization of

asphaltene nanoaggregates (*Eyssautier et al.*, 2011). Although some asphaltene samples had asphaltene concentrations as high as 5 vol. %, all conclusions are based on samples at or below 2 vol. %, which is inside the dilute regime; therefore, positional correlation between asphaltene fractal clusters can be neglected without concern. The form factor, $P(q)$, has the property of tending toward unity at low- q while the structure factor, $S(q)$, tends toward unity at high- q . Therefore, the scattering intensity at high- q is dominated by the structure of individual asphaltene nanoaggregates, and the scattering intensity at low- q is dominated by the fractal structure of asphaltene clusters.

The size of asphaltene fractal clusters will be estimated using the Zimm approximation, as has been commonly performed previously (*Zimm*, 1948b; *Roux et al.*, 2001; *Hoepfner et al.*, 2013b):

$$I(q) = I_0 \left[1 + \frac{(qR_g)^2}{3} \right]^{-1} \quad (5.2)$$

where I_0 is the zero-angle scattering intensity and R_g is the radius of gyration. If the scattering results are on an absolute cross-section, the zero-angle scattering intensity, I_0 , can be used to estimate the weight-averaged molecular weight, M_W , of the asphaltenes in each sample (*Lindner and Zemb*, 2002):

$$I_0 = \frac{\phi M_W (\Delta\rho)^2}{d N_A} \quad (5.3)$$

where d is the mass density and N_A is Avogadro's number. The zero-angle scattering intensity is typically out of the range where it can be experimentally measured; however, the Zimm approximation in Equation (5.2) will be used to calculate I_0 . The fractal dimension, D_f , of a material can be obtained by plotting the M_W vs R_g (*Schaefer et al.*, 1984; *Fenistein and Barré*, 2001; *Eyssautier et al.*, 2012b; *Hoepfner et al.*, 2013b):

$$M_W \propto R_g^{D_f} \quad (5.4)$$

A comparison between SAXS and SANS results of asphaltenes has previously revealed that there are compositional moieties in asphaltene nanoaggregates (i.e., an aromatic core and alkyl shell) (*Barré et al.*, 2009; *Eyssautier et al.*, 2011). In a two-level system, the only difference between SAXS and SANS is the contrast, $\Delta\rho^2$. However, if there are local compositional moieties in asphaltenes, the form factor, $P(q)$, will be different between SAXS and SANS. The difference between SAXS and SANS results for asphaltenes is most significant at high- q , indicating that the individual asphaltene nanoaggregates possess the internal structure. Both SAXS and SANS results of asphaltenes will be presented in this investigation to study whether the local shape of asphaltene nanoaggregates is modified as a function of dilution.

It has been previously reported that the scattering from asphaltene nanoaggregates at high- q (where $S(q) \approx 1$) remains largely unchanged even if the size of the fractal clusters is different (*Roux et al.*, 2001; *Fenistein et al.*, 1998; *Hoepfner et al.*, 2013b). Over this q -range, the scattering intensity can be used to measure the volume fraction of asphaltene nanoaggregates, ϕ , using Equation (5.1) (*Hoepfner et al.*, 2013b). Taking the ratio of two scattering intensities, $I(q)$ and a reference scattering intensity, labeled $I_{Ref}(q)$, yields the following relationship:

$$\frac{I(q)}{I_{Ref}(q)} = \frac{\phi}{\phi_{Ref}}. \quad (5.5)$$

Equation (5.5) reveals that several unknown terms from Equation (5.1) cancel out after taking the ratio between two scattering runs. If the two samples are in the same solvent, it is clear that the scattering contrast ($\Delta\rho^2$) will be identical, and in order to eliminate V_P and $P(q)$, it must be assumed that the structure of asphaltene nanoaggregates is constant as a function of asphaltene concentration. If it is further

assumed that molecularly dispersed asphaltenes do not cause small-angle scattering, the scattering intensity can be used to estimate the fraction of asphaltenes that exist in nanoaggregates, which will be represented by χ . The potential consequences of these assumptions will be discussed later. Therefore, ϕ represents the volume fraction of asphaltene nanoaggregates and ϕ^0 will represent the total asphaltene volume fraction. The fraction of asphaltenes that exist as nanoaggregates, χ , can be determined by:

$$\chi = \frac{\phi}{\phi^0} \quad (5.6)$$

Note that ϕ is unknown and ϕ^0 is known based on the sample preparation procedure. Equation (5.6) can be substituted into equation Equation (5.5) and rearranged to calculate the relative amount of asphaltenes in the nanoaggregate state compared to a reference sample:

$$\frac{\chi}{\chi_{Ref}} = \frac{I(q)/\phi^0}{I_{Ref}(q)/\phi_{Ref}^0} \quad (5.7)$$

It would be desirable to assume that all asphaltenes exist in the nanoaggregate state for the reference sample (i.e., $\chi_{Ref} = 1$); however, this assumption would violate the principles of thermodynamic equilibrium. If $\chi_{Ref} = 1$, the nanoaggregation process would have to be irreversible and dissociation could never occur, which is not the case. If asphaltene dissociation occurs at low asphaltene concentrations (i.e., $\phi < \phi_{Ref}$), then $\chi/\chi_{Ref} < 1$. Conversely, if the opposite were to occur and the fraction of asphaltenes in the aggregated state were to increase, then $\chi/\chi_{Ref} > 1$; however due to Le Chatelier's principle, this possibility is not expected as the asphaltene concentration is decreased. Again, this analysis procedure assumes that molecularly dispersed asphaltenes are small enough as to not cause small-angle scattering. Therefore, only asphaltenes that are in a nanoaggregate will contribute to the scattering profiles. Additionally, the volume fraction of asphaltenes in the nanoaggregate state,

ϕ , should be used to calculate the cluster molecular weight, M_W , in Equation (5.3) instead of the total asphaltene volume fraction, ϕ^0 . The distinction between ϕ and ϕ^0 is due to the fact that molecularly dispersed asphaltenes are assumed to be undetectable by small-angle scattering and cannot contribute to the zero-angle intensity, which is used to calculate M_W .

5.2.2 Two-State Aggregation Model

A thorough derivation of the two-state aggregation model, as applied in this work, is shown in Appendix F. Briefly, the two-state aggregation model was originally derived for the study of micelle formation (*Debye*, 1949; *Israelachvili et al.*, 1976) and has been used previously for asphaltene aggregation by *Lisitiza et al.* (*Lisitiza et al.*, 2009) The application of the two state model to the results presented here improves on the work of *Lisitiza et al.* by directly determining the aggregation number and free energy change associated with the aggregation process. In the two-state model, asphaltenes can reversibly exchange between two states, (1) molecularly dispersed or (2) in a nanoaggregate with a monodisperse aggregation number, n . The aggregation number represents the number of molecules in a nanoaggregate and is fixed; therefore, the two-state model is a simplified representation of the asphaltene nanoaggregation process. From the derivation in Appendix F, it is shown that the free energy of association for the reversible nanoaggregation process, ΔG , can be represented by the following relationship:

$$e^{\frac{-\Delta G}{RT}} = C_S^{n-1} \frac{C_T - C_M}{nC_M^n} \quad (5.8)$$

where R is the universal gas constant, T is the temperature, C_S is the solvent molar concentration, C_T is the total asphaltene molar concentration (regardless of the aggregated state), and C_M is the molar concentration of molecularly dispersed asphaltenes. Assuming an asphaltene molecular weight allows for direct calculation

of C_T based on the sample preparation. The asphaltene molecular weight was assumed to be 750 g/mol, which is within previously reported molecular weight distributions (McKenna *et al.*, 2013; Pomerantz *et al.*, 2008). Changing the M_W from 500 to 1500 g/mol resulted in an insignificant change in the measured aggregation number, n , and less than a 10% change in the free energy of association. The molar concentration of molecularly dispersed asphaltenes can be obtained from the scattering results using Equation (5.7). Only two unknowns exist in Equation (5.8) and the aggregation number can be obtained by linear regression if $-\ln(C_T - C_M)$ is plotted against $\ln(C_M)$. The free energy of association per interaction, $\Delta G/(n - 1)$, was calculated with Equation (5.8). Therefore, the free energy change associated with the aggregation process and the aggregation number can both be determined. The only unknown parameter in the model is the fraction of asphaltenes in the aggregated state at some arbitrary reference state, χ_{Ref} , which was used as a tunable parameter in order to obtain quality linear regressions.

5.2.3 Asphaltene Extraction and Solution Preparation

Asphaltenes from two crude oils, A1 and K1, were extracted by 40:1 dilution of heptane:oil. Each mixture was stirred for over 24 hours and was then centrifuged at 4000 g for 10 minutes in a Sorvall Legend X1R centrifuge to separate the precipitated asphaltenes. The asphaltenes were then soxhlet washed for 24 hours with heptane to remove residual non-asphaltene components. The asphaltenes were dried in an oven at 75 °C for 4 hours to evaporate any residual heptane. Samples were prepared for each solvent with volume percents ranging from from 5 to 0.000125 vol. % asphaltenes. Samples more concentrated than 1 vol. % were prepared with solid asphaltenes and had a Teflon stirbar to aid in dissolution. Dilute solutions (less than 1 vol. %) were prepared taking a small volume of a more concentrated solution and adding additional solvent. All samples were prepared and stored in glass vials with

Teflon lined caps. All samples were prepared at least 6 days before scattering was to be performed to ensure the asphaltenes had reached their equilibrium state. The maximum relative uncertainty in concentration for the prepared samples is less than 3.2%. Numerous solvents were used for SAXS measurements and all were fully hydrogenated and supplied from Fisher Scientific: toluene (>99.9%), tetrahydrofuran (THF, >99.9%), and 1-methylnaphthalene (1-MN, >97%). Deuterated solvents (d-toluene and d-THF) used for SANS were supplied from Cambridge Isotope Labs and were >99.5% deuterated.

5.2.4 Scattering Procedure

Scattering experiments were performed over the course of several trips to neutron and synchrotron scattering facilities. These instruments and facilities are: the D11 instrument at Institut Laue-Langevin (ILL) in Grenoble, France; the EQ-SANS instrument at the Spallation Neutron Source (SNS) at Oak Ridge National Laboratory in Oak Ridge, Tennessee; and the 12-ID-B instrument at the Advanced Photon Source (APS) at Argonne National Laboratory in Argonne, Illinois. All neutron scattering samples were loaded into either 2mm or 5mm path length quartz ‘banjo’ cells with a tolerance of $\pm 0.01\text{mm}$ (Hellma Analytics, Type: 120-QS). Neutron scattering results were normalized by transmission and converted to an absolute scale by the open beam intensity at ILL and using an internal standard at the SNS (Porasil-B). At the ILL, 6 Å neutrons were used with up to three detector positions (28m, 8m and 1.2m) to span a q -range from 1.5×10^{-3} to 0.52 \AA^{-1} . The EQ-SANS instrument utilizes spallation neutrons, and takes advantage of the time-of-flight of the neutrons with a spectrum of wavelengths to measure the scattering intensity as a function of q . In this case, the instrument was operated in the frame-skip mode where two bands of neutron wavelengths (2.3 - 6.0 Å and 9.3 - 14.55 Å) were used for each of the two detector positions (4m and 1.3m). For the 4m detector position, the long

wavelength neutrons (9.3 - 14.55 Å) were used to measure low- q intensities and the short wavelength neutrons (2.3 - 6.0 Å) were used at the near detector position for high- q intensities. The q -range at the SNS spanned from 4.7×10^{-3} to 0.6 \AA^{-1} .

Simultaneous SAXS (Pilatus 2M detector) and WAXS (Pilatus 300k detector) results were generated on the 12-ID-B beamline at the APS. Samples were loaded into a round quartz flow-through capillary with a 1.5 mm inner diameter and were normalized by transmission and converted to an absolute scale using toluene as a standard. The theoretical scattering cross section for toluene was calculated using classical fluctuation theory (*Guinier and Fournet, 1955; Dreiss et al., 2006*). The q -range for SAXS and WAXS results were from 6.0×10^{-3} to 0.74 \AA^{-1} and from 0.88 to 2.44 \AA^{-1} , respectively. The SAXS and WAXS results were generated with 1 \AA wavelength synchrotron X-rays; however, for easy comparison of the WAXS profiles to previously reported XRD results (*Yen et al., 1961; Andersen et al., 2005*), the WAXS profiles are presented as a function of 2θ for Cu K α radiation (1.5418 \AA).

All scattering samples were transmission and background corrected before converting to an absolute scattering cross section. For SAXS and WAXS results, the background was the flow-through capillary filled with solvent and backgrounds were performed after each asphaltene sample to ensure accurate background correction. For SANS results, the background was the empty scattering cell and incoherent scattering was subtracted by inspection of the flat portion of the results at high- q (typically $0.45\text{-}0.6 \text{ \AA}^{-1}$). Background correction concerns are trivial when using concentrated samples, which is not the situation in this investigation. The SAXS round capillary cell exhibited flat scattering for q -values greater than 0.1 \AA^{-1} and significant surface scattering was observed below this value. The ability to study asphaltene structure in dilute mixtures is limited by a variety of effects using SAXS and SANS. For SAXS, the strong surface scattering from the sample holder prevents accurate measurement of the low- q scattering intensity for dilute asphaltene systems. For SANS, the long

data collection times that are a consequence of the low neutron incident flux limits the lowest concentration that can be used. Appendix F contains the asphaltene elemental composition and the scattering length densities of the asphaltenes and solvents.

5.3 Results and Discussion

5.3.1 Synchrotron SAXS Results

Figure 5.2 shows the SAXS results for A1 asphaltenes in THF at asphaltene concentrations ranging from 0.0025 to 2 vol. %. Only a selection of the scattering profiles from various asphaltene concentrations are presented and only one third of the measured scattering SAXS intensities are plotted to avoid cluttering the figures. In addition, Figure F.1 (A-C) in Appendix F shows additional SAXS results for K1 asphaltenes in THF, toluene and 1-MN, respectively. The results for K1 asphaltenes in THF, toluene and 1-MN all follow the same general trend as observed in Figure 5.2.

It can be seen that the scattering of asphaltenes is similar for different concentrations of A1 asphaltenes in THF. A decrease in the scattering intensity is observed at low- q as concentration is decreased, indicative of a reduction in the size of the fractal clusters. At sufficiently dilute concentrations (0.0025 %) the scattering intensity at low and high- q cannot be measured because the signal of the asphaltene scattering is not sufficiently strong in comparison to the background of the solvent in the cell (holder). However, there is a moderate q -region where coherent scattering can be observed, approximately 5×10^{-2} to $8 \times 10^{-2} \text{ \AA}^{-1}$. In this region, an arbitrary scaling factor can be used to superimpose the samples with significant high- and low- q data loss due to the background with a sample at higher asphaltene concentrations. This arbitrary scaling factor is χ/χ_{Ref} and provides the relative dissociation of asphaltene nanoaggregates, which will be discussed in greater detail later. The assumptions used in the derivation of Equation (5.7) are valid because the scattering of the most

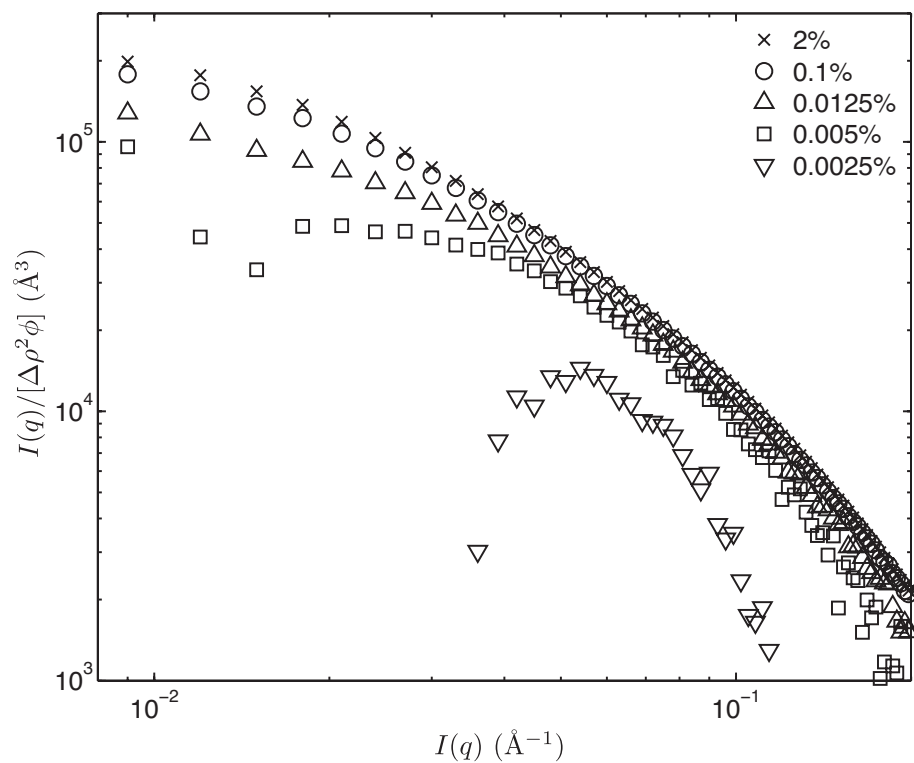


Figure 5.2: SAXS results of A1 asphaltenes in THF, normalized by scattering contrast and volume fraction.

dilute sample and a reference sample at a higher concentration superimpose over the moderate q -range when factored by χ/χ_{Ref} . This superposition indicates that there has not been a significant structural change in the asphaltene nanoaggregate shape and that only the dissociation of nanoaggregates has occurred. Coherent small-angle scattering was observed for K1 asphaltenes in toluene at the lowest concentration studied, 0.00125 vol. % (15 mg/L), indicating that aggregated asphaltene structures persist down to extremely dilute concentrations. However at this dilute of concentration, the statistical uncertainty of the SAXS intensities was too large to extract any quantitative structural parameters. The qualitative assessment of the synchrotron SAXS results above will be quantitatively expanded in the following sections.

5.3.2 Cluster Breakup: Shape-Independent Fits

Starting with analysis of the largest asphaltene structures, fractal clusters, the Zimm approximation was used to obtain shape independent size measurements for asphaltene fractal clusters as a function of concentration. The fit was performed to ensure that $R_g * q_{Max} < 2$ for all samples. Figures 5.3 and 5.4 show the R_g and M_W for the SAXS results. Size and molecular weight calculations were performed on all scattering samples, regardless if there was a loss of low- q scattering results due to background correction. For these sample, a linear region was still present on a plot of $1/I(q)$ vs q^2 and the fits satisfied the criteria that $R_g * q_{Max} < 2$. Additional discussion of the decision to include these samples will be provided momentarily. The q -range for performing the Zimm fits was approximately $0.01 < q < 0.05$.

All asphaltene types in all solvents tested showed a reduction in both the R_g and M_W when diluted below approximately 0.05 vol. %. The smallest R_g for all samples was 2 nm for K1 asphaltenes in 1-MN. Previously reported high temperature SANS experiments on asphaltenes in 1-MN also showed that the size decreased to 1-2 nm; however, in those experiments the temperature was elevated to 300 °C to

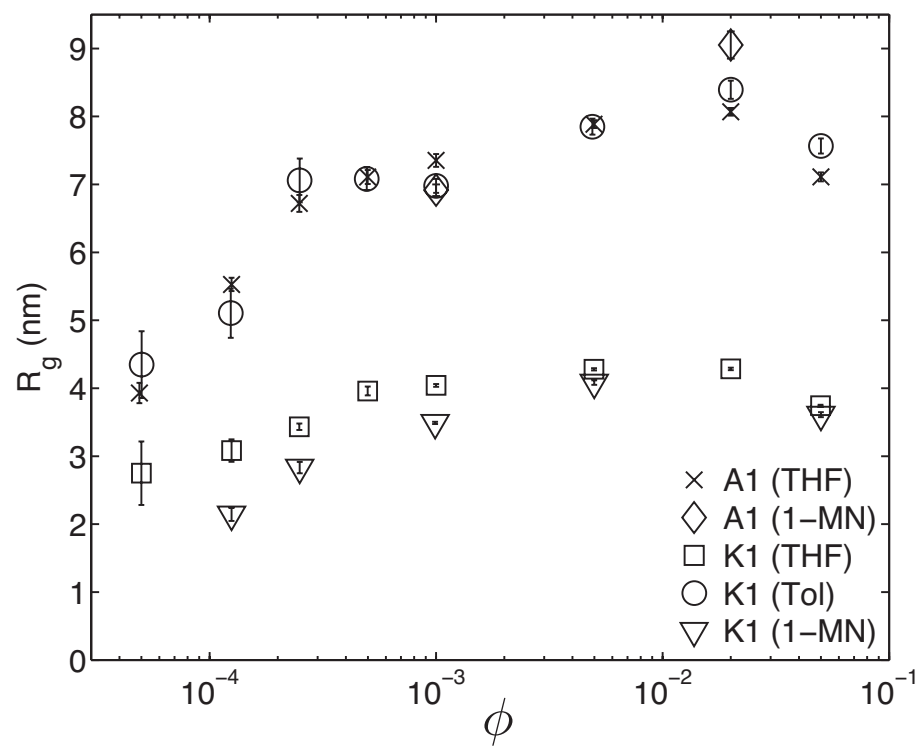


Figure 5.3: Radii of gyrations for the SAXS samples as obtained by the Zimm Approximation.

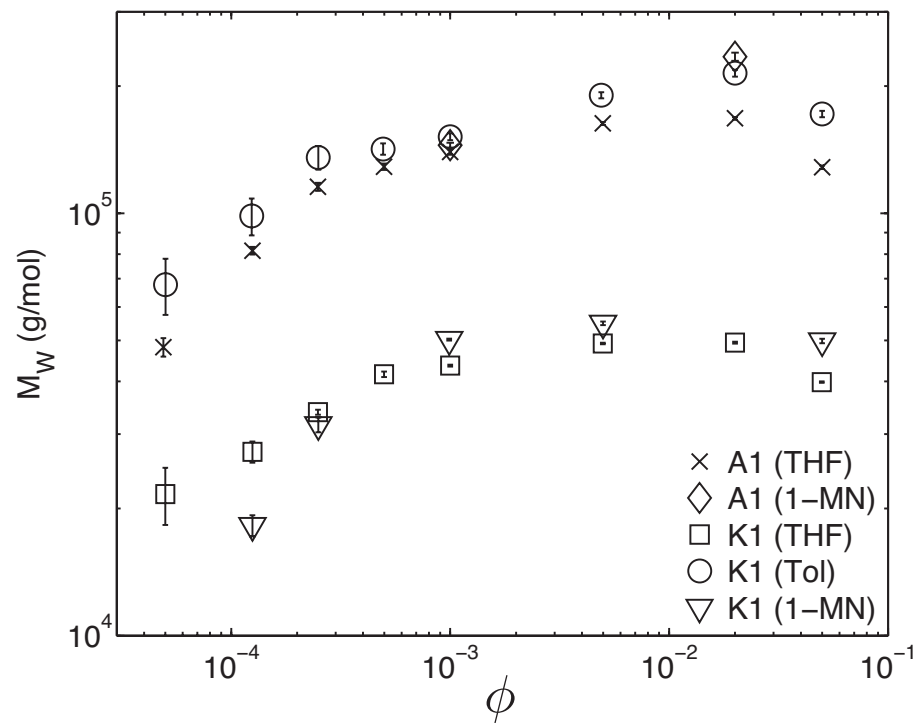


Figure 5.4: Molecular weights of the asphaltenes in the SAXS samples using the Zimm Approximation to calculate the zero-angle intensity.

observe the size decrease (*Thiyagarajan et al.*, 1995). It was also observed that the size of asphaltene clusters appeared to decrease for concentrations above 2 vol. % asphaltenes, which is believed to be the onset of asphaltene cluster-cluster positional correlation. The onset of cluster-cluster positional correlation above 2% asphaltenes matches previous investigations (*Roux et al.*, 2001; *Barré et al.*, 2008).

The fractal dimension of asphaltenes was extracted from a plot of M_W vs R_g and is shown in Figure 5.5. It was found that all samples were found to fall reasonably on a single line on a log-log plot. This finding reveals that the size reduction as a result of dilution conforms to the breakup of fractal clusters with a fractal dimension of 1.7 ± 0.1 . Therefore, *even at the most dilute asphaltene concentrations, the structural organization of asphaltene nanoaggregates into clusters is fractal*. Additionally, this fractal organization reveals that asphaltene nanoaggregates form clusters even at dilute concentrations, which may impede studies that try to isolate the structure or behavior of individual nanoaggregates. Omitting the results from scattering runs where a loss of low- q scattering intensity was observed did not change the observed fractal dimension from Figure 5.5. Consequently, it is believed that the Zimm fits on samples with low- q data loss are appropriate.

Eyssautier et al. recently reported that when asphaltene clusters decrease in size upon heating in vacuum residue, the size decrease also follows a fractal scaling law with a fractal dimension of 1.7 (*Eyssautier et al.*, 2012a), which draws parallels between the size decrease from dilution and heating. Therefore, it is proposed that the observed fractal dimension of asphaltene clusters is related to the fundamental interactions of asphaltene nanoaggregates due to their anisotropic shapes. Increasing the temperature or decreasing the asphaltene concentration does not modify the basic interactions between asphaltene nanoaggregates, but instead simply reduces the overall size of the fractal clusters. Additionally, the concentration range studied encompasses the both the proposed CMC (*Sheu et al.*, 1992; *Rogel et al.*, 2000; *Oh et al.*, 2004) and

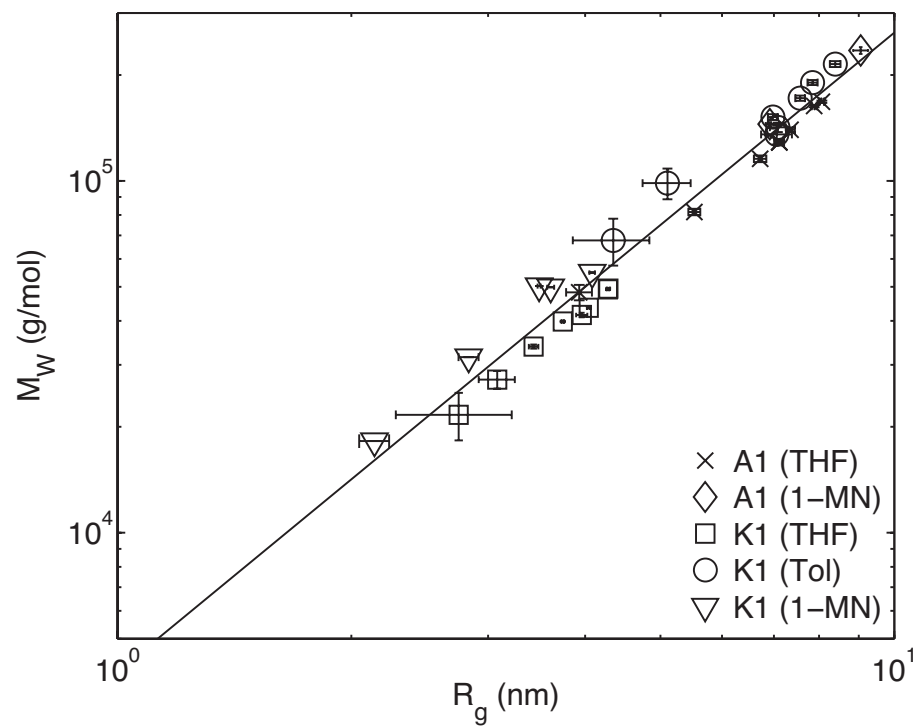


Figure 5.5: Plot of the molecular weight vs. radii of gyration to estimate the average fractal dimension. Solid line represents a fractal dimension of 1.7 ± 0.1 .

CCC (Goual *et al.*, 2011) without revealing any significant modification of behavior when crossing these critical thresholds. It is possible that the trends observed at the CMC and CCC may only involve a small sub fraction of asphaltenes and that the bulk behavior of asphaltenes is not significantly modified when transitioning across the CMC or CCC.

5.3.3 Local Structural Moieties

Figure 5.6 shows both SAXS and SANS results as a function of asphaltene concentration that are normalized by the mean scattering contrast for A1 asphaltenes in THF. It can be seen that for scattering vectors above approximately 0.05 \AA^{-1} the SAXS and SANS results deviate for both A1. This deviation is due to local compositional variations that exist between the aromatic core of asphaltenes and their alkyl shell (Barré *et al.*, 2009; Eyssautier *et al.*, 2011). It can be seen in Figure 5.6 that the deviation between SAXS and SANS results persists to concentrations as low as 0.0125 vol. %, indicating that the core-shell structure of asphaltene nanoaggregates is preserved down to low concentrations. Figure F.1 (D) in Appendix F shows a similar comparison between SAXS and SANS for K1 asphaltenes in toluene.

5.4 Asphaltene Nanoaggregate Dissociation

Equation (5.7) was applied to the scattering results of both asphaltene types (A1 and K1) in both THF and toluene to determine the relative fraction of asphaltenes that exist in nanoaggregate state compared to a reference, χ/χ_{Ref} . For all samples, a q -range was used to perform the calculation to reduce statistical uncertainty and was approximately $q > 0.05 \text{ \AA}^{-1}$. The q -range used was such that a scaling factor, χ/χ_{Ref} , could superimpose all scattering results, which ensured that there were minimal asphaltene structural differences between samples at different concentrations, which validated the assumptions for the derivation of Equation (5.7).

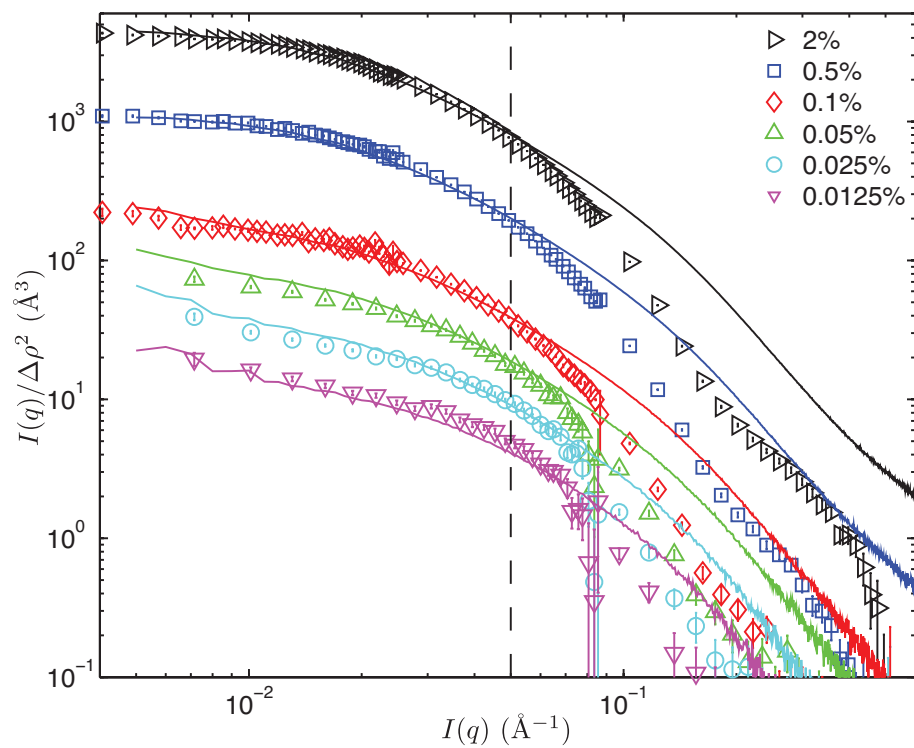


Figure 5.6: SANS (markers) and SAXS (solid lines) results of A1 asphaltenes in THF, normalized by scattering contrast. Scattering intensity decreases with decreasing asphaltene concentration and only one third of the measured SANS scattering intensities are shown to avoid cluttering the figure.

Both asphaltene types in both solvents showed similar behavior and dissociation was detected as high as 0.1 vol. % asphaltenes (1,200 mg/L). The dissociation of nanoaggregates was observed to be a gradual function of the asphaltene concentration and no sharp transition was observed. Figure 5.7 shows the relative fraction of asphaltenes in the nanoaggregate state, χ/χ_{Ref} , for A1 asphaltenes in THF and K1 asphaltenes in THF and toluene as a function of the volume fraction, ϕ_i . The 2 vol. % asphaltene sample was used as the reference, $I_{Ref}(q)$, for all combinations of asphaltenes and solvents. In addition, there are two lines plotted along with the results. The solid line represents the best fit of the two-state aggregation model (i.e., molecules to nanoaggregates) and the dashed line represents the two-state aggregation model with an arbitrarily high aggregation number of $n=50$. Both of these two lines will be discussed in detail shortly.

The results presented in Figure 5.7 provide the first estimate of the fraction of asphaltenes that exist in the nanoaggregate state as a function asphaltene concentration. Recall, it is unknown what fraction of the total asphaltenes form nanoaggregates, and the estimates in Figure 5.7 are only the relative fraction of asphaltenes in nanoaggregates compared to a reference sample. Asphaltene nanoaggregate dissociation appears to occur more readily at higher concentrations in THF compared to toluene, the standard solvent. The fraction of asphaltenes in the aggregated state could not be estimated for asphaltenes in 1-MN because of the low scattering contrast between asphaltenes and 1-MN due to the similar elemental composition and mass density.

As discussed earlier, the analysis assumes that molecular asphaltenes do not cause small-angle scattering. If this assumption is invalid, the estimates of the fraction of asphaltenes in the nanoaggregates state would be reduced because the scattering intensity of molecular asphaltenes would have to be eliminated from the measured scattering profiles. This elimination would reduce the scattering intensity to a greater

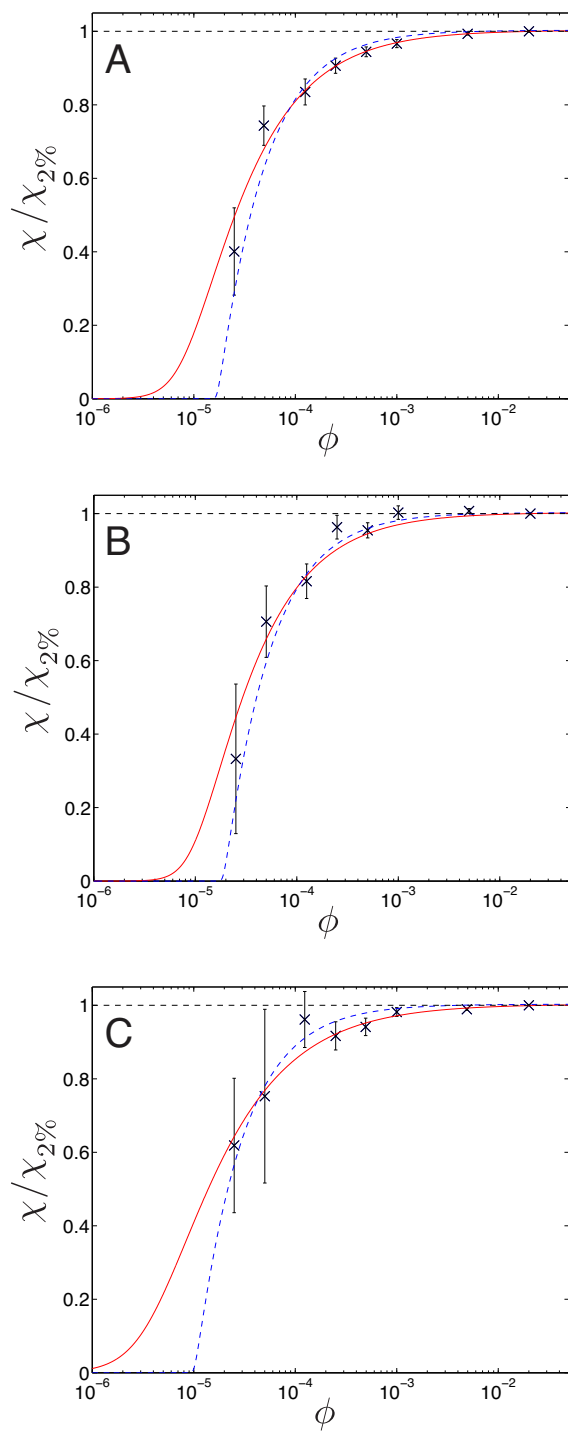


Figure 5.7: The relative fraction of asphaltenes in the nanoaggregate state for A1 in THF (A), K1 in THF (B), and K1 in toluene (C) as a function of the volume fraction. Solid line represents the best fit from two-state aggregation model and dashed line represents fit with a large aggregation number of $n=50$.

degree for samples with large relative amounts of molecular asphaltenes. Additionally, if molecular asphaltenes scatter, any small-angle scattering that persists at extremely low concentrations would represent scattering from asphaltene molecules and it is possible that nearly complete nanoaggregate dissociation occurs within the range of asphaltene concentrations studied. The presence of water also adds a potential complication to the analysis procedure. The THF and toluene solvents contained a maximum of 0.02 % water as per the manufacturer threshold. For the most dilute samples, this concentration is in excess of the asphaltene concentration and water has a scattering length density of $9.4 \times 10^{-6} \text{ \AA}^{-2}$, which is lower than that of asphaltenes for X-rays. Therefore, if water adsorbs on the surface of asphaltenes in a significant quantity, the contrast and scattering intensity will be lowered, mimicking the dissolution trends reported above. In order for water adsorption on the asphaltene surface to account for the apparent dissolution results in shown Figure 5.7, the volume of water adsorbed must be 3-4 times greater than that of the asphaltenes, and would consequently cause an increase in the R_g measurements by increasing the overall size of asphaltenes plus water. However, the measured size of the asphaltenes decreases (Figure 5.3) as a function of dilution, and suggests that the effect of water adsorption is negligible.

In the section, *Asphaltene Nanoaggregate Dissociation*, the fraction of asphaltenes in that exist in nanoaggregates was measured for the first time. As expected, a greater quantity of asphaltenes become molecularly dispersed as the asphaltene concentration decreases. This process was observed to occur gradually as a function of asphaltene concentration.

5.4.1 Two-State Aggregation Model Results

The solid lines in Figure 5.7 represent the best fit of the two-state aggregation model. It was found that a constant value of 0.997 for the tunable parameter, χ_{Ref} ,

resulted in quality linear regressions for all combinations of asphaltene and solvent types. For comparison with the experimental results, the model predictions were divided by χ_{Ref} . It should be noted, that in order to obtain quality linear regressions, some data points were not considered in the regression. For K1 asphaltenes in THF (Figure 5.7-B), these include the 0.1 and 0.5 vol. % samples because they predicted $\chi/\chi_{Ref} > 1$ and the 0.025 vol. % sample because it violated the trend of dissociation as a function of dilution. For K1 asphaltenes in toluene (Figure 5.7-C), the 0.0125 vol. % sample was removed from the analysis for the same reason. Minor deviations in the background level can cause significant error in the scattering intensity because of the low asphaltene concentrations, and is a likely cause of these samples being unsuitable for model fitting. Table 5.1 shows the best fitted values of the aggregation number, n , and the free energy change of association per asphaltene-asphaltene interaction, $\Delta G/(n-1)$, from the two-state aggregation model. The uncertainty estimates in Table 5.1 represent the statistical uncertainty of regression analysis and do not consider the uncertainty in the calculation of the fraction of asphaltenes in the aggregated state (shown in Figure 5.7).

Table 5.1: Two-state aggregation model results of the aggregation number and free energy of association, ΔG , which has been divided by $n-1$ to highlight the average free energy change of each individual asphaltene-asphaltene interaction. Results were calculated based on $\chi_{Ref} = 0.997$.

Type (Solvent)	n	$\Delta G_{Agg}/(n-1)$ (kJ/mol)
A1 (THF)	4.5 ± 1.1	-31.4 ± 1.5
K1 (THF)	5.2 ± 3.0	-31.1 ± 5.4
K1 (Toluene)	3.3 ± 1.3	-32.0 ± 5.2

The aggregation numbers calculated by the two-state aggregation model showed significant relative uncertainty, and the model was not sensitive to large changes in n . To illustrate this lack of sensitivity, the two-state model was applied to the results in Figure 5.7 but with an arbitrarily high aggregation number of 50. In this calculation, $\Delta G/(n-1)$ was held constant to the best fitted value, and the results are shown in

Figure 5.7 with dashed lines. Increasing the aggregation number to 50 resulted in a sharper increase of the fraction of asphaltenes in the aggregated state as a function of concentration. Low aggregation numbers result in a more gradual transition between the aggregated and molecular state as a function of asphaltene concentration. However, the two-state model was sensitive to the free energy change of association and does not need to be modified when changing the aggregation numbers, as evidenced by the reasonable fit obtained with $n=50$ and the relatively low uncertainty in the $\Delta G/(n - 1)$ calculations shown in Table 5.1.

The free energy of association calculated from the two-state model (approximately -31 kJ/mol) is in rough agreement with previous experimental (-25.3 kJ/mol) (*Lisitza et al.*, 2009) and simulated estimates for asphaltene aggregates (-19.1 kJ/mol) (*Sedghi et al.*, 2013). Additionally, *Sedghi et al.* found that the absolute value of the free energy change of trimerization (i.e., adding an additional molecule to an existing asphaltene-asphaltene association or dimer) was approximately 50% higher than the dimerization free energy change (*Sedghi et al.*, 2013). This observation revealed that the creation of a trimer from a dimer is more energetically favorable than the original dimer formation, and the trend would presumably continue for the formation of larger aggregates. The free energy change of association presented in Table 5.1 represent the average free energy change per interaction for an entire asphaltene nanoaggregate with up to 5.2 molecules. Therefore, as the scope of computational studies of asphaltene nanoaggregation increases to the point where free energy changes can be estimated for higher aggregation numbers, they might reveal similar values to what is estimated experimentally in this investigation.

Due to the uncertainty in the asphaltene molecular weight and structure, it is difficult to benchmark the calculated free energy of association of asphaltenes with other materials with known molecular structure. Free energies of association for ring systems with two to four aromatic rings in organic solvents have been previously

measured to be on the order of -5 to -18 kJ/mol (*Cubberley and Iverson, 2001; Meyer et al., 2003*). Given the large size of asphaltene molecules ($MW > 750$, 6-8 aromatic rings (*Mullins et al., 2012*)), a free energy of association of -31 kJ/mol is not immediately unreasonable. In addition, asphaltene fractal clusters have been observed to contain up to approximately 3200 molecules (*Hoepfner et al., 2013b*), and such large non-covalently bonded structures should only be expected to form with large free energies of association.

The aggregation numbers calculated from the model are in reasonable agreement with previous estimates (*Mullins et al., 2012; Yen et al., 1961; Andersen et al., 2005*). The results of Figure 5.5 reveal that estimates of the aggregation number based on the asphaltene hydrodynamic radius are likely influenced by asphaltene secondary clustering. *Eyssautier et al.* recently proposed a thin disc structure of asphaltene nanoaggregates in toluene that was based on detailed contrast variation SANS results that eliminated the influence of fractal clustering on the scattering results (*Eyssautier et al., 2011*). It was found that the shape of the aggregates that best fit the scattering results were 6.7 Å tall, which corresponded to aggregation numbers of approximately 3 (based on a 3.5 Å separation distance between asphaltene molecules), which is in excellent agreement to the aggregation numbers calculated with the two-state model. However, a precise estimate of the aggregation number of asphaltenes is likely unobtainable due to the probable polydispersity in aggregate sizes, and the differences between asphaltenes of different origins. Therefore predications of “moderate” aggregation numbers of 3-8 molecules should primarily serve as first level of validation for modeling or analysis approaches, and little significant emphasis on the exact numbers predicted. The measured free energies of association for asphaltenes could be used to benchmark molecular simulation investigations that study asphaltenes.

5.4.2 Local Molecular Ordering

Wide-angle X-ray scattering was used to investigate the local molecular structure of asphaltenes. Recall that the WAXS results are presented as if they were generated using a Cu K- α (1.5418 Å) benchtop X-ray source. Figure 5.8 shows the results for 5 vol. % A1 asphaltenes in THF and 5 vol. % K1 asphaltenes in THF, toluene, and 1-MN. It can be clearly seen in the K1 THF WAXS results that there are three distinct peaks. At approx. 17°, a shoulder can be seen in the K1 in toluene results and a subtle peak is observed in the K1 in 1-MN results. Each WAXS profile was fit with three Gaussian functions to obtain an estimate of the peak locations. The three Gaussian fits unfortunately result in a lack of uniqueness; however, the fits provide an estimate of the characteristic separation distances observed in the asphaltene WAXS signals. A constant background was used for the toluene and 1-MN results, while a linear background was necessary to fit the THF results. The three individual Gaussian functions, the background level, and the resulting best fit are also presented in Figure 5.8. Table 5.2 summarizes the separation distances, d , of the three peaks using Bragg's law: $\lambda = 2d\sin(\theta)$ (Bragg, 1913). Eyssautier *et al.* has recently reported WAXS results of asphaltenes in vacuum residue and showed that the [002] graphite peak is observed for asphaltenes in a liquid environment; however, it was not possible to background correct their WAXS results (Eyssautier *et al.*, 2012a). The results presented in Figure 5.8 represent the first detailed description of the local molecular structure in asphaltene aggregates in a liquid environment. The WAXS results in Figure 5.8, along with the free energy of association results from the two-state model could prove invaluable as validation for molecular dynamic simulations (Headen *et al.*, 2009a; Sedghi *et al.*, 2013).

From solid XRD, only two distinct scattering peaks at approximately 17° and 25° have been identified in the range $10 < 2\theta < 35$; however, three distinct peaks are visible in the liquid WAXS results. The three peaks are most easily identified for

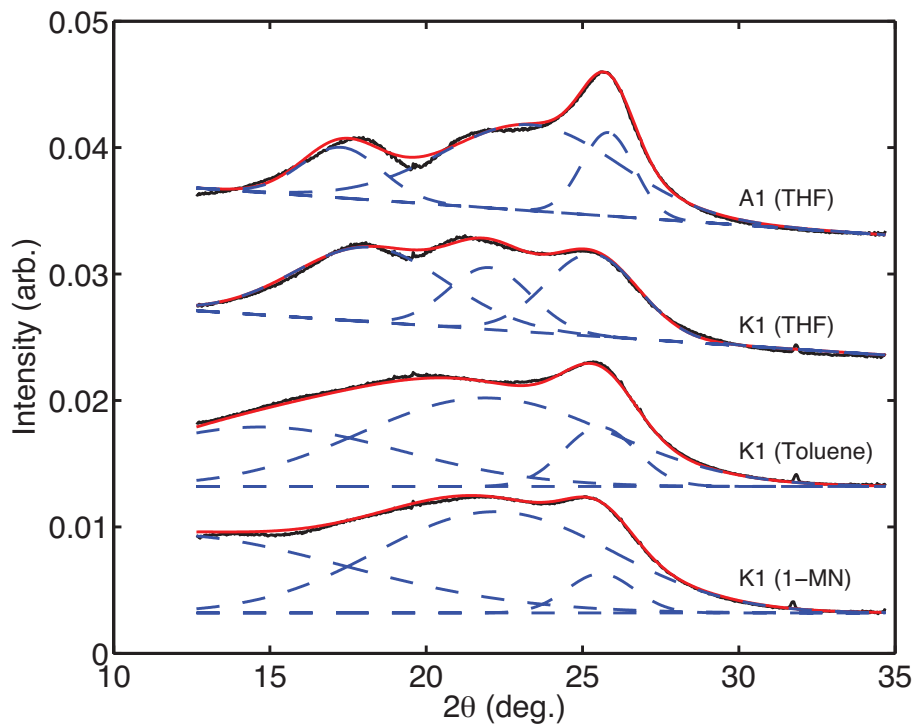


Figure 5.8: WAXS results for A1 asphaltenes in THF, K1 asphaltenes in toluene, THF, and 1-MN. All samples have an asphaltene concentration of 5 vol. %. Results are arbitrarily shifted for clarity. Dashed lines represent individual Gaussian fits and background level. Red line represents the combined fit of the three Gaussians and background.

Table 5.2: Summary of WAXS separation distances for the γ , $[002]'$, and $[002]$ peaks.

Type (Solvent)	d_{γ} (Å)	$d_{[002]}'}$ (Å)	$d_{[002]}$ (Å)
A1 (THF)	5.13	3.81	3.45
K1 (THF)	4.87	4.04	3.52
K1 (Toluene)	6.03	4.06	3.49
K1 (1-MN)	7.71	4.01	3.48

asphaltenes dispersed in THF. In THF, the three peak locations at approximately 17° , 22° , and 25° correspond to separation distances of approximately 5, 4, and 3.5 Å. The peak at 25° is most likely the [002] graphite peak as this location is nearly constant for all solvents and identical to solid XRD results (*Yen et al.*, 1961; *Andersen et al.*, 2005). Solid XRD results have been analyzed by characterizing the peak at 17° as the γ peak of alkyl organization. The γ peak is clearly visible for the samples dispersed in THF; however it is nearly indiscernible for asphaltenes dispersed in toluene and 1-MN. A general broadening and reduction in intensity is expected in the γ peak for asphaltenes in a liquid environment because of solvent penetration. The difference in the γ peak position between aromatic (toluene and 1-MN) and non-aromatic (THF) solvents suggests that *the solvation shell or conformation of the asphaltene aromatic shell is different with various classes of solvents*, and is motivation for future investigation.

The peak at 22° has not been previously identified, and due its broadness, it corresponds to a poorly defined separation distance. The separation distance of this peak is similar to the [002] graphite peak and may represent disordered packing of asphaltene aromatic cores, in contrast to the well-defined packing of the [002] peak. Consequently, the peak is labeled as the [002]' peak. Interestingly, the [002] and [002]' peaks are separate, as opposed to a single broad Bragg reflection. This observation reveals that there are two distinct and dominant separation distances between asphaltene molecules in a nanoaggregate, as opposed to a single broad continuum with a lone maximum. It should be noted that the XRD experiments performed by Anderson et al. (*Andersen et al.*, 2005) reveal an additional broad peak at approximately $2\theta = 45^\circ$, which is outside the range available in the WAXS results. It is possible that the broad peak at $2\theta = 45^\circ$ may slightly alter the peak positions reported in Table 5.2.

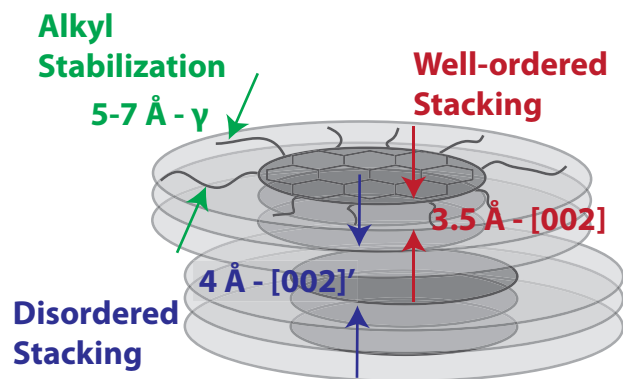


Figure 5.9: Schematic representation of the the three characteristic separation distances in an asphaltene nanoaggregate based on WAXS results of asphaltenes in a liquid environment.

5.5 Conclusions

A combination of X-ray and neutron scattering results on asphaltene solutions were used to investigate the breakup of fractal clusters, the dissociation of nanoaggregates, and the intermolecular spacings between asphaltene molecules. The breakup of clusters and the dissociation of nanoaggregates were induced by diluting asphaltene solutions with organic solvents. It was discovered that for asphaltene concentrations below approximately 0.05 vol. %, the fractal cluster size decreased with decreasing asphaltene concentration. This size decrease followed a fractal scaling law, which revealed that some degree of asphaltene clustering should be expected even at extremely dilute concentrations. At scattering vectors greater than approximately $0.5 q^{-1}$, the scattering intensity was used to estimate the fraction of asphaltenes in the aggregated vs. molecularly dispersed state. Both the breakup of fractal clusters and the dissociation of nanoaggregates are expected as asphaltenes are diluted following Le Chatlier's principle. Asphaltene nanoaggregates were observed at concentrations as low as 0.00125 vol. % (15 mg/L). These measurements of the fraction of asphaltenes in the aggregated vs. molecular state were fit to an aggregation model that provided the aggregation number and free energy change of association. Aggregation numbers

ranged from 3.3 to 5.2 and free energy changes were all approximately -31 kJ/mol per asphaltene-asphaltene interaction. Finally, solvent corrected WAXS results of asphaltene in a liquid environment provide a first of their kind description of the local molecular structure inside asphaltene nanoaggregates. Three correlation lengths were identified from the WAXS results, one additional than is observed in solid phase asphaltene diffraction measurements. Additionally, significant variations were observed in the WAXS results for asphaltenes in different solvents, revealing that the solvation shell around asphaltenes or asphaltene molecular conformation is different with various solvents. Both the WAXS and free energy change results could prove invaluable for benchmarking and validation of molecular dynamic simulations of asphaltenes.

CHAPTER VI

Conclusions and Future Work

6.1 General Conclusions

In this dissertation, several fundamental asphaltene behaviors were discovered from the macro to the micro scale. The general structure of the dissertation was to move from bulk/macroscopic behavior down to increasingly smaller length scales, beginning by investigating the macroscopic asphaltene precipitation and deposition process. Small-angle neutron scattering was then applied to similar systems as the first project, but SANS studied the incipient stages of the destabilization process on the nanometer length scale. The final project of the dissertation delved further into the asphaltene structure using a combination of SAXS, SANS and WAXS. The dissertation ultimately closed with a discussion of the smallest length scale investigated, the local molecular ordering of asphaltene molecules as revealed by WAXS. The overarching goal of this dissertation was to investigate basic and fundamental asphaltene behaviors, structures and mechanisms. This approach was believed to impact the most fields because asphaltenes are known to cause a number of petroleum production, transportation and processing concerns.

In Chapter II, a capillary deposition apparatus was used as both a tool to measure the asphaltene deposition rate and a general means of asphaltene instability detection. Stable asphaltenes are not known to deposit, and the presence of any deposit

indicates that a destabilization process has occurred. Deposits were detected by monitoring the differential pressure drop across a capillary where the solutions containing unstable asphaltenes were flown through at a constant volumetric flow rate. After the discovery of slow asphaltene precipitation kinetics, it was prudent to revisit asphaltene deposition at low precipitant concentrations. It was found that the capillary deposition apparatus is a robust tool that can be used to detect asphaltene instability at low precipitant concentrations. Asphaltene deposition was observed to also occur at these low precipitant concentrations, which revealed that there are no “onset” conditions where asphaltene deposition does or does not occur. In fact, Chapter II revealed that there can be deposition so long as there is a fraction of asphaltenes precipitating from a crude oil. All measured pressure drop profiles were found to collapse onto a single curve when the results were normalized by the concentration of insoluble asphaltenes and the mixture viscosity. This finding allowed for the asphaltene solubility to be directly estimated by the capillary deposition apparatus and revealed the importance of obtaining an accurate estimate of the asphaltene solubility in crude oil. This finding also opens the possibility of considering alternative approaches to study asphaltene deposition. If the primary driving force to induce deposition is the asphaltene solubility, then destabilizing asphaltenes with a temperature gradient may be a new and intriguing approach to investigating the deposition process. This idea is discussed in detail in the next section.

After it was discovered that asphaltenes can deposit at low heptane concentrations, small-angle neutron scattering was applied to similar oil-heptane mixtures in order to study the destabilization process on the nanometer length scale. The SANS results presented in Chapter IV are in excellent agreement with the capillary deposition work. The destabilization of asphaltenes from the same crude oil, Oil A, was studied by both capillary deposition and SANS in this dissertation. Both bodies of work detected the instability of asphaltenes at low heptane concentrations (i.e.,

significantly below the instantaneous onset point). In addition, SANS results from Chapter IV revealed an important finding about the fractal structure of asphaltenes. Through a novel background correction procedure, it was discovered that insoluble asphaltenes that are in the process of aggregating/precipitating are also fractal and possess a fractal dimension higher than that of the soluble asphaltenes. It is believed that the fundamental asphaltene-asphaltene binary interactions are modified when asphaltenes transition from soluble (and not able to precipitate) to insoluble (able to precipitate) upon the addition of heptane. Additionally, it is believed that obtaining a detailed understanding of the modification of interactions can provide the microscopic asphaltene destabilization mechanism (i.e., how heptane induced asphaltene precipitation). The fractal dimension change associated with asphaltene precipitation is an invaluable tool to validate destabilization mechanisms and inspires future simulation investigations, which will be discussed momentarily.

Finally, Chapter V expands on the investigations of the previous chapter and studies the structure of asphaltenes over several length scales, from large scale fractal clusters to intermolecular spacings. The primary motivation for this project was to better understand the aggregation/dissociation process of asphaltenes and their secondary fractal clustering. It was found that the asphaltene cluster size decreases as asphaltene mixtures are diluted with solvents. This size decrease was found to obey a fractal scaling law, which reveals that the asphaltene structure always has fractal characteristics. Additionally, some degree of secondary asphaltene clustering is to be expected regardless of the asphaltene concentration and it may not be possible to distinguish between the primary aggregation process (i.e., with well-defined aromatic stacking) from secondary fractal clustering. A future proposed project to better understand the fractal clustering process is discussed in great detail in the final section of this chapter. The SAXS results of Chapter V also demonstrated evidence of asphaltene aggregate dissociation, and the fraction of asphaltenes in the aggregated vs.

molecularly dispersed state was measured for the first time. These results were fit to a simplified aggregation model to elucidate the aggregation number and the free energy of association (found to be approximately -31 kJ/mol). As expected, the free energy of association is negative, as is true for all spontaneous processes. Finally, novel solvent-corrected WAXS results present the first picture of the local molecular structure of asphaltenes in a liquid environment. These results, along with the estimated free energy of association can likely be used to validate molecular and coarse grained simulations of asphaltene systems.

6.2 Further Asphaltene Deposition Studies

Asphaltene deposition can occur in the porous rock formations, wellbore, transportation lines, and refinery equipment (*Speight, 2007*). Obtaining an improved understanding the asphaltene destabilization and deposition mechanism will aid in the development of more accurate remediation techniques and simulation tools. Chapter II illustrated that the primary driving force for asphaltene deposition is the solubility of asphaltenes that have destabilized from a crude oil. In the laboratory, asphaltene deposition is most commonly induced by normal alkane addition (*Wang et al., 2004; Boek et al., 2010; Lawal et al., 2012*); however, a few investigations utilize pressure reduction of a HTHP oil (*Eskin et al., 2011a*). HTHP studies of asphaltenes are the most representative to real production environments, but are cost prohibitive. Precipitant addition to destabilize asphaltenes is not easily reversible; therefore, crude oil samples are only used once and small fluid volumes are used. In addition, the proper mixing of oil and precipitant is a serious concern (see Appendix C). In contrast to asphaltene deposition, the understanding of paraffin deposition (another serious concern in the transportation of crude oil) is relatively advanced. This advanced understanding is largely due to the easily reversible nature of temperature-induced paraffin deposition, which allows for the development of low-cost and high

productivity recirculating flow loops (*Singh et al.*, 2000; *Hoffmann and Amundsen*, 2010; *Huang et al.*, 2011).

Although temperature induced asphaltene destabilization is not commonly observed in production environments, it can still effectively be used to study the destabilization and deposition mechanism. A temperature-induced asphaltene destabilization flow-loop can explore a wide variety of experimental conditions (e.g., shear rates) and can be easily modeled due to symmetry. Asphaltenes destabilized by different approaches (i.e., pressure depletion vs precipitant addition) have been shown to possess different properties (*Klein et al.*, 2006c; *Deo and Parra*, 2012); however, there is no evidence to support that the different destabilization approaches result in different aggregation and deposition mechanisms. Before subtle differences in asphaltene properties are considered, the destabilization and deposition mechanism of asphaltenes needs to be well understood. In this potential future project, a high throughput asphaltene deposition flow-loop apparatus will be designed to study the asphaltene deposition and destabilization process.

6.2.1 Asphaltene Flow-Loop Design and Operation

Asphaltenes will be dispersed in a solvent (with or without low precipitant concentrations) and the solubility of the asphaltenes will be measured as a function of temperature. The deposition test section will be submerged in a cold bath to destabilize the asphaltenes. The asphaltene mixture will be continuously stirred and held at a constant temperature and then recirculated through the test section by a pump appropriate for the specified shear rate. The apparatus can be configured to simulate low shear rates that would be experienced in the porous rock formations in reservoirs and can simulate high shear rate environments as is experienced in the wellbore. Pressure depletion and precipitant induced asphaltene destabilization requires massive volumes of asphaltenes and oil to produce high shear rates. The recirculat-

ing flow-loop design will also allow for the testing of low deposition rates that are caused by the most unstable asphaltenes, which is the scenario experienced in the oil wellbore, without requiring massive amount of oil. The solubility and aggregation behavior of asphaltenes will be compared to the deposition rates. A schematic of the proposed flow-loop is shown in Figure 6.1.

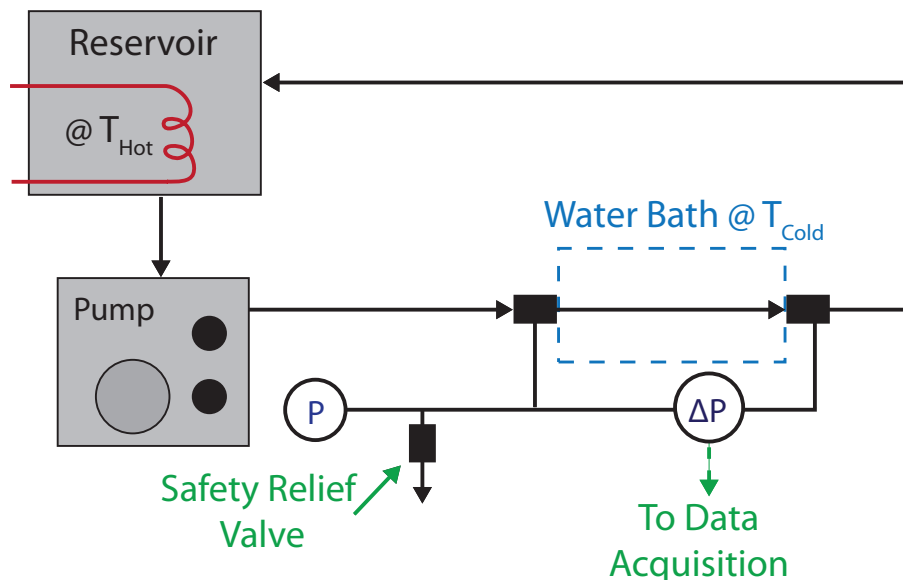


Figure 6.1: Proposed temperature-induced asphaltene deposition flow-loop apparatus.

6.2.2 Asphaltene Deposition Modeling

Current asphaltene deposition simulation tools utilize boundary conditions with tunable parameters that are fit to the deposition rate (*Eskin et al.*, 2011a; *Vargas et al.*, 2010; *Kurup et al.*, 2011, 2012). In other words, asphaltene deposition models attempt to predict the deposition of asphaltenes by fitting the model to match the deposition rates, and therefore cannot be relied on for predictive purposes. In this potential future project, transport modeling will be used to compare the measured to predicted deposition rates. The model will use independently obtained values for particle-particle and particle-wall collision efficiency from aggregation models (*Maq-*

bool et al., 2011a) or atomic force microscopy measurements (AFM) (*Wang et al.*, 2010; *Natarajan et al.*, 2011). Knowledge of the asphaltene-deposit binary interaction potential, which can be obtained from AFM measurements, will allow for estimation of the particle-deposit collision efficiency and the deposition rate using the interaction force boundary layer approximate (IFBLA) (*Eskin et al.*, 2011a; *Spielman and Friedlander*, 1974). Additionally, at high enough flow rates, the simplified deposition model presented in Appendix A can be easily applied to the results generated with this proposed apparatus.

6.3 Simulation and Measurement of Asphaltene Superstructures

Chapters IV and V, along with many previous scattering investigations, have supported the fractal structure of asphaltenes (*Bardon et al.*, 1996; *Fenistein and Barré*, 2001; *Barré et al.*, 2008; *Eyssautier et al.*, 2011); however, simulation of the asphaltene structure has been limited to the interactions of only a few asphaltene molecules (*Headen et al.*, 2009a) or amorphous structures (*Ortega-Rodriguez et al.*, 2003). Fully atomistic molecular dynamics simulations have shown the molecular interactions of asphaltenes (*Headen et al.*, 2009a), but the size and time length of these simulations is limited and cannot be expanded to the scale of the fractal clusters. The results in Chapter IV suggest that asphaltenes may be best viewed as self-assembling anisotropic molecules or aggregates (*Glotzer and Solomon*, 2007) that interact to form fractal clusters. As such, simulation tools that have been developed to study the nano and colloidal scale self-assembly will provide critical insight into the assembly of asphaltenes in fractal superstructures. The fractal clusters measured in Chapter IV were large enough to contain 400 nanoaggregates (approx. 3200 molecules), which is too large to consider performing fully atomistic simulations. As such, the most

appropriate approach to study the association of fractal clusters is to use asphaltene aggregate analogs and coarse grained simulations.

Additionally, the results in Chapter IV reveal that the fractal dimension of the asphaltene clusters increases when transitioning from soluble to insoluble. Figure 4.12 presents a possible mechanism for the formation of the denser insoluble asphaltene clusters where there is an increase of side-side asphaltene interactions. The proposed simulations will be able to test this hypothesis by controlling the shape of and interaction potentials between asphaltene nanoaggregates. This potential future project will focus on determining the possible interaction forces and structure that asphaltene nanoaggregates possess in order to generate the fractal structures that have been observed by scattering investigations.

6.3.1 Simulation Tools and Validation

Course-grained molecular dynamics (MD) simulations with implicit solvent (i.e., brownian dynamics) will be performed with core-shell thin discs for asphaltene nanoaggregate analogs using a software package optimized to run on graphical processor units (GPUs) to achieve large scale and computationally efficient simulations (e.g., LAMMPS (*Trott et al.*, 2010) or HOOMD (*Anderson et al.*, 2008).) Equilibrium MD simulations will be performed to assess the structure of asphaltene fractal clusters and Fourier transform on the equilibrium structure will be compared to SAXS results to validate the simulations and to provide a more complete picture of asphaltene structure. Non-equilibrium MD simulations with the SLLOD procedure (*Hess*, 2002) can also be used to better understand the intrinsic viscosity of the asphaltenes clusters for additional validation/insight.

The first step in this proposed project is to coarse grain an asphaltene nanoaggregate into a collection of core and shell spherical entities (see Figure 6.2 A). There will be three binary interactions: core-shell, core-core and shell-shell interactions (see

Figure 6.2 B). Finally, the individual parameters for the binary interaction potentials ($U(r)$) will need to be defined for each interaction (see Figure 6.2 C). It is unknown what course graining scheme or structure will succeed in replicating the observed asphaltene structure in the simulations. Therefore, there are several potential structural variables that can be modified in order to determine the ideal course grained asphaltene nanoaggregate structure. These include: size polydispersity, core-shell ratio, aspect ratio and interaction strength. A schematic representation of the coarse graining procedure is shown in Figure 6.2 and a visual representation of the potential structural variables is shown in Figure 6.3.

In addition, the simulation of asphaltene structures will assist in the analysis of scattering results. The standard procedure for interpreting scattering results is to guess a structure, and then perform a Fourier transform to calculate the scattering profile. This procedure cannot be accurately used for highly anisotropic, polydisperse, concentrated and interacting systems (all characteristics of asphaltenes and heavy oil systems). As such, the generation of asphaltene fractal structures can be used as a less biased and more accurate approach to determine asphaltene structural details. Once an asphaltene structure is validated by comparison to scattering results, the system conditions can be altered to predict asphaltene behavior.

This proposed project has the potential to provide an improved understanding of the nanostructure of asphaltenes and will provide validation for the proposed asphaltene destabilization mechanism (Figure 4.12). If this mechanism is validated, it will provide important direction into the design of asphaltene chemical inhibitors to prevent asphaltene deposition. In addition, understanding the destabilization mechanism of asphaltenes will provide new thermodynamic modeling opportunities. In oils with high asphaltene concentrations, the structure of the asphaltene will influence the ability of the oil to flow through narrow pores. The asphaltene structure can potentially influence the ability for solvents to diffuse into the pores (for solvent ex-

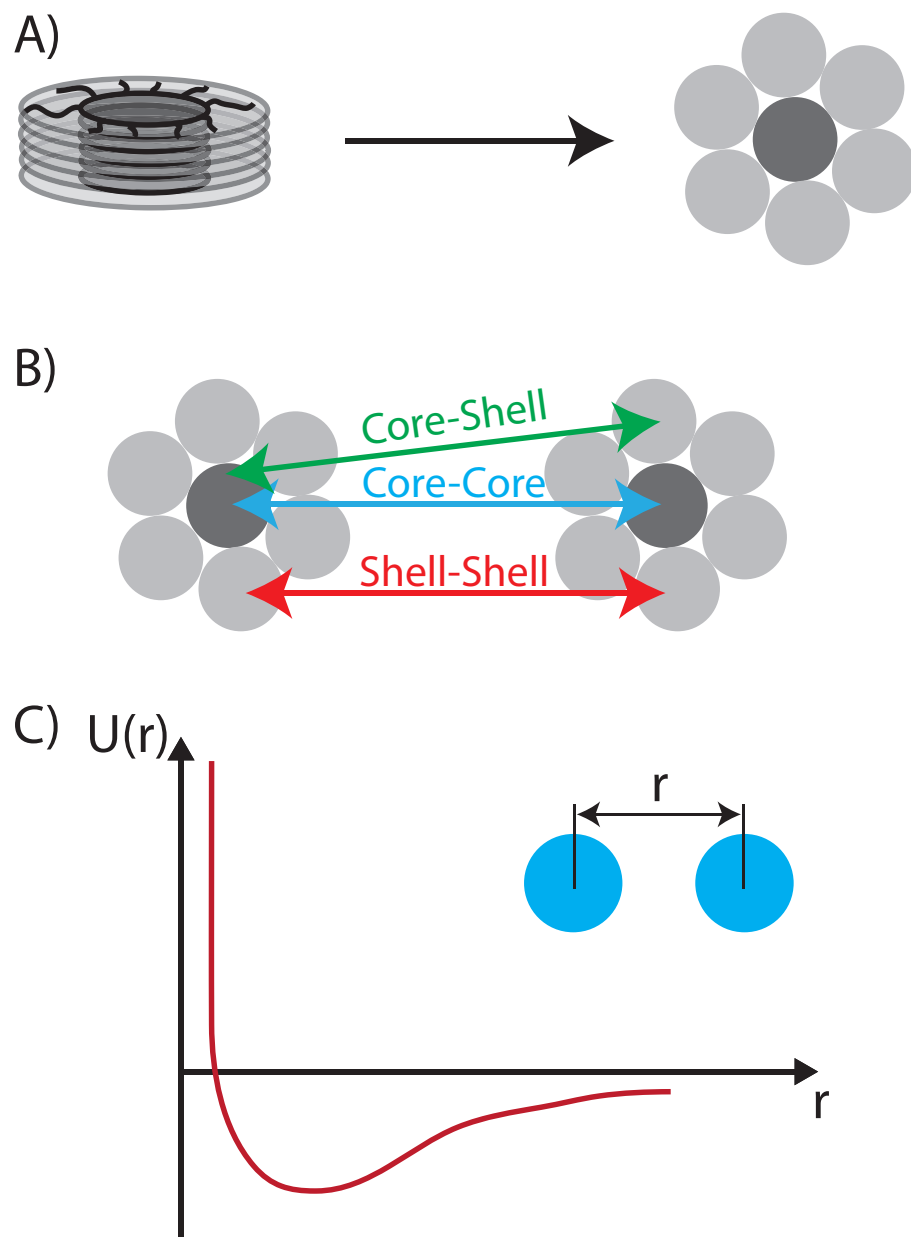


Figure 6.2: Schematic representation of the asphaltene nanoaggregate coarse graining procedure. A) Representation of a core-shell asphaltene nanoaggregate as a collection of spherical entities. B) Three possible binary interaction parameters between the two coarse grained type particles: core and shell. C) Qualitative representation of the interaction potential for binary interactions.

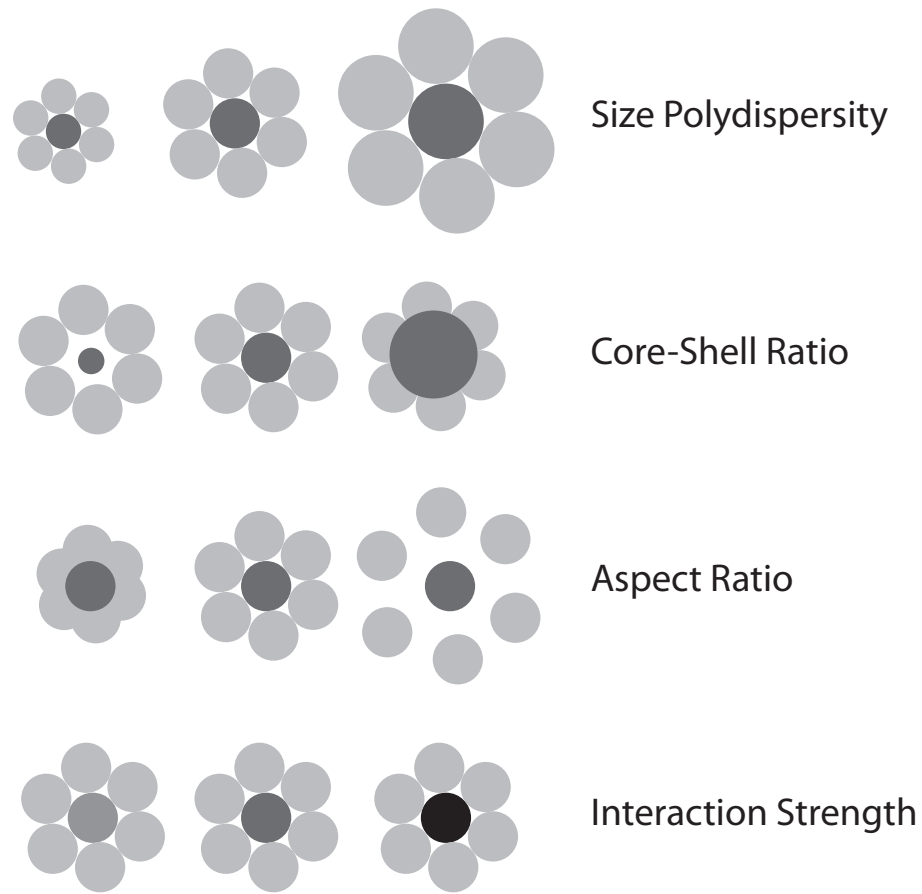


Figure 6.3: Potential structural variables in coarse graining procedure.

traction or enhanced oil recovery) or imbibition with water for secondary and tertiary oil recovery. The dissociation of asphaltene clusters at high temperature has been observed by scattering and can reduce the viscosity significantly (*Thiyagarajan et al.*, 1995; *Luo and Gu*, 2007), which can also be simulated. Additionally, the influence of high shear rates on the structure and viscosity of asphaltene systems can also be investigated.

6.4 Asphaltene Clustering Population Balance Model

The observed cluster size decrease during asphaltene dilution, shown in Chapter V, can likely be described by similar (but expanded) equilibrium relationships as presented in Chapter V with the two-state aggregation model. However in this proposed future project, a continuous size distribution will be considered where the aggregation process occurs only by an exchange of asphaltene nanoaggregates (monomers). In such a population balance model, the clustering process for clusters of arbitrary size can be described by the general relationship (for $i > 1$):



where n_1 is a monomer/nanoaggregate, n_{i-1} is a cluster with $i - 1$ monomers, and n_i is a cluster with i nanoaggregates. If M represents the maximum cluster aggregation number (i.e., number of nanoaggregates in the largest cluster), then $2 < i < M$. The general expression for chemical equilibrium for the clustering reaction above, assuming ideal mixtures, is (*Sandler*, 2006):

$$K_{Eq}^i = \frac{x_i}{x_1 x_{i-1}} = C_S \frac{C_i}{C_1 C_{i-1}} \quad (6.2)$$

where x represents the mole fraction, C represents the molar concentration, and C_S represents the total molar concentration of the mixture (approximately equivalent to

solvent molar concentration for dilute asphaltene solutions). The equilibrium constant is independent of concentration and the qualitative behavior of the system can be described by the equilibrium relationship above. Regardless of the degree of clustering in the system, the concentration of asphaltene nanoaggregates in the system, C_{Total} , must be constant:

$$C_{Total} = \sum_{i=1}^M iC_i \quad (6.3)$$

When an asphaltene mixture is diluted, C_{Total} decreases. The extent of reaction, E , is a term used to describe the progression of a chemical reaction (*Sandler, 2006*). The concentrations of reactants and products in a single chemical reaction can all be related by a single extent of reaction. For the monomer exchange population balance model with a maximum cluster aggregation number of M , there are $M - 1$ extents of reactions that will full define the concentration distribution of the system. Each cluster, except the monomer can only be involved in two reactions:

1. $n_1 + n_{i-1} \longleftrightarrow n_i$
2. $n_1 + n_i \longleftrightarrow n_{i+1}$

The extent of reaction for item 1 above will be E_i and for item 2 will be E_{i+1} . Assuming a initial condition of only monomers, $C_{Total} = C_1$, the concentration of species C_i (for $1 < i < M$) can be described by the following relation:

$$C_i = E_i - E_{i+1} \quad (6.4)$$

The monomer concentration requires additional consideration, because two monomers are consumed to form a dimer cluster and the monomer is involved in all reaction ($M - 1$ total reactions). The monomer concentration, C_1 , can be described in terms of the extents of reactions by the following relationship:

$$C_i = C_{Total} - E_2 - \sum_{i=2}^M E_i \quad (6.5)$$

The maximum cluster size, n_M , cannot aggregate further and its concentration is described by:

$$C_M = E_M \quad (6.6)$$

The general equilibrium expression can now be rewritten in terms of the extent of reaction, E :

$$K_{Eq}^i = C_S \frac{(E_i - E_{i+1})}{(C_1^0 - E_2 - \sum_{i=2}^M E_i)(E_{i-1} - E_i)} \quad (6.7)$$

For uniformity, the extents of reaction will be normalized by the total molar concentration of asphaltene molecules, C_{Total} :

$$K_{Eq}^i = \frac{C_S}{C_T} \frac{(\bar{E}_i - \bar{E}_{i+1})}{(1 - \bar{E}_2 - \sum_{i=2}^M \bar{E}_i)(\bar{E}_{i-1} - \bar{E}_i)} \quad (6.8)$$

where $\bar{E}_i = E_i/C_{Total}$. Normalizing the extent of reaction with C_{Total} , forces the criteria of $E_2 < 0.5$ and $\sum_{i=2}^M E_i < 1$. Additionally, to satisfy the criteria that all $K_{Eq} > 0$, $E_i > E_{i+1}$. The equilibrium relation for the largest cluster is:

$$K_{Eq}^M = \frac{C_S}{C_T} \frac{\bar{E}_i}{(1 - \bar{E}_2 - \sum_{i=2}^M \bar{E}_i)(\bar{E}_{i-1} - \bar{E}_i)} \quad (6.9)$$

Decreasing the volume fraction of asphaltenes will decrease C_{Total} and the individual extents of reactions, E_i , must alter to satisfy a constant K_{Eq}^i . It can be shown that decreasing C_{Total} must result in asphaltene cluster dissociation. If C_{Total} decreases then the quantity C_S/C_{Total} will increase. In order to maintain a constant K_{Eq}^i the remaining terms in the equilibrium expression must have an overall net decrease. This is most clearly illustrated when considering the relationship for K_{Eq}^M . Adding all

clustering reactions together yields the following relationships:



$$K_{Eq}^{M*} = C_S^{M-1} \frac{C_M}{C_1^M} = \frac{C_S^{M-1}}{C_T} \frac{\bar{E}_M}{(1 - \bar{E}_2 - \sum_{i=2}^M \bar{E}_i)^M} \quad (6.11)$$

A decrease in C_{Total} in the above equilibrium relationship can be counteracted by two possible effects:

1. Decrease in E_M ; a dissociative process.
2. Increase in $(1 - \bar{E}_2 - \sum_{i=2}^M \bar{E}_i)$, accomplished by a net decrease in $(\bar{E}_2 + \sum_{i=2}^M \bar{E}_i)$; also a dissociative process.

Therefore, once asphaltene clusters are in the dilute regime and are non-interacting (except for monomer exchange), further dilution will only decrease the size of clusters, as observed in Chapter V. This behavior is to be expected in order for the dissociation process to follow Le Chatelier's principle.

In order to validate the cluster population balance model, the equilibrium constants for each reaction need to be estimated. Additionally, for the clustering model to predict a finite size distribution, there must be a dissociative process occurring. The purpose of the model is to predict the *equilibrium* cluster size distribution, not the *kinetic* aggregation process. It is proposed to estimate the equilibrium constants through a competition of forward (clustering) and reverse (dissociation) rates. The forward rate of clustering, $R_{Forward}^i$, and reverse rate, $R_{Reverse}^i$, are provided by:

$$R_{Forward}^i = k_{Forward}^i C_1 C_{i-1} \quad (6.12)$$

$$R_{Reverse}^i = k_{Reverse}^i C_i \quad (6.13)$$

where $k_{Forward}^i$ is provided by the Smoluchowski collision kernel (*Maqbool et al.*, 2011a):

$$k_{Forward}^i = \frac{2RT}{3\mu} \frac{(R_{g,1} + R_{g,i-1})^2}{R_{g,1}R_{g,i-1}} \quad (6.14)$$

where R_g represents the cluster radius of gyration, R is the ideal gas constant, T is the temperature, and μ is the solvent viscosity. The rate constant for the reverse (dissociation) process ($k_{Reverse}^i$) requires additional consideration. As a first approximation, $k_{Reverse}^i$ will be represented by the following relationship:

$$k_{Reverse}^i = k_{Reverse}^0 i^\alpha \quad (6.15)$$

where $k_{Reverse}^0$ and α are constant but tunable parameters for the reversible rate constant. Recall that i represents the number of nanoaggregates in a cluster. The form of $k_{Reverse}^0$ allows for the rate of dissociation to increase as the clusters grow in size by modifying α . This approach is reasonable because as clusters grow in size, there are more nanoaggregates and a higher probability that a nanoaggregate will leave over an arbitrary time period due to a thermal fluctuation in the mixture.

Using the forward and reverse rates, the equilibrium constant can be calculated by (*Sandler*, 2006):

$$K_{Eq}^i = C_S \frac{R_{Forward}^i}{R_{Reverse}^i} \quad (6.16)$$

The tunable parameters, $k_{Reverse}^0$ and α , can be modified to obtain size distributions for asphaltene cluster sizes. The model results can be directly compared to scattering results through calculation of the weight-averaged molecular weight, which was calculated for all scattering samples in Chapter V. Once validated, the model will provide insight in the process of asphaltene superstructure formation.

APPENDICES

APPENDIX A

Theoretical Analysis on the Dynamics of Deposit Buildup for Chapter II

In order to determine the driving force for asphaltene deposition, the experimental results from Chapter II of pressure vs. time will be related to a mass flux of asphaltenes depositing on the capillary wall. We begin by differentiating the Hagen-Poiseuille equation with respect to time for a region with uniform deposition, noting that only ΔP and r are a function of time:

$$\Delta P = \frac{8\mu LQ}{\pi r^4} \quad (\text{A.1})$$

$$\frac{\partial \Delta P}{\partial t} = \frac{-32\mu LQ}{\pi r^5} \frac{\partial r}{\partial t} \quad (\text{A.2})$$

where μ is the viscosity, L is the length of the section where deposition occurs and Q is the volumetric flow rate. The rate of change in the volume of the deposit, $V_{Dep} = \pi L(R^2 - r^2)$, over time can be obtained by differentiating an expression of the volume of an annulus:

$$\frac{\partial V_{Dep}}{\partial t} = -2\pi r L \frac{\partial r}{\partial t} \quad (\text{A.3})$$

As a first approximation, the asphaltene deposition process at the oil-deposit interface will be modeled as first order asphaltene surface reaction with respect to the mass concentration of unstable asphaltenes at the surface. The capillary will be modeled as a differential reactor, i.e., no concentration gradients, with the concentration equal that at the inlet. In order for this approximation to be valid, the capture efficiency, or fraction of asphaltenes depositing compared to the total insoluble fraction must be small to ensure that the concentration does not vary significantly throughout the system. The Brownian motion of asphaltenes colliding with the wall has been previously modeled as a first order surface reaction for the asphaltene deposition process (*Eskin et al.*, 2011b). Under these conditions, the flux of asphaltenes into the deposit, J_{Dep} (kg/m^2s) will be the rate of increase in the volume of the deposit and is given by:

$$J_{Dep} = kC_A^o = \frac{\partial V_{Dep}}{\partial t} \frac{d_{Asph}}{2\pi rL} \quad (A.4)$$

where k (m/s) is the surface reaction rate constant, C_A^o is the concentration of asphaltenes that have been destabilized from the oil and are in the process of precipitating/aggregating, and d_{Asph} is the mass density of asphaltenes, which is also assumed to be the density of the deposit. Substituting $\frac{\partial V_{Dep}}{\partial t}$ into Equation (A.4) and rearranging, the rate of deposit growth is given by the following relationship:

$$\frac{\partial r}{\partial t} = \frac{-kC_A^o}{d_{Asph}} \quad (A.5)$$

For convenience, the concentration of destabilized asphaltenes will be rewritten as a mass fraction of the oil:

$$C_A^o = d_{Oil}\phi_{Oil}F \quad (A.6)$$

where d_{Oil} is the mass density of the crude oil (inclusive of asphaltenes), ϕ_{Oil} is the

volume fraction of crude oil in the deposition experiment, and F is the mass fraction of unstable asphaltene precipitating from the crude oil (g asphaltene per g crude oil).

Combing equations, the rate of pressure drop increase can be related to the concentration of destabilized asphaltene at the oil-deposit interface:

$$\frac{\partial \Delta P}{\partial t} = \frac{32\mu L Q}{\pi d_{Asph} r^5} (k d_{Oil} \phi_{Oil} F) \quad (A.7)$$

A particle-deposit collision efficiency term, β_{P-D} , is defined as the fraction of asphaltene-asphaltene collisions that result in adhesion compared to the total number of collisions. It is used as an approximation for reaction limited aggregation/deposition by scaling the maximum theoretical flux for a diffusion limited process. The boundary condition as derived by Eskin *et al.* (Eskin *et al.*, 2011b) will be used to calculate the asphaltene-deposit collision efficiency once the deposition flux is determined from the capillary deposition experiments:

$$\beta_{P-D} = \frac{2J_{Dep}}{\sum N_i m_i u_i} \quad (A.8)$$

where β_{P-D} is the collision efficiency (independent of particle size, shown to be true for the colloidal deposition of latex spheres (Elimelech and O'Melia, 1990)), m is the mass of particle, N is the number concentration, and u is the most probable velocity induced by Brownian fluctuations. The β_{P-D} value is calculated by summing over all particle sizes in the system. The number concentration and mass of asphaltene aggregates as a function of size can be determined by the geometric population balance model written by Maqbool *et al.* (Maqbool *et al.*, 2011a).

It was previously found that the particle-particle collision efficiency, β_{P-P} , is a function of the heptane concentration for batch asphaltene aggregation modeling (Maqbool *et al.*, 2011a). As a first approximation, the particle-deposit collision

efficiency, β_{P-D} , will be set as a constant value and the surface reaction rate will be independent of heptane concentration. The surface reaction rate will be estimated at a moderate heptane concentration and then used for all other deposition runs. If the collision efficiency decreases with heptane concentration, the analysis procedure described above will over predict the deposition at low heptane volume fractions.

All of the constant parameters can combined be into a new term, k' , called the deposition proportionality constant that relates the insoluble asphaltene fraction to the slope of the pressure drop profile:

$$\frac{\partial \Delta P}{\partial t} = k' \mu \phi_{Oil} F \quad (\text{A.9})$$

where:

$$k' = \frac{32LQd_{Oil}}{\pi d_{Asph} r^5} k \quad (\text{A.10})$$

For crude oils with known asphaltene solubility, the value for k' in Equation (A.9) can be determined from the slope of the pressure vs. time in a capillary deposition experiment. The relationship between solubility and deposition rate can be used to predict either the deposition or solubility depending on the available experimental data. For a thin deposit, the pressure drop from the Hagen-Poiseuille equation can be expanded in a Taylor series to show the increase in pressure drop is linearly related to the reduction in radius (*Wang et al.*, 2004), thus $\partial \Delta P / \partial t$ will be approximated by a straight line in this region. The linear approximation does not only apply to the initial deposit that is formed, but it can also be applied to a deposit that has already formed and can be used to model the growth of a new thin deposit.

For the differential reactor approximation to be accurate, the capture efficiency must be small. The instantaneous capture efficiency, χ , can be calculated by comparing the rate of asphaltenes depositing to the rate of asphaltenes entering the capillary:

$$\chi = \frac{d_{Dep} \frac{\partial V_{Dep}}{\partial t}}{C_A^o Q} = \left(\frac{d_{Dep} \pi^2 r^6}{16 d_{Oil} \phi_{Oil} F \mu Q^2} \right) \frac{\partial \Delta P}{\partial t} \quad (\text{A.11})$$

The capture efficiency is a strong function of the capillary radius, with the greatest capture efficiency occurring when the radius is the least constricted at the start of the experiment for a given $\frac{\partial \Delta P}{\partial t}$. As the deposit grows and the radius and surface area available for deposition is reduced, the system will approach the ideal case of a differential reactor. Any deviation from differential reactor conditions will introduce uncertainty into the calculated value for the surface reaction constant, k . However, even with uncertainty, an order of magnitude estimate for k can still be obtained. Even if the error introduced by the differential reactor approximation is largely independent of the heptane concentration, the analysis procedure will still predict the relative trends of the asphaltene deposition process.

The slope of the pressure drop profile for the 35% heptane in Oil A deposition run was used as the reference experiment to determine the deposition proportionality constant, k' , that relates the solubility to the deposition. For an order of magnitude estimate of the surface reaction rate constant, k , calculations assume that the deposit is uniform axially and occurring only in the first 2 inches of the capillary. To assess the accuracy of the differential reactor approximation, the instantaneous collection efficiency was calculated using Equation (A.11). Using the initial capillary radius and the slope of the initial deposit formation (3.1 psi/hr) in the 35% heptane experiment as the base case, the instantaneous collection efficiency was calculated to be 0.26 for the first deposit that forms. This calculation reveals that the accuracy of the differential reactor approximation can be increased by increasing the flow rate of oil and heptane through the capillary deposition apparatus.

To determine the surface reaction rate constant, k , the initial slope of the 35% heptane in Oil A experiment (3.1 psi/hr), shown in Figure 2.8, was used for calculations. At 35% heptane and at 60°C the fraction precipitating, F , is 0.026 ± 0.001 , and

the viscosity was estimated by logarithmic averaging. Substituting all these values in to Equation (A.9) resulting in a calculated surface reaction rate constant of $9.3 \times 10^{-6} \text{ m/s}$.

Utilizing the particle size distribution calculated at the capillary inlet using the population balance model (Figure 2.11) and Equation (A.8), the particle-deposit collision efficiency, β_{P-D} , was calculated to be 7.05×10^{-6} , a value that is on the same order of magnitude with previous estimations for asphaltene-asphaltene and asphaltene-deposit collision efficiencies (*Maqbool et al.*, 2011a; *Eskin et al.*, 2011b). Recall from Chapter II that particle-particle collision efficiency, β_{P-P} , measured using the geometric population balance was found to be 1.79×10^{-5} , larger than the particle-deposit value. *Eskin et al.* also found a larger particle-particle collision efficiency of 5×10^{-5} , compared to the particle-deposit efficiency value of 1×10^{-5} (*Eskin et al.*, 2011b). *Maqbool et al.* found particle-particle collision efficiency values ranging from 3×10^{-6} to 2×10^{-5} (*Maqbool et al.*, 2011a; *Eskin et al.*, 2011b). Additionally, the collision efficiency values for particle-particle and particle-deposit collisions estimated in this study are similar to value obtained by pressure depletion deposition experiments by *Eskin et al.*, suggesting that the mechanism for live oil vs. precipitant induced asphaltene deposition is the similar. The calculation parameters are summarized in Table A.1.

Table A.1: Summary of key parameters for surface reaction rate constant calculation.

Parameter	Value
Capillary Radius (μm)	125
Capillary Length (m)	0.05
Surface Reaction Constant, k (m/s)	9.3×10^{-6}
Particle-Particle Collision Efficiency, β_{P-P}	1.79×10^{-5}
Particle-Deposit Collision Efficiency, β_{P-D}	7.05×10^{-6}

APPENDIX B

Capillary Deposition Apparatus Standard Operating Procedure for Chapter II

Obtaining accurate and reproducible results from the capillary deposition apparatus requires strict adherence to the standard operating procedure (SOP) outlined below. The procedure has been designed to prevent asphaltene destabilization by eliminating any oil-precipitant contact prior to when the system is at the experimental flow rate, temperature and back-pressure. If the experiment is simply started by flowing oil and precipitant initially at the desired flow rate there would be extensive contact between the two fluids and virtually no flow as the back pressure is established. The SOP is divided into subtasks in order to simplify the procedure.

Performing a Deposition Experiment

1. Turn on water bath to desired temperature
 - Do not begin experiment until set temperature is reached
2. Turn on computer
3. Start up the data acquisition (DAQ) program
4. Set frequency to 0.05, set number of points to be maximum
5. Record start time and start DAQ
6. Ensure the outlet of the system is at the same level as the oil canister

7. Allow 5 minutes of a steady ΔP measurement to be made to get a baseline offset for ΔP
8. Prefill the system with oil (See below)
9. Once the system has been prefilled, start pumps at the experimental flow rate
10. Oil will likely be in the precipitant line after prefilling, this is normal and allow this to happen
 - Always keep 1-2' of oil in precipitant line
 - If oil flows past this point, increase precipitant flow rate to equalize the pressure
11. Once sufficient back pressure has been generated, oil will begin to flow out the back pressure regulator
12. Ensure that experimental flow rates are set on the pumps and allow precipitant to slowly push oil out of line
13. Only oil will be flowing through the system for the start of the experiment. Both the oil and precipitant line will be supplying oil into the mixing tee until the air pocket in the precipitant line is pushed through the mixing tee
14. Allow oil and precipitant to flow until stop time
15. Every 30 minutes, record each pump pressure and differential pressure in laboratory notebook

Prefilling the Deposition Apparatus with Oil

1. Print out experimental header sheet
 - Determine if there is sufficient oil/precipitant for the time, flow rate, concentration, etc. for the full experiment
2. Construct the tubing system completely except:
 - Do not connect the back pressure regulator
 - Do not connect the lines to the pressure transducer
 - Make sure that precipitant line has at least 2 inches of air between the outlet and the fluid
3. Once everything is constructed, the next step is to purge the system of air
4. Begin running the oil pump at 1-2 mL/min
5. Oil will begin to flow into the precipitant line. Increase the precipitant flow rate gradually (starting as low as 0.05 mL/min) to ensure the oil does not reach the precipitant reservoir. Also, do not increase flow rate so much that the air pocket between oil and precipitant collapses or precipitant enters the system before prefilling is complete.

6. Oil will fill to the $+\Delta P$ lines and flow up
7. Before the oil starts to flow out the disconnected $+\Delta P$ outlets, connect to the large tubing filled with water, the $+\Delta P$ bleeding is finished
8. Oil will continue to fill the system and travel up the $-\Delta P$ line
9. Before the oil flows out of the $-\Delta P$ line, connect it to the large tube filled with water attached to the pressure transducer
10. Once effluent line is bled, connect to back pressure regulator
11. Stop the pumps

Shutdown and Cleaning the Apparatus

1. When experiment is finished, shut off pumps
2. Immediately after turning off pumps, close the Micro-Splitter valve
3. Slowly open the Micro-Metering valve to relieve the system pressure
4. Disconnect capillary lines from connections
5. Hold a paper towel at the outlet of the capillary test section to drain excess oil
6. Using a syringe, gently push air through the capillary test section to remove the excess oil in the capillary
7. Link all capillary lines together with unions
8. Flow toluene through the joined capillary lines until the effluent is colorless
9. Clean tees and other fittings with toluene
 - Hold fitting with tweezers above collection container
 - Squirt toluene to clean fittings
 - Place fitting on paper towel to allow solvent to evaporate

APPENDIX C

CFD Simulations on Capillary Deposition Apparatus Mixing for Chapter II

To investigate the mixing in the capillary deposition apparatus, computational fluid dynamic (CFD) simulations were performed on the mixing tee and connecting line. The goal was to determine if the oil and heptane were fully mixed at the desired bulk composition when the mixture enters the capillary. The simulation was performed in FLUENT v.12.0.16 using the following settings: 3D, laminar, pressure based and species. The grid was generated with GAMBIT v.2.4.6 and consisted of 242,654 tetrahedral cells. The mixing frit was modeled as porous media (porosity = 0.35, random close packed spheres) and no additional structural features of the frit were considered. Simulating the frit in this manner will represent the “worst possible case scenario” for system mixing because none of the advantageous structural features of the frit are represented and only the superficial velocity is increased in the frit. The mixing system consists of oil and heptane inlet lines (0.03” ID) connected to the mixing tee (round 0.02” ID thru holes). The frit is cylindrical (1/16” in diameter and 1/16” in length) and located at the outlet of the thru hole. The connecting line is a 5 cm section of 0.03” ID capillary. The true length of the connecting line in experiments is 5 cm, however, the CFD simulation used a 2” length section. The

difference between 5 cm and 2" is less than 2% and the difference will not influence the conclusions of the CFD simulation results. The oil and heptane entrance lines were sufficiently long in order to ensure that each line had fully developed hydrodynamics by the entrance of the mixing tee (*Wilkes, 2006*).

The diffusivity for heptane in oil was estimated by the Hayduk-Minhas correlation and was calculated to be $4.04 \times 10^{-10} \text{ m}^2/\text{s}$ (*Hayduk and Minhas, 1982; Green and Perry, 2007*). Heat capacities and thermal conductivities were not considered because the simulation was performed isothermally at 60°C. Table C.1 lists the required material properties used in simulation and Figure C.1 shows both the results and dimensions of the mixing system.

Table C.1: Input parameters for the CFD simulations.

<i>Compound</i>	<i>Density (kg/m³)</i>	<i>Viscosity (mPa*s)</i>
Oil	869	8.93
Heptane	680	0.276

CFD Simulation Results The CFD simulation result converged to an acceptable level and the results can be seen in Figures C.1 and C.2. Three important views of the mixing system are presented. The top view, Figure C.1, shows a horizontal cross section of the oil (from the right) and heptane (left) mixing in the frit and connecting line. Heptane is less dense than oil, and thus due to the low flow rate, gravitational flow is significant. The side view (Figure C.2 - Left) clearly indicates that the concentration of heptane is higher near the top of the mixing frit and at the solution is not well mixed by the exit of the frit. As can be seen in the outlet cross section (Figure C.2 - Right), the oil and heptane are homogenous by the outlet of the mixing section, in support of good mixing for the deposition experiments.

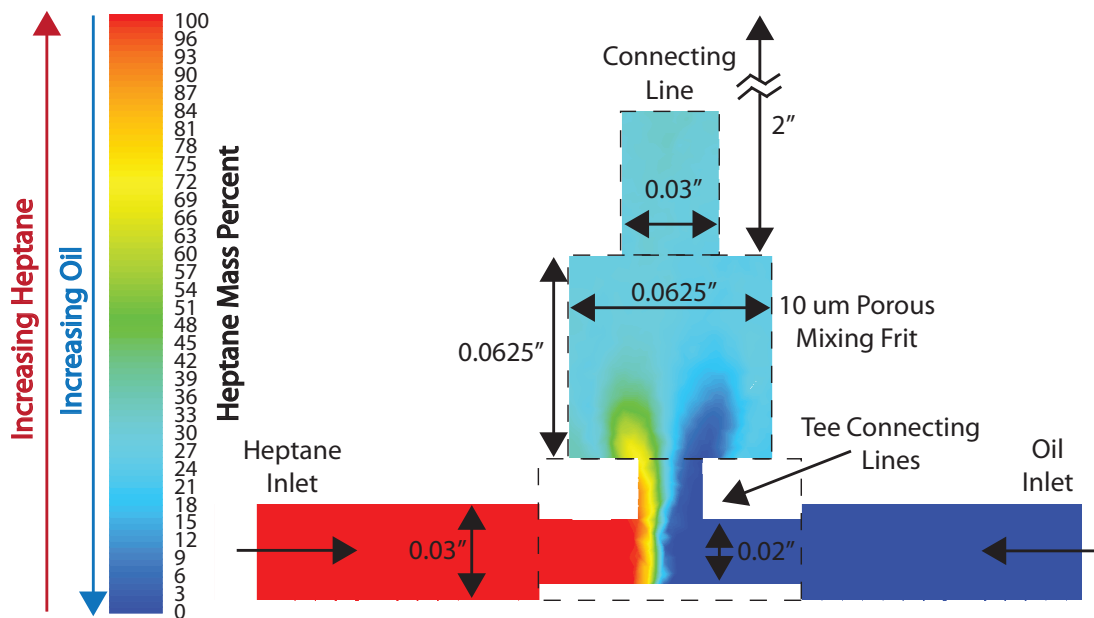


Figure C.1: Top view of the CFD simulations of the mixing system. NOTE: the connecting line extends for 5 cm but not all of the result was shown due to the large aspect ratio.

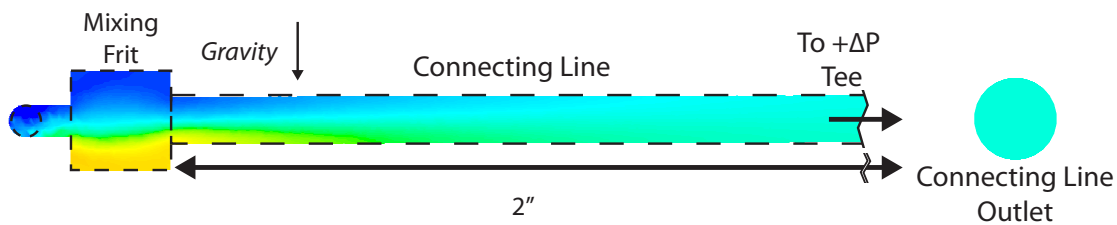


Figure C.2: Side view (left) and outlet view (right) of the CFD simulations of the mixing system. NOTE: the connecting line extends for a full 5 cm but figure was shortened due to the large aspect ratio. By the time the mixture reaches the outlet, it is completely mixed.

APPENDIX D

Derivation of Pressure Drop Comparisons for Deposit Locations for Chapter II

To determine the uniformity or the location of the asphaltene deposit axially, independent experiments were performed in a long and short capillary. Four scenarios are possible for the deposit to form inside a capillary:

1. The deposit is uniform along the length of the capillary
2. The deposit is non-uniform and contained entirely in the length of the short capillary
3. The deposit is non-uniform and present in both the initial short section and the long section
4. The deposit is non-uniform and present near the outlet of the long capillary, with no deposition near the inlet in the short section

First, if the deposit is uniform along the length of the capillary, the pressure drop as a function of time scaled by the length will be the same for a long or short capillary. This can be seen by comparing the Hagen-Poiseuille equation for a long and short capillary:

$$\Delta P_{Long}(t) = \frac{8\mu L_{Long}Q}{\pi r_{Long}^4(t)} \quad (D.1)$$

$$\Delta P_{Short}(t) = \frac{8\mu L_{Short}Q}{\pi r_{Short}^4(t)} \quad (D.2)$$

where, ΔP is the pressure drop through the capillary, μ is the viscosity, Q is the flow rate and r is the capillary radius. If the deposit is uniform, the radius will be changing the same between the long and short capillary and uniformly along the length of the capillary:

$$r^4(t) = r_{Long}^4(t) = r_{Short}^4(t) \quad (D.3)$$

Solving the pressure drop equations of the long and short capillary for $r^4(t)$ yields:

$$\frac{8\mu L_{Long}Q}{\pi P_{Long}(t)} = \frac{8\mu L_{Short}Q}{\pi P_{Short}(t)} \quad (D.4)$$

It is clear that once you eliminate the flow rate, viscosity and constants that the following relation exists for a uniform deposit is capillaries of two lengths are compared:

$$\frac{P_{Long}(t)}{L_{Long}} = \frac{P_{Short}(t)}{L_{Short}} \quad (D.5)$$

The second possibility is if the deposit is non-uniform enough that it is entirely contained within the short capillary and preferentially forms near the inlet. To determine the relationship between a long and short capillary, lets assume that the capillary is split into two sections: the first section contains the entire deposit, “Deposit” and the second contains no deposit “Clean”. Neglecting and pressure drop associated with expansion, the Hagen-Poiseuille can be split into the pressure drop from the two sections.

$$\Delta P(t) = \frac{8\mu L_{Deposit} Q}{\pi r_{Deposit}^4(t)} + \frac{8\mu L_{Clean} Q}{\pi r_o^4(t)} = \frac{8\mu Q}{\pi} \left(\frac{L_{Deposit}}{r_{Deposit}^4(t)} + \frac{L_{Clean}}{r_o^4(t)} \right) \quad (D.6)$$

At the start of the experiment there is no deposit, and an initial pressure drop, ΔP_o can be measured:

$$\Delta P_o(t) = \frac{8\mu L Q}{\pi r_o^4(t)} \quad (D.7)$$

$$L = L_{Deposit} + L_{Clean} \quad (D.8)$$

where r_o is the initial radius. If we shift both the long and short capillaries by their initial pressure drops:

$$\Delta P_{Short}(t) - \Delta P_{o,Short}(t) = \frac{8\mu Q}{\pi} \left(\frac{L_{Deposit}}{r_{Deposit}(t)^4} + \frac{L_{Clean,Short}}{r_o^4} - \frac{L_{Short}}{r_o^4} \right) \quad (D.9)$$

$$= \frac{8\mu Q L_{Deposit}}{\pi} \left(\frac{1}{r_{Deposit}(t)^4} - \frac{1}{r_o^4} \right) \quad (D.10)$$

$$\Delta P_{Long}(t) - \Delta P_{o,Long}(t) = \frac{8\mu Q}{\pi} \left(\frac{L_{Deposit}}{r_{Deposit}(t)^4} + \frac{L_{Clean,Long}}{r_o^4} - \frac{L_{Long}}{r_o^4} \right) \quad (D.11)$$

$$= \frac{8\mu Q L_{Deposit}}{\pi} \left(\frac{1}{r_{Deposit}(t)^4} - \frac{1}{r_o^4} \right) \quad (D.12)$$

Both the long and short capillary equations reduce to the same form, and we can thusly conclude that:

$$\Delta P_{Long}(t) - \Delta P_{o,Long}(t) = \Delta P_{Short}(t) - \Delta P_{o,Short}(t) \quad (\text{D.13})$$

The relation above says that if we compare $\Delta P(t) - \Delta P_o(t)$, as is the standard procedure for the pressure drop results, the results from a long and short capillary will be the same if the second case is occurring.

The third scenario is where the deposit forms non-uniformly but the deposit is not entirely contained within the short capillary. In such a case, neither the scaling or shifting derived above for the first and second scenarios will unify the long and short capillary results. The fourth scenario is where the deposit exists near the outlet of the long capillary, in which case, no deposition will be measured in the short capillary.

APPENDIX E

Additional Scattering Calculations and Results from Chapter IV

Density and Elemental Composition of the Oil Solvent

The density of the crude oil solvent can be calculated on an asphaltene-free basis by assuming ideal mixing of the crude oil solvent and asphaltenes. Starting with a volume balance and assuming no volume change in mixing:

$$v_{Oil} = v_{Asph} + v_{Oil,Solv} \quad (\text{E.1})$$

where v_i is the volume of component i . Subscript *Oil* is for the total crude oil, *Asph* is for the asphaltene fraction, and *Oil,Solv* is for the crude oil solvent (i.e., asphaltene-free). Using the individual densities, the above expression can be rewritten:

$$\frac{m_{Oil}}{d_{Oil}} = \frac{m_{Asph}}{d_{Asph}} + \frac{m_{Oil,Solv}}{d_{Oil,Solv}} \quad (\text{E.2})$$

where m_i is the mass and d_i is the mass density. The above expression can be

rewritten in terms of the mass fraction of asphaltenes in the oil, $F_{Asph}^{Oil} = m_{Asph}/m_{Oil}$, with units of g of asphaltenes per g of crude oil:

$$\frac{m_{Oil}}{d_{Oil}} = \frac{m_{Oil}F_{Asph}^{Oil}}{d_{Asph}} + \frac{(1 - F_{Asph}^{Oil})m_{Oil}}{d_{Oil,Solv}} \quad (E.3)$$

Superscripts represent the basis of the measurement (e.g., F_{Asph}^{Oil} is the mass fraction of asphaltenes on an oil basis). The above expression can then be rearranged to solve for the density of the oil solvent, noting that the mass of the oil cancels out:

$$d_{Oil,Solv} = \frac{d_{Oil}d_{Asph}(1 - F_{Asph}^{Oil})}{d_{Asph} - d_{Oil}F_{Asph}^{Oil}} \quad (E.4)$$

In order to get the most accurate measurement of oil composition, the asphaltenes were left in the crude oil for the elemental composition measurement. The following expression can be obtained for an elemental balance over element i :

$$m_{Oil}F_i^{Oil} = m_{Asph}F_i^{Asph} + m_{Oil,Solv}F_i^{Oil,Solv} \quad (E.5)$$

where F_i is the mass fraction of element i . The mass fraction of element i for the oil solvent (i.e., asphaltene free) can be obtained by rearranging the above expression:

$$F_i^{Oil} = \frac{m_{Asph}}{m_{Oil}}F_i^{Asph} + \frac{m_{Oil,Solv}}{m_{Oil}}F_i^{Oil,Solv} \quad (E.6)$$

$$F_i^{Oil} = F_{Asph}^{Oil}F_i^{Asph} + (1 - F_{Asph}^{Oil})F_i^{Oil,Solv} \quad (E.7)$$

$$F_i^{Oil,Solv} = \frac{F_i^{Oil} - F_{Asph}^{Oil}F_i^{Asph}}{(1 - F_{Asph}^{Oil})} \quad (E.8)$$

The mass density and mass fraction of each element in the oil solvent will be used to calculate the scattering length density.

Scattering Length Density and Contrast Calculation

The scattering length density (SLD), ρ , for a particular material can be determined by the following relation (*Lindner and Zemb, 2002*):

$$\rho = \frac{1}{V} \sum_{i=1}^N n_i b_i \quad (\text{E.9})$$

where n_i is the number of atoms in the sample volume of a particular element, b_i is the scattering length for that particular element and radiation type (neutrons vs. X-rays), and V is the volume over the summation. The summation is typically taken over one molecule, thus n_i is the number of atoms of type i in the molecule and V is the molecular volume. For neutrons, the scattering length of various elements and isotopes have been experimentally measured (*Feigin and Svergun, 1987*). For asphaltenes, the molecular weight and volume are not known, but the scattering length density can be calculated by the elemental composition and mass density, d :

$$\rho = \frac{d}{m} N_A \sum_{i=1}^N \frac{F_i}{A_{W,i}} b_i \quad (\text{E.10})$$

where F_i is the mass element i (mass fraction if the total mass, m , is taken to be unity), $A_{W,i}$ is the atomic weight of element i , N_A is Avogadro's number and d is the mass density of the material. The elemental compositions and calculated SLDs for the oil, asphaltenes and solvents can be found in Table E.1.

The SLD for a mixture of miscible liquids is the volume average of the individual SLDs. The volume fraction of oil solvent in the sample on an asphaltene free basis, $\phi_{Oil,Solv}^{Solv}$, can be calculated with the following equation:

$$\phi_{Oil,Solv}^{Solv} = \frac{v_{Oil,Solv}}{v_{Oil,Solv} + v_{Dil}} = \frac{m_{Oil,Solv}/d_{Oil,Solv}}{m_{Oil,Solv}/d_{Oil,Solv} + m_{Dil}/d_{Dil}} \quad (\text{E.11})$$

where the subscript *Dil* refers to the diluent (e.g., heptane precipitant). The mean SLD of the solvent (oil solvent + diluent), ρ_{Solv} , can be calculated by:

Table E.1: Elemental analysis (wt. %) and scattering length density (SLD) of solvents and asphaltenes

<i>Material</i>	<i>C</i>	<i>H</i>	<i>N</i>	<i>O</i>	<i>S</i>	<i>SLD</i> ($\times 10^{-6} \text{ \AA}^{-2}$)
Oil A	86.11	11.79	0.19	2.4	0.58	-
Oil A Asph.	88.83	6.83	0.71	1.54	1.2	1.80
Oil A Solv.	85.78	12.39	0.13	2.50	0.51	0.143
MO Asph.	84.24	6.36	1.29	1.91	4.5	1.80
d8-Toluene	-	-	-	-	-	5.66
d14-C7	-	-	-	-	-	6.30
h14-C7	-	-	-	-	-	-0.567

$$\rho_{Solv} = \phi_{Oil,Solv}^{Solv} \rho_{Oil,Solv} + (1 - \phi_{Oil,Solv}^{Solv}) \rho_{Dil} \quad (\text{E.12})$$

The scattering contrast, $\Delta\rho^2$, between asphaltenes and solvent is calculated by:

$$\Delta\rho^2 = (\rho_{Solv} - \rho_{Asph})^2 \quad (\text{E.13})$$

Mass Separated by Centrifugation

Each sample was centrifuged before loading into the scattering cells, and the separated mass was used to calculate the asphaltene volume fraction remaining in each sample. The centrifugation rotation speed and time were not high enough to remove any material below 50 nm in diameter and only insoluble asphaltenes were separated. Figure E.1 shows the mass of asphaltenes remaining in each sample, in units of g of asphaltenes per 100 g of crude oil. As expected, the amount of insoluble asphaltenes separated by centrifugation increased for all three oils as both the mixing time and heptane concentration increased. As the heptane concentration is increased, the oil-precipitant mixture is less capable of dispersing asphaltenes and the amount of asphaltenes precipitating increases. As the mixing time is increased, more asphaltenes are separated by centrifugation because the asphaltenes have had

more time to aggregate and grow to a separable size (*Maqbool et al.*, 2011a). At low heptane concentrations, virtually no material was separated from each oil.

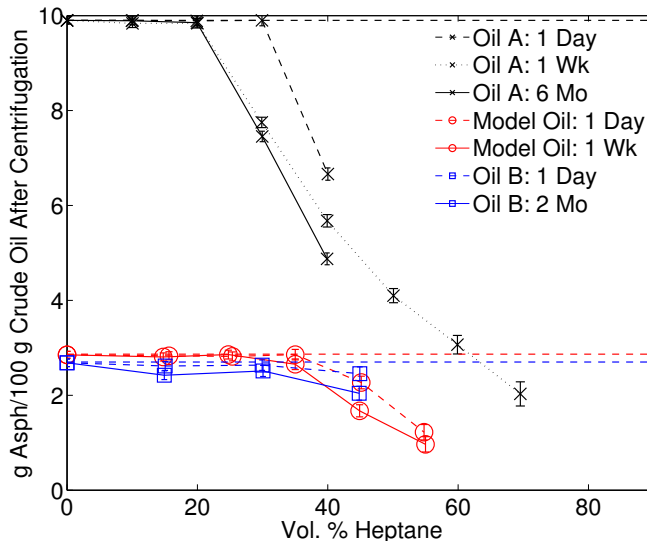


Figure E.1: The quantity of heptane-insoluble asphaltenes remaining in each sample after centrifugation in units of g asphaltenes per $100 g$ crude oil. Dashed lines represent the total asphaltene contents for Oil A, Oil B and the MO.

The quantity of asphaltenes precipitating from a mixture of 40% heptane in Oil A increases from one week to six months, as seen in Figure E.1, while the R_g and M_W remain unchanged, shown in Figures 6 and 7. Two possible explanations for this observation are proposed. First, oxidation effects could cause additional asphaltenes to slowly precipitate over time (*Beck et al.*, 2005); however, the samples were sealed and unopened between sample preparation and performing the scattering experiments. An alternative explanation is that there is a slow rearrangement of nanoaggregates and fractal clusters to free an insoluble asphaltene molecule that is trapped near the core or center of mass. In either scenario, because the scattering profiles superimpose between the one week and 6 month mixing time samples after normalizing by the volume fraction (not shown), the amount of asphaltenes precipitating between the two samples is not significant to change the overall structure of the asphaltene clusters.

Volume Fraction of Asphaltenes

The mass separated from each sample by centrifugation can be used to determine the volume fraction of asphaltenes remaining for normalization of the scattering results. Assuming ideal mixing and using a basis of 1 g of crude oil in each sample, the volume fraction of each component can be determined. The mass of asphaltenes in each sample before centrifugation, m_A^0 , and the mass of the oil solvent, $m_{Oil,Solv}$ can be determined from the the following relations:

$$m_A^0 = F_{Asph}^{Oil} m_{Oil} \quad (\text{E.14})$$

$$m_{Oil,Solv} = (1 - F_{Asph}^{Oil}) m_{Oil} \quad (\text{E.15})$$

Each sample was prepared by weight measurements, so the mass fraction of oil, F_{Oil} , in each sample is known. Using the basis of 1 g of crude oil, the mass of the diluent in each sample, m_{Dil} , can be calculated:

$$F_{Oil} = \frac{m_{Oil}}{m_{Oil} + m_{Dil}} \Rightarrow m_{Dil} = \frac{1}{F_{Oil}} - 1 \quad (\text{E.16})$$

The initial (before centrifugation) mass for each component is now known and the volume for each component can be determined by:

$$v_i = \frac{m_i}{d_i} \quad (\text{E.17})$$

The mass of asphaltenes after centrifugation, m_A , can be calculated by:

$$m_A = m_A^0 - m_{Cent} \quad (\text{E.18})$$

where m_{Cent} is the mass of asphaltenes separated from the crude oil on a basis of 1 g of oil. The volume fraction of asphaltenes after centrifugation for each sample can be calculated with:

$$\phi_T = \frac{v_A}{V} = \frac{m_A/d_{Asph}}{m_A/d_{Asph} + m_{Oil,Solv}/d_{Oil,Solv} + m_{Dil}/d_{Dil}} \quad (\text{E.19})$$

The above relation is useful when it is desired to scale the scattering results by the total asphaltene volume fraction. The results in Figure E.1 have been converted to the volume fraction of asphaltenes remaining in each sample after centrifugation and are shown in Figure E.2. The volume fraction decreases linearly at low heptane concentrations due to dilution and once asphaltenes are separated due to precipitation, the asphaltene volume fraction drops below the simple dilution linear behavior. The volume fraction of a majority of the samples are below 5% percent and are in the dilute regime. Consequently, little influence on the scattering results from cluster position correlation is expected in most samples.

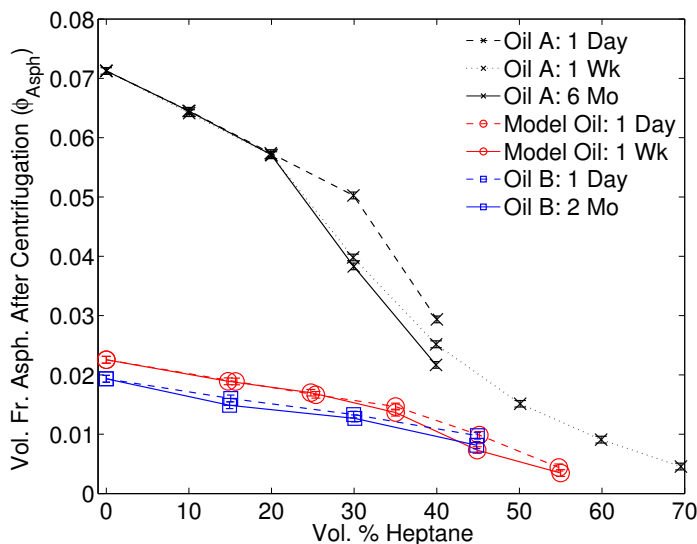


Figure E.2: The volume fraction of asphaltenes in each scattering sample after centrifugation as a function of mixing time, precipitant concentration, and oil type.

Additional Scattering Profiles

Figure E.3 shows the unmodified scattering profiles of Oil A and the Model Oil before and after incoherent scattering removal. As expected, the incoherent scattering background was significantly lower for the Model Oil due to the fully deuterated solvent. Both Oil A and the Model Oil showed Porod scattering ($I(q) \propto q^{-4}$) after incoherent background removal. Figure E.4 shows a before and after centrifugation comparison for Oil A and Oil A +20% heptane. The centrifuged and uncentrifuged Oil A samples show no noticeable difference, and the 20% heptane diluted sample shows only a minor decrease in scattering intensity at low- q . This is to be expected, and the centrifugation procedure may remove a small fraction of insoluble asphaltenes at 20% heptane, which will reduce the low- q scattering intensity.

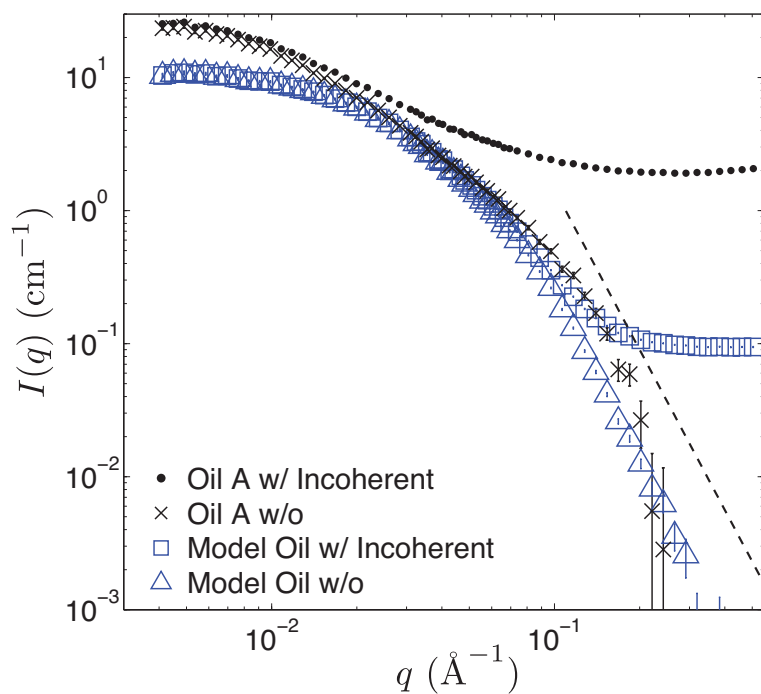


Figure E.3: SANS results of Oil A and Model Oil before and after incoherent background removal. Dashed line represents a slope of -4, characteristic of surface scattering. As expected, Oil A has significantly higher incoherent scattering due to the strong incoherent scattering of hydrogen.

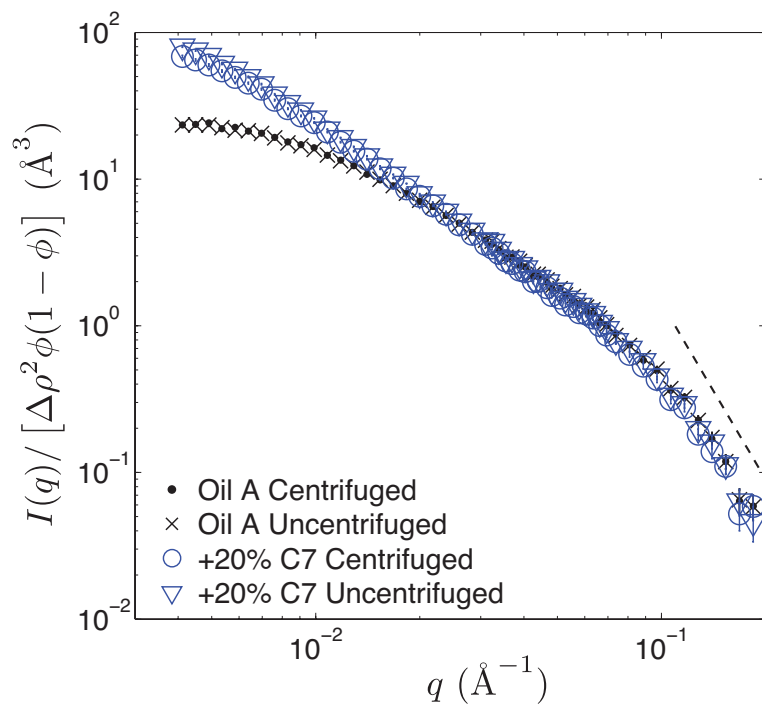


Figure E.4: SANS results of Oil A and Oil A +20% heptane before and after centrifugation. Dashed line represents a slope of -4, characteristic of surface scattering. The centrifugation procedure had no influence on the scattering of Oil A and resulting in a minor decrease in scattering intensity at low- q for Oil A +20% heptane.

Additional Discussion and Examples of the Scattering from Insoluble Asphaltenes

Neglecting asphaltene cluster correlation (i.e., $S(q) = 1$), the scattering intensity of a combined sample, $[I(q)]_{Combined}$, (i.e., containing both soluble and insoluble asphaltenes) can be written as the sum of the scattering from the soluble asphaltenes, $[I(q)]_{Soluble}$ and insoluble asphaltenes, $[I(q)]_{Insoluble}$:

$$[I(q)]_{Combined} = [\phi(1 - \phi)\Delta\rho^2V_pP(q)]_{Soluble} + [\phi(1 - \phi)\Delta\rho^2V_pP(q)]_{Insoluble} \quad (\text{E.20})$$

After sufficient time has elapsed, the insoluble asphaltenes have grown to a size where they can be separated by centrifugation, and the scattering of only the soluble asphaltene fraction, $[I(q)]_{Soluble} = [\phi(1 - \phi)\Delta\rho^2V_pP(q)]_{Soluble}$, can be measured. It should be noted that removing the insoluble asphaltenes will slightly increase the concentration of the soluble asphaltenes remaining in solution. Therefore, the volume fraction of soluble asphaltenes in the sample used to measure $[I(q)]_{Soluble}$ is slightly higher than the volume fraction of the same asphaltenes in the combined sample, which will slightly increase the scattering intensity. However, the removal of the insoluble asphaltenes was determined to alter the concentration of the soluble asphaltenes by less than 1.3% for all samples; consequently, this concentrating effect was neglected. The removal of the insoluble asphaltenes does not significantly alter the scattering of the soluble asphaltenes and the combined scattering profile, $[I(q)]_{Combined}$, can be determined by the following relation, without concern for the changes in volume fraction:

$$[I(q)]_{Combined} = [I(q)]_{Soluble} + [I(q)]_{Insoluble} \quad (\text{E.21})$$

The above expression can be rearranged to extract the scattering from the insol-

uble asphaltene fraction, $[I(q)]_{Insoluble}$. Figures E.5, E.6, and E.7 show the scattering of the combined, soluble and insoluble asphaltenes for 40% heptane in Oil A, 45% d-heptane in the MO, and 55% d-heptane in the MO, respectively. For all results, the fractal dimension is higher for the insoluble asphaltenes. All samples use the day of mixing scattering result for the combined scattering profile and the one week mixing time result for the soluble asphaltene scattering profile.

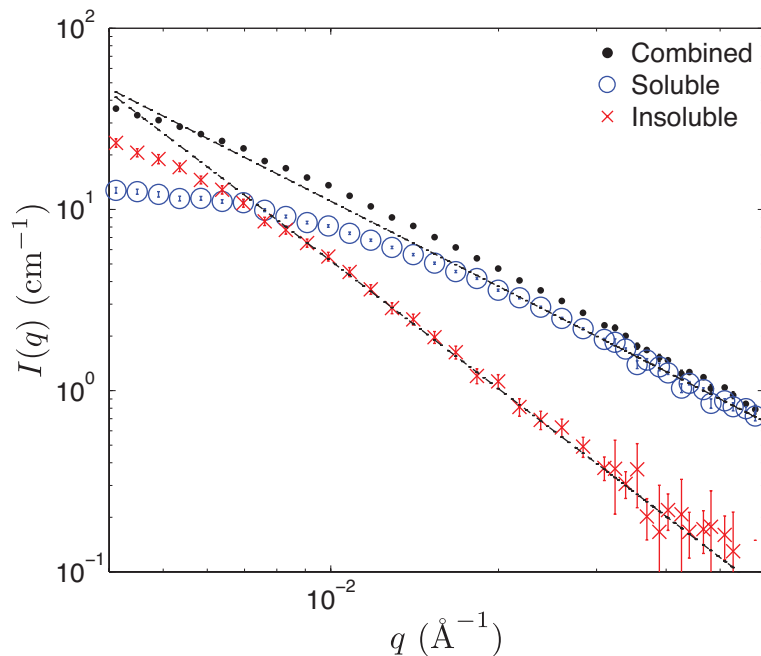


Figure E.5: Fractal dimension measurements of soluble (1.56 ± 0.06 , blue \circ) and insoluble (2.34 ± 0.04 , red X) asphaltenes in a sample of 40% heptane in Oil A. The scattering of the combined sample (black \bullet) from where the insoluble scattering is inferred is also included.

Volume Fraction from the Reduction in Scattering Intensity

For a two-level system (i.g., particles in a liquid environment) (*Lindner and Zemb, 2002*):

$$I(q) \propto \Delta\rho^2\phi(1 - \phi) \tag{E.22}$$

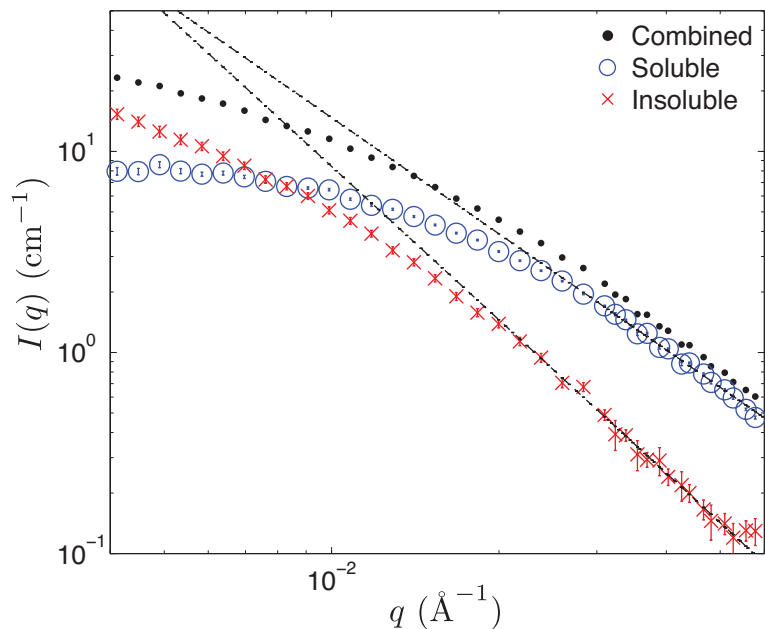


Figure E.6: Fractal dimension measurements of soluble (1.92 ± 0.05 , blue \circ) and insoluble (2.53 ± 0.07 , red X) asphaltenes in a sample of 45% d-heptane in MO. The scattering of the combined sample (black \bullet) from where the insoluble scattering is inferred is also included.

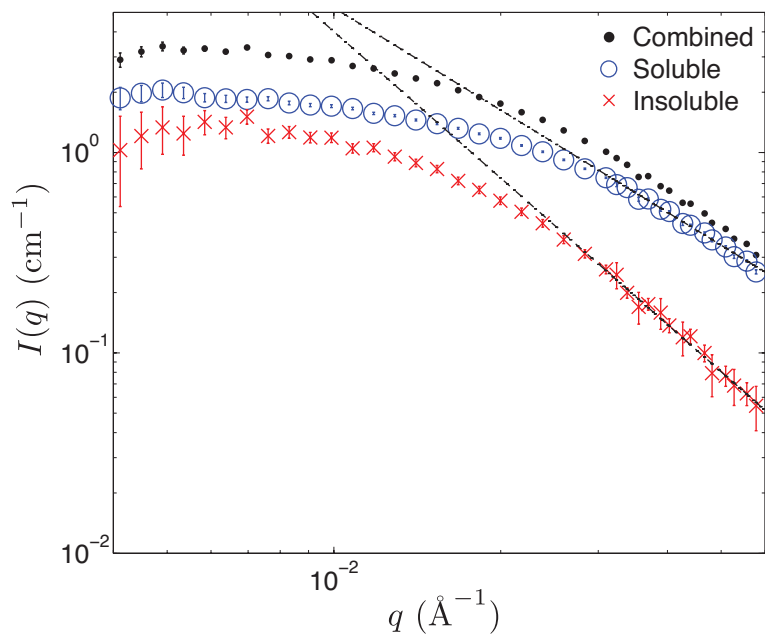


Figure E.7: Fractal dimension measurements of soluble (1.70 ± 0.07 , blue \circ) and insoluble (2.43 ± 0.13 , red X) asphaltenes in a sample of 55% d-heptane in MO. The scattering of the combined sample (black \bullet) from where the insoluble scattering is inferred is also included.

Assuming no change in the shape of the asphaltenes, the following relationship can be written for the relative scattering intensity between two samples (labeled i and j):

$$\frac{I_i(q)}{I_j(q)} = \frac{\Delta\rho_i^2\phi_i(1-\phi_i)}{\Delta\rho_j^2\phi_j(1-\phi_j)} \quad (\text{E.23})$$

The above expression can be rearranged to solve for the unknown volume fraction of sample i compared to a sample with known or assumed volume fraction, j :

$$\frac{I_i(q)/\Delta\rho_i^2}{I_j(q)/\Delta\rho_j^2}\phi_j(1-\phi_j) = \phi_i(1-\phi_i) \quad (\text{E.24})$$

Taking sample j as the undiluted Oil A, the volume fraction ϕ_j , is the volume fraction of heptane insoluble asphaltenes in Oil A. The volume fraction of asphaltenes in sample i can be calculated by solving the quadratic equation above. Once ϕ_i is obtained, it must be normalized by the volume fraction of crude oil, Φ , in the sample to obtain the asphaltene volume fraction on an oil basis, ϕ_i^{Oil} :

$$\phi_i^{Oil} = \frac{\phi_i}{\Phi} \quad (\text{E.25})$$

The volume fraction of asphaltenes in sample i on an oil basis, ϕ_i^{Oil} , is then subsequently converted to units of g soluble asphaltenes per 100 g crude oil for presentation in Figure 9.

APPENDIX F

Additional Scattering Calculations and Results from Chapter V

Material Properties

The scattering length density (SLD), ρ , of asphaltenes can be calculated by (*Feigin and Svergun, 1987*):

$$\rho = dN_A \sum_{i=1}^N \frac{F_i}{A_{W,i}} b_i \quad (\text{F.1})$$

where F_i , $A_{W,i}$, and b_i are the mass fraction, atomic weight and scattering length of element i , respectively. The scattering lengths of elements or isotopes are measured experimentally for SANS; however in SAXS, the scattering lengths are calculated using the atomic number and the Thomson scattering length of an electron (*Feigin and Svergun, 1987*). The scattering length of an element for SAXS increases linearly with the number of electrons (i.e., atomic number). All asphaltene densities are assumed to be 1.2 g/mL, and previous measurements have not deviated significantly from this value (*Roux et al., 2001; Eyssautier et al., 2011; Fenistein and Barré, 2001*). The elemental compositions and calculated SLDs for the two asphaltene types used

in this investigation (A1 and K1), and solvents can be found in Table F.1. Scattering contrast, $\Delta\rho^2$, is the difference between the SLD of asphaltenes and solvent squared. When comparing SAXS and SANS results, it is important to recognize that the scattering contrast is different for each radiation source.

Table F.1: Elemental analysis (wt. %) and scattering length density (SLD) of solvents and asphaltenes

<i>Material</i>	<i>C</i>	<i>H</i>	<i>N</i>	<i>O</i>	<i>S</i>	<i>Neutron SLD</i> ($\times 10^{-6} \text{ \AA}^{-2}$)	<i>X-Ray SLD</i> ($\times 10^{-6} \text{ \AA}^{-2}$)
A1 Asphaltenes	88.83	6.83	0.71	1.54	1.2	1.80	10.8
K1 Asphaltenes	84.24	6.36	1.29	1.91	4.5	1.80	10.6
(d-)Toluene	-	-	-	-	-	5.66	7.98
(d-)THF	-	-	-	-	-	5.96	7.83
1-MN	-	-	-	-	-	-	9.08

Two-State Aggregation Model Derivation

In a two-state aggregation model, the asphaltene nanoaggregation process is simplified to a single reversible “reaction” where n molecules associate into a single nanoaggregate and vice versa (*Debye, 1949; Israelachvili et al., 1976; Lisitza et al., 2009*):



The two-state model does not allow for the sequential breakup of particles into smaller and smaller aggregates. The asphaltene aggregate dissociation process was modeled with the two-state model in order to estimate the aggregation number and free energy change of asphaltene aggregation. The equilibrium constant of a reaction, K_{Eq} , is related to the activities of individual species, a_i , and the free energy change, ΔG , by the following relationships (*Sandler, 2006*):

$$K_{Eq} = \prod_i a_i^{\nu_i} = e^{\frac{-\Delta G}{RT}} \quad (\text{F.3})$$

where ν is the stoichiometric coefficient, R is the gas constant and T is the temperature. Assuming an ideal mixture, the activities are replaced by the mole fractions, x_i , and Equation (F.3) becomes:

$$K_{Eq} = \frac{x_A}{x_M^n} \quad (\text{F.4})$$

where x_A is the mole fraction of asphaltene nanoaggregates and x_M is the mole fraction of molecularly dispersed asphaltenes. The mole fraction of any single component in a mixture, x_i , can be related to their molar concentration, C_i , by:

$$C_i = x_i C_S \quad (\text{F.5})$$

where C_S is the total molar concentration of the mixture (solvent, asphaltene nanoaggregates, and molecularly dispersed asphaltenes). The samples investigated in this study are in the dilute regime and the molar concentration of the solvent is much greater than that of the asphaltene constituents; therefore, C_S can be accurately approximated as the molar concentration of the solvent. The free energy change of nanoaggregation can be rewritten as:

$$K_{Eq} = C_S^{n-1} \frac{C_A}{C_M^n} = e^{\frac{-\Delta G}{RT}} \quad (\text{F.6})$$

where C_A is the asphaltene nanoaggregate molar concentration and C_M is the molar concentration of molecularly dispersed asphaltenes. In each sample, the total molar concentration of asphaltenes, C_T , is a known quantity and can be calculated by:

$$C_T = nC_A + C_M = \frac{\phi^0 d_{Asph}}{M_{W,Asph}} \quad (\text{F.7})$$

where d_{Asph} is the asphaltene mass density (ca. 1.2 g/mL), and $M_{W,Asph}$ is the asphaltene molecule molecular weight. Without *a priori* knowledge of the aggregation number, the nanoaggregate molar concentration, C_A , can be calculated by:

$$C_A = \frac{C_T - C_M}{n} \quad (\text{F.8})$$

The concentration of asphaltene molecules can be determined from the scattering results using:

$$C_M = (1 - \chi) \frac{\phi^0 d_{Asph}}{M_{W,Asph}} \quad (\text{F.9})$$

Recall that χ is the fraction of asphaltenes in the aggregated state; however, analysis of the scattering results only provides $\left(\frac{\chi}{\chi_{Ref}}\right)$ because it is unknown what fraction of asphaltenes are in the aggregated state in the reference sample. The fraction of asphaltenes in the aggregated state in the reference sample, χ_{Ref} , is the only unknown parameter in the model and will be used as a tunable parameter. Substituting Equation (F.8) into Equation (F.6) yields:

$$e^{\frac{-\Delta G}{RT}} = C_S^{m-1} \frac{C_T - C_M}{nC_M^n} \quad (\text{F.10})$$

The above expression can be linearized to:

$$-\ln(C_T - C_M) = \frac{\Delta G}{RT} + (n - 1)\ln(C_S) - \ln(n) - n\ln(C_M) \quad (\text{F.11})$$

where $(-n)$ is the slope when $-\ln(C_T - C_M)$ is plotted against $\ln(C_M)$.

Additional SAXS and SANS Results

Figure F.1 additional scattering results as a function of asphaltene concentration for: (A) SAXS results of K1 asphaltenes in toluene, (B) SAXS results of K1 asphaltenes in THF, (C) SAXS results of both A1 and K1 asphaltenes in 1-MN, and (D) SAXS and SANS results for K1 asphaltenes in toluene. The results in (A) and (B) were used to estimate the fraction of asphaltenes in the aggregated state, χ . The same general conclusions and analysis for A1 asphaltenes in THF found in Figures 5.2 and 5.6 apply to the results in Figure F.1.

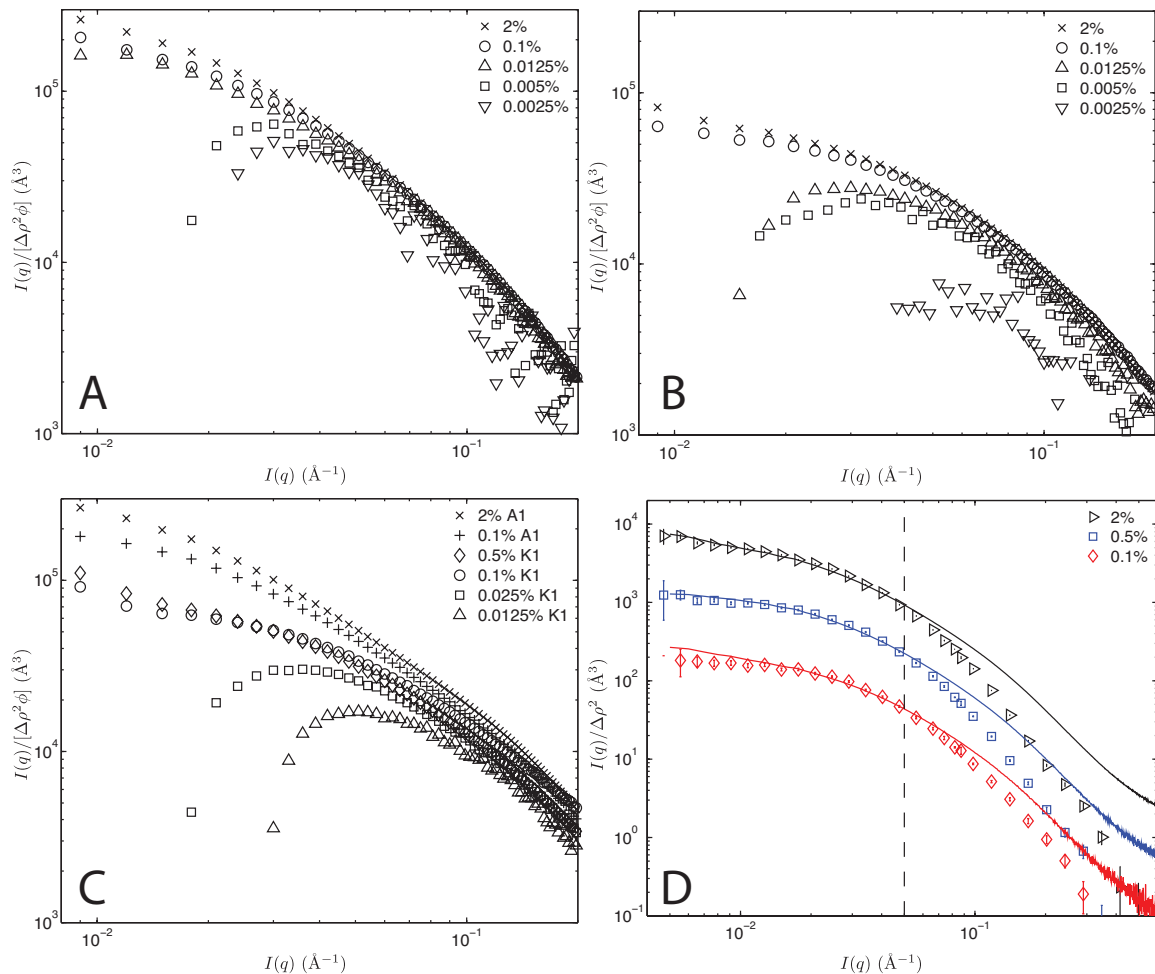


Figure F.1: SAXS results for K1 asphaltenes in toluene (A); SAXS results for K1 asphaltenes in THF (B); SAXS results for A1 and K1 asphaltenes in 1-MN (C); SAXS and SANS runs for K1 asphaltenes in toluene (D). Only one third of the measured scattering intensities are presented to avoid cluttering the figures. (A-C) are normalized by scattering contrast and volume fraction, while (D) is normalized by the volume fraction.

BIBLIOGRAPHY

BIBLIOGRAPHY

- Abraham, H. (1920), *Asphalts and Allied Substances*, 2 ed., D. Van Nostrand Company, New York, NY.
- Andersen, S. I., J. O. Jensen, and J. G. Speight (2005), X-ray diffraction of subfractions of petroleum asphaltenes, *Energy & Fuels*, *19*(6), 2371–2377, doi:10.1021/ef050039v.
- Anderson, J. A., C. D. Lorenz, and A. Travesset (2008), General purpose molecular dynamics simulations fully implemented on graphics processing units, *Journal of Computational Physics*, *227*(10), 5342–5359, doi:10.1016/j.jcp.2008.01.047.
- Andreatta, G., N. Bostrom, and O. C. Mullins (2005), High-q ultrasonic determination of the critical nanoaggregate concentration of asphaltenes and the critical micelle concentration of standard surfactants, *Langmuir*, *21*(7), 2728–2736, doi:10.1021/la048640t.
- Andrews, A. B., R. E. Guerra, O. C. Mullins, and P. N. Sen (2006), Diffusivity of asphaltene molecules by fluorescence correlation spectroscopy, *The Journal of Physical Chemistry A*, *110*(26), 8093–8097, doi:10.1021/jp062099n.
- Angle, C. W., Y. Longa, H. Hamzaa, and L. Lue (2006), Precipitation of asphaltenes from solvent-diluted heavy oil and thermodynamic properties of solvent-diluted heavy oil solutions, *Fuel*, *85*, 492–506.
- ASTM D 6560 - 00 (2005), Standard test method for determination of asphaltenes (heptane insolubles) in crude petroleum and petroleum products.
- Bardon, C., L. Barré, D. Espinat, V. Guille, M. H. Li, J. Lambard, J. C. Ravey, E. Rosenberg, and T. Zemb (1996), The colloidal structure of crude oils and suspensions of asphaltenes and resins, *Fuel Science and Technology International*, *14*(1-2), 203–242.
- Barré, L., S. Simon, and T. Palermo (2008), Solution properties of asphaltenes, *Langmuir*, *24*(8), 3709–3717.
- Barré, L., J. Jestin, A. Morisset, T. Palermo, and S. Simon (2009), Relation between nanoscale structure of asphaltene aggregates and their macroscopic solution properties, *Oil & Gas Science and Technology - Revue de l'Institut Français du Pétrole*, *64*(5), 617 – 628, doi:10.2516/ogst/2009022.

- Bayat, M., M. Sattarin, and M. Teymouri (2008), Prediction of asphaltene self-precipitation in dead crude oil, *Energy & Fuels*, *22*(1), 583–586, doi:10.1021/ef700536z.
- Beck, J., W. Y. Svrcek, and H. W. Yarranton (2005), Hysteresis in asphaltene precipitation and redissolution, *Energy & Fuels*, *19*(3), 944–947, doi:10.1021/ef049707n.
- Boek, E. S., H. K. Ladva, J. P. Crawshaw, and J. T. Padding (2008), Deposition of colloidal asphaltene in capillary flow: Experiments and mesoscopic simulation, *Energy Fuels*, *22*(2), 805–813.
- Boek, E. S., T. F. Headen, and J. T. Padding (2010), Multi-scale simulation of asphaltene aggregation and deposition in capillary flow, *Faraday Discussions*, *144*, 271–284.
- Boussingault, M. (1836), On the constitution of bitumens, *The London and Edinburgh Philosophical Magazine and Journal of Science*, *9*.
- Boussingault, M. (1837), Mémoire sur la composition des bitumes, *Annales de Chimie et de Physique*, *64*, 141–151.
- Bragg, W. L. (1913), The diffraction of short electromagnetic waves by a crystal, *Proceedings of the Cambridge Philosophical Society*, *17*, 43–57.
- Broseta, D., M. Robin, T. Savvidis, C. Féjean, M. Durandea, and H. Zhou (2000), Detection of asphaltene deposition by capillary flow measurements, *Society of Petroleum Engineers, SPE 59294*.
- Buenrostro-Gonzalez, E., C. Lira-Galeana, A. Gil-Villegas, and J. Wu (2004), Asphaltene precipitation in crude oils: Theory and experiments, *AIChE Journal*, *50*(10), 2552–2570.
- Cosultchi, A. Cosultchi, Bosch, P. Bosch, Lara, and V. Lara (2003), Small-angle x-ray scattering study of oil- and deposit-asphaltene solutions, *Colloid & Polymer Science*, *281*(4), 325–330, doi:10.1007/s00396-002-0772-2.
- Creek, J. L. (2005), Freedom of action in the state of asphaltenes: Escape from conventional wisdom, *Energy & Fuels*, *19*(4), 1212–1224.
- Cubberley, M. S., and B. L. Iverson (2001), ¹H NMR investigation of solvent effects in aromatic stacking interactions, *Journal of the American Chemical Society*, *123*(31), 7560–7563, doi:10.1021/ja015817m.
- De Smedt, E. J. (1893), Asphalt and asphalt pavements, *Paving and Municipal Engineering*, *5*(5), 205–208.
- Debye, P. (1949), Light scattering in soap solutions, *Annals of the New York Academy of Sciences*, *51*(4), 575–592, doi:10.1111/j.1749-6632.1949.tb27293.x.

- Deen, W. M. (1998), *Analysis of Transport Phenomena*, 1st ed., Oxford University Press, New York, NY.
- Deo, M., and M. Parra (2012), Characterization of carbon-dioxide-induced asphaltene precipitation, *Energy & Fuels*, *26*(5), 2672–2679, doi:10.1021/ef201402v.
- Dreiss, C. A., K. S. Jack, and A. P. Parker (2006), On the absolute calibration of bench-top small-angle x-ray scattering instruments: a comparison of different standard methods, *Journal of Applied Crystallography*, *39*(1), 32–38, doi:10.1107/S0021889805033091.
- Dwiggins, C. W. (1965), A small angle x-ray scattering study of the colloidal nature of petroleum, *The Journal of Physical Chemistry*, *69*(10), 3500–3506, doi:10.1021/j100894a041.
- Elimelech, M., and C. R. O’Melia (1990), Effect of particle size on collision efficiency in the deposition of brownian particles with electrostatic energy barriers, *Langmuir*, *6*(6), 1153–1163, doi:10.1021/la00096a023.
- Eskin, D., J. Ratulowski, K. Akbarzadeh, and S. Andersen (2011a), Modeling of asphaltene deposition in a production tubing, *AIChE Journal*, *58*(9), 2936–2948, doi:10.1002/aic.12800.
- Eskin, D., J. Ratulowski, K. Akbarzadeh, and S. Pan (2011b), Modelling asphaltene deposition in turbulent pipeline flows, *The Canadian Journal of Chemical Engineering*, *89*(3), 421–441, doi:10.1002/cjce.20507.
- Espinat, D., J. C. Ravey, V. Guille, J. Lambard, T. Zemb, and J. P. Cotton (1993), Colloidal macrostructure of crude-oil studied by neutron and x-ray small-angle scattering techniques, *Journal de Physique IV*, *3*(C8), 181–184.
- Evdokimov, I. N., N. Y. Eliseev, and B. R. Akhmetov (2006), Asphaltene dispersions in dilute oil solutions, *Fuel*, *85*(10–11), 1465–1472, doi:10.1016/j.fuel.2006.01.006.
- Eyssautier, J., P. Levitz, D. Espinat, J. Jestin, J. Gummel, I. Grillo, and L. Barré (2011), Insight into asphaltene nanoaggregate structure inferred by small angle neutron and x-ray scattering, *The Journal of Physical Chemistry B*, *115*(21), 6827–6837, doi:10.1021/jp111468d.
- Eyssautier, J., D. Espinat, J. Gummel, P. Levitz, M. Becerra, J. Shaw, and L. Barré (2012a), Mesoscale organization in a physically separated vacuum residue: Comparison to asphaltenes in a simple solvent, *Energy & Fuels*, *26*(5), 2680–2687, doi:10.1021/ef201411r.
- Eyssautier, J., D. Frot, and L. Barré (2012b), Structure and dynamic properties of colloidal asphaltene aggregates, *Langmuir*, *28*(33), 11,997–12,004, doi:10.1021/la301707h.

- Eyssautier, J., I. Henaut, P. Levitz, D. Espinat, and L. Barré (2012c), Organization of asphaltenes in a vacuum residue: A small-angle x-ray scattering (SAXS)–Viscosity approach at high temperatures, *Energy & Fuels*, *26*(5), 2696–2704, doi:10.1021/ef201412j.
- Feigin, L. A., and D. I. Svergun (1987), *Structure Analysis by Small-Angle X-Ray and Neutron Scattering*, 1 ed., Plenum Press, New York, NY.
- Fenistein, D., and L. Barré (2001), Experimental measurement of the mass distribution of petroleum asphaltene aggregates using ultracentrifugation and small-angle x-ray scattering, *Fuel*, *80*(2), 283–287, doi:10.1016/S0016-2361(00)00072-7.
- Fenistein, D., L. Barré, D. Broseta, D. Espinat, A. Livet, J.-N. Roux, and M. Scarsella (1998), Viscosimetric and neutron scattering study of asphaltene aggregates in mixed Toluene/Heptane solvents, *Langmuir*, *14*(5), 1013–1020, doi:10.1021/la9709148.
- Freund, H., et al. (2012), The composition of heavy petroleum, 13th International Conference on Petroleum Phase Behavior and Fouling, St. Petersburg Beach, Florida, June 10-14.
- Gawrys, K. L., and P. K. Kilpatrick (2005), Asphaltenic aggregates are polydisperse oblate cylinders, *Journal of Colloid and Interface Science*, *288*(2), 325–334, doi:10.1016/j.jcis.2005.03.036.
- Gawrys, K. L., P. M. Spiecker, and P. K. Kilpatrick (2003), The role of asphaltene solubility and chemical composition on asphaltene aggregation, *Petroleum Science and Technology*, *21*(3-4), 461–489.
- Glotzer, S. C., and M. J. Solomon (2007), Anisotropy of building blocks and their assembly into complex structures, *Nature Materials*, *6*(8), 557–562, doi:10.1038/nmat1949.
- Gonzalez, D. L., P. D. Ting, G. J. Hirasaki, and W. G. Chapman (2005), Prediction of asphaltene instability under gas injection with the PC-SAFT equation of state, *Energy & Fuels*, *19*(4), 1230–1234.
- Gonzalez, D. L., G. J. Hirasaki, J. Creek, and W. G. Chapman (2007), Modeling of asphaltene precipitation due to changes in composition using the perturbed chain statistical associating fluid theory equation of state, *Energy & Fuels*, *21*, 1231–1242.
- Gosh, R. E., S. U. Egelhaaf, and A. R. Rennie (2006), A computing guide for small-angle scattering experiments, 5th ed., <http://www.ill.eu/?id=2160>.
- Goual, L., M. Sedghi, H. Zeng, F. Mostowfi, R. McFarlane, and O. C. Mullins (2011), On the formation and properties of asphaltene nanoaggregates and clusters by DC-conductivity and centrifugation, *Fuel*, *90*(7), 2480–2490, doi:10.1016/j.fuel.2011.02.025.

- Green, D., and R. Perry (2007), *Perry's Chemical Engineers' Handbook*, 8 ed., McGraw-Hill Professional, New York, NY.
- Guinier, A., and G. Fournet (1955), *Small Angle Scattering of X-rays*, John Wiley & Sons Inc., New York, NY.
- Haji-Akbari, N., P. Masirisuk, M. P. Hoepfner, and H. S. Fogler (2013), A unified model for aggregation of asphaltenes, *Energy & Fuels*, *27*(5), 2497–2505, doi:10.1021/ef4001665.
- Hammami, A., C. H. Phelps, T. Monger-McClure, and T. M. Little (2000), Asphaltene precipitation from live oils: An experimental investigation of onset conditions and reversibility, *Energy & Fuels*, *14*(1), 14–18, doi:10.1021/ef990104z.
- Haskett, C. E., and M. Tartera (1965), A practical solution to the problem of asphaltene deposits - hassi messaoud field, algeria, *Journal of Petroleum Technology*, *17*(4), 387–391.
- Hayduk, W., and B. S. Minhas (1982), Correlations for prediction of molecular diffusivities in liquids, *The Canadian Journal of Chemical Engineering*, *60*(2), 295–299, doi:10.1002/cjce.5450600213.
- Headen, T. F., E. S. Boek, and N. T. Skipper (2009a), Evidence for asphaltene nanoaggregation in toluene and heptane from molecular dynamics simulations, *Energy & Fuels*, *23*(3), 1220–1229, doi:10.1021/ef800872g.
- Headen, T. F., E. S. Boek, J. Stellbrink, and U. M. Scheven (2009b), Small angle neutron scattering (SANS and v-SANS) study of asphaltene aggregates in crude oil, *Langmuir*, *25*(1), 422–428, doi:10.1021/la802118m.
- Hess, B. (2002), Determining the shear viscosity of model liquids from molecular dynamics simulations, *The Journal of Chemical Physics*, *116*(1), 209–217, doi:10.1063/1.1421362.
- Hoepfner, M. P., V. Limsakoune, V. Chuenmeechao, T. Maqbool, and H. S. Fogler (2013a), A fundamental study of asphaltene deposition, *Energy & Fuels*, *27*(2), 725–735, doi:10.1021/ef3017392.
- Hoepfner, M. P., C. Vilas Bôas Fávero, N. Haji-Akbari, and H. S. Fogler (2013b), The fractal aggregation of asphaltenes, *Langmuir*, *29*(28), 8799–8808, doi:10.1021/la401406k.
- Hoffmann, R., and L. Amundsen (2010), Single-phase wax deposition experiments, *Energy & Fuels*, *24*(2), 1069–1080, doi:10.1021/ef900920x.
- Huang, Z., H. S. Lee, M. Senra, and H. S. Fogler (2011), A fundamental model of wax deposition in subsea oil pipelines, *AIChE Journal*, *57*(11), 2955–2964, doi:10.1002/aic.12517.

- Israelachvili, J. N., D. J. Mitchell, and B. W. Ninham (1976), Theory of self-assembly of hydrocarbon amphiphiles into micelles and bilayers, *Journal of the Chemical Society, Faraday Transactions 2: Molecular and Chemical Physics*, 72(0), 1525–1568, doi:10.1039/F29767201525.
- Jaffe, A. M., K. B. Medlock III, and R. Soligo (2011), The status of world oil reserves: Conventional and unconventional resources in the future supply mix, James A. Baker III Institute for Public Policy, Rice University.
- Joshi, N. B., O. C. Mullins, A. Jamaluddin, J. Creek, and J. McFadden (2001), Asphaltene precipitation from live crude oil, *Energy & Fuels*, 15(4), 979–986, doi:10.1021/ef010047l.
- Katz, D. L., and K. E. Beu (1945), Nature of asphaltic substances, *Industrial & Engineering Chemistry*, 37, 195–200.
- Kilpatrick, P. K. (2012), Water-in-crude oil emulsion stabilization: Review and unanswered questions, *Energy & Fuels*, 26(7), 4017–4026, doi:10.1021/ef3003262.
- Klein, G. C., A. Angstrom, R. P. Rodgers, and A. G. Marshall (2006a), Use of Saturates/Aromatics/Resins/Asphaltenes (SARA) fractionation to determine matrix effects in crude oil analysis by electrospray ionization fourier transform ion cyclotron resonance mass spectrometry, *Energy & Fuels*, 20(2), 668–672, doi:10.1021/ef050353p.
- Klein, G. C., S. Kim, R. P. Rodgers, A. G. Marshall, and A. Yen (2006b), Mass spectral analysis of asphaltenes. II. detailed compositional comparison of asphaltenes deposit to its crude oil counterpart for two geographically different crude oils by ESI FT-ICR MS, *Energy & Fuels*, 20(5), 1973–1979, doi:10.1021/ef0600208.
- Klein, G. C., S. Kim, R. P. Rodgers, A. G. Marshall, A. Yen, and S. Asomaning (2006c), Mass spectral analysis of asphaltenes. i. compositional differences between pressure-drop and solvent-drop asphaltenes determined by electrospray ionization fourier transform ion cyclotron resonance mass spectrometry, *Energy & Fuels*, 20(5), 1965–1972, doi:10.1021/ef0600199.
- Kotlarchyk, M., and S.-H. Chen (1983), Analysis of small angle neutron scattering spectra from polydisperse interacting colloids, *The Journal of Chemical Physics*, 79(5), 2461–2469, doi:doi:10.1063/1.446055.
- Kraiwatanawong, K., H. S. Fogler, S. G. Gharfeh, P. Singh, W. H. Thomason, and S. Chavadej (2007), Thermodynamic solubility models to predict asphaltene instability in live crude oils, *Energy & Fuels*, 21(3), 1248–1255.
- Kurup, A. S., F. M. Vargas, J. Wang, J. Buckley, J. L. Creek, H. Subramani, and W. G. Chapman (2011), Development and application of an asphaltene deposition tool (ADEPT) for well bores, *Energy & Fuels*, 25(10), 4506–4516, doi:10.1021/ef200785v.

- Kurup, A. S., J. Wang, H. J. Subramani, J. Buckley, J. L. Creek, and W. G. Chapman (2012), Revisiting asphaltene deposition tool (ADEPT): field application, *Energy & Fuels*, doi:10.1021/ef300714p.
- Lawal, K. A., J. P. Crawshaw, E. S. Boek, and V. Vesovic (2012), Experimental investigation of asphaltene deposition in capillary flow, *Energy Fuels*, *26*(4), 2145–2153, doi:10.1021/ef201874m.
- Lindner, P., and T. Zemb (Eds.) (2002), *Neutrons, X-rays and light: scattering methods applied to soft condensed matter*, Elsevier Science B.V., Amsterdam, The Netherlands.
- Lisitza, N. V., D. E. Freed, P. N. Sen, and Y.-Q. Song (2009), Study of asphaltene nanoaggregation by nuclear magnetic resonance (NMR), *Energy & Fuels*, *23*(3), 1189–1193, doi:10.1021/ef800631a.
- Liu, Y. C., E. Y. Sheu, S. H. Chen, and D. A. Storm (1995), Fractal structure of asphaltenes in toluene, *Fuel*, *74*(9), 1352–1356, doi:10.1016/0016-2361(95)00098-P.
- Luo, P., and Y. Gu (2007), Effects of asphaltene content on the heavy oil viscosity at different temperatures, *Fuel*, *86*(7–8), 1069–1078, doi:10.1016/j.fuel.2006.10.017.
- Mack, C. (1932), Colloid chemistry of asphalts, *Journal of Physical Chemistry*, *36*(12), 2901–2914, doi:10.1021/j150342a005.
- Mansoori, G. A. (1997), Modeling of asphaltene and other heavy organic depositions, *Journal of Petroleum Science and Engineering*, *17*, 101–111.
- Maqbool, T., A. T. Balgoa, and H. S. Fogler (2009), Revisiting asphaltene precipitation from crude oils: A case of neglected kinetic effects, *Energy & Fuels*, *23*(7), 3681–3686, doi:10.1021/ef9002236.
- Maqbool, T., S. Raha, M. P. Hoepfner, and H. S. Fogler (2011a), Modeling the aggregation of asphaltene nanoaggregates in crude oil-precipitant systems, *Energy & Fuels*, *25*(4), 1585–1596, doi:10.1021/ef1014132.
- Maqbool, T., P. Srikiratiwong, and H. S. Fogler (2011b), Effect of temperature on the precipitation kinetics of asphaltenes, *Energy & Fuels*, *25*(2), 694–700, doi:10.1021/ef101112r.
- Martin, J. E., and B. J. Ackerson (1985), Static and dynamic scattering from fractals, *Physical Review A*, *31*(2), 1180–1182, doi:10.1103/PhysRevA.31.1180.
- Martin, J. E., and A. J. Hurd (1987), Scattering from fractals, *Journal of Applied Crystallography*, *20*(2), 61–78, doi:10.1107/S0021889887087107.
- Mason, T. G., and M. Y. Lin (2003a), Asphaltene nanoparticle aggregation in mixtures of incompatible crude oils, *Physical Review E*, *67*(5), 050401, doi:10.1103/PhysRevE.67.050401.

- Mason, T. G., and M. Y. Lin (2003b), Time-resolved small angle neutron scattering measurements of asphaltene nanoparticle aggregation kinetics in incompatible crude oil mixtures, *The Journal of Chemical Physics*, *119*(1), 565–571.
- McKenna, A. M., L. J. Donald, J. E. Fitzsimmons, P. Juyal, V. Spicer, K. G. Standing, A. G. Marshall, and R. P. Rodgers (2013), Heavy petroleum composition 3. asphaltene aggregation, *Energy & Fuels*, doi:10.1021/ef3018578.
- Meyer, E. A., R. K. Castellano, and F. Diederich (2003), Interactions with aromatic rings in chemical and biological recognition, *Angewandte Chemie International Edition*, *42*(11), 1210–1250, doi:10.1002/anie.200390319.
- Morimoto, M., T. Morita, T. Takanohashi, and K. Nishikawa (2013), Specific asphaltene aggregation in toluene at around 50 mg/L, *Journal of the Japan Petroleum Institute*, *56*(1), 58–59.
- Mullins, O. C., S. S. Betancourt, M. E. Cribbs, F. X. Dubost, J. L. Creek, A. B. Andrews, and L. Venkataramanan (2007), The colloidal structure of crude oil and the structure of oil reservoirs, *Energy & Fuels*, *21*(5), 2785–2794, doi:10.1021/ef0700883.
- Mullins, O. C., et al. (2012), Advances in asphaltene science and the yen-mullins model, *Energy & Fuels*, *26*(7), 3986–4003, doi:10.1021/ef300185p.
- Nabzar, L., and M. E. Aguilera (2008), The colloidal approach. a promising route for asphaltene deposition modelling, *Oil & Gas Science and Technology - Revue de l'Institut Français du Pétrole*, *63*(1), 21–35.
- Natarajan, A., J. Xie, S. Wang, Q. Liu, J. Masliyah, H. Zeng, and Z. Xu (2011), Understanding molecular interactions of asphaltenes in organic solvents using a surface force apparatus, *The Journal of Physical Chemistry C*, *115*(32), 16,043–16,051, doi:10.1021/jp2039674.
- Oh, K., T. A. Ring, and M. D. Deo (2004), Asphaltene aggregation in organic solvents, *Journal of Colloid and Interface Science*, *271*(1), 212–219, doi:10.1016/j.jcis.2003.09.054.
- Ortega-Rodriguez, A., S. Cruz, A. Gil-Villegas, F. Guevara-Rodriguez, and C. Lira-Galeana (2003), Molecular view of the asphaltene aggregation behavior in asphaltene-resin mixtures, *Energy & Fuels*, *17*(4), 1100–1108.
- Papoutsakis, E., D. Ramkrishna, and H. C. Lim (1980), The extended graetz problem with prescribed wall flux, *AIChE Journal*, *26*(5), 779–787, doi:10.1002/aic.690260511.
- Pedersen, J. S. (1997), Analysis of small-angle scattering data from colloids and polymer solutions: modeling and least-squares fitting, *Advances in Colloid and Interface Science*, *70*, 171–210, doi:10.1016/S0001-8686(97)00312-6.

- Peramanu, S., C. Singh, M. Agrawala, and H. W. Yarranton (2001), Investigation on the reversibility of asphaltene precipitation, *Energy & Fuels*, *15*(4), 910–917, doi:10.1021/ef010002k.
- Podgorski, D. C., Y. E. Corilo, L. Nyadong, V. V. Lobodin, B. J. Bythell, W. K. Robbins, A. M. McKenna, A. G. Marshall, and R. P. Rodgers (2012), Heavy petroleum composition. 5. compositional and structural continuum of petroleum revealed, *Energy & Fuels*, doi:10.1021/ef301737f.
- Pomerantz, A. E., M. R. Hammond, A. L. Morrow, O. C. Mullins, and R. N. Zare (2008), Two-step laser mass spectrometry of asphaltenes, *Journal of the American Chemical Society*, *130*(23), 7216–7217.
- Ramirez-Jaramillo, E., C. Lira-Galeana, and O. Manero (2006), Modeling asphaltene deposition in production pipelines, *Energy & Fuels*, *20*, 1184–1196.
- Rastegari, K., W. Y. Svrcek, and H. W. Yarranton (2004), Kinetics of asphaltene flocculation, *Industrial & Engineering Chemistry Research*, *43*(21), 6861–6870, doi: 10.1021/ie049594v.
- Ravey, J., G. Ducouret, and D. Espinat (1988), Asphaltene macrostructure by small angle neutron scattering, *Fuel*, *67*(11), 1560–1567, doi:10.1016/0016-2361(88)90076-2.
- Rogel, E., O. León, G. Torres, and J. Espidel (2000), Aggregation of asphaltenes in organic solvents using surface tension measurements, *Fuel*, *79*(11), 1389–1394, doi:10.1016/S0016-2361(99)00273-2.
- Roux, J.-N., D. Broseta, and B. Demé (2001), SANS study of asphaltene aggregation: Concentration and solvent quality effects, *Langmuir*, *17*(16), 5085–5092, doi:10.1021/la0101651.
- Sandler, S. I. (2006), *Chemical, Biochemical, and Engineering Thermodynamics*, 4 ed., John Wiley, Hoboken, N.J.
- Schaefer, D. W., J. E. Martin, P. Wiltzius, and D. S. Cannell (1984), Fractal geometry of colloidal aggregates, *Physical Review Letters*, *52*(26), 2371–2374, doi: 10.1103/PhysRevLett.52.2371.
- Sedghi, M., L. Goual, W. Welch, and J. Kubelka (2013), Effect of asphaltene structure on association and aggregation using molecular dynamics, *The Journal of Physical Chemistry B*, *117*(18), 5765–5776, doi:10.1021/jp401584u.
- Sheu, E. Y. (2006), Small angle scattering and asphaltenes, *Journal of Physics: Condensed Matter*, *18*(36), S2485–S2498.
- Sheu, E. Y., M. M. De Tar, D. A. Storm, and S. J. DeCanio (1992), Aggregation and kinetics of asphaltenes in organic solvents, *Fuel*, *71*(3), 299–302, doi:10.1016/0016-2361(92)90078-3.

- Singh, P., R. Venkatesan, H. S. Fogler, and N. Nagarajan (2000), Formation and aging of incipient thin film wax-oil gels, *AIChE Journal*, *46*(5), 1059–1074, doi:10.1002/aic.690460517.
- Sirota, E. (1998), Swelling of asphaltenes, *Petroleum Science and Technology*, *16*(3&4), 415–431.
- Sirota, E. (2005), Physical structure of asphaltenes, *Energy & Fuels*, *19*(4), 1290–1296.
- Sirota, E., and M. Lin (2007), Physical behavior of asphaltenes, *Energy & Fuels*, *21*(5), 2809–2815.
- Sivia, D. S. (2011), *Elementary Scattering Theory*, 1st ed., Oxford University Press Inc., New York, NY.
- Speight, J. G. (2007), *The Chemistry and Technology of Petroleum*, 4th ed., CRC Press/Taylor & Francis, Boca Raton, FL.
- Speight, J. G. (2009), *Enhanced Recovery Methods for Heavy Oil and Tar Sands*, Gulf Publishing Company, Houston, Texas.
- Spiecker, P. M., K. L. Gawrys, C. B. Trail, and P. K. Kilpatrick (2003), Effects of petroleum resins on asphaltene aggregation and water-in-oil emulsion formation, *Colloids and Surfaces A: Physicochemical and Engineering Aspects*, *220*(1-3), 9–27, doi:10.1016/S0927-7757(03)00079-7.
- Spielman, L. A., and S. Friedlander (1974), Role of the electrical double layer in particle deposition by convective diffusion, *Journal of Colloid and Interface Science*, *46*(1), 22–31, doi:10.1016/0021-9797(74)90021-6.
- Storm, D. A., and E. Y. Sheu (1995), Characterization of colloidal asphaltenic particles in heavy oil, *Fuel*, *74*(8), 1140–1145, doi:10.1016/0016-2361(95)00062-A.
- Tanaka, R., J. E. Hunt, R. E. Winans, P. Thiyagarajan, S. Sato, and T. Takanohashi (2003), Aggregates structure analysis of petroleum asphaltenes with small-angle neutron scattering, *Energy & Fuels*, *17*(1), 127–134, doi:10.1021/ef020019i.
- Teixeira, J. (1988), Small-angle scattering by fractal systems, *Journal of Applied Crystallography*, *21*(6), 781–785, doi:10.1107/S0021889888000263.
- Thiyagarajan, P., J. E. Hunt, R. E. Winans, K. B. Anderson, and J. T. Miller (1995), Temperature-dependent structural changes of asphaltenes in 1-methylnaphthalene, *Energy & Fuels*, *9*(5), 829–833, doi:10.1021/ef00053a014.
- Ting, P. D., G. J. Hirasaki, and W. G. Chapman (2003), Modeling of asphaltene phase behavior with the SAFT equation of state, *Petroleum Science and Technology*, *21*(3&4), 647–661.

- Torrey, D. (1894a), Physical properties of asphalts, *Paving and Municipal Engineering*, 6(5), 193–200.
- Torrey, D. (1894b), The properties of asphalt, *Paving and Municipal Engineering*, 6(3), 95–97.
- Trott, C. R., L. Winterfeld, and P. S. Crozier (2010), General-purpose molecular dynamics simulations on GPU-based clusters, *arXiv:1009.4330*.
- Vafaie-Sefti, M., and S. Mousavi-Dehghani (2006), Application of association theory to the prediction of asphaltene deposition: Deposition due to natural depletion and miscible gas injection processes in petroleum reservoirs, *Fluid Phase Equilibria*, 247(1-2), 182–189, doi:10.1016/j.fluid.2006.06.019.
- Vargas, F. M., D. L. Gonzalez, J. L. Creek, J. Wang, J. Buckley, G. J. Hirasaki, and W. G. Chapman (2009), Development of a general method for modeling asphaltene stability, *Energy & Fuels*, 23(3), 1147–1154, doi:10.1021/ef800666j.
- Vargas, F. M., J. L. Creek, and W. G. Chapman (2010), On the development of an asphaltene deposition simulator, *Energy & Fuels*, 24(4), 2294–2299, doi:10.1021/ef900951n.
- Wang, J. (2000), Predicting asphaltene flocculation in crude oils, Ph.D. thesis, New Mexico Institute of Mining & Technology, Socorro, New Mexico.
- Wang, J., and J. Buckley (2006), Estimate thickness of deposit layer from displacement test, http://baervan.nmt.edu/petrophysics/group/prrc_06-16.pdf.
- Wang, J., J. S. Buckley, and J. L. Creek (2004), Asphaltene deposition on metallic surfaces, *Journal of Dispersion Science and Technology*, 25(3), 1–12.
- Wang, S., J. Liu, L. Zhang, J. Masliyah, and Z. Xu (2010), Interaction forces between asphaltene surfaces in organic solvents, *Langmuir*, 26(1), 183–190, doi:10.1021/la9020004.
- Wiehe, I., and R. Kennedy (2000), The oil compatibility model and crude oil incompatibility, *Energy & Fuels*, 14(1), 56–59.
- Wilkes, J. O. (2006), *Fluid Mechanics for Chemical Engineers*, 2nd ed. ed., Prentice Hall PTR, Upper Saddle River, NJ.
- Yen, T. F., J. G. Erdman, and S. S. Pollack (1961), Investigation of the structure of petroleum asphaltenes by x-ray diffraction, *Analytical Chemistry*, 33(11), 1587–1594, doi:10.1021/ac60179a039.
- Zeng, H., Y.-Q. Song, D. L. Johnson, and O. C. Mullins (2009), Critical nanoaggregate concentration of asphaltenes by direct-current (DC) electrical conductivity†, *Energy & Fuels*, 23(3), 1201–1208, doi:10.1021/ef800781a.

- Zhao, B., and J. M. Shaw (2007), Composition and size distribution of coherent nanostructures in athabasca bitumen and maya crude oil, *Energy & Fuels*, 21(5), 2795–2804, doi:10.1021/ef070119u.
- Zhao, B., M. Becerra, and J. M. Shaw (2009), On asphaltene and resin association in athabasca bitumen and maya crude oil, *Energy & Fuels*, 23(9), 4431–4437, doi:10.1021/ef900309j.
- Zimm, B. H. (1948a), Apparatus and methods for measurement and interpretation of the angular variation of light scattering; preliminary results on polystyrene solutions, *The Journal of Chemical Physics*, 16(12), 1099–1116, doi:10.1063/1.1746740.
- Zimm, B. H. (1948b), The scattering of light and the radial distribution function of high polymer solutions, *The Journal of Chemical Physics*, 16(12), 1093–1099, doi:10.1063/1.1746738.